Numerical analysis of hysteresis in granular media down inclined plane

Clovis Lambert

RÉPUBLIQUE FRANÇAISE
Liberté Égalité Fraternité

Université de Toulouse

Doctorat de l'Université de Toulouse

préparé à Toulouse INP

Analyse numérique de l'hystérésis en milieux granulaires sur plan incliné

Thèse présentée et soutenue, le 26 novembre 2024 par

Clovis LAMBERT

École doctorale
MEGEP - Mécanique, Energétique, Génie civil, Procédés

Spécialité
Dynamique des fluides

Unité de recherche
IMFT - Institut de Mécanique des Fluides de Toulouse

Thèse dirigée par
Pascal FEDE

Composition du jury
M. Laurent LACAZE, Président, CNRS Occitanie Ouest
M. Olivier POULIQUEN, Rapporteur, Aix Marseille Université
M. Patrick RICHARD, Rapporteur, Université Gustave Eiffel
Mme Lydie STARON, Examinatrice, CNRS Paris-Centre
M. Raphaël MAURIN, Examinateur, Toulouse INP
M. Pascal FEDE, Directeur de thèse, Toulouse INP

Résumé

La transition entre le régime d'écoulement dense et le régime statique des milieux granulaires est un enjeu scientifique dans la description de ces milieux pour des applications autant industrielles, comme le stockage et transport de minerais, que géophysique, dans la modélisation et prédiction d'avalanches granulaires par exemple. Développer des modèles théoriques permettant de modéliser cette transition de phase est donc central pour la physique des milieux granulaires. Cette transition de phase a la particularité de présenter un comportement hystérétique : les conditions de changement d'état dépendent de l'histoire, c'est-à-dire du chemin de contraintes empreinté. Ce phénomène n'est pas pris en compte dans les modèles classique et empêche une description unifié des milieux granulaires dans les régimes solides et liquides. Son origine physique, entre effets d'inertie et frottement des grains, fait aujourd'hui encore débat dans la littérature.

Le présent travail de thèse a pour objectif d'étudier l'origine de l'hystérésis pour un milieu granulaire idéal dans une configuration de plan incliné rugueux, à partir d'une modélisation par éléments discrets. Le travail s'attache dans un premier temps à étudier qualitativement la réponse du milieu à la contrainte, c'est-à-dire à l'angle d'inclinaison du plan, mettant en évidence les régimes granulaires statiques et d'écoulements dense, en jeu dans cette transition de phase à laquelle est associée le phénomène d'hystérésis. La dynamique et la statique du milieu sont ensuite caractérisés de manière macroscopique à l'aide des variables d'état classiques décrivant la densité et l'écoulement du système. Une description de la micro-structure du système est aussi développée afin de mieux caractériser ces régimes, elle met en évidence l'importance du réseau de contact et plus particulièrement de l'évolution du nombre moyen de contacts entre grains avec l'angle d'inclinaison. L'influence de la dissipation collisionnelle entre grains est étudiée et aucun effet notable n'est observé sur les angles critiques définissant les conditions de stabilité du système ainsi que sur leur différence qui quantifie l'hystérésis. Le frottement inter-particulaire a, en revanche, un effet majeur sur ces quantités. Les résultats des simulations montrent que ce mécanisme de dissipation est, comme attendu, central dans la transition de phase et l'hystérésis.

Dans un second temps, afin de quantifier l'influence de l'inertie des grains sur le mécanisme d'hystérésis, l'effet d'un fluide environnant est modélisé au premier ordre dans les simulations. Les résultats montre un impact de la variation d'inertie des grains et mettent en évidence un effet combiné de l'inertie et du frottement sur l'hystérésis permettant de rationaliser les différents résultats de la littérature. Ensuite, afin d'établir une description quantitative de l'influence couplée de l'inertie et du frottement entre grains, les angles critiques ainsi que l'hystérésis sont caractérisés à l'aide de l'évolution de la micro-structure au niveau des transitions de phase lorsque le frottement et l'inertie des grains varient.

Finalement, cette étude permet de clarifier l'origine de l'hystérésis et propose une nouvelle interprétation de ce phénomène par le biais de la micro-structure. Elle pose ainsi les bases pour une modélisation plus complète du phénomène.

Abstract

The transition between dense flow and static granular regimes is a major scientific challenge in the description of granular media, both for industrial applications, such as mineral storage and transport, and for geophysical applications such as the modeling and prediction of granular avalanches. Developing theoretical models for this phase transition is therefore central for the physics of granular media. A particular feature of this phase transition is its hysteretic behavior: the conditions of transition between both regimes depend on the history, i.e. the stress path. This phenomenon is not taken into account in conventional models, and prevents a unified description of granular media in both solid and liquid regimes. Its physical origin, between inertia effects and grain friction, is still debated in the literature.

The aim of this work is to study the origin of hysteresis for an ideal granular medium in a rough inclined plane configuration, using discrete element modeling. The work begins with a qualitative study of the response of the medium to stress, i.e. to the angle of inclination of the plane, highlighting the dense flow and static granular regimes involved in this phase transition, which are associated with the hysteresis phenomenon. The dynamics and statics of the medium are then characterized macroscopically using classical state variables describing the density and flow of the system. A description of the microstructure of the system is also developed to better characterize these regimes, highlighting the importance of the contact network and, more specifically, the evolution of the average number of contacts between grains with the angle of inclination. On the one hand, the impact of dissipation by collisions between grains was studied and no significant effect was observed on the critical angles defining the system's stability conditions, or on their difference, which quantifies hysteresis. Conversely, inter-particle friction has a major effect on these quantities. Simulation results show that this dissipation mechanism is, as expected, central to phase transition and hysteresis.

Secondly, in order to quantify the influence of grains inertia on the hysteresis mechanism, the effect of a surrounding fluid is modeled at first order in the simulations. The results show the impact of varying grain inertia and highlight the combined effect of inertia and friction on hysteresis, rationalizing the various results reported in the literature. Then, in order to establish a quantitative description of the coupled influence of inertia and friction between grains, critical angles and hysteresis are characterized using the evolution of the micro-structure at phase transitions when friction and grains inertia are varied.

Finally, this study clarifies the origin of hysteresis and proposes a new interpretation of this phenomenon via the micro-structure. It thus lays the foundations for a more complete modeling of the phenomenon.

Remerciements

Mes années de doctorat s'achèvent et je suis désormais docteur. Je profite de ces dernières lignes de rédaction pour remercier toutes les personnes qui ont participé de près ou de loin à ces trois ans de travail.

Tout d'abord, merci à Toulouse INP d'avoir financé ce sujet de recherche. Je tiens ensuite à remercier les membres de mon jury de thèse pour avoir accepté d'en faire partie, pour avoir lu mon travail de thèse, avoir été présent lors de la soutenance et pour avoir contribué à rendre la discussion autour de mon sujet aussi intéressante et scientifiquement stimulante. En particulier, merci à Patrick Richard et Olivier Pouliquen d'avoir accepté d'être rapporteurs, d'avoir soigneusement analysé et évalué mon travail de recherche et d'avoir formulé des remarques et des questions aussi pertinentes. Merci à Lydie Staron d'avoir apporté une lecture très juste et fine sur ce sujet. Enfin, merci à Laurent Lacaze pour avoir présidé ce jury, ses retours et sa bienveillance ont été à l'image de ces années durant lesquelles son regard très avisé m'a beaucoup aidé durant mon doctorat. Je tiens à remercier aussi les membres de mon comité de suivi de thèse, Raphaelle Pouhet pour ses conseils et son accompagnement, Chris Johnson pour les échanges scientifiques qui se poursuivront à l'avenir, je l'espère.

Je souhaite aussi remercier mes encadrants de thèse sans qui je n'en serais pas là aujourd'hui. Je tiens à exprimer ma gratitude à Pascal Fede pour son regard extérieur, son esprit critique et sa rigueur, qui ont été précieux pour ma recherche, notamment lorsqu'il a fallu parfois recentrer les idées. Un immense merci à Raphaël Maurin sans qui ce sujet n'existerait pas. Merci d'avoir été un mentor du début à la fin, d'avoir su me laisser l'autonomie dont j'avais besoin tout en ayant une vision globale du sujet. Grâce à cet équilibre, nous avons mené de nombreux échanges autour de réflexions passionnantes, nous permettant peu à peu de formuler une compréhension de ce sujet aussi complexe que fondamental. Merci d'avoir porté et apporté beaucoup, tant pour ce sujet scientifique que pour ma formation de chercheur. J'ai particulièrement apprécié la bienveillance de ton encadrement, alliant exigence et sympathie et j'espère que l'on continuera à échanger et collaborer à l'avenir.

Merci aussi à tous les membres de l'IMFT de m'avoir accueilli, merci à Sylvie et Florence grâce à qui j'ai pu partir sereinement en conférences, merci à Sylvain pour ton humour et ta sympathie. Merci à Matthieu pour ton soutien, ta gentillesse et tes conseils dûment appréciés. Merci à Alexandre et Abigaël pour votre bonne humeur, j'ai apprécié partager un bout de votre quotidien. Merci à Bastien et à Noé à qui je souhaite bon courage pour la suite, je ne me fais aucun souci pour vos thèses !

Enfin, je souhaite remercier mes proches pour leur soutien et leur amour ou amitié durant ces trois années et je l'espère pour encore un moment. Merci à mes colocs Enzo, Riwan, Margot, Palo, Lala et Bapt. Merci Flore, bien sûr, pour tout ce que tu as fait ! Merci à ma famille et mes amis qui ont toujours été là lorsque j'en avais besoin, et pour me faire oublier la physique !

Contents

List of Symbols

d	Grains diameter
D	Dimension (2 or 3)
ρ_p	Grains density
ρ_f	Fluid density
η_f	Fluid dynamic viscosity
P	Isostatic pressure
P_g	Granular pressure
P_{max}	Maximum pressure a grain holds under the layer weight
$\dot{\gamma}$	Shear rate
Γ	Strain rate tensor
σ	Stress tensor
τ	Shear stress
$\mathcal{I}$	Inertial number
ϕ	Solid volume fraction
ϕ_J	Jamming solid volume fraction
ϕ_{RCP}	Random close packing granular density
ϕ_{RLP}	Random loose packing granular density
ϕ_c	Critical solid volume fraction in the static regime
V_g	Volume of a grain
N_p	Total number of grains
N_c	Total number of contacts
μ	Shear to normal stress ratio, effective granular friction
μ_{stop}	Critical shear to normal stress ratio at the cessation of flow
μ_{start}	Critical shear to normal stress ratio at the initiation of flow

$\Delta\mu$	Shear to normal stress ratio absolute hysteresis
μ_p	Inter-particle friction coefficient
θ	Plane inclination angle
θ_{stop}	Critical plane inclination angle at the cessation of flow
θ_{start}	Critical plane inclination angle at the initiation of flow
$\Delta\theta$	Plane inclination angle absolute hysteresis
h	Granular layer thickness
h_{stop}	Critical granular layer thickness at the cessation of flow
h_{start}	Critical granular layer thickness at the initiation of flow
u_p	Grain velocity
u	Granular medium velocity
v	Fluid velocity
$\mathcal{Z}$	Coordination number
$\mathcal{Z}_c$	Critical coordination number in the static regime
$\mathcal{Z}_{iso}$	Isostatic coordination number
s^c	Staticity criterion
A^c	Contact network anisotropy tensor
a^c	Contact network anisotropy amplitude
K	Isotropic elastic mudulus
G	Shear elastic modulus
E	Young modulus
ν	Poisson's ratio
χ	Sliding contact proportion
Ω	Proportion of particles free to rotate
α	Proportion of particles with one or less contacts
$\langle\rangle$	Averaging over various simulation runs for various plane configurations
St	Stokes number
κ	Relative normal contact stiffness
e_N	Restitution coefficient
r	Density ratio
Re	Reynolds number

Re_p	Particle Reynolds number
C_D	Drag coefficient
Δt	Resolution time step
τ_i	Characteristic inertial time
τ_{ff}	Characteristic free-fall time
τ_v	Characteristic viscous time
t_c	Characteristic contact time
L	Plane length
W	Plane width
$\delta\theta/\delta t$	Inclination angle rate

List of Figures

List of Tables

Chapter 1

Introduction

1.1 Context

Granular materials are usually defined as sets of solid grains. From sands on beaches to cereals, they represent a wide range of materials, placing them second on the list of the most common materials found on the global industry in terms of weight after water (*De Gennes*, 1999). Yet, the finding of a universal constitutive law remains elusive (*GDR MiDi*, 2004; *Forterre and Pouliquen*, 2008; *Kamrin et al.*, 2024). The complexity of such law lies in the variety of granular systems including the diversity of granular materials themselves, as well as the environments in which they evolve. With this respect, the study of granular materials initiated by Coulomb (*Rhodes*, 1990; *Popova and Popov*, 2015), is the subject of several scientific fields, from engineering to fundamental research, within which several branches have emerged over the years.
One of them is the geomechanics community that is an engineering and research community that study among others soil mechanics. Soils of various earth landscapes are composed of granular materials: canyons, deserts and dunes, rivers and coasts are examples of natural earth environments where granular materials evolves. Such canyons landscapes are also present on other planets of our solar system (*Greeley*, 2013). Another research field, called geomorphology, studies geophysical flows that changes landscapes shapes as presented above (*Jerolmack and Daniels*, 2019). Geomorphology studies a diverse number of systems at various timescales: geological timescales at which the earth itself is considered as a soft granular material leading to the study of mountains relaxation; shorter timescales, closer to laboratory experiment duration, at which coastal dynamic or sediment transport affects the morphology of coasts and river beds (*Maurin*, 2015); finally, very short timescales at which natural hazards occurs and can affect lives and infrastructures, such as granular avalanches, landslides or debris flows (*Delannay et al.*, 2017).

Granular materials are also presents in various industries: grain silo; excipients, granules and pills in pharmaceutical industry; mineral extraction and building industry (*Mollon*, 2015).

In view of the diversity of granular systems, their study is particularly complex. The latter complexity relies on a number of specific aspects linked to the nature of granular media and their applications. First, the grains size is a parameter that governs the existence

of several interactions. As such, the choice of a characteristic size of order $d > 100\mu m$ is made since above this limit Van der Waals interactions and air drag (without wind) are negligible. Similarly humidity effects are usually negligible or too complex to be considered. Solid contacts are then preponderant in granular materials with such size (*Andreotti et al.*, 2013).
In several applications, the number of particles in the granular medium considered is greater than 10 to 100 million and often than one billion. That raises time and data storage space cost issues for numerical simulations of many realistic systems, hence a discrete numerical description becomes inadequate and a continuous modeling prevails.
For such grains sizes, thermal fluctuations are negligible, raising issues to develop continuous descriptions. Indeed, thermal fluctuations allows fluids to explore stable configuration of minimum potential energy (Brownian motion in gas and liquids). In granular media these fluctuations are negligible in front of the weight of the grains. This implies, in the case of a grain pile for example, a multitude of local minimum of potential energy at which the medium is stable, i.e. not flowing. It is then difficult to develop a statistical/thermodynamic theory of granular media.
In granular systems, grains interact with each others with typical solid-solid repulsive forces. For example, in three-dimensional dense flows, with typical grains packing density above 30%, there are multiple contacts for each particle. A grain is on average in contact with about 2 to 4 other grains and a little more when not flowing, which makes interactions between grains more complex.
In addition, although humidity and air drag are usually neglected, in a numerous applications cited above, non-negligible fluid-particle interactions exist. These interactions are complex to model because of the presence of many particles that influence fluid environment and dynamics.
Finally, in many systems as grains silos, the macroscopic scale of the granular flow (characteristic size of the system geometry) is close to the characteristic size of a grain. It can then be difficult to define a representative volume for continuous description. It also raises issues about finite size effects or boundary conditions effects on the dynamic and stability of the materials.

Because of the intrinsic complexity of granular media, the classical approach in the physician community is to start from the characterization of idealized granular media before adding complexity progressively and returning to application. Then, we will consider in this work a granular medium made of spherical monodisperse grains interacting without cohesion.

1.2 Description of granular materials

The main characteristic of granular media can be illustrated with a little experience we have all made by taking sand in our hand: when the hand is closed the grains are immobile, it is not possible to crush the grains and the media is similar to a solid. If now we open the hand, the grains will first flow between the fingers as a liquid and then fall as a fine rain into the ground as a gas. Assembly of grains can then behaves as solids, liquids or gas.

1.2.1 The states of a granular media

To better characterize these three different states, let us consider a more rigorous approach. To do so, we consider a dry idealized granular medium, hence without fluid interactions, made of grains of diameter d and density ρ_p in a shear cell (see Figure (1.1)) at a confining pressure P and a shear rate $\dot{\gamma}$ imposed. The bottom plate of the cell

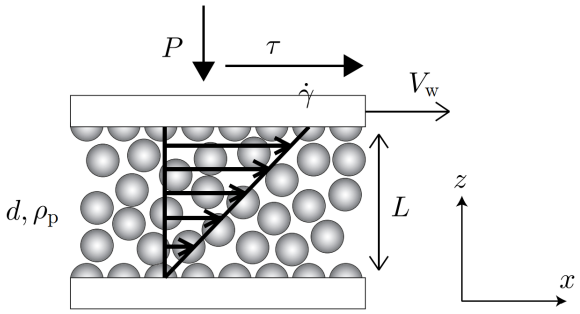

Figure 1.1 – Shear cell configuration. Source : *Andreotti et al.* (2013)

is steady and at a distance L from the upper plate that moves at an imposed velocity V_w. It is important to note that the volume is not imposed here so L is free to evolve. The shear rate can be expressed as $\dot{\gamma} = V_w/L$. At steady state, the problem can be considered on average as unidirectional so that the force balance reduces to: $\partial\sigma_{xz}/\partial z = 0$ and $\partial\sigma_{zz}/\partial z = 0$, which implies $|\sigma_{xz}| = \tau$ and $|\sigma_{zz}| = P$. Considering the rigid grain limit for which the grain deformation is negligible, and $L/d \gg 1$, only four parameters control the problem : d, ρ_p, $\dot{\gamma}$ and P. Those parameters involve three units : length, mass and time, so the Buckingham Π theorem (*Barenblatt*, 2003) tells us that the problem is controlled by $4 - 3 = 1$ dimensionless number. The one usually defined is the inertial number $\mathcal{I}$ and is written as:

$$\mathcal{I} = \frac{\dot{\gamma} d}{\sqrt{P/\rho_p}}. \tag{1.1}$$

It can also be expressed as a ratio of time scale (*Andreotti et al.*, 2013):

$$\mathcal{I} = \frac{t_{micro}}{t_{macro}}, \tag{1.2}$$

where $t_{macro} = \dot{\gamma}^{-1}$ is the horizontal characteristic time linked to the macroscopic deformation of the granular media under the shear rate and $t_{micro} = d/\sqrt{P/\rho_p}$ is the vertical characteristic time linked to the microscopic rearrangement of grains under the confining pressure, see Figure (1.2). At low inertial numbers, typically $\mathcal{I} < 10^{-3}$, the macroscopic deformation is slow compared to the time of local rearrangement, a regime characteristic of the plastic deformation of granular media. This is the quasi-static/static regime, where the assembly of grains is rigid under loading stress and behaves like a solid, see Figure (1.3). At higher inertial number, $10^{-3} < \mathcal{I} < 1$, and lower density, the assembly of grains densely flows, it behaves as a liquid; at even higher inertial number, $\mathcal{I} > 1$, and lower density, the assembly is diluted and flows as a gas, see Figure (1.3).

The solid state is associated to both static case for which $\mathcal{I} = 0$ (granular pile at rest) and to the quasi-static case where $0 < \mathcal{I} \leq 10^{-3}$ (*Andreotti et al.*, 2013). In the

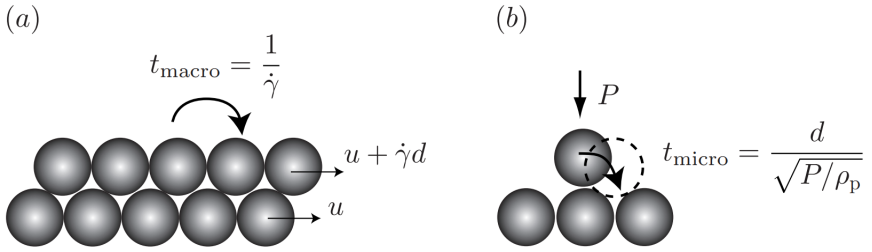

Figure 1.2 – Physical interpretation of the inertial number, $\mathcal{I}$, in term of (a) characteristic time of deformation of the media which corresponds to the time that takes a layer of grains of size d to be sheared from one diameter and (b) microscopic time of rearrangement under the confining pressure, P, which is the time that takes to a grain to fall in a hole of size diameter under the pressure P. Source : *Andreotti et al.* (2013).

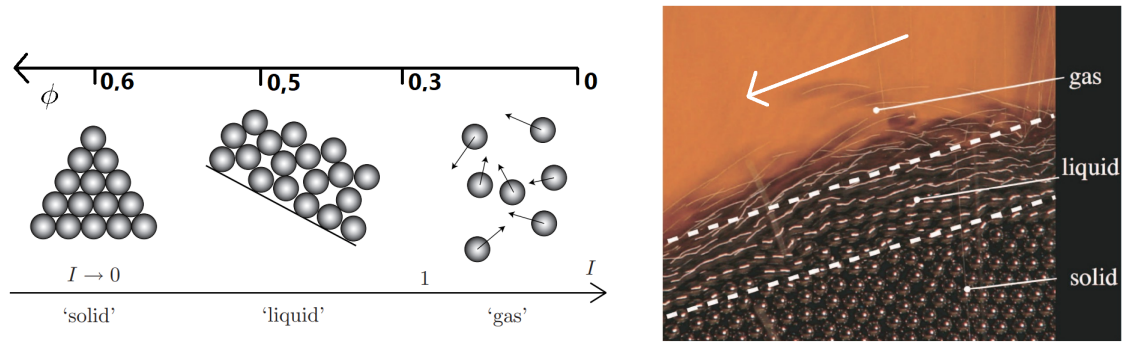

(a) (b)

Figure 1.3 – (a) Classification of the different regimes of a dry granular media : solid/liquid/gas as a function of the inertial number $\mathcal{I}$ and the volume fraction ϕ. (b) Pictures of the three different regimes of a granular media. Source : *Andreotti et al.* (2013).

former regime, the behavior of the system under loading stress is characterized by elastic deformations where the strain is low enough to induce reversible deformations. If strain reaches higher values, some failures are observed within the granular systems where local displacement become irreversible and rearrangement occurs, leading to a different position of some grains in the system. This regime is called plasticity or quasi-static regime, and remains in the solid regime since rearrangement leads in these cases to others equilibrium states of the medium that are still rigid. Solid regime of granular media is characterised at first order by the density of grain samples measured by solid volume fraction ϕ, defined for a sample of granular media of total volume V_{tot} :

$$\phi = \frac{V_g}{V_{tot}}, \tag{1.3}$$

where V_g is the volume occupied by grains in the sample. In the case of a mono-disperse sample of perfect spheres, the volume of each sphere is $V_p = 1/6\pi d^3$, with d the diameter of particles. Hence the volume fraction reads:

$$\phi = \frac{N_p \pi d^3}{6 V_{tot}}, \tag{1.4}$$

with N_p the total number of particles. In such systems, the densest samples corresponding to the highest possible value of the volume fraction, ϕ_{max}, is the densest crystal configuration in the face-centered cubic configuration where $\phi_{max} = \phi_{cfc} = 0.74$. It is the most stable state of the granular medium, at which the level of potential energy is the lowest possible. This theoretical result is rarely obtained in applications and experiments. Classically the volume fraction value of a given sample is observed to stand between two values (*Andreotti et al.*, 2013) : $\phi_{RLP} = 0,55 \leqslant \phi \leqslant \phi_{RCP} = 0,64$, where ϕ_{RLP} is the Random Loose Packing, i.e the loosest random stack at which the media is stable in the static regime under its own weight. The other bound, ϕ_{RCP}, is the Random Close Packing, i.e. the densest random stack. These limits are due to notions of geometrical equilibrium of grain arrangement and also to notions of mechanical equilibrium due to tangential friction generated by the surface roughness of the grains. This range of solid volume fraction illustrates the existence of a multitude of equilibrium states of a granular media, which greatly complicates their description.
In the view of developing continuous description of granular behavior in the solid regime some models were established equivalently to continuum solid materials, see Appendix A.1, for which the forces are homogeneously distributed at each points of the medium. If the same hypothesis is made for granular materials, it enables to write scaling laws in the static and quasi-static states. Such scaling laws are detailed in the book of *Andreotti et al.* (2013). Nevertheless, these theoretical scaling laws are not strictly verified experimentally. One of the main reasons is that it makes the assumption of homogeneous distribution of forces between grains, which is not observed in practice, demonstrating the complexity of granular systems and the need for more complex modeling.

When the inertial number, $\mathcal{I}$, is increased above unity and the volume fraction is low $\phi \lesssim 0,3$, see Figure (1.3), the macroscopic deformations are dominant and the behaviour of the media is similar to a gas. This regime is called the dilute flow. This regime is classically described with a kinetic theory approach based on the equation of Boltzmann for a gas (*Andreotti et al.*, 2013). Unlike a molecular gas, a granular gas includes an inelastic dissipation term, leading to more complex theoretical developments. This regime will nevertheless not be studied in the following work and is then not developed here.

In-between these regimes, for intermediate inertial number values, $10^{-3} < \mathcal{I} < 1$, the assembly of grains is in the dense flow regime. In this regime, macroscopic deformations as well as local rearrangements are of the same order and the system displays a liquid-like behaviour. In this regime, the system loses its rigidity and grains flow continuously. Hence, plastic deformations do not lead to others equilibrium states of the system, as it does in the quasi-static regime.
The physical approach describing the behavior of granular systems in the dense flow regime, i.e. dense granular rheology, is the starting point of this present work and is presented in the following section.

1.3 Rheology of dense granular flow

In this Section we focus on the behavior of the system at high strain or strain-rate, when local failures or rearrangements lead to global failure and the medium flows. Going

back to the initial picture depicted by Figure (1.1), in the dense flow regime where $10^{-3} \leq \mathcal{I} \leq 1$, grains interacts by friction due to long-time interactions and tangential motions and collisions (*Maurin et al.*, 2016; *Andreotti et al.*, 2013; *Silbert et al.*, 2001). Different canonical configurations are classically used in order to study granular flows (*GDR MiDi*, 2004; *Forterre and Pouliquen*, 2008), shown by Figure (1.4). Considering plane shear

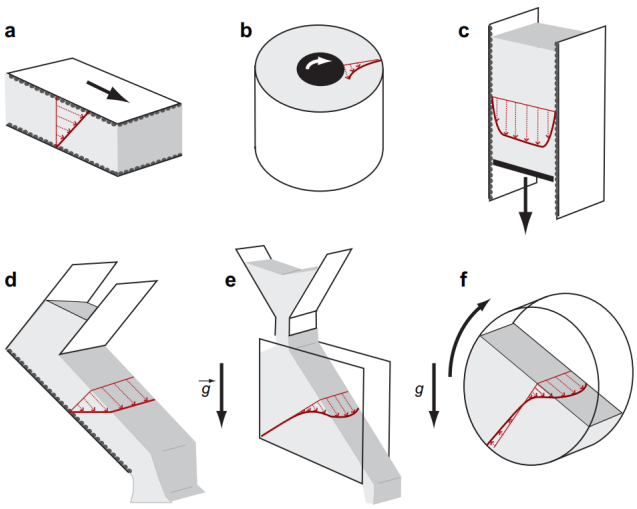

Figure 1.4 – Different configurations of granular flow studied in literature (a) plane shear (b) Couette cell (c) silo (d) flow on inclined plane (e) flow on pile (f) rotating drum. Source: *Forterre and Pouliquen* (2008).

configuration without gravity, *Bagnold* (1954) showed that the pressure and shear stress scaling of a granular neutrally-buoyant suspension depends on the shear rate regime. He showed that at high shear rate when contacts between grains are predominant, the granular pressure and shear stress scale as:

$$P \sim \rho_p d^2 \dot{\gamma}^2, \tag{1.5}$$

$$\tau \sim \rho_p d^2 \dot{\gamma}^2. \tag{1.6}$$

These scaling enables one to get access to the velocity profile of the medium. In addition, he extended the model in another work (*Bagnold*, 1966) and gave a description in terms of stress ratio.

His pioneering works form the basis of the $\mu(\mathcal{I})$ rheology approach that will be described below and in which our work is embedded. They also prefigured the link between the description of immersed granular media and suspensions by considering fluid viscous effect on granular dynamics.

As highlighted in the Appendix A.1.3, in order to model the dynamics of granular material, one needs to develop constitutive relations between the stress tensor and the strain-rate. This domain of physics is called rheology and focuses on the behavior of flowing systems under various loadings.
In the configurations presented above, such as the plane shear cell, the granular dynamic is controlled by a single non dimensional parameter: the inertial number $\mathcal{I}$. Every other

dimensionless number that can be formed from the system is therefore a unique function of the inertial number. The rheological approach in the $\mu(\mathcal{I})$ framework (*Da Cruz et al.*, 2005; *Jop et al.*, 2006; *Forterre and Pouliquen*, 2008) is to consider that the volume fraction and the global friction coefficient or stress ratio μ between the shear stress and the normal stress are functions of the inertial number:

$$\frac{\tau}{P} = \mu(\mathcal{I}), \tag{1.7}$$

and

$$\phi = \phi(\mathcal{I}). \tag{1.8}$$

These relationships assume a local rheology in the sense that stresses only depends on the local shear rate and granular pressure through the inertial number and that the corresponding flow is homogeneous within the medium. This homogeneity of the flow is indeed observed in dense granular flows on various configurations (e.g. *Da Cruz et al.*, 2005; *GDR MiDi*, 2004; *Forterre and Pouliquen*, 2008; *Baran et al.*, 2006; *Silbert et al.*, 2001; *DeGiuli and Wyart*, 2017). If such assumption is made, then one can develop a three-dimensional tensorial viscoplastic constitutive law (*Jop et al.*, 2006). Nevertheless, this model also needs to assume that the pressure is isotropic, i.e there is an equality between the diagonal terms of the tensor, i.e $\sigma_{xx} = \sigma_{yy} = \sigma_{zz} = P/3$, and that the shear stress is colinear with the shear rate tensor. It gives a Cauchy stress tensor:

$$\sigma = PI + \tau, \tag{1.9}$$

with I the identity tensor. Hence, at imposed τ or P, it remains one degree of freedom as τ and P are related with the above Equation (1.7). This degree of freedom is resolved with following flow curves or constitutive relation at low inertial number (*Kamrin et al.*, 2024):

$$\mu(\mathcal{I}) = \mu_{stop} + b\mathcal{I}. \tag{1.10}$$

With b a fitted constant for a given material and μ_{stop} the constant static stress ratio in the limit $\mathcal{I} \to 0$. The latter depends on material friction coefficient μ_p (*Da Cruz et al.*, 2005; *DeGiuli and Wyart*, 2017; *Srivastava et al.*, 2022) and geometrical entanglement. Note that μ_{stop} allows one to recover the Drücker-Prager (or Mohr-Coulomb) criterion as $\mu_{stop} = sin(\delta_f)$ (*Andreotti et al.*, 2013).
Equation (1.10) is only true in the dense flow regime at low enough inertial number, see Figure (1.5). Another form, more accurate at higher inertial number, is given by *Jop et al.* (2006) which gives:

$$\mu(\mathcal{I}) = \mu_1 + \frac{\mu_2 - \mu_1}{\mathcal{I}_0/\mathcal{I} + 1} \quad \text{et} \quad \phi = \phi_c - (\phi_c - \phi_m)\mathcal{I}. \tag{1.11}$$

Constants $\mu_1 = \mu_{stop}$ and μ_2 in the Equation (1.11) are the threshold values of the ratio between the normal and tangential constraints respectively at the transition liquid-solid ($\mathcal{I} \to 0$) and at the transition liquid-gas ($\mathcal{I} \to \mathcal{I}_0$). ϕ_c and ϕ_m corresponds to phenomenological volume fraction depending on the inter-particle friction coefficient μ_p.

Such constitutive relations enable one to predict the flow curve of dry granular materials in many configurations. One of them is presented by Figure (1.5) for the plane shear

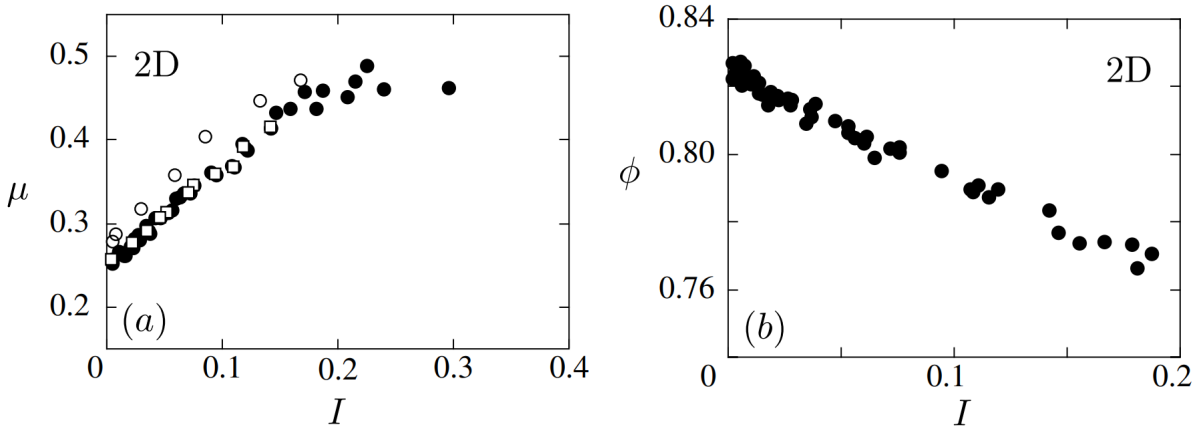

(a) (b)

Figure 1.5 – (a) Global friction coefficient μ as a function of the inertial number $\mathcal{I}$ (b) Volume fraction ϕ as a function of the inertial number I. Source : (*Da Cruz et al.*, 2005; *Andreotti et al.*, 2013).

cell configuration in two dimensions. As expected, μ and ϕ evolves linearly with the inertial number. Nevertheless, some departure from the linear behavior are observed at high inertial numbers near the liquid-gas transition. In the case of fully-immersed assembly of grains in a fluid, fluid-grain interactions are no more negligible. Indeed, (*Bagnold*, 1954) showed that the behavior of the suspension is viscous and hydrodynamic interactions dominate at low shear rates. The grains are considerably slowed down by the surrounding fluid. In that regime, the pressure is constant and the shear stress scales as:

$$\tau \sim \eta_f \dot{\gamma}. \tag{1.12}$$

For such dense non-Brownian suspensions, a rheological flow curve equivalent to Equation (1.11) has been developed and links both volume and pressure imposed approaches (*Boyer et al.*, 2011; *Guazzelli and Pouliquen*, 2018). More details about dense non-Brownian suspensions are given in Appendix A.2.

1.4 Challenges in granular media rheology

The validity of $\mu(\mathcal{I})$ rheology to model dense granular flow has been proved in various configurations (e.g. *Da Cruz et al.*, 2005; *GDR MiDi*, 2004; *Forterre and Pouliquen*, 2008; *Baran et al.*, 2006; *Silbert et al.*, 2001; *DeGiuli and Wyart*, 2017). However, some complex behaviors of granular media flows show the limits of this model. In particular, these behaviors usually occurs at the transitions between the dense flow regime and the others regimes. They highlighted the complexity of these systems as discussed in Section 1.1 and represents challenges to current research. This section focuses first on the description of these limit behaviors and then presents what challenges they represent for continuous modeling.

1.4.1 Heterogeneity and finite size effect

The complex behaviors are mainly of two kinds: non-homogeneous flows and finite-size effects. Both occurs in several conditions, a few of them will be presented here.

Creeping

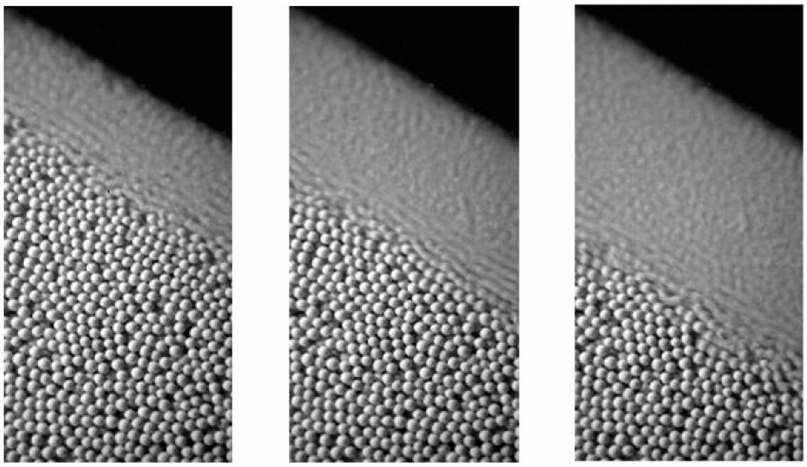

Figure 1.6 – Creep granular flow on a heap, pictures are taken with various exposure time $1s$, $1min$ and $1h$ from left to right showing the creeping flow of the granular region far from the free-surface. Source: (*Komatsu et al.*, 2001)

One important heterogeneity observed in granular flows is creeping. When a granular medium is subjected to low strain rate or stress, for a bunch of geometries (heap flow, shear flow with gravity etc.), flow appears to have a well defined solution by the $\mu(\mathcal{I})$ model but creeps decays are observed, where grains in regions of the medium below the flowing layer are moving at significantly lower velocities than the flowing layer. The flow in these regions is then observed, for long observation times, and where the model predicts no flow (*Kamrin et al.*, 2024; *Crassous et al.*, 2008). Such creep decay was observed on heap flow for example by *Komatsu et al.* (2001) and presented by Figure 1.6. Creep means, as seen on the picture, that the displacement of given regions are not observable at small timescales but at large ones non-zero velocities are measured in those areas of the medium.

Shear localization

Shear localization is an heterogeneity related to most of the others presented here. Indeed, for most of them, the stress is localised in some regions of the flow implying heterogeneous flow field. Shear-banding is a well-known example of stress localisation. It is similar to creeping. Shear-banding occurs in shear stress imposed configurations and defines the coexistence of regions within the medium that displays different shear rates (*GDR MiDi*, 2004; *Mandal et al.*, 2021a). Such heterogeneous flows were observed and studied both experimentally and numerically (see e.g. *Fenistein and van Hecke*, 2003; *GDR MiDi*, 2004; *Mandal et al.*, 2021a; *Vågberg et al.*, 2017).

Finite-size effects

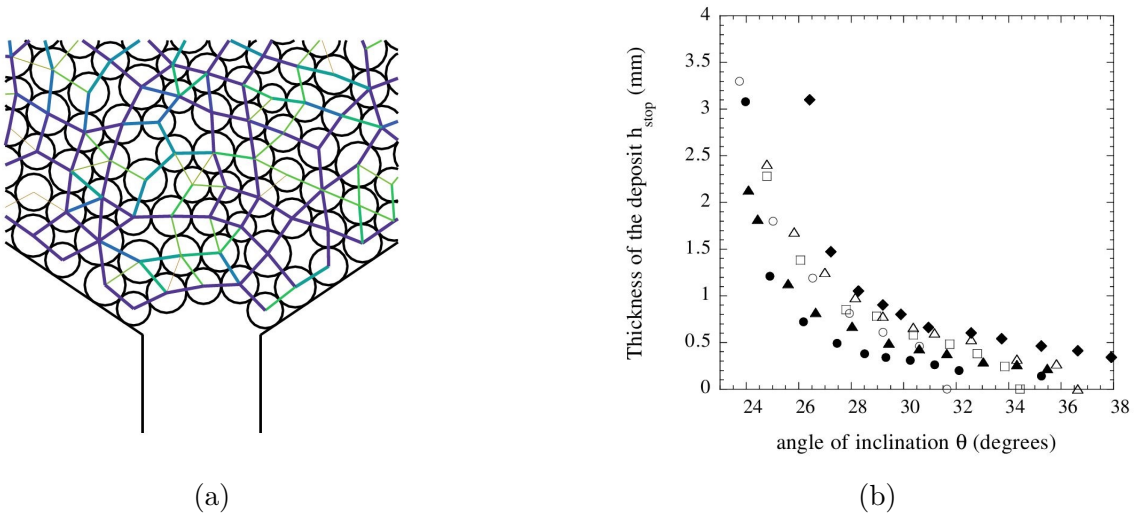

(a) (b)

Figure 1.7 – (a) Illustration of a clogged hopper due to arch creation at the exit. Source: (*Hong et al.*, 2017) (b) $h_{stop}(\theta)$ curves for various ratios between the size of the flowing grains and the size of the grains that constituted the plane. Source: (*Goujon et al.*, 2003).

Another challenging physical behavior observed in granular flows are the finite-size effects, where the characteristic size of the geometry, i.e. of the configuration studied, is of the order of the grains diameter d. In the discharge of hoppers for example, the size of the exit can be typically of the order of grains sizes, leading to arch creation and clogging (*Hong et al.*, 2017), as illustrated by Figure 1.7a.
Another example of interest in this thesis is the finite-size effect on a rough inclined plane. When flowing on a rough inclined plane, a granular layer of thickness h will stop flowing when the inclination angle of the plane eventually reach the value θ_{stop}. Equivalently, at a given inclination angle of the plane θ, the thickness of the deposit, resulting from a flowing granular layer that come to rest, is worth h_{stop}. It gives the curve $h_{stop}(\theta)$ of deposit layer thicknesses at various angles on a rough inclined plane, see Figure 1.7b. This curve shows that for small layers, the repose angle θ_{stop} is higher than for layers that exceed $10d$ and highly depends on the layer thickness. This influence of the layer thickness on the repose angle shows that the stability of the system depends on its characteristic size, here h, when it is of the same order than the characteristic size of grains, d. It is called finite-size effect.

Hence, both examples show that when the geometric characteristic length scale is close to the diameter of grains the medium response to external stress is much stronger (*Kamrin et al.*, 2024).

Anisotropy

One key to understand heterogeneous flows is the shear-induced anisotropy. It is a consequence of the application of shear in addition to isotropic pressure on the system. In purely isotropic external stress applied on a granular medium, the deviatoric part of

the granular stress tensor, τ, is zero and the normal stress components are equals. In sheared granular flows, normal stress differences are observed both between the two normal components in the flow plane and between the average normal components in the flow plane and the component in the vorticity direction. The former is a consequence of an anisotropy, i.e. misalignement, between the strain tensor Γ and the stress tensor σ in the flow plane (see e.g. *Seto and Giusteri*, 2018; *Srivastava et al.*, 2021; *Guazzelli and Pouliquen*, 2018). The latter normal stress difference appears to be related to the anisotropy of the contact network of grains (*Srivastava et al.*, 2021). More details about normal-stress differences and its link to suspensions are given on Appendix A.4.
These contact and stress anisotropies are keys to understanding flow heterogeneities. For example, according to *Vågberg et al.* (2017), shear-banding occurs due to the presence of shear-induced stress anisotropy.

Equivalently to dry granular systems, dense non-Brownian suspensions also displays similar heterogeneous behaviors such as discontinuous shear thickening at the transition of plastic and inertial regimes, see Appendix A.2 for more details. These challenges are common to others granular systems which reinforces the importance of resolving them.

1.4.2 Modeling heterogeneities

In the results presented above, a part of the research work is to model these behaviors using rheological models. As such, $\mu(\mathcal{I})$-rheology was tested in order to compare its prediction to observed non-homogeneous flows. In *Kamrin et al.* (2024), the authors take as an example the numerical simulations from the work of *Koval et al.* (2009) in annular shear flows in two dimensions in order to illustrate the modelling of heterogeneity. In particular, at low strain rates, the $\mu(\mathcal{I})$-rheological model does not predict the evolution of the actual measured flow curve, which suggests the presence of non negligible strain-rate gradients. *Kamrin et al.* (2024) also explains that such behavior implies the possible existence of an intrinsic length scale related to the characteristic size of grains d that competes against flow gradients. As such, the dependence of the flow curve to such length scale and d is a signature of what is called non-local effects.
Similarly, finite-size effect influences the flow in hoppers, where departures from $\mu(\mathcal{I})$-rheology prediction are observed (*Staron et al.*, 2012). On an inclined plane, the finite-size effect is also not predicted by $\mu(\mathcal{I})$, which predicts a single repose angle for every layer thicknesses of a given material.

The term non-local is defined in opposition to the local rheological model $\mu(\mathcal{I})$ presented in the above Section, see Equation (1.10). The latter model for dense granular steady homogeneous flows is indeed local in the sense that it is a constitutive relation of the material that gives an algebraic relation between the stress σ and the the velocity gradient ∇u through the strain rate tensor $\Gamma = (1/2)(\nabla u + \nabla u^T)$ at a given position (x, y, z) (*Jop et al.*, 2006; *Forterre and Pouliquen*, 2008; *GDR MiDi*, 2004; *Kamrin et al.*, 2024). The lack of size separation between the characteristic size of grains, d and the characteristic size of the given studied geometry, as discussed in Section 1.1, raises issues about the homogeneity assumption. Indeed, the rheology does not work in the case of non-homogeneous flows as explained by *Kamrin et al.* (2024) and seen above.

As a consequence, for such flows, non-local models are needed to describe the evolution of the flow field properly. Non-local Granular Fluidity (NGF) model (*Kamrin and Koval*, 2012), partial fluidization theory from *Aranson and Tsimring* (2006), or the $\mathcal{I}$-gradient model from *Bouzid et al.* (2013) are examples of such models.

1.4.3 The need for micro-structure description

In a majority of the non-local effects, their experimental study is hard to set up since they results from the history of the micro-structure of the material. The measure of macroscopic state variables such as the velocity field, the volume fraction, the inertial number or stress response, characterizes on the one hand the macroscopic response of the material to external stress or strain (or strain rate). The departure of such measurements from rheological models predictions are the signature of consequence of heterogeneities within the granular materials. On the other hand, the micro-structure description enables to highlights these heterogeneities and to study their origin (*Cundall and Strack*, 1979; *Srivastava et al.*, 2019; *Bonn et al.*, 2017; *Henkes et al.*, 2016) through state variables. These variables, such as coordination number, contact anisotropy or sliding contact ratio, describe the evolution of the micro-structure in response to imposed stress or strain. They are then used as internal variables in continuous models that considered heterogeneous flows (see e.g. *Aranson et al.*, 2008). More details are given in Appendix A.3 about the various micro-structure state variables that can be defined.
One major result that highlights the heterogeneity of granular systems is the heterogeneous distribution of forces in a granular packing. Indeed, it has been shown that the probability distribution function of forces follow an exponential tail meaning that the contact forces are not equals at each contact of the system, some contacts support a significantly higher force that others (*Radjai et al.*, 1999, 1998), see Appendices A.3 and A.5 for more details. The evolution of the micro-structure, not considered by the models presented here above, is key to develop finer models that predicts particular behaviors of granular materials.

1.5 Hysteresis at the solid-liquid transition

The present work focuses on the phase transition between the dense flow, liquid, granular state and the solid state. The idea is to study in which conditions the medium loses rigidity and starts flowing or, conversely, in which conditions it becomes rigid and stops flowing. This seemingly simple transition is in fact more complex, involving various physical mechanisms such as friction and grains inertia. In addition, it lies at the heart of the complexity of granular media, as it highlights the different types of heterogeneity described above. As shown by Figure (1.7b), which plots the transition curves from the dense flow state to the static state of a granular layer on an inclined plane, the conditions of transition are subjected to finite size effects and in-homogeneous flow gradients like shear-bands or creeping can be observed near the transition (*Silbert et al.*, 2001; *Fenistein and van Hecke*, 2003; *Mandal et al.*, 2021b). The main feature that characterizes the complexity of the transition is the presence of hysteresis, meaning that the external stress or strain rate conditions leading the system to flow from the solid state is greater than the external stress or strain rate conditions leading the system to stop flowing in the dense

flow state. This phenomenon is observed in various configurations presented in Figure (1.4). For cylindrical and plane shear cell configurations, a difference is observed between the values of stress ratio at the boundary walls when the granular flow starts and stops (*Da Cruz et al.*, 2002; *Mowlavi and Kamrin*, 2021). In the rotating drum configuration, a difference is observed between the values of free surface inclination angle when the flow starts and stops (*Courrech Du Pont et al.*, 2003; *Perrin et al.*, 2019; *Peng et al.*, 2023).

For the inclined plane configuration, the observed hysteresis illustrates intuitively the

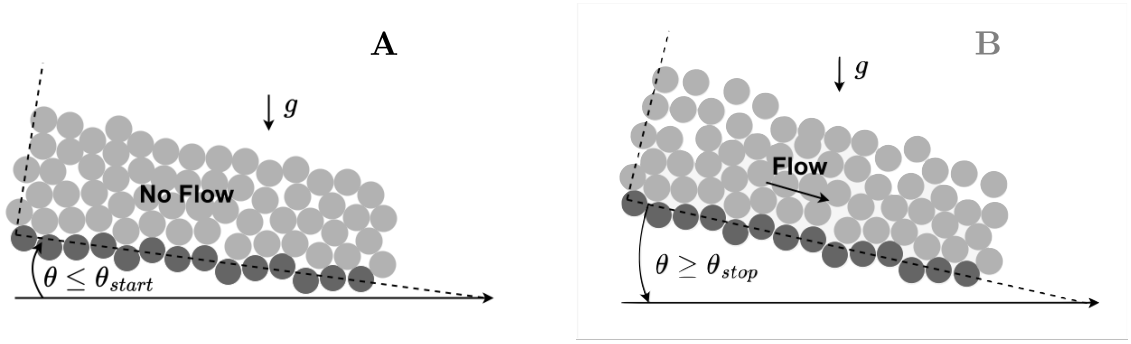

(a) (b)

Figure 1.8 – (a) Scheme of the process **A**, where the inclination angle is increased in the static regime to reach the avalanche angle θ_{start} (b) Scheme of the process **B**, where the inclination angle is decreased in the dense flow regime to reach the stopping angle θ_{stop}

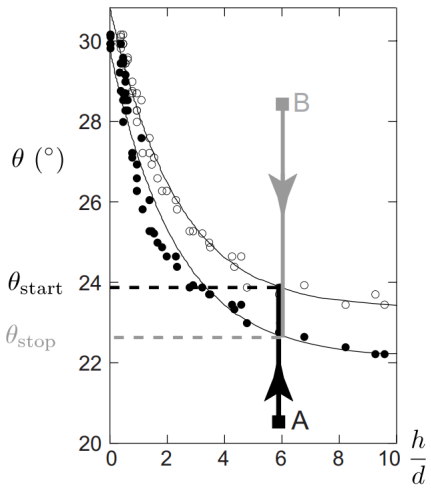

Figure 1.9 – Critical angles θ_{start} and θ_{stop} as a function of the layer thickness h/d in the inclined plane configuration, source: (*Pouliquen and Forterre*, 2002)

phenomenon from real-life applications. At a given layer thickness h, starting from a static bed and increasing progressively the plane, the granular medium is set in motion at a given angle θ_{start}. Conversely, starting from a flowing granular medium, of same thickness, and decreasing progressively the inclination angle, one observes a stopping angle, θ_{stop} at which a medium goes to rest. These two angles are not the same, with a larger inclination angle to set the medium in motion than the one at which it stops, defining an hysteresis. Indeed, the behavior of the granular medium at this transition therefore

depends on the stress path followed (from rest to motion, or from motion to rest), so on the loading history. The processes leading to the avalanche and stopping angle for a given layer thickness are illustrated on Figure (1.8). The corresponding inclination angle paths are represented on Figure (1.9). This figure presents the curves for both critical inclination angles θ_{start} and θ_{stop} measured by processes **A** and **B** for various layer thicknesses h. It shows two distinct curves $\theta_{start}(h)$ and $\theta_{stop}(h)$ with, as explained above, the avalanche angle greater than the stopping angle for all layer thicknesses. As such, it shows the angle range, in between the critical angles, quantifying hysteresis.
Understanding hysteresis phenomenon and characterizing the phase transition between liquid-like and solid-like granular behaviors is fundamental for the description and unification of granular media models. Nevertheless, hysteresis in granular media at the solid-liquid transition has been the subject of few studies in the past (*Courrech Du Pont et al.*, 2003; *DeGiuli and Wyart*, 2017; *Perrin et al.*, 2019, 2021; *Peng et al.*, 2023). The different authors have pointed out the influence of grains inertia (*Courrech Du Pont et al.*, 2003; *Perrin et al.*, 2019) and friction (*DeGiuli and Wyart*, 2017; *Perrin et al.*, 2019; *Peng et al.*, 2023) on the phenomenon. Yet, no consensus is established on its origin and characteristics, which are still debated.

1.6 Main objectives and thesis outline

This thesis is part of a drive to unify models at the solid-liquid transition. In this modeling vision, it is necessary to characterize hysteresis and understand its physical origin, to better describe it. To do this, we choose to work with the inclined plane configuration because the nature of hysteresis has been little studied in this configuration, which nevertheless illustrates well the phenomenon for actual applications. The thesis work carries out a numerical study at the grain to gain access to a wide range of state variables of the system and, in particular, to the granular micro-structure. We consider spherical monodisperse assembly of grains interacting without cohesion. We investigate the influence of inter-particle friction and inertia on the hysteretic phenomenon to try to unify the results of the literature on the subject and provide a better understanding of hysteresis origin.

To do so, we will first review the literature and identify what is known, and the main issues in the field, in Chapter 2. The notions of jamming and unjamming of granular systems transition, the phase diagrams related, and their link with hysteresis is discussed. Then, the numerical model used and the methodology adopted to study the problem are presented in Chapter 3.
Chapter 4 describes qualitatively the results observed at the transition, the different states and physical mechanisms at stake in hysteresis phenomenon, by varying the physical parameters of the grains. It allows us to make the connection with the literature on phase transitions, confirm the existence of two distinct transitions and the major role of inter-particle friction.
After that, a systematic quantitative study is presented in Chapter 5 investigating the influence of inter-particle friction and grains inertia on hysteresis and rationalising the different results from literature.
Finally, we conclude on the contributions this thesis work provides to the research on the subject and present the perspectives it opens up, in Chapter 6.

Chapter 2

State of art on the phase transition between static and flowing regimes and hysteresis

Hysteresis represents the difference in external stress or strain rate conditions between the cessation and the initiation of flow. It is the result of two distinct transitions that are respectively identified as jamming and unjamming transitions. As such jamming transition refers to the critical stress, strain rate or packing fraction conditions where the medium stops flowing. By opposition, the unjamming transition refers to the critical conditions where the medium starts to flow from the static regime. The hysteretic behavior shows that it does not exist a single well-defined critical point of transition but some critical points that depends on the density and the path taken to apply an external stress or strain. This behavior have often been attributed to the micro-structure (*Da Cruz et al.*, 2002; *DeGiuli and Wyart*, 2017), i.e. forces chains and contact network evolution, that influence the response of the granular material to the external stress or shear rate near the jamming (*Silbert et al.*, 2002a; *O'Hern et al.*, 2001; *O'Hern et al.*, 2003) and unjamming transitions (*Staron et al.*, 2002; *Silbert et al.*, 2002b; *Staron and Radjai*, 2005).
There is an extensive literature on jamming and unjamming transitions in granular media, while few studies have specifically focused on hysteresis. It is then interesting to study the literature on jamming and unjamming separately to understand the approaches and tools needed to study hysteresis phenomenon and appreciate the complexity of the subject.

The present state of art aims first to explain the jamming approach as a global paradigm of research about various amorphous materials, in order to position granular materials in this field of study. Indeed, the study of the liquid-solid transition of granular materials has undergone a paradigm shift from the elastoplastic theories (*Savage*, 1998) to the study of jammed systems (*Liu and Nagel*, 1998; *Silbert et al.*, 2002a). It enabled granular materials research to understand the transition between static and dense flow regimes through the physical theory of phase transitions. The emergence of this new field have launched a series of research projects that focused on the approach to jamming (*Rothenburg and Kruyt*, 2004; *Da Cruz et al.*, 2005; *Song et al.*, 2008; *Srivastava et al.*, 2022) and unjamming (*Silbert et al.*, 2005; *Wyart et al.*, 2005; *Staron*, 2008) with the use of micro-structure descriptors.

The idea of this literature review chapter is to start from the results in the simplest configurations and progressively complexify, to end up with results on the dry and immersed frictional inclined plane configuration studied in the present work. Considering first the jamming and unjamming transition, it details several interesting results, needed to understand the behavior of granular system at both transitions.
It starts with the study of jamming and unjamming transitions of an idealized configuration of frictionless system without gravity under isotropic and anisotropic external conditions.
Then, the studies presented focus on jamming and unjamming of systems with finite inter-particle friction without gravity.
Hence, the chapter presents results from more realistic configurations where gravity and inter-particle friction are present at both transitions.
Finally, the chapter focuses on the inclined plane configuration considered in the present study and presents the phase diagram of granular systems down rough inclined planes, highlighting the presence of hysteresis. The link between the latter phenomenon and the jamming/unjamming literature is discussed. Various results from the investigations of physical mechanisms responsible for the hysteresis are also discussed and several constitutive models considering hysteresis are presented. The development of these state of art enables us to identify more specifically and precisely the objectives of the thesis that we aim to investigate in the following chapters.

2.1 The paradigm of jamming

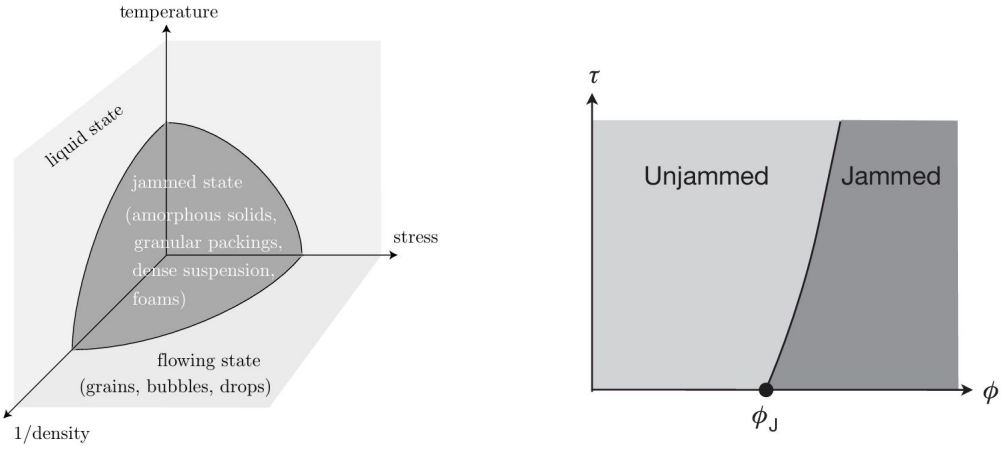

(a) (b)

Figure 2.1 – (a) Hypothetical phase diagram for the jamming transition of disordered systems by *Liu and Nagel* (1998). (b) Hypothetical phase diagram for the jamming transition of granular athermal systems, only in the density-stress plane of the previous phase diagram, source: (*Bi et al.*, 2011).

Jamming can be defined in several ways. First, under external stress, strain rate, jamming is the point where a granular media develops rigidity, in the sense that it can no

longer flow since the dynamic has dramatically slowed down (*Liu and Nagel*, 2010; *Biroli*, 2007).
It has also been defined as a "paradigm of thinking" for the accession to rigidity of any type of amorphous material, from molecular liquids to macroscopic dry granular materials (*Liu and Nagel*, 2010). Conversely to the study of granular elasticity and plasticity introduced in Section 1.2, the study of granular jamming does not assumes homogeneity of the system and attempt to consider non-affine motions, where fluctuations in the velocity field of the assembly of grains does not follow an affine motion (*Radjai and Roux*, 2002), and heterogeneities are present within the medium.

This paradigm emerged from the apparent analogy between the rigidity transition of granular materials and the glass transition, especially the disorder of these system in the rigid state (*Liu and Nagel*, 1998; *O'Hern et al.*, 2003; *Biroli*, 2007). An hypothetical jamming phase diagram emerged from this paradigm (*Liu and Nagel*, 1998), presented on Figure 2.1a assumes the three order parameters that would lead this type of amorphous materials to be jammed: the temperature, the stress or the packing density. In this diagram, the state of a granular athermal material is for example only defined by the density ϕ or $1/\phi$ and the stress τ giving a two dimensional phase diagram, see Figure 2.1b. The medium will then be unjammed at high stress and/or low density and jammed at high density and/or low stress. Figure 2.1b also presents the Jamming point, or point-J, corresponding to the jamming density ϕ_J at which the system is jammed with zero applied stress and zero temperature in the frictionless case and defined as the "epitome of disorder" (*O'Hern et al.*, 2003).
Although this kind of analogy has enables to show that the jamming of simple colloidal materials behaves as a glass transition (*Bonn et al.*, 2017), dense non-Brownian suspensions and dry granular materials fundamentally differ from glass transitions. The fundamental difference lies on the athermal feature of such systems implying an absence of spontaneous dynamic. Hence, the emergence of solidity, i.e. rigid response to external stress, in such materials does not results from the competition between time scales (spontaneous dynamic time scale of thermal fluctuation and time scale from shearing). As such, the transition is defined as static resulting from a sharp change in the microstructure of the system (*Bonn et al.*, 2017; *Liu and Nagel*, 2010). The term static is used to express this fundamental difference to thermodynamic phase transitions in which intrinsic dynamic exist (thermal fluctuations), but the usual term to describe the jamming transition of athermal granular materials is dynamical phase transition. Finally, the challenge in stuying such phase transition is to preciselly define phase diagrams between the imposed variables and response of granular media, equivalently to the hypothetical ones of Figure 2.1, that define regions in which the system is rigid or flows. These diagrams then gives information on the yield values of the imposed or measured (in response) variables that can help developing constitutive and continuum description of such materials.

The following sections will then focus on an overview of the jamming and unjamming transitions of athermal granular materials under various conditions. Starting from idealized systems and adding complexity to approach more realistic systems as the inclined plane configuration, the following sections will enables us to identify key features of the jamming and unjamming transitions and present various corresponding phase diagrams.

This is necessary for a better understanding of this global phase transition of granular systems, and ultimately hysteresis.

2.2 Jamming and unjamming of frictionless granular media

The notion of jamming and unjamming are directly related to the stability of an assembly of grains. They represent respectively the accession and lose of stability of a granular system. This section focuses on the study of such transitions for idealized frictionless grains, for which the accession and lose of stability appears to be simpler. The accession to stability is intrinsically related to the notion of staticity of a mechanical system, corresponding to the mechanical equilibrium between the number of equations and the number of constraints. This approach can be used to define the mechanical stability conditions for an assembly of grains. Isostaticity is then a mechanical criterion defining the limit between hypostatic, unstable system, and hyperstatic, stable system.

2.2.1 Isostaticity of frictionless and infinitely frictional grains

In athermal systems, since no thermal fluctuations are present, the system is always in mechanical equilibrium in the jammed state and the contact forces on all particles balance (*Liu and Nagel*, 2010). As such, the stability of the whole system is given by the Maxwell's criterion on the order parameter $\mathcal{Z}$, the coordination number or average number of contacts in the assembly of grains (*Liu and Nagel*, 2010; *Silbert et al.*, 2002a; *Wyart*, 2009; *Henkes et al.*, 2016). Such criterion gives well defined isostatic values in the frictionless and infinite friction limits. By contrast, for particles with finite inter-particle friction, the isostatic criterion is harder to define due to Coulomb's criterion of tangential forces. The idea of this section is then to detail the isostatic criterion in both frictionless and infinite frictional cases that are intrinsically hypothetical but gives two intersting isostatic boundaries of the frictional jamming transition.

The isostatic criterion is given through the coordination number that is calculated at the scale of the granular media with the total number of contacts, noted N_c, and the number of particles, noted N_p, as: $\mathcal{Z} \equiv 2N_c/N_p$. Maxwell's criterion on mechanical stability is set by considering the total number of degrees of freedom in the system, related to the dimensions of the system (2 or 3D), and the total number of constraints, related to the coordination number. As such, the isostatic condition of a frictional granular media in D dimensions is only given by its coordination number that respects (*Liu and Nagel*, 2010; *Wyart*, 2009):

$$D + 1 \leq \mathcal{Z} \leq 2D. \tag{2.1}$$

In 3D, $D = 3$, it gives:

$$4 \leq \mathcal{Z} \leq 6. \tag{2.2}$$

These inequalities are given considering each bounds as limit isostatic cases in the frictionless and infinite frictional case. The upper bound is defined considering the case of frictionless particles in D dimension. There are then N_pD degrees of freedom in the system with N_p the total number of particles, D degrees of freedom by translation for each

particle. No degree of freedom are counted for the rotation, since all contacts necessarily slides for frictionless particles. It also represents the total number of force balanced equations in the system. There are N_c constraints in the system, corresponding to the total number of contacts and also representing the total number of unknown normal forces. In that case the system is stable if $N_p D \geq N_c$ giving the upper bound of Equation (2.1), which is the limit at $\mu_p = 0$. There, $N_p D = N_c$ or $\mathcal{Z} = 2D = 6$ in three dimensions.
The lower bounds of the equations are defined at the limit $\mu_p \to \infty$ where the Coulomb friction criteria is respected for every contacts. Then $D(D-1)/2$ degrees of freedom by rotation are added to the D degrees of freedom by translation per particle. The former notation is simply used to obtain 3 in 3D and 1 in 2D. In addition, in that case each contact brings 1 constraint per translation (as in the frictionless case), i.e. one unknown normal force, and $D-1$ constraints by rotation, i.e. $D-1$ unknown tangential force. Indeed, in 3D a contact only allow rotation along the axis formed by the center of the particle and the contact point. Then, it constrains the two others degrees of freedom of rotation. In 2D, a contact constrains the only degree of freedom possible by rotation. That leads to the lower bound of the inequality, $\mathcal{Z} = D + 1 = 4$ in three dimensions.

2.2.2 Jamming at point J under isotropic or anisotropic conditions

Reaching such isostatic conditions is possible with isotropic conditions either by imposing the volume fraction ϕ or by imposing normal stress with no deviatoric stress. For frictionless particles isotropic jamming was observed with volume-imposed simulations with zero applied stress (*O'Hern et al.*, 2003). The system is considered jammed when the average potential energy in the system has reached a minimum. The result show that frictionless particles reach jamming in isotropic conditions if the volume fraction reaches a limit value, noted ϕ_J. This value is equal to $\phi_J = 0.64 = \phi_{RCP}$ in three-dimension. This point is called the jamming point or J point. At that volume fraction, *O'Hern et al.* (2003) observed a discontinuous jump in the coordination number from $\mathcal{Z} = 0$ at $\phi < \phi_J$ to $\mathcal{Z} = 6 = \mathcal{Z}_{iso}$ (in three-dimension) at $\phi = \phi_J$. Such discontinuity has been interpreted as the signature of a first-order phase transition (*Liu and Nagel*, 2010) by opposition to second-order phase transitions where the evolution of the order parameters are continuous. Similarly, such isostatic conditions were observed in numerical simulations with isotropic pressure (normal stress) showing equivalent values of the coordination number and volume fraction for frictionless particles (*Song et al.*, 2008).
Such packing fraction and coordination number were investigated under anisotropic normal stress conditions by *Silbert et al.* (2002b). They calculated numerically the packing fraction and coordination number of a granular media that settle under gravity on a rough horizontal plane. They demonstrated that in these more realistic conditions, frictionless particles displays similar isostatic packing fraction and coordination number than in isotropic conditions.

2.2.3 Scaling laws in the jammed state

One interesting behavior of frictionless jammed materials is that above the critical jamming values $\phi > \phi_c$ and $\mathcal{Z} > 6 = \mathcal{Z}_{iso}$, if the medium is compressed by increasing pressure or volume fraction, scaling laws relating the several quantities appears (*O'Hern et al.*, 2003; *Wyart et al.*, 2005). This compression process is only possible in the case of deformable particles. Numerical simulations usually allows particles to be deformable but restricts this effect in order to model rigid particles. Nevertheless, the presence of such small deformations does not contradicts experimental results where real rigid grains can effectively slightly deforms under compression depending on the material stiffness. First, the excess of contacts created by compression is related to the increase of volume fraction thought the relation (*Liu and Nagel*, 2010):

$$\mathcal{Z} - \mathcal{Z}_{iso} \sim (\phi - \phi_c)^{1/2}. \tag{2.3}$$

O'Hern et al. (2003) extracted from numerical simulations in such jammed frictionless compressed packing conditions scaling laws between the elatic moduli and the excess of contacts:

$$K \sim E(\mathcal{Z} - \mathcal{Z}_{iso}) \sim E(\phi - \phi_c)^{1/2}, \tag{2.4}$$

for the isotropic elastic modulus, and:

$$G \sim E(\mathcal{Z} - \mathcal{Z}_{iso})^2 \sim E(\phi - \phi_c), \tag{2.5}$$

for the shear modulus. These moduli are intrinsic quantities of the granular material that characterize respectively the isotropic and shear constant ratios between corresponding stress and elastic strain response of the system equivalent to the Young modulus and Poisson's ratio for continuous solids, see Appendix A.1.4.
The scaling relations imply that, in the jammed state, the approach to jamming is continuous, characteric of a second-order phase transition. This transition then has then both features of first and second-order phase transitions which is not common in phase transitions theories (*Liu and Nagel*, 2010). In addition, the second-order transitions commonly implies the existence of a diverging lengthscale approaching the transition (*Liu and Nagel*, 2010) (from the jammed state here).

2.2.4 Diverging lengthscales and second-order phase transition

The presence or absence of a diverging lengthscale at jamming and unjamming is of importance to determine the nature of the unjamming transition. Considering frictionless particles, it has been the subject of several research, which are developed below.

While the physical origin and form of such lengthscale is still debated, *Silbert et al.* (2005); *Wyart et al.* (2005) used different analytical approach to study the vibrational states of the system in the jammed state. This approach enables them to study the stability of the equilibrium positions, i.e. local potential energy minima and investigate the potential existence of lengthscale characterizing the approach to unjamming. They calculated the density of vibrational state (DOS) of the system. The DOS is calculated

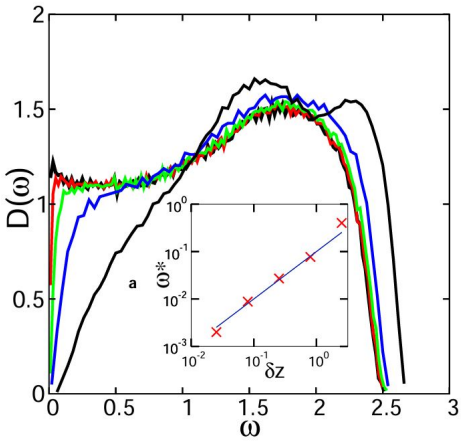

Figure 2.2 – Density of vibrational states (DOS) $D(\omega)$ at various relative packing fractions $\phi - \phi_c$, the curve labelled a is for $\phi - \phi_c = 0.1$ and proceeding to the left, the values are respectively 10^{-2}, 10^{-3}, 10^{-4}, 10^{-8}. The curves corresponds to the results from *O'Hern et al.* (2003). The inset corresponds to the scaling of ω^* with the relative coordination number $\delta z = (\mathcal{Z} - \mathcal{Z}_{iso})$. Source: (*Wyart et al.*, 2005)

by the second derivative of the pairwise potential energy for each pair of particles. This potential energy is given in the linear spring-dashpot model as:

$$V(r < 0) = V_0 \left(1 - \frac{r}{d}\right)^2, \tag{2.6}$$

where $V_0 = (1/2)k_N$ is derived from the grains stiffness k_N, d is the diameter and r is the distance between the centers of the two grains in contact. Note that if $r > d$ then V is set at 0. Or equivalently for Hertzian contacts:

$$V(r < 0) = V_0 \left(1 - \frac{r}{d}\right)^{5/2}. \tag{2.7}$$

Then the second derivative of each of these potentials is calculated, forming a tensor of size $N_p \times N_p$ giving the stability of each pairwise potential energy. Hence this tensor is diagonalised and the eigenvalues are calculated as well as the associated eigenfrequencies. The number, $\mathcal{D}$, of eigenvalues that have the same eigenfrequency, ω, is calculated. The DOS is the curve $\mathcal{D}(\omega)$, as presented on Figure 2.2. The DOS is expected to scale like $\mathcal{D}(\omega) \sim \omega$ in two-dimensions (*Andreotti et al.*, 2013) and then does not have any low frequency modes. In such case, the modes of vibrations would have wavelength larger than the sizes of heterogeneities as it is observed far from the jamming transition on Figure 2.2. Surprisingly, at the approach to the unjamming transition, some low frequency modes are observed. The DOS displays a plateau above a wavelength noted ω^* that scales with the excess of contacts (*Wyart et al.*, 2005):

$$\omega^* \sim (\mathcal{Z} - \mathcal{Z}_{iso})^{3/2} \tag{2.8}$$

These low frequency modes are called soft modes or floppy modes (specific soft mode). They are the signature of low vibrational modes that are close to be unstable. A decreasing characteristic frequency for non-zero soft mode when going toward unjamming is the

signature of possible rearrangements. Indeed, it means an increase of pairwise potential energy needing a low amount of vibration in order to be unstable leading to potential rearrangements. These rearrangments corresponds to floppy modes, characterized by the fact that no energy is needed to induce motion. The increase of such modes leads to collective loss of rigidity, i.e. unjamming, at $\mathcal{Z} = \mathcal{Z}_{iso}$. Some lenghtscales can be theoretically built to characterize the size of these rearrangements (*Liu and Nagel*, 2010; *Wyart et al.*, 2005; *Silbert et al.*, 2005). Appendix A.7 details how lengthscales are theoretically built. The divergence of such lenthscales theoretically predicts the loss of stability of the whole system when their value match the size of the system. As such, the existence of such lengthscales diverging near unjamming is the signature of the continuous evolution of the system, hence a second-order phase transition, from the jammed state into the unjammed state.

In this section we have seen that frictionless granular systems displays complex features of phase transitions between the jammed and unjammed state when reaching and leaving the stable state at isostatic coordination number value $\mathcal{Z}_{iso} = 6$ and jamming volume fraction $\phi_J = 0.64$. The coordination number displays a discontinuity between its value in the unstable state and its value in the stable state, characteristic of a first-order phase transition. The evolution of the system in the jammed state when over-constrained, enables one to study its behavior at the approach to unjamming. The existence of scaling laws in the jammed state suggests the existence of diverging lengthscales that were built studying the stability of the system through the vibrational state of the contact potentials. The results show that the system continuously approach unjamming from the jammed state, which is characteristic of a second-order phase transition.

2.3 Frictional jamming and unjamming

2.3.1 Frictional isostaticity

By contrast to the jamming state of frictionless and infinitely frictional grains (under isotropic conditions for the latter), the jamming state of finite frictional grains cannot be determined solely by the contact network (*Behringer and Chakraborty*, 2019). Indeed, *Song et al.* (2008) also showed that under isotropic pressure, highly frictional particles displays equivalent values of coordination number to the predicted value for infinite friction particles, i.e. $\mathcal{Z} = 4$ (in three dimensions), as presented by Figure 2.3a. In these conditions, the packing density of the jammed highly frictional particles is below the J point and is equal to the random loose packing $\phi_c(\mu_p \gg 1) = 0.55 = \phi_{RLP}$ as shown by Figure 2.3b. However, such packing fraction and coordination number were investigated for highly frictional particles in anisotropic normal stress conditions by *Silbert et al.* (2002b). They showed that the coordination number and packing density are higher than the isostatic value at infinite friction coefficient. Such departure from the theoretical value lies in the geometry of the configuration implying anisotropy (anisotropic stress tensor and presence of a rigid boundary), which is enhanced by friction between grains.

As such, some attempts of generalising and extending the isostatic conditions at finite

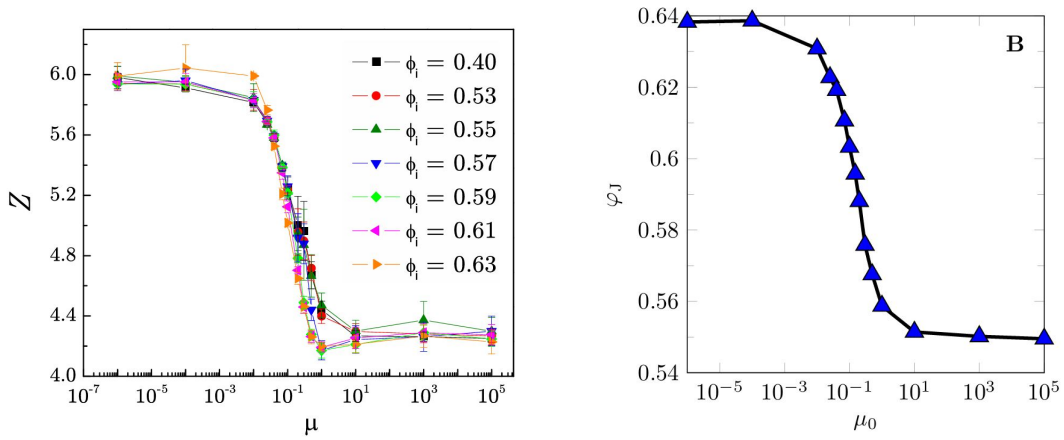

(a) (b)

Figure 2.3 – (a) Coordination number versus inter-particle friction coefficient (noted μ) in the jammed state under isotropic conditions at various initial packing fractions from numerical simulations of *Song et al.* (2008). (b) Jamming volume fraction versus inter-particle friction coefficient (noted μ_0) for numerical simulations under isotropic conditions, results from *Song et al.* (2008), Figure from *Pan et al.* (2023).

friction values were made by introducing others micro-structure descriptors (*Silbert et al.*, 2002a; *Song et al.*, 2008; *Henkes et al.*, 2010; *Liu and Nagel*, 2010). *Song et al.* (2008) has proposed such detailed calculation of the isostatic value of the coordination number. They defined N_n as the number of unknown normal forces in the system, N_t the number of unknown tangential forces, E_t the number of torque balanced equations and E_f the number of force balanced equations. The calculation of each of these numbers are detailed in table 2.1 depending on the value of μ_p: for $\mu_p = 0$, $\mu_p \to \infty$ and for finite values of μ_p. The calculation depends on D the dimension of the system (3D or 2D), the fraction of sliding contacts χ - i.e. contacts reaching Coulomb criterion $F_t = \mu_p F_n$ - and the fraction of particles that are free to rotate, Ω. Note that χ and Ω are defined in a way that $\chi(\mu_p = 0) = 1$, $\chi(\mu_p \to \infty) = 0$ and $\Omega(\mu_p = 0) = 1$ and $\Omega(\mu_p \to \infty) = 0$. The Maxwell criterion of stability for mechanical systems gives that a granular media is isostatic when the number of contact forces equal the number of force and torque balance equations leading to:

$$N_n + N_t = E_f + E_t. \tag{2.9}$$

Which gives according to table 2.1 in 3D (*Song et al.*, 2008):

$$Z_{iso} = \frac{3 + 3(1 - \Omega)}{1/2 + (1 - \chi)} \tag{2.10}$$

Equation (2.10) recovers the well known limits of the coordination of a granular media for both friction limits, defined above: $Z_{iso}(\mu_p = 0) = 6$ and $Z_{iso}(\mu_p \to \infty) = 4$. The results obtained in the jammed state at various friction coefficient in isotropic conditions is presented by Figure 2.3a. Figure 2.3b presents the corresponding values of jamming packing fraction at various inter-particle friction coefficients. These results show that by varying friction, the J-point become a J-line in the sense that jamming conditions depends on the friction coefficient between grains. However, Equation (2.10) fails to capture the

Friction	N_n	N_t	E_f	E_t
$\mu_p = 0$	$N_c = \frac{1}{2}N_pZ$	0	$3N_p$	0
finite μ_p	$N_c = \frac{1}{2}N_pZ$	$2N_c(1-\chi)$	$3N_p$	$3N_p(1-\Omega)$
$\mu_p \to \infty$	$N_c = \frac{1}{2}N_pZ$	$2N_c = N_pZ$	$3N_p$	$3N_p$

Table 2.1 – Number of constraints and variables determining the isostatic condition in 3 dimensions (see *Song et al.* (2008))

variations of the coordination number in various configurations. The dependence of the jamming conditions (packing fraction and coordination number) to preparation (*Bonn et al.*, 2017) such as the initial packing fraction (*Song et al.*, 2008; *Silbert et al.*, 2002b) or the packing rate (*Pan et al.*, 2023) leads to non strictly defined values of the isostatic coordination, see Figure 2.3a. These preparation effects are the consequences of the anisotropy induced by friction in granular materials, leading to an accession to jamming at lower values of ϕ and $\mathcal{Z}$ than the isostatic condition in the presence of finite friction and a dependence on the configuration (*Silbert et al.*, 2002b). As such, *Song et al.* (2008)

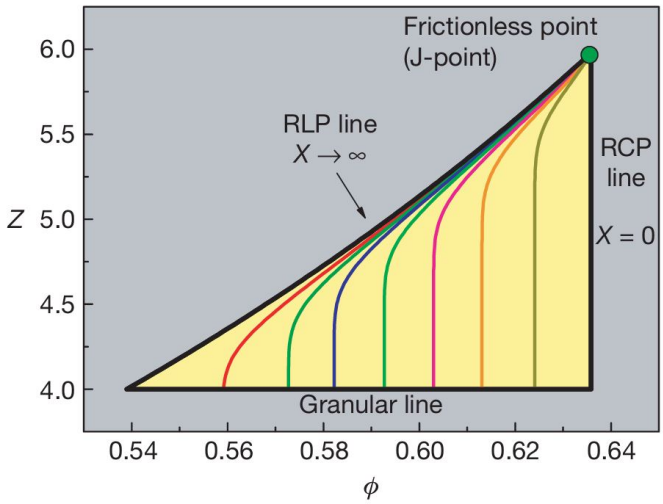

Figure 2.4 – Phase diagram of jamming. Theoretical prediction of statistical theory of the phase diagram of jamming. All disordered packing lie in the yellow area. Source: (*Song et al.*, 2008)

were only able to define a jammed phase diagram $(\mathcal{Z}, \phi)$, see Figure 2.4, in which the system is jammed. The diagram defines an area in the $\mathcal{Z} - \phi$ parameter space where a granular system is necessarily jammed. This area is bounded between three lines. The first is the jamming-line, or RLP-line, defined by the following Equation:

$$\phi_{RLP} = \frac{\mathcal{Z}}{\mathcal{Z} + 2\sqrt{3}}. \tag{2.11}$$

This equation results of the theoretical prediction from the statistical *Edwards and Oakeshott* (1989) theory of powder and developed in *Song et al.* (2008). It defines the possible random loose-packing values reached by the granular system under isotropic compression varying the inter-particle friction. Such evolution of the coordination number and volume fraction following the curve of Equation (5.1) was actually obtained numerically by *Song et al.* (2008) with the initially loosest packing fraction preparation in their study. It defines then the loosest jamming conditions in which a frictional system can be stable and give the lowest random loose packing $\phi_{RLP}^{min} = 0.55$ in the case of highly frictional particles at $\mathcal{Z} = 4$. The latter coordination number value defines the second line, called 'Granular line' on Figure 2.4, bounding the jammed diagram. Finally, the last bound of the diagram is defined by by the highest packing fraction $\phi_{RCP} = 0.64$ only reached for frictionless particles.

The existence of this diagram and the absence of universal jamming condition shows that frictional particles displays anisotropy of the force and contact network that cannot be only predicted by an isostatic condition.

2.3.2 Shear jamming

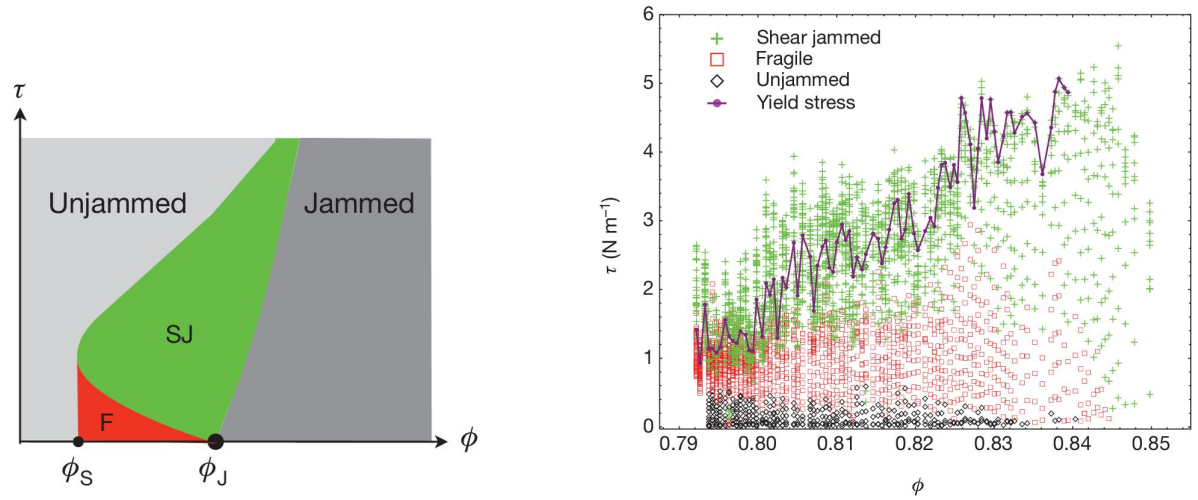

(a) (b)

Figure 2.5 – (a) Hypothetical phase diagram for the shear jamming transition of granular systems porposed by *Bi et al.* (2011). It is an extention of the phase diagram proposed by *Liu and Nagel* (1998), see Figure 2.1b. (b) Phase diagram in the parameter space (τ, ϕ) respectivaly the shear stress and volume fraction, obtained from experimental results of *Bi et al.* (2011) on sheared system at low shear.

So far, we have reviewed the literature on jamming without shear. Considering a case with shear stress or strain rate allows one to have a more complete picture of the jamming issue. In the case of frictional materials, an interesting behaviors was observed experimentally by *Bi et al.* (2011) in two dimensional shear cell (in the horizontal plane). They investigated volume imposed system without stress initially applied. They imposed

packing fraction just below the jamming packing fraction such that the grains are not initially in contact, i.e. $\mathcal{Z}_{ini} = 0$ and the system is unjammed. Interestingly, if a shear stress is imposed at sufficiently low value, the system can jam under increasing value of shear stress. This behavior has been called shear jamming since the driving mechanism for the accession to the jammed state is by shearing the system (*Bi et al.*, 2011; *Behringer and Chakraborty*, 2019) conversely to density-driven jamming where jamming occurs due to increase of packing density. Thus, they constructed a phase diagram as presented on Figure 2.5 where the system can be unjammed below a given amount of shear rate, adding complexity to the phase diagram proposed by *Liu and Nagel* (1998), see Figure 2.1b. The critical value of shear stress at which jamming occurs depends on the initial packing fraction, see Figure 2.5b. This shear jamming effect has been shown by looking experimentally at the force network's evolution at low shear. When the shear strain or stress is low, force chains appears within the system but the system is not completely jammed: it is fragile and cannot support loading reversal. When the shear strain or stress reaches the critical jamming values, force chains percolates between boundaries (within the whole system) in the direction of compression and creates a stress response to strain which appears as a yield stress (*Bi et al.*, 2011; *Behringer and Chakraborty*, 2019), see Figure 2.5b.

The origin of yield stress

Shear jamming has demonstrated that in frictional materials, the yield stress results from the presence of forces chains inducing rigidity of the system under shear (*Bi et al.*, 2011; *Behringer and Chakraborty*, 2019). Similarly, for dense non-Brownian neutrally-buoyant suspensions, if the packing fraction is below the jamming value and the normal stress is low enough, no yield stress exist if no effective contacts exist (*Bonn et al.*, 2017). This means that in such materials a yield stress emerges from contacts and geometrical entanglement which vanishes if particles does not sediments under gravity (at matched densities) or are not pushed to be in contact.

Link between shear jamming and heterogeneity

In dense suspensions a high enough shear rate is necessary for shear jamming to take place because grains need to overcome lubrication forces in order to be in contact (*Pan et al.*, 2023), as discussed above. Similarly, the onset of shear stress in discrete shear thickening is governed by hydrodynamic forces. As such, *Pan et al.* (2023) make a parallel between shear jamming and DST explaining that grains must be drawn close enough at high strain rates so that interparticle friction can create mechanically stable configurations. Then, DST occurs when anisotropic force chains percolate in a limited region of the medium, while shear jamming occurs when these chains percolate across the entire system (*Pan et al.*, 2023).

Similar parallel was made in the review of *Behringer and Chakraborty* (2019) between shear jamming and the capacity of dense suspensions to sustain shear bands. This frictional shear jammed behavior of granular systems enables to highlights and understand some heterogeneity observed in gravity-less shear frictional granular systems. Nevertheless, these behaviors are observed either at low shear stress or strain rate, or in presence of

hydrodynamic forces competing against contact forces. In less idealized frictional systems, yield stress is usually always observed and no fragile state exists.

Shear jamming in stress imposed configurations

In a majority of stress imposed configurations, the external normal stress is sufficiently high relatively to the shear stress to imply the presence of a yield stress (*Srivastava et al.*, 2022; *DeGiuli and Wyart*, 2017). In such configurations, when the medium stops flowing at the corresponding yield stress, the final state is shear jammed hence not fragile and can support a loading reversal (*Behringer and Chakraborty*, 2019).

Similarly, in gravity-driven configurations of dry granular systems or buoyant dense suspensions, the presence of gravity always create a sufficient initial stress in the system to create contacts, i.e. $\mathcal{Z}_{initial} \neq 0$. Hence, it is interesting to understand how does dynamical jamming happen from the dense flow regime and unjamming happen from the static regime in such systems.

2.3.3 Dynamical jamming of frictional spheres

As discussed above, shear jamming occurs at low shear stress of strain rate, below the yield values, for granular systems initially not flowing and not jammed. In a majority of granular systems, jamming occurs as a dynamical process resulting from the decrease of the loading quantity from the dense flow regime where stress or strain rate are larger than their yield values. It is therefore essential to study this dynamic phase transition, which differs from the so-called shear jamming transition.

Nature of the dynamical jamming phase transition

As discussed in Section 2.2, the dynamical accession to jamming from the dense flow state is a first-order phase transition under isotropic stress or volume imposed conditions since a discontinuous jump is observed on the coordination number. This behavior is also observed in shear, anisotropic stress-imposed, configurations. Indeed, jamming in shear stress imposed configurations appears to be really similar to isotropic jamming in that it also results from a density-driven jamming mechanism and also displays a jump of coordination number (*Pan et al.*, 2023; *Silbert et al.*, 2002a; *Srivastava et al.*, 2022).

Nevertheless, recent studies have attempted to demonstrate that the accession to jamming for frictional materials behaves as a second-order continuous phase transition (*Henkes et al.*, 2016). *Henkes et al.* (2016) adapted ideas from the percolation theory to study the formation of clusters in 2D sheared granular media close to jamming using a pebble game algorithm. The algorithm is based on an identification of the particles which have a number of constraints equal to their degrees of freedom. This enable them to observe the formation of rigid clusters within the system, i.e. regions where groups of particles are all constrained in their motion and appears as a rigid boundary. They demonstrated with this model that frictional materials can be globaly jammed below the global isostaticity conditions in the whole system, given by Equation (2.10), if the system

contains both floppy regions (where particles can easily be mobile) and a system-spanning rigid cluster that imply the rigidity through all boundaries. Then, they computed the cluster sizes as a response to externally applied shear stress.
In their model, frictionless jamming still has features of first-order phase transition since the cluster sizes display discontinuous jumps at the transition. However their model allows them to consider the jamming transition of frictional materials also as second-order phase transition since it exhibits power-law scaling, hence continuous evolution of the cluster sizes near the transition.

Although interesting, the idea that jamming frictional transitions is a simple percolation transition is still debated (*Bonn et al.*, 2017). Indeed, this model does not consider the anisotropy of the stress network that is not negligible near the jamming transition (*Srivastava et al.*, 2021) and that is key to study this transition (*Behringer and Chakraborty*, 2019).
However, some evidences of increasing lenghtscale in the dense flow regime approaching the jamming transition was observed numerically for shear and normal stress imposed simulations (*Staron*, 2008; *Mills et al.*, 2008). As presented above, the fluctuations of velocity displays non-affine behavior with local correlated vortices (*Staron*, 2008). *Staron* (2008) and *Mills et al.* (2008) then built a correlation function on the fluctuations of velocities from which emerge a lenghtscale representing the typical length of correlated motion. This length appears to increase when approaching the static state, i.e. decreasing the inertial number. These lengthscale does not strictly diverge hence does not show a continuous jamming transition. In these results, frictional jamming transition behaves as a first-order transition. However, increasing lenghtscales near jamming are a signature of the formation of clusters within the system approaching the static jammed state showing that the system displays non-local behaviors at the approach from the jammed state.

Dynamical jamming phase diagrams and stochastic nature of the transition

Couples of recent studies (*Ciamarra et al.*, 2011; *Grob et al.*, 2014; *Srivastava et al.*, 2019, 2022) have focused on the frictional jamming transition in various configurations. The idea is to build phase diagrams by investigating the imposed conditions leading the system to jams and the state of the system when jammed. *Ciamarra et al.* (2011); *Grob et al.* (2014) have investigated the frictional jamming transition for volume-imposed configurations with shear rate and stress imposition. Interestingly, the former have depicted the existence of several regimes depending on the volume fraction and the shear stress leading to phase diagrams in the parameter-space (ϕ, τ) depending on the inter-particles friction coefficient leading to another extension of the phase diagram proposed by *Liu and Nagel* (1998), see Figure 2.1b, adding the inter-particle friction as order parameter of the jamming transition, see Figure 2.6a. Such diagram is presented on Figure 2.6b for $\mu_p = 0.8$. It shows first at low packing fraction, a flowing regime of steady state dense granular flow. For a range of higher packing fraction, there is a 'flow & jam' regime where the system displays steady state flow but dramatically jams after a time t_{jam}. They also observe for a higher range of volume fraction a 'slip & jam' regime where tangential contacts are mobilised leading to slow flow that dramatically decrease and lead to the jamming state. Finally, above a given packing fraction, the system is always jammed.

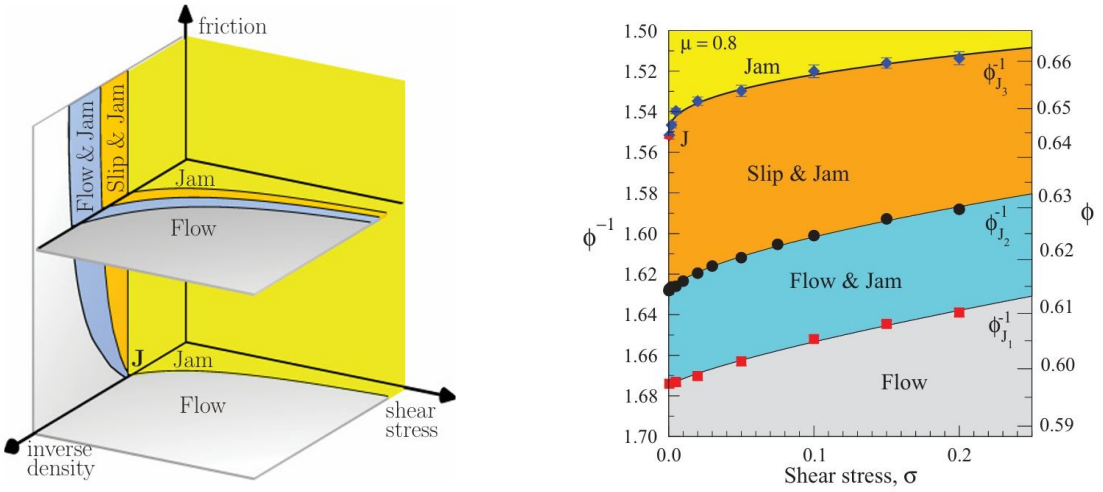

(a) (b)

Figure 2.6 – (a) Hypothetical phase diagram for the jamming transition of frictional granular systems porposed by *Ciamarra et al.* (2011). It is an extention of the phase diagram proposed by *Liu and Nagel* (1998), see Figure 2.1b. (b) Phase diagram in the parameter space (σ, ϕ) respectivaly the shear stress and volume fraction, obtained from numerical simulations of *Ciamarra et al.* (2011). The latter shows different regimes of frictional behavior dependig on the volume fraction and the shear stress.

These packing fraction ranges depends on the shear rate τ (noted σ on the figure) and the inter-particle friction. Interestingly, the existence of the 'flow & jam' regime lies in the fact that waiting in the steady state flow regime at high enough packing fraction can lead to the jamming of the medium. The corresponding time, i.e. t_{jam}, diverges when the packing fraction approaches the lower bound of the 'flow & jam' regime at constant shear stress. The lower bound, ϕ_{J1}, is then defined as the asymptotic value in the limit $t_{jam} \to \infty$. Equivalently, *Srivastava et al.* (2019) have shown, in stress-imposed configuration, that the mean time, t_c, to reach the static (jammed) state, diverges when the stress ratio μ approaches μ_{stop}. The latter is then defined as the asymptotic value in the limit $t_c \to \infty$. In both studies, the evolution of the critical times with the order parameter can be interpreted as the fact that approaching the transition's actual critical conditions, i.e. the asymptotic values, decreases the probability of reaching a stable arrangement of grains. Conversely, exceeding the asymptotic critical value, above ϕ_{J1} or below μ_{stop}, increases the probability that the arrangement of grains reach a stable configuration decreasing the critical jamming times. This behavior, supported by the non-negligible dispersion of the critical times when repeating the simulations, demonstrates the stochastic behavior of the granular system near the transition. It shows that the arrest, near the critical volume fraction or stress ratio, is unpredictable and depends on the friction between grains (*Srivastava et al.*, 2019).

Besides the stochastic nature, dynamical jamming can be studied as the quasi-static limit of dense granular flow rheology. This approach enables to study the physical mechanisms involved and to investigate their influence on the conditions leading to the cessation of flow.

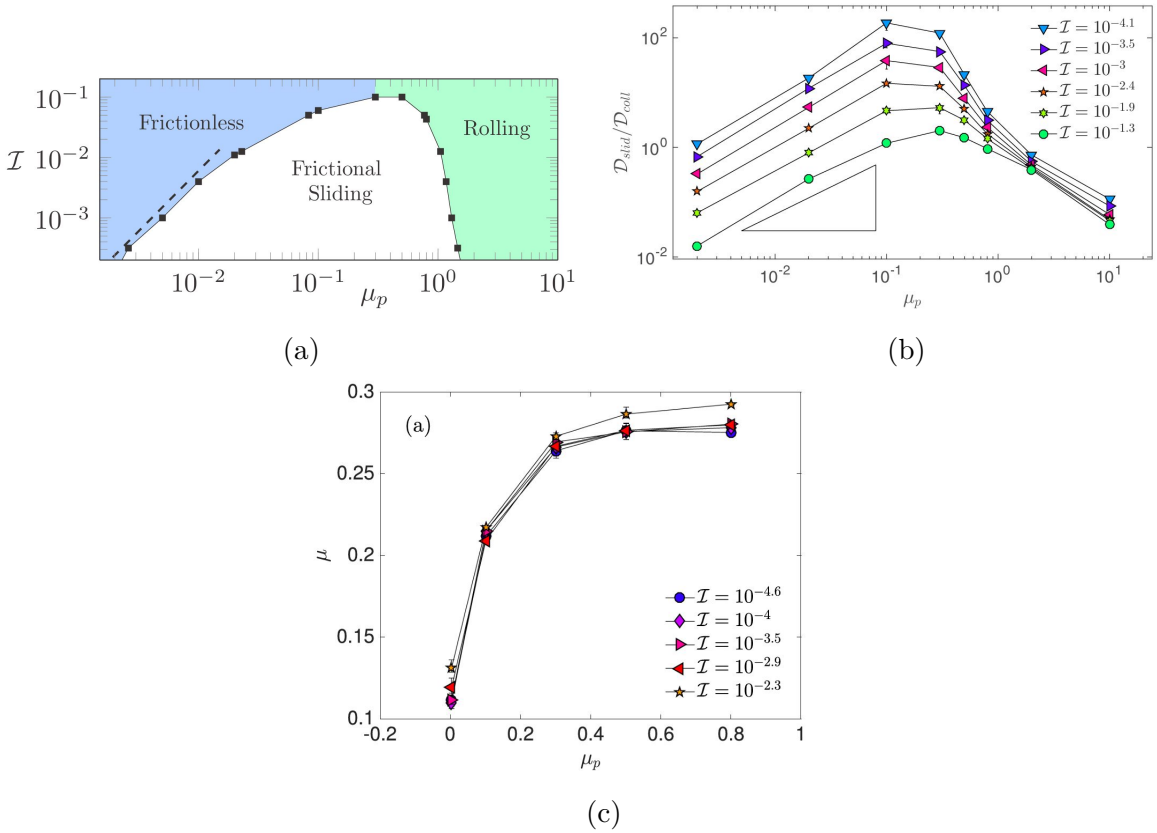

Figure 2.7 – 2D numerical simulations in plane shear cell results from *DeGiuli et al.* (2016); *DeGiuli and Wyart* (2017) (a) Ratio between energy dissipation by sliding friction and energy dissipation by collisions. (b) Friction regimes in a sheared granular system depending on the inter-particle friction and inertial number. (c) Critical global friction coefficient μ at the jamming transition versus inter-particle friction coefficient.

Jamming appears to be the result of the dissipation of the grains motion by frictional and collisional contacts (*DeGiuli et al.*, 2016; *Silbert et al.*, 2001), see Figure 2.7b. As a result, critical global friction coefficient at jamming also similarly increases with inter-particle friction *Peng et al.* (2023); *Perrin et al.* (2019); *Srivastava et al.* (2022), see Figure 2.7c, showing a strong effect of the sliding Coulomb criterion on the stability of the granular material at the jamming transition. This effect saturates when the microscopic friction coefficient reaches approximately $\mu_p \approx 0.5$ *DeGiuli and Wyart* (2017), see Figure 2.7c. Above this value, a granular medium enters in the rolling regime in which all contacts respect the Coulomb criterion at the grain scale leading to a constant effect of microscopic friction on granular stability *DeGiuli et al.* (2016), see Figure 2.7a. In this regime the dominant dissipation mechanism is by collision, see Figure 2.7b. Below this limit, *DeGiuli et al.* (2016) defined two frictional regimes, see Figure 2.7a: the frictional sliding regime for intermediate inter-particle friction coefficient $10^{-3} \leq \mu_p \leq 1$ where tangential contacts are easily mobilised and where friction dissipation is dominant, see Figure 2.7b. The last regime is the frictionless regime at really low inter-particle friction $\mu_p \leq 10^{-3}$ where collisions dissipation become greater than frictional dissipation, see Figure 2.7b. These results highlight the non-trivial influence of friction between grains on the behavior

of the granular system in the dense flow regime as well as in the quasi-static limit near the jamming transition.

2.3.4 The unjamming of frictional spheres

The initiation of flow from the static to a dense flow state is in another word a destabilisation of the granular medium. A granular medium in the static state under shear stress or shear rate exhibits local rearrangements that are local plasticity or fluidity of the granular material (*Staron et al.*, 2002; *Amon et al.*, 2013; *Zaitsev et al.*, 2008). The characteristic size of these rearrangements is increasing with increasing imposed shear stress or shear rate. The size of these structures diverges when the granular medium is about to flow leading to rearrangement size of the order of the system size and destabilising the assembly of grains that finally flows (*Aranson and Tsimring*, 2006; *Staron et al.*, 2002; *Staron and Radjai*, 2005).

In addition, the initiation of flow for frictional grains displays Reynolds dilatancy (*Reynolds*, 1885; *Bagnold*, 1966; *Pouliquen and Renaut*, 1996) by contrast with frictionless particles (*Peyneau and Roux*, 2008). This phenomenon appears to be intrinsically related to friction between grains. *Pan et al.* (2023) exposed that shear jamming, shear hardening and dilatancy seems to share a similar origin that lies on the presence of microscopic friction. Finally, *Pouliquen and Renaut* (1996) studied the dilatancy of a granular layer on a rough plane at the initiation of flow and found that it increases with increasing avalanche angle θ_{start} as well as with decreasing layer thickness.
These results show that equivalently to jamming, unjamming highly depends on inter-particle friction as well as geometrical entanglement of particles in the jammed state. These effect highlight the influence of both the inter-particle friction and finite-size effects, such as layer thickness, on the critical unjamming stress ratio and Reynolds dilatancy.

2.4 Conclusion on the litterature review on jamming and unjamming

These results on jamming and unjamming of granular systems showed us the complexity of the transition in idealized systems of frictionless grains in gravity-less configurations. The transition presents features of both first and second-order phase transition with clear discontinuities between jammed, well defined state, and unjammed state and a continuous accession to the critical isostatic condition leading to unjamming. Results also show that for finite inter-particle friction the jammed state is harder to characterize, as it depends on both inter-particle friction and preparation. The accession to jamming also displays sharp discontinuities as well as stochastic nature with a range of imposed parameter (volume fraction or stress ratio) where jamming has various probabilities to happen. These ranges depends on inter-particle friction and potentially grains collisions in a non-trivial way with three frictional regimes.
The stochastic effect is also observed on the geometrical finite-size effect on conditions of jamming and unjamming. As such, jamming and unjamming conditions vary with both

inter-particle friction and finite size effects. However, the phenomenology of unjamming of frictional sphere packings is similar to unjamming of frictionless particles in the sense that local rearrangements are observed forming local platicity structures growing when approaching unjamming.

2.5 Phase diagrams for the inclined plane configuration

Now that the jamming and unjamming processes have been detailed from idealized to more realistic configurations, it is interesting to focus on the consequences of the various effects observed above on the phase diagrams of a granular layer on an inclined plane. The latter being the configuration considered in our work, phase diagrams already built in various studies will be helpful in the understanding and characterization of hysteresis at the transition on a rough inclined plane.
The idea of this section is then to compare the phase diagrams built in this configuration with the results in more idealized systems discussed above to identify the common points and foundamental differences of jamming and unjamming in these various cases.
When a granular material is subjected to a high enough stress induced by gravity, the assembly of grains densely flows within the geometry of the configuration. On the inclined plane configuration the assembly of grains is organised as a layer of thickness h on the top of the rough plane. At a given inclination angle, higher than the avalanche angle (about $20-25°$ in three dimensions) and lower than a maximum angle (about $30°$ in three dimensions) a stable uniform steady state flow is observed for the whole grain layer *Silbert et al.* (2001), see Figure 2.8a. Above the maximum angle an unstable accelerated flow is observed *Silbert et al.* (2001), see Figure 2.8a. Under the avalanche angle there is a an angle range where the medium can be either in the flowing regime or in the static regime depending on the history of the stress path. This range is bounded by the avalanche angle above which a flow is always observed and the stopping angle below which no flow is observed. This specificity highlights hysteresis phenomenon and the complexity of the phase transition between fluid-like and solid-like granular behavior. Indeed, the system can exist in multiple stable or metastable states (*Quartier et al.*, 2000). The challenge is to understand hysteresis nature, which will be the subject of the following Section 2.6, and then to define a phase diagram and estimate the size of the hysteresis, i.e. the angle range for which the medium states depends on loading history. Such phase diagrams have already been studied for various material sizes. For a single grain in two-dimensions experiments on a rough plane, *Quartier et al.* (2000) have proposed a theoretical model that depicts the phase transition of the grain in the velocity-angle parameter space.
For larger granular medium sizes, especially larger layer thickness, where the model of *Quartier et al.* (2000) does not apply anymore, the values of critical angles, i.e. the avalanche angle θ_{start} and the stopping angle θ_{stop}, depends on the size of the system, see Figures 2.8b and 2.8c. On a rough inclined plane, the phase diagram can then be constructed considering the size of the layer in the direction normal to the plane, usually noted h that measures the thickness of the layer. Hence, the phase diagram in the thickness-angle parameter space was proposed by *Pouliquen and Forterre* (2002), Figure 2.8b. It completes the diagram of *Silbert et al.* (2001) on Figure 2.8a, by showing the hysteresis

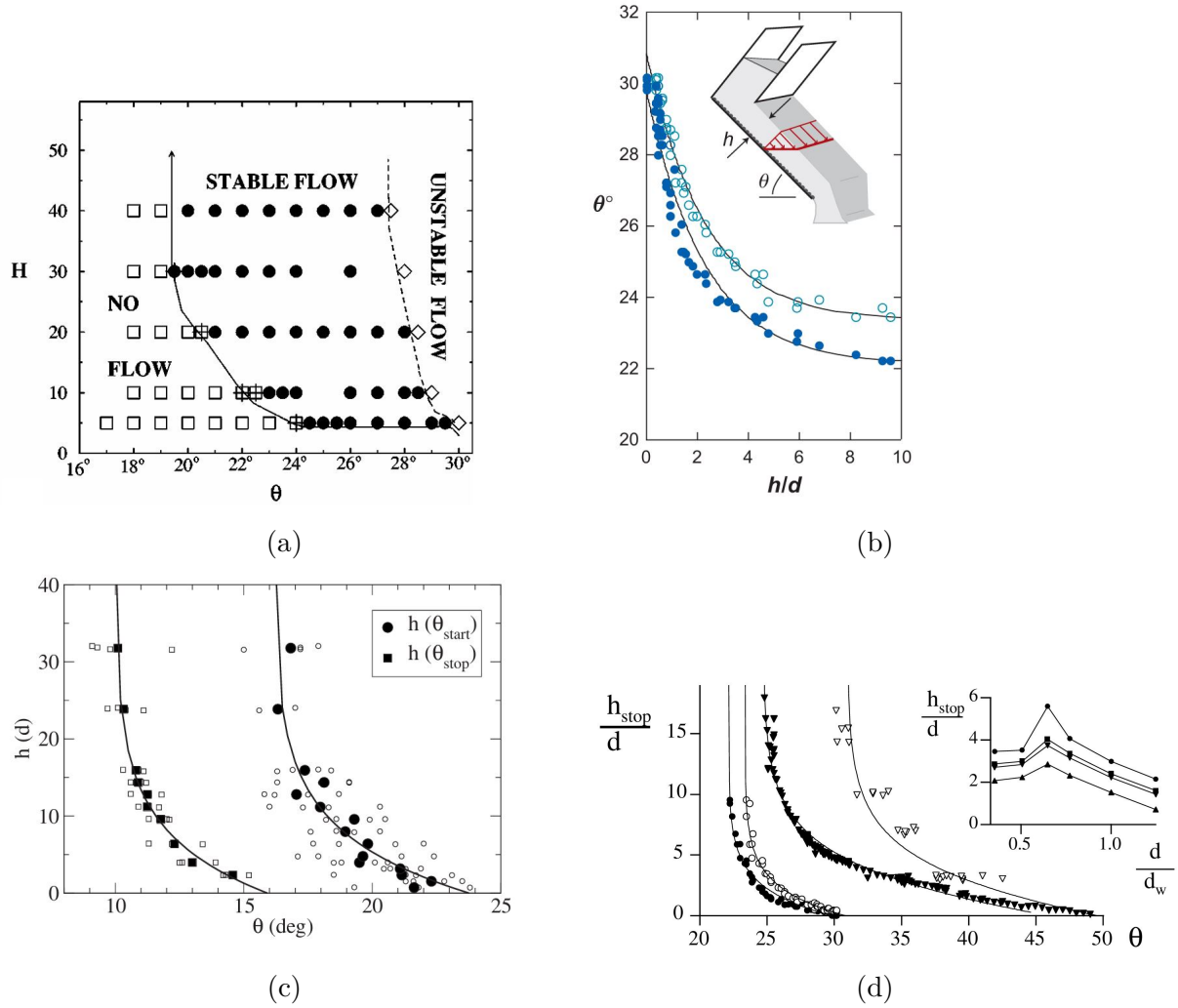

Figure 2.8 – (a) Phase diagram of a granular layer of thickness h on an rough plane inclined at angle θ from numerical simulations results from *Silbert et al.* (2001). (b) Critical angles θ_{stop} and θ_{start} at various layer thickness from experimental results (*Pouliquen and Forterre*, 2002) (Figure from *Forterre and Pouliquen* (2008)). Equivalently, the critical layer thicknesses h_{stop} and h_{start} can be plotted at various inclination angles θ (c) from numerical results *Staron* (2008) (d) from experimental results *Goujon et al.* (2003). The latter plot show h_{stop} with black markers and h_{start} with white markers, the triangles represents the measures for glass beads of diameter $d = 0.24mm$ on velvet plane and the circles represented the measures for glass beads of diameter $d = 0.5$ with a plane with glued particles. The inset shows the evolution of h_{stop} at various inclination angles (various markers) versus the glass beads grains diameter d on the same plane with glued particles at fixed diameter d_w.

angle range as a function of the layer thickness. They show that between zero and ten times the diameters of grains the angle range is significantly evolving since granular stability is dominated at those thicknesses by the geometrical finite-size effect of the bottom plane. For larger system sizes investigated by *Staron* (2008) for example, see Figure 2.8c, the boundary effect saturates and the critical angles are constant with variations of the

layer thickness. However boundary effect does not disappear, when the plane roughness characteristics are varied, see Figure 2.8d. When the size ratio between the grains of the bottom plane and the flowing grains or the compactness of the bottom plane grains or even the type of plane, the phase diagram in the thickness-angle space parameters are significantly evolving (*Goujon et al.*, 2003; *GDR MiDi*, 2004). Figure 2.8d shows the critical thicknesses evolution with θ for two distinct plane (velvet and glued particles) and two distinct flowing grain diameters. The asymptotic values of critical angles for infinite layer thickness varied from one bottom plane to another. In addition, the inset shows the evolution of h_{stop} with the ratio between the flowing grains diameter d and the wall grains diameter d_w for glued particles plane and shows a non-constant and non-monotonic evolution of h_{stop} with a higher value at $d/d_w \approx 2/3$. Surprisingly, this value does not depends on the inclination angle. Finally, these results show that the boundary condition, here the plane roughness, has a major influence on the stability of the granular layer hence on the critical angles values and probably on hysteresis. These results show that the conditions of jamming and unjamming on a rough inclined plane are significantly influenced by the finite size effects as well as the roughness condition at the bottom plane. By contrast with idealized frictionless systems, where the isostatic condition drives the behavior of the system around the transition, on an inclined plane the presence of gravity and the rough bottom plane induces anisotropy in the external applied stress as well as in the geometry itself.

Other known parameters plays a role in the phase transition. Inertia of grains appears to play a slight role in the critical angles but most importantly on the hysteresis (*Courrech Du Pont et al.*, 2003). The grains stiffness also appear to play a slight role in the phase diagram (*DeGiuli and Wyart*, 2017; *Favier De Coulomb et al.*, 2017) since it influences the geometrical entanglement of grains as well as the dynamic of grains.
The inter-particle friction coefficient, μ_p, has a crucial role in the stability of the granular system, as presented in Section 2.3 and Figure 2.7c, hence on the phase transition diagram, here in the $\mu_p - \theta$ parameter space, as shown by *DeGiuli and Wyart* (2017), *Perrin et al.* (2019, 2021) and *Peng et al.* (2023). These effects on phase transition, and in particular hysteresis, have been little studied on an inclined plane in literature. Therefore, their study is necessary for the present thesis.

These phase diagrams highlights the angle or stress ratio range between the stop and starts of flow, quantifying hysteresis phenomenon which is at the intersection of jamming and unjamming. Hysteresis is detailed and discussed in the following Section. Especially, the different works about the influence of the various physical mechanisms on hysteresis are presented.

2.6 Hysteresis in granular media

As explained previously, $\mu(I)$ rheology predicts the existence of a single global friction coefficient at the granular transition between static and dense flow regimes (Equations (1.10) and 1.11). Nevertheless, it is well known that this transition is subjected to an hysteresis phenomenon with two distinct global friction coefficients depending on the loading path. Hysteresis is well characterized for steady uniform granular flow down

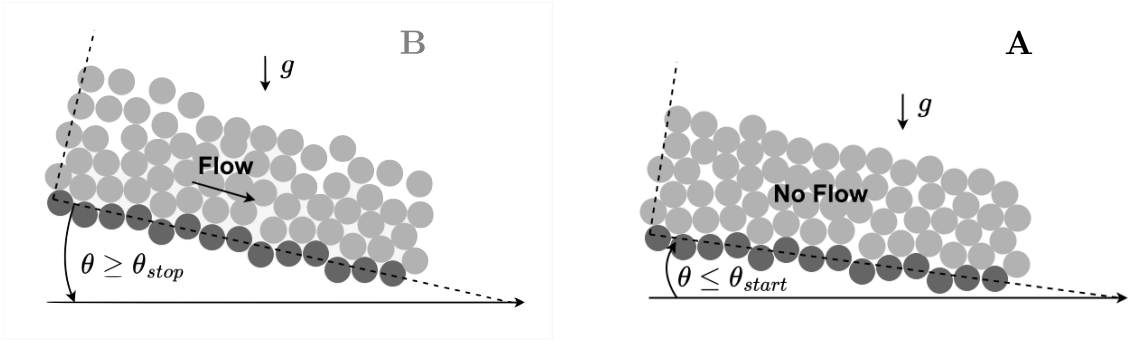

(a) (b)

Figure 2.9 – (a) Scheme of the process A, where the inclination angle is increased in the static regime to reach the avalanche angle θ_{start} (b) Scheme of the process B, where the inclination angle is decreased in the dense flow regime to reach the stopping angle θ_{stop}

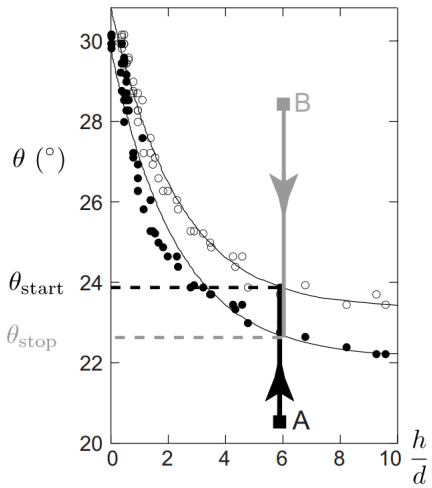

Figure 2.10 – Critical angles θ_{start} and θ_{stop} as a function of the layer thickness h/d in the inclined plane configuration, source: (*Pouliquen and Forterre*, 2002)

an inclined plane, where the inclination angle set the shear τ to normal P stress ratio, $tan(\theta) = \mu = \tau/P$ (*Pouliquen*, 1999). In this configuration, the inclination angle therefore sets the stress state of the granular medium. Considering a granular layer of a given thickness h made of grains of diameter d[1] and starting from the flowing state, point B on the Figure 2.10. When the inclination angle of the plane θ is decreased, see Figure 2.9b, the flow stops at a given angle, θ_{stop}. Starting from the static state, point A on the Figure 2.10. When increasing θ, see Figure 2.9a, the flow starts at the avalanche angle θ_{start} which is higher than θ_{stop}. The difference between the avalanche and stopping angle is characteristic of the hysteresis in the granular medium behavior. Hysteresis can be quantified through the difference between these angles : $\Delta\theta = \theta_{start} - \theta_{stop} > 0$. Figure 2.10 presents a set of measurement for several values of h/d obtained by *Pouliquen and Forterre* (2002). It shows that the avalanche angle is always higher than the stop angle and both the critical angles and hysteresis depends on the layer thickness as discussed in

1. average diameter in an experimental setup or diameter of all beeds in a monodisperse simulation

the previous Section.

This hysteresis has also been observed in other configurations: in a cylindrical Couette cell (*Da Cruz et al.*, 2002) see Figure (2.11b), in a plane shear cell (*Mowlavi and Kamrin*, 2021) see Figure (2.11c) and in a rotating drum (*Courrech Du Pont et al.*, 2003; *Perrin et al.*, 2019; *Peng et al.*, 2023) see Figure 2.11a. For all these results presented, the shear stress is imposed and the shear rate measured in order to know whether the medium is flowing of static. In the case of shear cells, annular and planar, the shear rate can also be imposed and the shear stress measured (*DeGiuli and Wyart*, 2017). For such protocol, hysteresis takes a different form, as shown by Figure 2.12 plotting the shear to normal stress ratio versus the inertial number. The Figure shows a non-monotonicity of the flow curve $\mu(\mathcal{I})$ resulting from hysteresis. In such cases, hysteresis is quantified as the difference $\Delta\mu$ between the the global friction coefficient, μ_{start}, in the limit $\mathcal{I} \to 0$ and the lowest global friction coefficient μ_{stop}.

Overall, hysteresis is a phenomenon that occurs at the phase transition between the dense flow regime and the static regime of granular materials. It is observed in various configurations with different geometries and is intrinsically related to both jamming and unjamming, i.e to the accession and loss of stability of granular assemblies. The review on these transitions has enabled us to understand the various approach that analyse the system behavior near the transitions. It also allowed us to identify key quantities that describe the evolution of the granular micro-structure in order to study hysteresis using these tools.

Hysteresis is globally linked to first-order phase transitions in the theory of phase transitions (*Hohenberg and Krekhov*, 2015). The jamming of granular assemblies displaying features of first-order phase transition, especially discontinuities of coordination number at transitions, hysteresis appears to be linked to that transitions behavior. We have seen that the granular transition depends on various effects, inter-particle friction is central for jamming and unjamming conditions, the stress anisotropy also plays a role, especially for frictional particles. In addition, the transition being stochastic, the conditions of transition depends on the rate of stress or strain imposition as well as on the size of the system. Finally, the configuration studied appears to impact the transition and hysteresis, as seen above. The configuration drives the geometry of the system, i.e the boundaries, creating additional geometrical anisotropy.

As a results, from all these effects, several studies have chosen to study various physical mechanisms influence on hysteresis in various configurations. Then, these results are discussed in the following Section in order to understand the nature of hysteresis in more detail and to identify the points that remains to be elucidated.

2.6.1 Hysteresis nature

Hysteresis relies on the combination of two different processes: the jamming, or cessation of flow, and the unjamming, or initiation of flow (e.g. *Silbert et al.*, 2001; *Pouliquen and Renaut*, 1996; *Staron et al.*, 2002; *Pouliquen and Forterre*, 2002; *Srivastava et al.*,

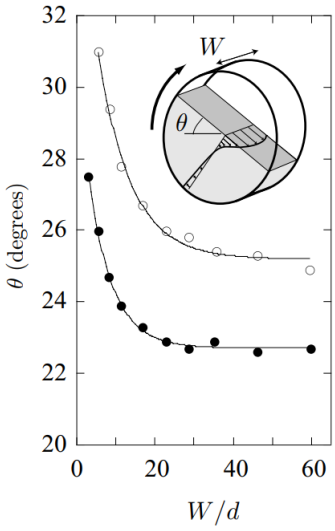

(a)

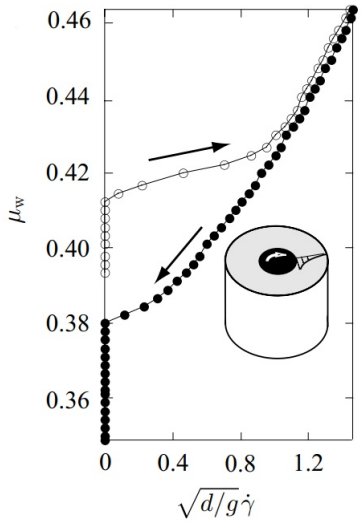

(b)

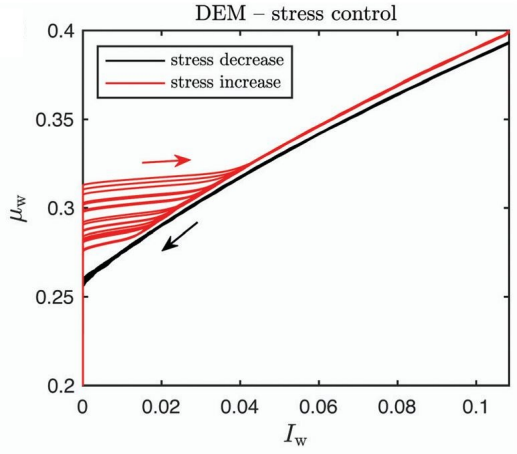

(c)

Figure 2.11 – Observation of hysteresis in (a) a rotating drum : critical angles θ_{stop} (filled circles) and θ_{start} (open circles) as functions of the thickness of the drum W (source : *Courrech Du Pont et al.* (2003); *Andreotti et al.* (2013)) and (b) a cylindrical Couette cell : friction coefficient μ_W at the inner circle cylinder as a function of the shear rate for increasing shear rate (open circles) and decreasing shear rate (filled circles) (source : *Da Cruz et al.* (2002); *Andreotti et al.* (2013)). (c) Flow curve $\mu(\mathcal{I})$ for stress imposed numerical simulations in plane shear cell configuration from *Mowlavi and Kamrin* (2021).

2022).

The physics of both initiation and cessation of flow in granular media is particularly rich, as highlighted above, so that most of the studies in the literature focus on one or the other phenomenon. Studying hysteresis at this transition requires to consider both phenomenon evolution as a function of relevant physical parameters. The nature of the hysteresis has first been assigned to particle inertia effect with experiments of dry and immersed granular system in a rotating drum (*Courrech Du Pont et al.*, 2003). They

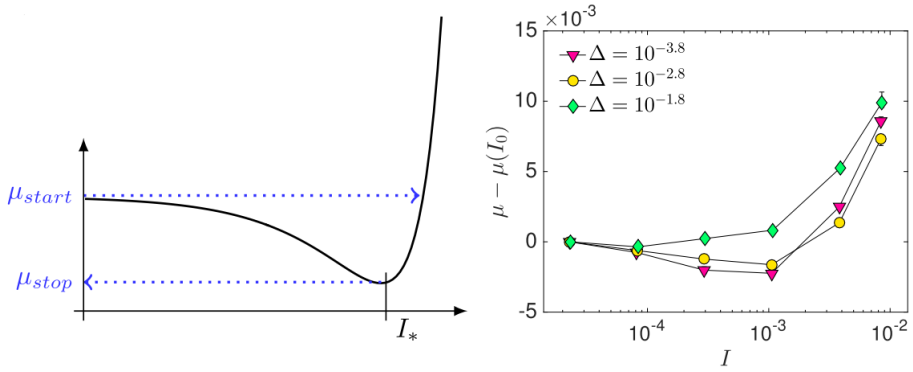

Figure 2.12 – Global friction μ of the granular media as a function of the inertial number. The left plot shows the definition of μ_{start} and μ_{stop} and the right plot the results of their simulations for different values of Δ, source : (*DeGiuli and Wyart*, 2017)

measured the evolution of the inclination angle of the free surface of the medium when rotating the drum at low angular velocities. They observed classical intermittent avalanches and rest states at the free surface (*Balmforth and McElwaine*, 2018; *Perrin et al.*, 2019; *Peng et al.*, 2023) as depicted by Figure 2.13a. Hysteresis $\Delta\theta$ is calculated for one avalanche as the difference of angles between the starting angle measured at the initiation of the avalanche following the static state that was reached at θ_{stop} previously (in time). This process was repeated with various Stokes number: $St = \sqrt{\rho_p \Delta \rho g d^3}/18\eta_f$ comparing viscous dissipation effect (low St) to inertial effect (high St). The hysteresis is then averaged over all avalanches and plotted as a function of the Stokes number, see Figure 2.13b. They showed that for $St \geq 20$ there is a large hysteresis that does not varies with the Stokes number. By contrast, for $St < 20$ hysteresis decreases with the Stokes number. These results suggest that when fluid dissipation effect becomes dominant and grain inertia negligible, hysteresis decreases significantly. Yet, more recent works (*Perrin et al.*, 2019; *Grob et al.*, 2014; *DeGiuli and Wyart*, 2017; *Peng et al.*, 2023) have shown that the inter-particle friction is a dominant mechanism in the hysteresis at the expense of the inertia of grains. *Perrin et al.* (2019) showed, in the same configuration as *Courrech Du Pont et al.* (2003), that reducing grains inertia can lead to higher hysteresis values. Indeed, they carried out rotating drum experiments of glass beads in water at $St = 4$ measuring $\Delta\theta = 1°$. Then, they changed the fluid by adding Ucon oil for the same beads. This induces a decrease of the Stokes number to $St = 6 \times 10^{-2}$ and gives an hysteresis of $\Delta\theta = 4°$. These results correspond to the stars markers on Figure 2.15. They conflict with the suggestion from *Courrech Du Pont et al.* (2003) results, that fully overdamped suspensions have no hysteresis, and rather suggest that another parameter plays a role in the hystereric phenomenon. As a consequence, *Perrin et al.* (2019) used the experimental setup detailed in *Clavaud et al.* (2017). It consists in using silica beads in ionised water that creates electrostatic repulsive forces at ranges greater than the roughness of the grains, preventing them from making solid contacts. This allows them to tune the friction between grains by varying the ionic concentration and to perform experiments without inter-particle friction. Figure 2.14 presents the evolution of the free surface angle with time in their experiment for frictional particles (green curve) and frictionless particles (grey curve). The figure shows that frictionless particles does not displays any

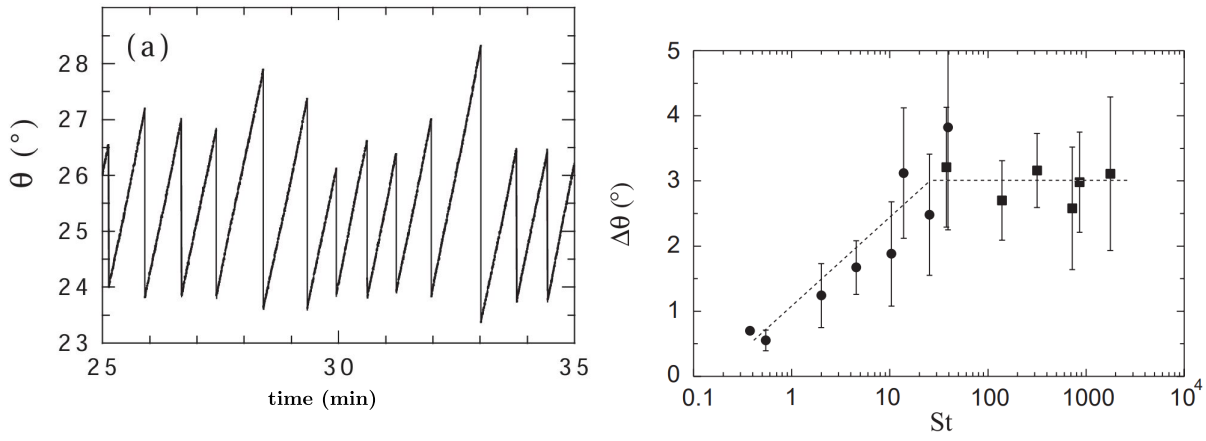

(a) (b)

Figure 2.13 – (a) Inclination angle of the free surface of the medium as a function of time of experiment. The increase of θ with time highlights the static state where the inclination angle linearly increase with time with a slope equal to the angular velocity until the angle reach θ_{start}. The sharp decreases of angle highlights granular avalanches at the free surface until the angle reach θ_{stop}. Source : (*Courrech Du Pont et al.*, 2003). (b) Hysteresis $\Delta\theta$ as a function of the Stokes number, source : (*Courrech Du Pont et al.*, 2003)

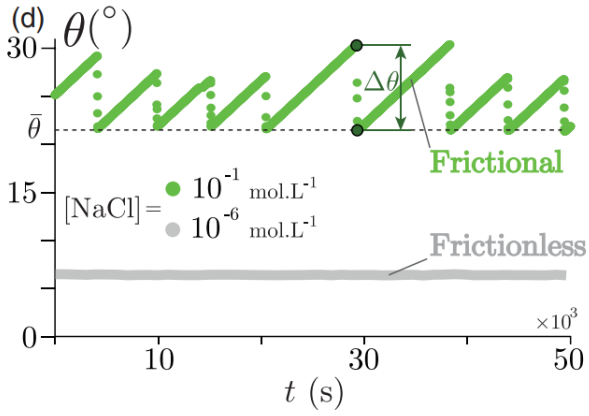

Figure 2.14 – Angle of the granular media free surface as a function of time of experiment (the max values correspond to θ_{start} and min values to θ_{stop}), source : *Perrin et al.* (2019)

intermittent flows of avalanches and static states, conversely to frictional particles, and thus does not have any hysteresis. They reported on Figure 2.15 their hysteresis measurement depending on the Stokes number and the concentration of ions and compare them to the results of *Courrech Du Pont et al.* (2003). The figure shows no clear trend but demonstrates that in the frictionless case no hysteresis is observed when varying the Stokes number.

Still in rotating drum, *Peng et al.* (2023) performed experiments for dry granular systems varying the friction between grains taking different grain materials listed here in *a*

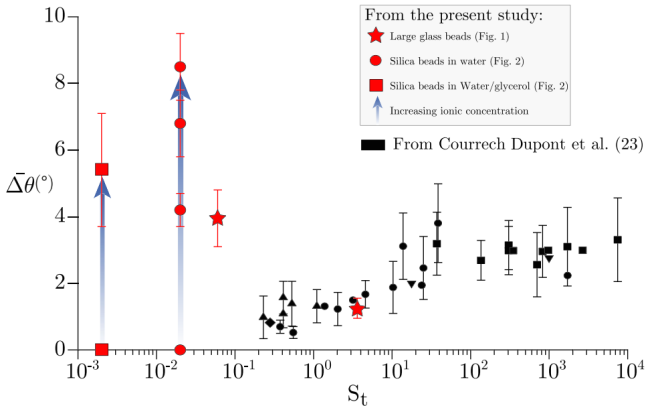

Figure 2.15 – Hysteresis $\Delta\theta$ as a function of the Stokes number, source : *Perrin et al.* (2019)

priori less to more frictional order: steel, ABS (thermo-plastic polymer), glass, 3D printed plastic grains and finally 3D printed grains with bumpy surface (BUMP). They observed a decrease of hysteresis of more than 6° between BUMP particles with $\Delta\theta = 10.7°$ and steel particles with $\Delta\theta = 4°$. The link with friction coefficient values is non-trivial since they did not performed tribology measurement of the grains surfaces but one can expect the more frictional particles to be with BUMP material and the less frictional to be with steel material.

Earlier work of *DeGiuli and Wyart* (2017) investigated hysteresis in simulations of granular system in plane shear-cell at imposed velocity. As explained previously, in that configuration hysteresis results from a non-monotonicity of the flow curve $\mu(\mathcal{I})$, see Figure 2.12, with decreasing global friction coefficient with increasing inertial number for $\mathcal{I} < \mathcal{I}_*$ (velocity-weakening) and increasing global μ for increasing $\mathcal{I}$ for $\mathcal{I} > \mathcal{I}_*$ (velocity-strengthening). From these flow curves, they measured hysteresis $\Delta\mu$ for two inter-particle friction coefficients $\mu_p = 0.3$ and $\mu_p = 0$ and plotted hysteresis for both μ_p at various system size, N, and grains relative stiffness $\Delta = P/k_N$ (p being the granular pressure and k_N the normal stiffness of grains) on Figure 2.16. They observed that without inter-particle friction, hysteresis is negligible, lower than 1×10^{-3} which gives at $\mu_p = 0$ for $\mu_{start} = 0.11$, $\mu_{stop} = \mu_{start} - \Delta\mu = 0.109$. Calculating the corresponding angles for gravity driven configurations, it gives $\theta_{start} = 6.28°$ and $\theta_{stop} = 6.22°$ and an hysteresis below $\Delta\theta = 0.06°$ for frictionless particles. For frictional particle $\mu_p = 0.3$, the bigger system size and highest particles stiffness, they measured $\mu_{start} = 0.27$, $\mu_{stop} = 0.2675$ and $\Delta\mu = 0.0025$. The corresponding angles are $\theta_{start} = 15.11°$ and $\theta_{stop} = 14.98°$ and an hysteresis of $\Delta\theta = 0.13°$. Hysteresis is significantly lower in the frictionless case, suggesting no hysteresis phenomenon for frictionless particles. However, the value for frictional grains is much lower than usual values for glass beads for example, for which inter-particle friction is about $\mu_p = 0.4$. Indeed, for dry glass beads, *Peng et al.* (2023) obtained $\Delta\theta = 5.4°$ in rotating drum, *Forterre and Pouliquen* (2008) obtained $\Delta\theta \approx 1.26°$, see Figure 2.10, on a rough inclined plane, and *Da Cruz et al.* (2002) obtained $\Delta\theta = 1.5°$ in annular Couette cell, with $\theta_{start} = 22.3°$ and $\theta_{stop} = 20.8°$ calculated from the measured critical stress ratios from Figure 2.11b with $\mu_{start} = 0.41$ and $\mu_{stop} = 0.38$ and an hysteresis of $\Delta\mu = 0.03$. Then,

this result show that the hysteresis is expected to depend on the geometrical configuration as well as the the driving process, i.e. velocity or stress imposed. In addition, *DeGiuli and*

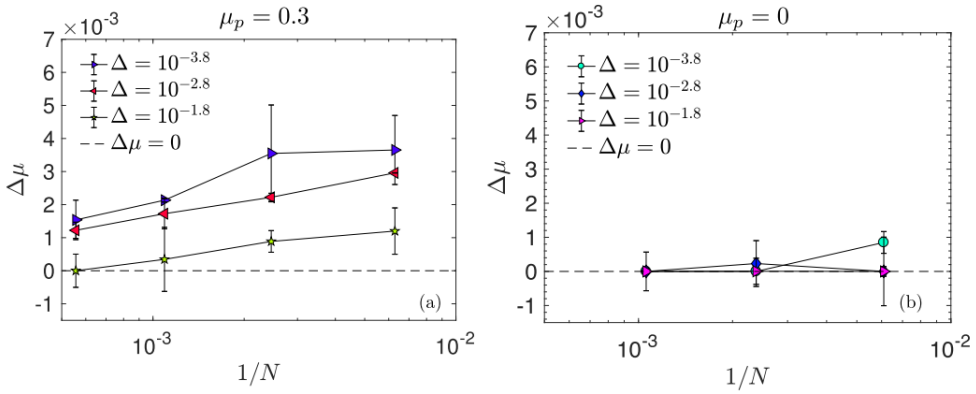

Figure 2.16 – Hysteresis $\Delta\mu$ as a function of the size of the 2D domain for different values of *Delta*, the plot at the left is for a particle friction coefficient of $\mu_p = 0.3$ and the right one for frictionless particles $\mu_p = 0$, source : *DeGiuli and Wyart* (2017)

Wyart (2017) varied the stiffness of grains through the parameter $\Delta = P/k_N$, see Figure 2.16. This parameter quantifies the grains stiffness relatively to the maximum pressure a grain is subjected to in the system. The lower Δ, the stiffer the grains. They show, see Figure 2.16, that decreasing grains stiffness decreases hysteresis and found vanishing hysteresis in the limit of high system size ($1/N \to 0$) for the softer grains. This result is interesting since it suggest a similar effect in the results of *Perrin et al.* (2019). Indeed, the classical solid-solid Hertz normal contact force is replaced by an electrostatic force. The comparison between both forces amplitudes is detailed in Appendix A.6. The effective relative stiffness decreases when switching from a classical solid-solid hertzian contact to a repulsive electrostatic contact, suggesting a potential stiffness effect in the work of *Perrin et al.* (2019).

Overall, The absence of hysteresis in the frictionless case can be related to the accession to the jammed state for frictionless assembly in the isostatic state as depicted in Section 2.2. In addition, the vanishing dilatancy in such case (*Peyneau and Roux*, 2008) suggests that the unjaming transition is continuous considering the macroscopic packing density ϕ. As such, several studies (*Bagnold*, 1966; *Perrin et al.*, 2019) suggested a link between hysteresis and dilatancy sharing a common origin in the friction between grains. Moreover, the effect of grains inertia on hysteresis is not clearly established yet and requires further study on viscous dissipation influence on jamming and unjamming transitions as well as on hysteresis.

2.6.2 Hysteresis in various constitutive models

The framework that emerges from the works presented above, proposed by *DeGiuli and Wyart* (2017) assigned the hysteresis behavior to the "self-fluidisation" of the granular medium in the flowing state. This process lowers the stress threshold, μ_{stop}, at which the medium stops compared to the one at which the medium starts flowing, μ_{start}. In this

framework the role of both friction and inertia are central since the ability of the granular medium to "self-fluidise" is based on the idea that a residual mechanical energy due to collisions and forces network vibrations destabilises contacts on the verge to sliding and that keep in motion the whole assembly of grains. The fraction of sliding contacts χ then becomes an internal parameter of the flow curve, allowing the model to quantify the decrease of global friction coefficient by tangentially mobilised contacts. As such, the classical flow curve from Equation (1.10), i.e. $\mu(I) = \mu_{stop} + b\mathcal{I}$, is adjusted to account for the decrease $\tilde{\mu_c} = g(\chi)\mu_{stop}$ of the critical stress ratio with a decreasing function of χ, $g(\chi) = 1 - \chi$, with $\alpha = 0.3$. The flow function become:

$$\mu(I) = \mu_{stop}(1 - \chi) + b\mathcal{I}. \tag{2.12}$$

The variations of χ are theoretically predicted by their model. They compare the energy from collisions related to the granular temperature to the potential energy of contacts and build a scaling of that ratio with the inertial number and grain stiffness. From here, they estimate the sliding contacts proportion induced by the theoretical mechanical noise and build a scaling of χ with the inertial number and grain stiffness as:

$$\chi \sim (\mathcal{I}/\Delta^{1/4})^a \tag{2.13}$$

This scaling accurately predict the evolution of χ with $\mathcal{I}$ and Δ in their numerical simulations, allowing them to compute Equation (2.12) with the proper scaling of χ. This Equation enables them to plot at a given inter-particle friction coefficient the flow curves from Figure 2.12 (right panel) that captures the trend of the observed flow curves from their numerical simulations. With their work, they highlighted that the ability of a tangential contact to be set in motion by this residual energy depends on the value of the friction coefficient between grains and the residual energy amplitude depends on the inertia of grains. This picture is supported by the fact that the hysteresis depends on inter-particle friction (*Perrin et al.*, 2019; *Peng et al.*, 2023) and contact stiffness (*DeGiuli and Wyart*, 2017). Indeed, the stiffness influences the residual energy and affect accordingly the hysteresis (*DeGiuli and Wyart*, 2017).

Based on these recent findings, some aspects remain to be elucidated. In particular the vibrations induced by collisions are not cancelled for frictionless material, and one expects the self-fluidization process to be partly present, even for frictionless particles, which is not experimentally observed. In addition, one expects the dissipation of contacts to influence this self-fluidization which is a dynamical process, but simulations from *Silbert et al.* (2001, 2003) have shown no effect of the restitution coefficient on the stopping angle. Nevertheless, the recent findings of *DeGiuli et al.* (2016) showing a non-trivial combined dissipation mechanism between friction and collisions requires to study both effects on hysteresis.
Since the experiments of *Perrin et al.* (2019) are performed in the viscous Stokes limit, i.e. with negligible particle's inertia and zero effective restitution coefficient, the residual energy is expected to be damped. The link with the self-fluidization process described in *DeGiuli and Wyart* (2017) is therefore not obvious. In addition, the hysteresis obtained in *Perrin et al.* (2019) is suprisingly high (of the same order than for highly frictional dry materials *Peng et al.* (2023)) considering the presence of a fluid damping the self-fluidization process.

Aranson et al. (2008) also developed a model of hysteresis based on the fitting of the evolution of the sliding contacts proportion. They defined an order parameter for the transition ρ which is similar to $1 - \chi$ but slightly adapted with a criterion on the contact time in order to consider only long-time contacts as rigid static contacts. They model the bifurcation, i.e. the hysteretic cycle of this parameter with imposed shear stress. They where able to predict the evolution of $h_{stop}(\theta)$ and $h_{start}(\theta)$ with discrepancies from experimental results near the limit $h \to 0$, especially on h_{start}, predicting its origin from the fitting of the order parameter in two dimensional simulations with low number of particles.

In the framework of the non-local granular fluidity model (NGF), *Mowlavi and Kamrin* (2021) modified the constitutive relation using a correction function in order to take into account the non-monotonicity of the flow curve without modeling the underlying physical mechanism responsible for this non-monotonicity. Then, they calibrate the model with DEM stress controlled simulations in plane shear without gravity. Hence, they compared the predictions from the calibrated model to DEM results obtained for two other configurations: the inclined plane and the plane shear cell with gravity (stress imposed). The model predicts well the hysteresis, the critical stresses and rheological behavior in the flowing state in the latter configuration but did not predicted well the hysteresis on an inclined plane since no single choice of boundary conditions on their model led to accurate predictions for both transitions.

The model of *Henkes et al.* (2016) based on the prediction of rigid clusters with the use of pebble game, detailed in Section 2.3, allows *Grob et al.* (2014) to predict the hysteresis behavior in discontinuous shear-thickening of dense suspensions.

The hydrodynamic model from *Artoni et al.* (2011) is an extension of the constitutive model from *GDR MiDi* (2004) adding dissipation energy terms from collisions through the granular temperature and by friction. This model allows them to predict the bifurcation in shear rate (or inertial number) observed as the hysteresis cycle depending on the energy dissipation process. As such, it models the history dependence of the flow curve at a given microscopic friction coefficient and layer thickness and extended the equations to account for thickness dependence by changing the boundary condition of hydrodynamic pressure as proposed by *Bocquet et al.* (2002). This enables to model the dependence of both critical angles with layer thickness, see Figure 2.10. Nevertheless, their model predicts a continuous jamming transition in the flowing regime at $\dot{\gamma} \to 0$ which is not observed in practice due to non-local clustering effects, see Section 2.3.

Edwards et al. (2019) also developed a hydrodynamic model that consider hysteresis via a non-monotonic function.

2.7 Objectives of the thesis

As depicted in the previous Section 2.6, some aspects about hysteresis remains unclear and need further research. First, inter-particle friction was shown to be central in hysteresis phenomenon as well as on jamming and unjamming transitions. The aim is therefore to characterize the accession and initiation of flow in the presence and absence of friction, in order to identify the fundamental differences between jamming and unjamming tran-

sitions and, above all, their consequences on hysteresis. In the frictional case, the system jams into various states that depend on the geometric configuration, the imposed stress or strain rate, and the initial preparation, i.e. the volume fraction. It is therefore necessary to establish these different states as a function of μ_p on an inclined plane.
We also need to develop a protocol that minimizes the stochastic and geometric effects on the transition, i.e. a sensitivity analysis to the applied strain rate (its time dependence) and the system size.
The effect of grain inertia and the transfer of momentum through collisions, as well as their dissipative effects, require systematic study. The combined impact of friction and inertia on hysteresis needs to be decorrelated with a combined study of St and μ_p varied independently. In particular, a result of granular hysteresis in the frictionless case in the absence of viscous dissipation, i.e. in the inertial regime, without imposing velocity to the system, is lacking.

The present work will therefore focus on studying the combination of the three dissipation processes, collision, friction and drag force on hysteresis. Characterizing the two granular regimes and transitions through the evolution of several variables describing the macroscopic evolution and the micro-structure evolution of the system under imposed stress. These latter objectives will be conducted in the inclined plane configuration using numerical simulations which enable us to decorrelate the various sources of dissipation and their influence on hysteresis. The configuration is presented as well as the numerical model in the following Chapter 3. The characterization of granular states as well as the effects of contact dissipation processes are qualitatively presented on Chapter 4. The last Chapter 5 focuses on the combined effect of friction and inertia on hysteresis. Finally, conclusions on the work and perspectives for further research will be presented in Chapter 6.

Chapter 3

Material and method

The work carried out over the three years of the present thesis focuses on numerical simulations, as described in the previous Section 2.7. With the aim of studying independently the influence of given major parameters such as stress, inter-particle friction coefficient or Stokes number on the response of a granular medium, we model the trajectory of each grain in the medium. To do so, we need physical models of grain-grain and fluid-grain interactions presented on Section 3.1. Then, we need to use a numerical code, presented in the second Section 3.3 of this chapter, that allows us to numerically solve the dominant grain-scale interactions developed in Section 3.2. Thus, the inclined plane configuration, i.e. the geometry in which the medium evolves, is presented on Section 3.4 as well as the protocol associated to this configuration. A sensitivity analysis has been performed and presented in Section 3.5 on the parameters of the model including the time step, that drive the numerical resolution of the code, and fixed parameters that may have an influence on hysteresis. Finally, the sensitivity analysis performed on parameters associated to the protocol on the inclined plane are presented on the last Section 3.6.

3.1 Physics of interactions at the grain scale

In the case of arthermal systems with a characteristic size above $100\mu m$ the forces acting on grains are of two kinds. The contact forces between two or more grains or the fluid forces between the grain and the surrounding fluid. For the former ones, the microscopic phenomenon that influence the contact properties are neglected leading to a classical elastic contact force framework at the scale of the grain. These interactions are presented in this section.

3.1.1 Normal contact force

We consider first the interaction between two solid particles as depicted by Figure 3.1. The force has a normal component noted F_N which is colinear with the vector that connects the centers of the particles n (vector normal to the contact area).

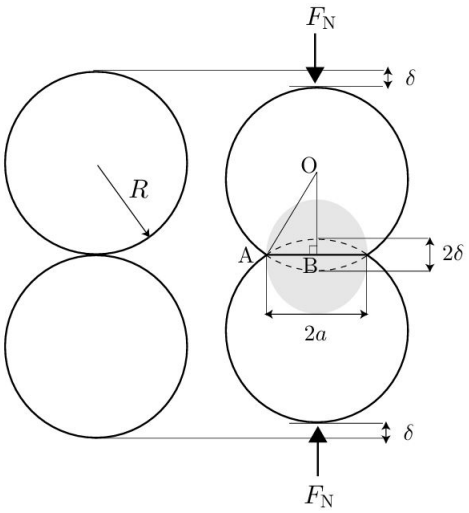

Figure 3.1 – Scheme of normal force interaction, F_N, between two grains of the same size. The surface of contact is $2a$ and the inter-penetration depth is δ. Source: (*Andreotti et al.*, 2013)

Hooke contact law

A first approximation of the normal force between two particles is a generalisation of the Hooke's law of Equation (A.10) but by neglecting the effect of the area of contact. In the interaction between two particles we define δ the interpenetration depth between grains as depicted by Figure 3.1 with $\delta = 1/2(d - (x_1 n + x_2 n))$ with d the diameter of grains and $(x_1 - x_2)n$ the distance between the centers of grains. In the absence of shear displacement, i.e. considering that δ is colinear with the normal vector n and without friction, the normal contact force gives:

$$F_N = k_N \delta, \tag{3.1}$$

with k_N the stiffness of the structure (here the sphere) that depends on the material property. k_N is calculated from the Young's modulus for a sphere as follow:

$$k_n = \frac{S_{sphere} E}{d} = \frac{\pi d^2 E}{d}. \tag{3.2}$$

Equation (3.1) is actually a rough approximation of the real normal force measured, especially at high strains where the force value depends on the contact surface area. Nevertheless, this model is broadly used in numerical simulations of dense or diluted flows where strains at the contact scale are limited in the calculation and does not hardly influence the flow dynamic.

Hertz contact law

A more rigorous model of contact force is the Hertz contact law that derived from the equations of linear elasticity for a sphere. It can be more simply calculated with Equation (A.6), considering the strain evenly distributed over the surface, and combined with the

Hooke's Equation (A.10) without shear, it gives:

$$F_N = \sigma S = K\epsilon S. \tag{3.3}$$

In three-dimension, $S = \pi a^2$, a represents the radius of the disk formed by the area of contact between the spheres. It can be expressed with d and δ with Pythagore's Theorem: $d^2/4 = a^2 + (d/2 - \delta)^2$ which gives considering $\delta \ll d$, $a = \sqrt{d\delta}$. In addition, we consider the strain as being equal to the interpenetration relative to the radius of the area of contact, $\epsilon = \delta/a$, it gives with the expression of the elastic modulus K:

$$F_N = K\sqrt{d}\pi\delta^{3/2} = \frac{\pi\sqrt{d}E}{3(1-2\nu_p)}\delta^{3/2}, \tag{3.4}$$

with ν_p the Poisson's coefficient of particles.

3.1.2 Tangential contact force

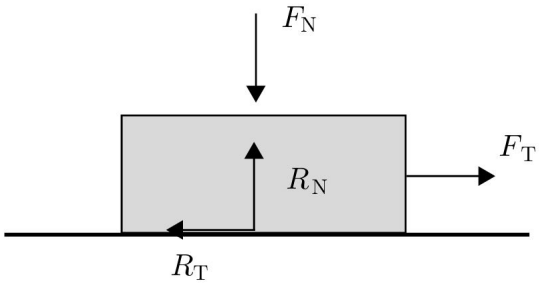

Figure 3.2 – Scheme of normal, F_N, and tangential, F_T, force interaction between a two solids. Source: (*Andreotti et al.*, 2013)

The tangential contact force, or friction contact force between two solids is still a subject of tribology's research. Nevertheless, for the contact between perfect spheres of same size, the Coulomb law is usually a broadly used model. Hence, only this model will be presented here. This model simply consider the tangential force at the contact F_T, see Figure 3.2. The Amontons-Coulomb law describe the behavior of two solids in contact through the following law:

$$F_T = \begin{cases} \mu_p^d F_N & \text{if } F_T^i \geq \mu_p^s F_N, \\ 0 & \text{otherwise.} \end{cases} \tag{3.5}$$

This means that there is a given force $F_T^i = \mu_p^s F_N$ needed to be initially imposed in order to initiate a tangential motion and which is proportional to the normal force F_N with the static friction coefficient μ_p^s. If the motion is not initiated the tangential force is unknown. If the motion is initiated, then the value measured of the tangential force is also proportional to the normal force $\mu_p^d F_N$ but is lower than the the force F_T^i meaning that the dynamic friction coefficient is lower than the static one, $\mu_p^d < \mu_p^s$. By definition there is an hysteresis in friction at the contact scale. Its modeling being unnecessary to observe granular hysteresis, in the following we take a single value noted μ_p.

3.1.3 Contact dissipation

Here above were presented the normal and friction forces models in the case of rate-independent interactions. In other words, the models presented above does not take into account the case of dynamical contacts but only the evolution of the force with strain. If two particles enters in collision, the Hertz's law and Coulomb law does not predict any dissipation of the motion of grains that are observed both in the normal contact direction and tangential contact direction. Hence, one should introduce dissipation terms in the models that render the above models not purely elastic.

The inelastic coefficient of normal contact interactions, also called restitution coefficient e_N is simply the ratio between the velocity of a grain before the collision, u_p^{in}, and the velocity after the collision u_p^{out} considering the collision between two identical particles with one immobile particle in the whole process:

$$e_N = \frac{u_p^{in}}{u_p^{out}}. \tag{3.6}$$

This coefficient is characteristic of the material. In the spring-dashpot inelastic model of normal contacts (*Schwager and Pöschel*, 2007), that will be presented for numerical simulations in Chapter 3, it is expressed as a function of the collision time, t_c, as:

$$e_N = e^{-\gamma_N t_c/m}, \tag{3.7}$$

with γ_N the viscous dissipation used in the spring-dashpot model, see Chapter 3, and m is the mass of the particle.

The collision time can be simply approximated considering that the the kinetic energy of the grains, $E_k = mu^2$, is converted into an elastic potential energy (from Hertz's law) $E_{el} \sim F_N\delta \sim E\sqrt{d}\delta^{5/2}$ within the collision time $t_c \sim \delta/u$, which gives:

$$t_c \sim \left(\frac{m^2}{dE^2u}\right)^{1/5}. \tag{3.8}$$

A more rigorous calculation of the collision time in the spring-dashpot model is given by *Schwager and Pöschel* (2007). This latter model will be used to perform numerical simulations in the work presented in this manuscript.

3.1.4 Fluid-grains interactions

By contrast with numerical simulations where a granular system can be simulated without any influence of fluid, actual granular systems in experiments or applications evolves in a surrounding fluid. This fluid can have negligible influence on the grains motion, big rocks in air for example, or significant influence, fine sand in water for example. To determine whether the influence of the surrounding fluid on grain dynamics is negligible or not for the considered system, we need to write down the conservation equations for the motion of a grain in the fluid. To do so, we consider the dynamic of a grain between two contacts so without contact forces. The grain is considered at first approximation isolated

in this section and the principal averaged fluid forces acting on the grain are presented. The grain is a sphere of diameter d and density ρ_p hence of mass $m_p = \rho_p \pi d^3/6$, in a fluid of density ρ_f and viscosity η_f with an undisturbed velocity field (in the absence of particles) $v = v(x,t)$. The translation velocity of the particle is u_p and the rotation velocity is Ω_p its moment of inertia is $J_p = m_p d^2/10 = \pi \rho_p d^5/60$. The motion of the particle is obtained by writing the conservation of its momentum and angular momentum:

$$\frac{\pi}{6} d^3 \rho_p \frac{du_p}{dt} = F, \tag{3.9}$$

$$\frac{\pi}{60} d^5 \rho_p \frac{d\Omega_p}{dt} = M. \tag{3.10}$$

F is the sum of the forces applied on the sphere and M is the sum of the moments applied on the sphere. The former is expressed as:

$$F = F_d + F_h + F_{am} + F_t + F_l + F_b + F_m, \tag{3.11}$$

with F_d the drag force, F_h the unstationary Basset's history force, F_{am} the added mass force, F_t is the Tchen force, F_l the shear induced lift force, F_b the buoyant weight and F_m the Magnus force. These models of each force are detailed in Appendix B.1. The following section focuses on the dominant fluid-grain interactions in a granular system which allows numerical resolution to simplify the physical model and capture dominant fluid effects.

3.2 Dominant fluid forces in an immersed granular medium

3.2.1 Stokes number and density ratio

Although fluid-grains interactions are complex, some approximations can be made in a granular systems neglecting some interactions depending on the configuration studied hence the flowing regimes. An assumption usually made is to consider the fluid as stationary and at rest with $v|_{x_p} = 0$, the motion of the particle without specific rotation, and with denser grain than the fluid $\rho_p > \rho_f$. Equation (3.9) gives in that context the following Equation of motion of the grain:

$$\frac{\pi}{6} \rho_p d^3 \frac{du_p}{dt} = \frac{\pi}{6} d^3 (\rho_p - \rho_f) g + F_d. \tag{3.12}$$

This Equation is classical to consider the motion of particles in a fluid (*Maurin*, 2015; *Courrech Du Pont et al.*, 2003; *Perrin et al.*, 2019), it considers that the dominant interactions resisting the inertial motion of the grains at the first order are the viscous fluid effect, accounted by the drag force, and the buoyant weight. Different regimes can be highlighted from this Equation considering the dominant fluid force in each regimes. First, in order to characterize the free fall regime where the viscous effect is neglected, the influence of the surrounding fluid is only considered in the buoyant weight. In that case the Equation (3.12) becomes :

$$\frac{\pi}{6} \rho_p d^3 \frac{du_p}{dt} = \frac{\pi}{6} d^3 (\rho_p - \rho_f) g, \tag{3.13}$$

which gives:

$$\frac{du_p}{dt} = \frac{(\rho_p - \rho_f)g}{\rho_p}. \tag{3.14}$$

Integrating twice over time gives the position $x(t)$ assuming that the initial position and velocity are zeros:

$$x(t) = \frac{(\rho_p - \rho_f)g}{\rho_p} t^2. \tag{3.15}$$

The characteristic time of free fall τ_{ff} of a grain travelling a distance of its own diameter d under buoyant weight, can then be calculated with $x(\tau_{ff}) = d$ which gives:

$$\tau_{ff} = \left(\frac{d\rho_p}{(\rho_p - \rho_f)g} \right)^{1/2}. \tag{3.16}$$

Now, if viscous effects are no more neglected, the drag force needs to be expressed in Equation (3.12). We have seen above that the expression of the drag force, specifically the drag coefficient, depends on the Reynolds number. In order to extract characteristic timescales, we consider two distinct regimes where the drag force is well-established. In the Stokes regime ($Re \ll 1$), replacing the drag coefficient with $C_d = 24/Re_p$ the drag force is expressed from the expression B.2 as:

$$F_d = -3\pi d\eta_f u_p \tag{3.17}$$

Replacing F_d in Equation (3.12) gives a first order ordinary differential equation that can be written as:

$$\frac{du_p}{dt} + \frac{18\eta_f}{\rho_p d^2} u_p = \frac{(\rho_p - \rho_f)g}{\rho_p}. \tag{3.18}$$

The coefficient in front of the velocity is then a characteristic viscous timescale τ_v which is:

$$\tau_v = \frac{\rho_p d^2}{18\eta_f}. \tag{3.19}$$

Out of the Stokes regime, in the Newton regime, see Figure B.1b the drag force is given by:

$$F_d = -0.44 \frac{\pi}{6} d^2 \rho_f u_p^2 \tag{3.20}$$

. Thus it gives the following equation:

$$\frac{du_p}{dt} + \frac{0.44\rho_f}{d\rho_p} u_p^2 = \frac{(\rho_p - \rho_f)g}{\rho_p}. \tag{3.21}$$

In that Equation the coefficient in front of the velocity has the same dimension as a length and is the characteristic lengthscale l_c of inertial motion of the grain in the Newton regime with $l_c = \frac{d\rho_p}{0.44\rho_f}$. Considering the terminal velocity as steady, the Equation (3.21) gives then the following terminal velocity:

$$u_{term} = \left(\frac{l_c(\rho_p - \rho_f)g}{\rho_p} \right)^{1/2} = \left(\frac{d(\rho_p - \rho_f)g}{0.44\rho_f} \right)^{1/2}. \tag{3.22}$$

The characteristic time of the inertial regime is then given with these two characteristic quantities $\tau_i = l_c/u_{term}$:

$$\tau_i = \left(\frac{l_c \rho_p}{(\rho_p - \rho_f)g}\right)^{1/2} = \left(\frac{\rho_p}{\rho_f}\right)^{1/2} \left(\frac{d\rho_p}{0.44(\rho_p - \rho_f)g}\right)^{1/2}. \tag{3.23}$$

Those characteristic timescales quantifies the time the particle takes to reach the terminal velocity traveling the characteristic lengthscales in the various regimes. Comparing those timescales allows one to build dimensionless numbers that quantifies which regime is dominant depending on the parameters. First, comparing viscous effect and free fall under gravity gives the enables to build the Stokes number:

$$St = \frac{\tau_v}{\tau_{ff}} = \frac{\sqrt{\rho_p \Delta \rho g d^3}}{18\eta_f}. \tag{3.24}$$

Comparing viscous and inertial regimes gives the density ratio:

$$r = \frac{\tau_i}{\tau_{ff}} = \left(\frac{\rho_p}{\rho_f}\right)^{1/2}. \tag{3.25}$$

These expressions of Stokes number and density ratio as the dimensionless numbers for gravity-driven granular system is classic (*Courrech Du Pont et al.*, 2003; *Cassar et al.*, 2005; *Perrin et al.*, 2019). Usually, the Reynolds number is expressed from the ratio of both dimensionless numbers:

$$Re = \frac{\tau_v}{\tau_i} = \frac{St}{r}. \tag{3.26}$$

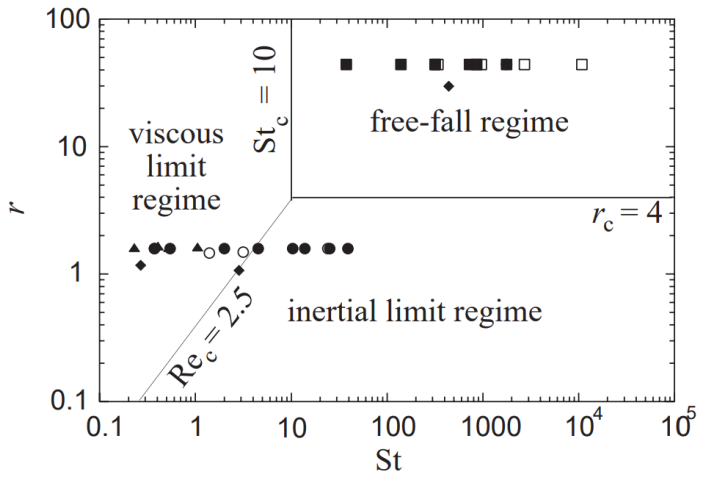

Figure 3.3 – Limit regimes of grain dynamic depending on dimensionless numbers St and r, source : *Courrech Du Pont et al.* (2003)

Courrech Du Pont et al. (2003) and *Perrin et al.* (2019) for example used this expression for immersed granular system in a rotating drum configuration correcting the Stokes number to consider the angle of the free surface as:

$$St = \frac{\sqrt{\rho_p \Delta \rho g sin\theta d^3}}{18\eta_f}. \tag{3.27}$$

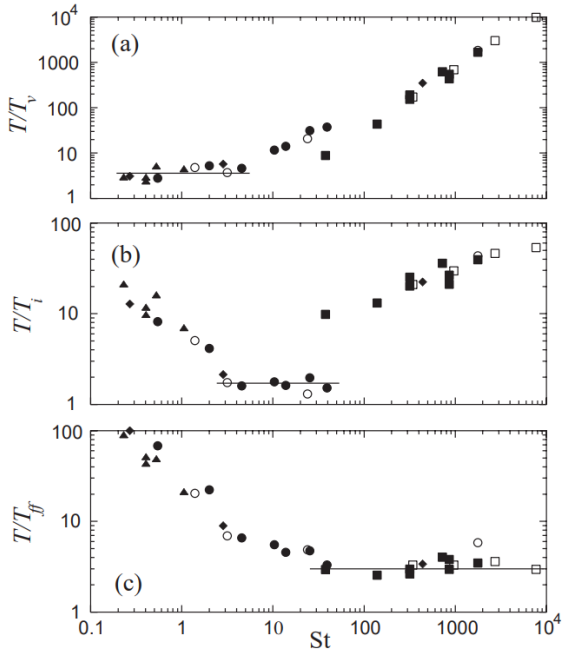

Figure 3.4 – Comparison between the time of avalanches in the experiment and the characteristic times of the grains dynamic (T_v for viscous time, T_i for inertial time and T_{ff} for free-fall time) as a function of the Stokes of the experiment, source : *Courrech Du Pont et al.* (2003)

Courrech Du Pont et al. (2003) show that those dimensionless numbers, i.e. St and r, give the physical regimes of the grains dynamic, see Figure 3.3: the free-fall regime in which the density of grain is higher than the density of fluid ($r > 1$) and for which inertia is dominant ($St > 10$) and fluid effects are negligible on grain dynamic (dry case). They defined two fluid regimes depending on the expression of the drag force as detailed above. In one regime where the Reynolds number is high, i.e. the density ratio is low $r \lesssim 1$ and the Stokes number is high: the inertial limit regime or turbulent regime. In this regime both fluid and inertia effects have an influence on the dynamics of the grains. The other fluid regime is the viscous limit regime for lower values of the Reynolds number, i.e. lower Stokes number $St \lesssim 1$ and non-limited values of the density ratio. This regime corresponds to dominant viscous fluid influence with negligible particle inertia. *Courrech Du Pont et al.* (2003) show that they were able to reach each regimes varying the Stokes number and density ratio r using different fluids and particles. Figure 3.4 shows the comparison of the time of avalanches observed in the rotating drum compared to the characteristic timescales at various Stokes number and density ratios. The figure shows that the timescales of the avalanche dynamic matched with the various timescales build in the different regimes for the corresponding values of Stokes number and density ratio, validating the diagram of Figure 3.3.

3.2.2 Lubrication force between grains

The viscous effect of the fluid also act at the contact scale between two particles through the lubrication force. When a particle come into contact with another particle,

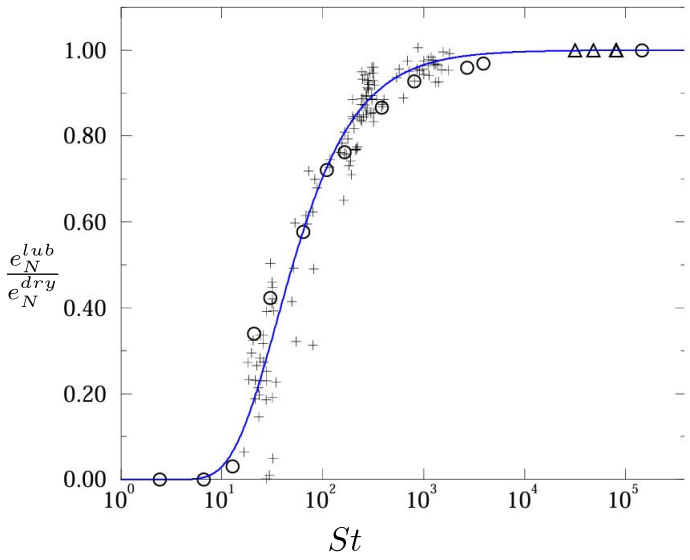

Figure 3.5 – Ratio of the restitution coefficient in presence of viscous fluid and the restitution coefficient in the dry case versus Stokes number. Adapted from *Gondret et al.* (2002)

the liquid separating the two surfaces must be flushed away. This is called drainage of the film formed between the two surfaces. The efficiency of the drainage depends on the ratio between the inertia involved in the particle's movement, which drives the drainage, and the viscous friction which opposes it. The comparison of these two effects is the Stokes number. The resulting force, found in the case of a grain approaching a wall, is expressed as a function of the distance between the particles $h_0(t)$:

$$F_{lub} = \frac{3\pi d^2 \eta_f u_p}{2(h_0(t) + h_{rough})}, \tag{3.28}$$

with h_{rough} the typical roughness size of the surface of the particle. This length enables to regularize the lubrication force so that it does not diverge when $h_0 \to 0$ (*Lecoq et al.*, 2004; *Andreotti et al.*, 2013). This force then influence collisions between grains. As such, it can be simply estimated measuring the resulting effective restitution coefficient e_N^{lub}. Comparing this latter to the restitution coefficient for dry coefficient e_N^{dry} enabled to plot the evolution of the ratio $\frac{e_N^{lub}}{e_N^{dry}}$ as a function of the Stokes number (*Gondret et al.*, 2002). This is presented on Figure 3.5. It dramatically decreases for Stokes lower than 1000 and approaches 0 when the Stokes number approaches 10, showing a strong viscous effect of the lubrication force on the effective restitution coefficient of collisions in the viscous regime. The restitution coefficient in presence of lubrication then scale as:

$$e_N^{lub} = e_N^{dry} exp(-35/St). \tag{3.29}$$

3.3 Numerical model

This section presents the numerical model, especially the Discrete Element Method (DEM) used in the simulations of the present thesis. This numerical model solve the

dynamic of each grains of the medium. The equations of motions including grain-grain interactions and grain-fluid interactions derived from the physical laws presented in Section 3.1 are also presented.

3.3.1 Discrete element method

The discrete element method or DEM is a numerical method widely used in granular material studies. It is based on the modelling of the trajectories of each particles. This method is powerful since it enables to get access to a large range of variables that are hardly or not measured in experiments such as contact network properties or stress or strain-rate tensors.
Two major methods are used in the simulation of granular flows. The first one is the Contact Dynamics method that uses an implicit resolution of the equation of motions of each particles that are considered to be perfectly rigid. The method models contact laws, Coulomb and Hertz, without any mathematical regularization of the contact forces (*Moreau*, 1983; *Jean*, 1999; *Staron et al.*, 2002; *Staron and Radjai*, 2005). Although this method allows numerical simulations to be carried out in a time-efficient way, since the time step is not restricted for stability reasons, the mathematical complexity of the model has nevertheless led the granular numerical community to use a simpler model. This model is the Molecular Dynamics method or soft-particle method.
This method have first been introduced by *Cundall and Strack* (1979) and propose an explicit resolution of the equations of motions of each particles, which limits the time step of resolution. The specificity of this method is that at the contact scale particles are considered as rigid grains that can interpenetrate each others. By contrast with Contact Dynamics, this mathematical assumption enables the soft-particle method to smooth the contact laws by regularizing contact forces as functions of the particles parameters, i.e. the velocities and the interpenetration lengths, δ. The regularization of the contact law lies in the expression of contact forces that rises issues in the time resolution of contact interactions. In order to understand that, we estimate the time step limitation due to the contact time of the interaction between two particles. Coming back from the expression of the normal contact force given in Section 3.1, the approximated rate-independent contact force from Hooke's law is used here from Equation (3.1), it gives $F_N = k_N\delta$ with k_N the normal stiffness that depends on the material. For such form of the normal contact force, the contact time is related to the normal stiffness as $t_c \sim \sqrt{m/k_N}$ with m the mass of the grain. As such, for rigid particles with high effective stiffness, typically the Young's modulus for glass beads is about $E \sim 100GPa \sim 10^11Pa$ leading for $1cm$ particles $k_n \sim 10^9 Pa.m$. Hence, the density of glass beads being of about $2g/cm^3$, the mass of the bead is $m = 2\pi/6 \approx 1g$, it gives $t_c \sim \sqrt{10^{-3}/10^9} \approx 10^{-6}s$. Adimensionalising this quantity with $\sqrt{d/g} \approx \sqrt{10{-}2/10} \approx 3 \times 10^{-2}$ is gives $t_c/\sqrt{d/g} \approx 3 \times 10^{-5}$. The main issue of such low contact time is that the time step must be limited to lower values than $t_c/\sqrt{d/g}$ in order to be sure that the contact are modelled and does not imply too high values of contact force if the strain increase within t_c. The usual method used to deal with this issue is to choose a value of effective stiffness k_N, lower than real materials stiffness, which enables to increase the time step, but sufficiently high in order to reproduce the behavior of a granular material constituted of rigid grains. This lower limit of effective stiffness is named the rigid grain limit (*Roux and Combe*, 2002).

The main advantage of the soft-particle method is its mathematical simplicity. Despite the temporal limitations due to a limited time step involving an expensive time of simulations, a large amount of simulations have been performed using this method to study the dense flow and static granular regimes and their transitions (e.g. *Silbert et al.*, 2001, 2002a,b,c; *GDR MiDi*, 2004; *Baran et al.*, 2006; *DeGiuli et al.*, 2016; *DeGiuli and Wyart*, 2017; *Srivastava et al.*, 2022). Since numerical simulations of this thesis are based on the soft-particle method, the word DEM will be used in the following to refer to this resolution method. The code used to perform DEM simulations in this work is the open-source code named YADE [1]. In the folowing section the principal formulation of the DEM including the equations of motion and the principal interactions encountered by a grain are presented. To see the full formulation of the DEM implemented on YADE the reader is sended to *Smilauer and Chareyre* (2015).

3.3.2 DEM formulation

The motion of each particle, $_p$, is solved using Newton's second law for both translational velocity $\overrightarrow{u}$ and angular velocity $\overrightarrow{\Omega}$:

$$\frac{\pi}{6} d^3 \rho_p \frac{d\overrightarrow{u_p}}{dt} = \frac{\pi}{6} d^3 \rho_p \overrightarrow{g} + \sum_{i=0}^{N_c} \overrightarrow{F_{C,i}} + \overrightarrow{F_F}, \tag{3.30}$$

$$\frac{\pi}{60} d^5 \rho_p \frac{d\overrightarrow{\Omega_p}}{dt} = \sum_{i=0}^{N_c} \overrightarrow{T_{C,i}}. \tag{3.31}$$

In Equation 3.30, the first term on the right-hand side is the weight of the particle with $\overrightarrow{g}$ the gravity acceleration and ρ_p the density of the particle. The second term corresponds to the sum of N_c solid contact forces, $\overrightarrow{F_{C,i}}$, applied by the neighbors on the particle, similarly the sum on the contacts of the torques $\overrightarrow{T_{C,i}}$ induce by contact forces is written in Equation 3.31. For each contact, the torque is defined as follows: $\overrightarrow{T_C, i} = d(-\overrightarrow{n}) \times (\overrightarrow{F_C, i})$. The third term of Equation 3.30 is the force induced by an external fluid when considering immersed-like granular flows. Note that as depicted in the Section 3.2 the dominant fluid forces in a granular system are oriented by a straight line passing through the center of the grains involving no torque in the Equation 3.31.

Contact law

The contact force betwen two particles is denoted $\overrightarrow{F_{C,i}} = \overrightarrow{F_N} + \overrightarrow{F_T}$. This force is the sum of the normal and tangential contact forces, respectively $\overrightarrow{F_N}$ and $\overrightarrow{F_T}$ which are modeled with a spring-dashpot and spring-friction models (*Schwager and Pöschel*, 2007):

$$\begin{aligned} \overrightarrow{F_N} &= -(k_N \|\overrightarrow{\delta_N}\| + \gamma_N \|\dot{\overrightarrow{\delta_N}}\|)\overrightarrow{n}, \text{with } \overrightarrow{n} = \overrightarrow{\delta_N}/\|\overrightarrow{\delta_N}\| \\ \overrightarrow{F_T} &= \begin{cases} k_T \overrightarrow{\delta_T} \dfrac{\|\overrightarrow{F_N}\|\mu_p}{\|k_T \overrightarrow{\delta_T}\|} & \text{if } \|k_T \overrightarrow{\delta_T}\| > \|\overrightarrow{F_N}\|\mu_p, \\ k_T \overrightarrow{\delta_T} & \text{otherwise,} \end{cases} \end{aligned} \tag{3.32}$$

1. https://yade-dem.org/doc/

where μ_p is the inter-particle friction coefficient, k_N and k_T are respectively the normal and tangential stiffness, $\overrightarrow{\delta_N}$ and $\overrightarrow{\delta_T}$ are the normal and tangential strains or inter-penetration vectors, γ_N is the normal viscous dissipation obtained from k_N and the normal restitution coefficient e_N (*Schwager and Pöschel*, 2007). The value of k_N is chosen in order to respect the rigid grain limit: $k_N = \kappa P_{max} d$, with κ the relative dimensionless stiffness, $\kappa > 10^4$ (*Roux and Combe*, 2002). In particular, this latter criterion prevents elasto-platic deformations close to the flow-arrest transition (*Favier De Coulomb et al.*, 2017). A sensitivity analysis has been performed on κ in the dry frictionless case (see Section 3.5). The maximum granular pressure a grain will experience in the system, P_{max}, is calculated in gravity-driven simulations considering a grain that is under the pressure of a horizontal grain layer, with h the characteristic size of the layer, it gives: $P_{max} = \rho_p \phi_{max} h g$. The restitution coefficient is fixed at $e_N = 0.9$, as classically used for glass beads. The tangential stiffness $k_T = \nu k_n$ is set to a typical value of $\nu = 0.5$ the Poisson coefficient (*Favier De Coulomb et al.*, 2017).

Fluid forces

When immersed in a fluid, a particle is also subjected to fluid forces, see Equation (3.30). In the present work, the idea is to model the influence of the fluid on particle behavior at first order. As such, on an inclined plane, the fluid is considered to be at rest and we focus on the main fluid forces, which are drag and buoyancy, $\overrightarrow{F_F} = \overrightarrow{F_D} + \overrightarrow{F_B}$. In the Stokes limit, one expects lubrication to appear and play a role in the close contact behavior. Considering that the viscous drag and the lubrication force have the same viscous scaling, the lubrication force is here discarded for the sake of modelling simplicity. In order to support this assumption, a sensitivity analysis has been performed on the restitution coefficient, see Section 3.5. The drag force $\overrightarrow{F_D}$ is classically written as:

$$\overrightarrow{F_D} = -\frac{1}{2}\rho_f \frac{\pi d^2}{4} C_D \| \overrightarrow{u} \| \overrightarrow{u}, \tag{3.33}$$

with the fluid density ρ_f and where the drag coefficient C_D is modeled in order to consider both Newton and Stokes regimes (*DallaValle*, 1948; *Maurin*, 2015):

$$C_D = \left(0.44 + \frac{24}{Re_p}\right). \tag{3.34}$$

The particle Reynolds number, Re_p, is calculated as follow:

$$Re_p = \frac{\rho_f \| \overrightarrow{u} \| d}{\eta_f}, \tag{3.35}$$

with η_f the dynamic viscosity of the fluid. The buoyancy force is defined as follow:

$$\overrightarrow{F_B} = -\frac{\pi}{6} d^3 \rho_f \overrightarrow{g}. \tag{3.36}$$

3.3.3 Numerical resolution

Since the resolution of the momentum Equation 3.30 is explicit, the time step is bounded for for a stable integration. The main restriction being as depicted in Section 3.3 on the contact forces. The contact network is constituted of a network of springs and dampers. Hence, to ensure the stability of integration, the time step might be lower than the time of propagation of the fastest wave within the contact network. In the code YADE, the times associated to the network of springs, $t_{springs}$, and the network of dampers, $t_{dampers}$, are calculated independently. The stiffness and damping matrices are diagonalized, $t_{springs}$ and $t_{dampers}$ are calculated from the maximum eigenvalue related to the fastest wave. The time step is selected as the lower value between $t_{springs}$ and $t_{dampers}$ with a safety coefficient, 0.7, that ensure no coupling propagation effect between the networks. It gives:

$$\Delta t = 0.7 min(t_{springs}, t_{dampers}) \tag{3.37}$$

This time step is calculated at each iteration. The function used within the code to perform such calculation is called 'GlobalStiffnessTimeStepper' and also needs as argument the maximum time step. Indeed, the time step often reaches the maximum time step sets in the function which can lead to non physical results. As a consequence, it is necessary to calculate the maximum time step required in order to observe granular flows that does not display non-excepted behaviors. This will be done for the inclined plane configuration in Section 3.5.

3.4 Inclined plane configuration

The first and main configuration used to perform numerical simulations in this thesis is the rough inclined plane configuration, see Figure 3.6. This configuration is particularly useful since it is close to actual granular systems where hysteresis occurs such as landslides or granular avalanches for which the physical mechanism that drives the medium to flow is gravity. In these applications the granular flow develops within a layer that flows above a static granular bed represented here by the rough plane. In addition, with the incline plane configuration the simplicity lies on the direct link between external stress and the inclination angle of the plane, θ.

In this section, the main physical quantities in this configuration are presented, the inclined plane numerical configuration and the protocol used to perform simulations are detailed.

3.4.1 Steady uniform granular flows down inclined plane

In the inclined plane configuration far from jamming transition, the flow is considered steady homogeneous and planar meaning that the flow is considered in two dimensions in the streamwise and plane-normal directions, noted respectively x and z. This flow results from an external shear stress, τ or σ_{xz}, and pressure, P or σ_{zz}, constant at a given inclination angle. For such flows in three dimensions, the stress tensor has the following

general form (*Silbert et al.*, 2001; *Srivastava et al.*, 2021):

$$\sigma = \begin{pmatrix} \sigma_{xx} & 0 & \sigma_{xz} \\ 0 & \sigma_{yy} & 0 \\ \sigma_{xz} & 0 & \sigma_{zz} \end{pmatrix}. \tag{3.38}$$

For such a system, the assumption of a Cauchy tensor implies $\sigma_{xx} = \sigma_{yy} = \sigma_{zz}$ and the tensor can be written as in Equation (1.9): $\sigma = PI + \tau$. Hence, there is only two independent variables: $\tau = \sigma_{xz}$ and $P = \sigma_{zz}$ and one constitutive relation is needed. In addition, both variables are directly related to the inclination angle in this configuration. This relation is given considering the steady-state equations:

$$\frac{\partial \sigma_{zz}}{\partial z} = \rho g cos(\theta), \tag{3.39}$$

$$\frac{\partial \sigma_{xz}}{\partial z} = \rho g sin(\theta). \tag{3.40}$$

ρ is the density of the system directly related to the volume fraction ϕ and the density of grains ρ_p by $\rho = \rho_p \phi$. At a given angle, equations 3.40 gives:

$$\sigma_{zz}(z) = \rho_p g cos(\theta) \int_z^h \phi(\tilde{z}) z, , \tag{3.41}$$

$$\sigma_{xz}(z) = \rho_p g sin(\theta) \int_z^h \phi(\tilde{z}) z, . \tag{3.42}$$

Considering the volume fraction constant in the whole layer, then it leads to:

$$\sigma_{zz}(z) = \rho_p g cos(\theta) \phi (h - z), \tag{3.43}$$

$$\sigma_{xz}(z) = \rho_p g sin(\theta) \phi (h - z). \tag{3.44}$$

This relation gives:

$$\frac{\sigma_{xz}}{\sigma_{zz}} = \frac{\tau}{P} = \mu = tan(\theta) \tag{3.45}$$

In the dense flow regime, for steady uniform flows the stress ratio is the directly related to the inclination angle.
The constitutive law needed to close the problem is given by the $\mu(I)$ rheology (*Jop et al.*, 2006; *Forterre and Pouliquen*, 2008), the latter is a direct function of the dimensionless shear rate, $\mathcal{I}$ with typical flow curve as written explained in Section 1.3 $\mu = \mu_{stop} + b\mathcal{I}$. As such, varying the slope allows one to explore the different granular flow regimes given by values of the inertial number. Finally, the depth average inertial number $\mathcal{I}$ is defined as:

$$\mathcal{I} = \frac{\dot{\gamma} d}{\sqrt{P_g / \rho_p}}, \tag{3.46}$$

with the shear rate $\dot{\gamma}$ and the granular pressure P_g.

Some studies in shear cell configurations (*DeGiuli and Wyart*, 2017; *Srivastava et al.*, 2022) used the stress ratio μ to measure the critical external stress conditions at which

the medium stops flowing (jamming), μ_{stop}, or starts flowing (unjamming), μ_{start} and define the hysteresis as the difference $\Delta\mu = \mu_{start} - \mu_{stop}$. In studies that used gravity-driven configurations (*Courrech Du Pont et al.*, 2003; *Perrin et al.*, 2019; *Peng et al.*, 2023), the critical external stress conditions are generally defined as critical angles $\theta_{stop} = arctan(\mu_{stop})$ and $\theta_{start} = arctan(\mu_{start})$ and hysteresis as $\Delta\theta = \theta_{start} - \theta_{stop}$. Hence, hysteresis comparisons needs to be done with care since $\Delta\theta$ is not equal to $arctan(\Delta\mu)$. However, the inclined plane being a gravity-driven configuration the notation of external stress as angles will be used most of the time.

In the Bagnold's theory (*Bagnold*, 1954, 1966), the volume fraction is considered constant along the layer and the stress tensor components are considered linear with depth. It gives a constitutive relation between the shear stress and the square of the shear rate, when the contact interaction dominates, as (*Bagnold*, 1954, 1966; *Silbert et al.*, 2001):

$$\sigma_{xz} \propto \dot{\gamma}^2. \tag{3.47}$$

With the shear rate:

$$\dot{\gamma}(z,t) = \frac{\partial u_x}{\partial z}(z,t). \tag{3.48}$$

This equation with Equation (3.44) gives a scaling for the shear rate profile:

$$\frac{\partial u_x(z,t)}{\partial z} \propto (h-z)^{1/2}. \tag{3.49}$$

Which gives the following scaling relation on the velocity by integration between zero and z:

$$u_x(z,t) \propto h^{3/2} - (h-z)^{3/2}. \tag{3.50}$$

The dependence of the profile with time lies in the prefactor that depends on the inclination angle that varies with time.

3.4.2 Presentation of the inclined plane setup

Conversely to experiments that require the use of grain container above the inclined plane, see Figure 1.4, and to fill that container with grain in order to reproduce the experiment, the use of bi-periodic cells in numerical simulations enables all grains to remain within the domain. That allow us to perform long time simulations. The bi-periodic cells are such that the grains that passing through the downstream plane normal to the streamwise direction emerges through the opposite upstream plane normal to the streamwise direction. Similarly with the lateral planes normal to the spanwise direction. The inclined plane simulations are performed with cohesionless monodisperse spherical particles of diameter d forming a granular layer of size $h/d = 10$, see Figure 3.6. The layer thickness have been selected in order to limit the computational time, considering the absence of size effect of h past $10d$ on the critical constraint ratio values (*Pouliquen and Forterre*, 2002; *Perrin et al.*, 2021). We use a bi-periodic domain of size $L \times W = 30d \times 15d$, L being the length in the streamwise direction and W in the spanwise direction, see Figure 3.6. The roughness of the plane is built using fixed particles with the same properties as the dynamic ones, see Figure 3.6. The fixed particles are organised in a square paving in the streamwise and spanwise directions and their positions in the wall-normal direction

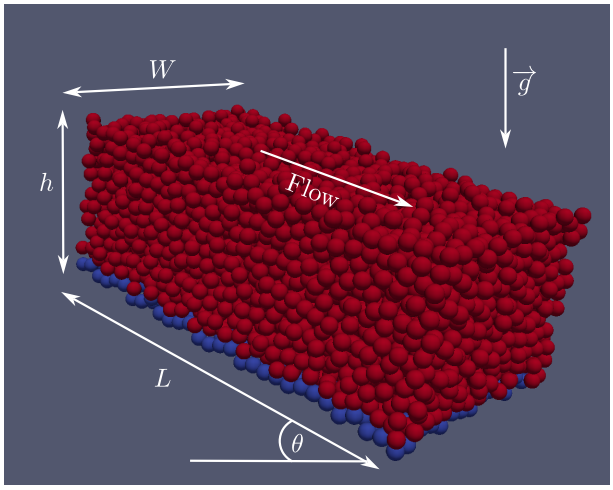

Figure 3.6 – Typical 3D snapshot for granular medium flowing on a inclined plane, $L \times W = 30d \times 15d$, $h/d = 10$. Red particles corresponds to unfixed particles, blue ones corresponds to fixed particles that constituted the plane.

follow a random uniform repartition between $-\frac{d}{2}$ and $\frac{d}{2}$. The code is made dimensionless choosing d as unit of length, $\sqrt{d/g}$ as unit of time, g being the gravitational constant, and the mass of a grain m as unit of mass. Note that in the following the mass of a grain will always be replaced by $m = V_p \rho_p$ with the volume of a particle $V_p = \frac{\pi}{6} d^3$ and ρ_p the density of the grain.
The inclined plane configuration is considered with and without a surrounding fluid. In the model-immersed case, considering the equation of motion of a grain between two contacts in the granular system, Equation (3.30) without the contact forces (between two contacts), the dimensionless numbers that drive the behavior of the system are the Stokes number St and the density ratio r (*Courrech Du Pont et al.*, 2003; *Perrin et al.*, 2019):

$$St = \frac{\sqrt{\rho_p(\rho_p - \rho_f) g d^3}}{18\eta_f}, \tag{3.51}$$

$$r = \frac{\rho_p}{\rho_f}. \tag{3.52}$$

The Stokes number, St, measures the ratio between the inertia of grains versus viscous dissipation of the fluid. At high Stokes numbers, grain inertia is dominant, equivalent to the dry case ($St = \infty$), while at small Stokes numbers, the grain dynamics is strongly affected by viscous dissipation, in the so-called viscous regime.
The density ratio, r, compares the effect of the buoyancy and the weight of grains and is chosen at $r = 1000$ in order to get rid of buoyancy effect and study specifically the effect of viscous dissipation on hysteresis.

In Chapter 5 the interparticle friction μ_p as well as the Stokes number St will be varied on this configuration in order to study their influence on hysteresis. Before studying that, one may define a protocol to measure the hysteresis on an inclined plane.

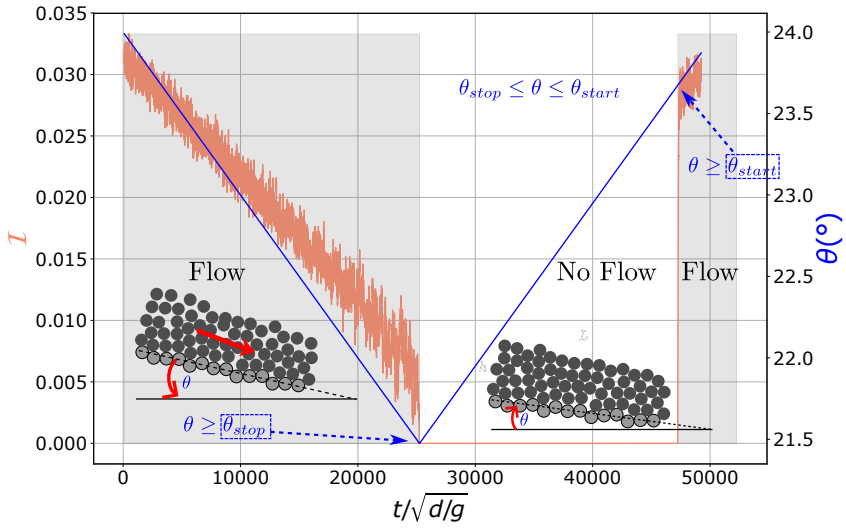

Figure 3.7 – Inertial number $\mathcal{I}$ (left) and inclination angle θ (right) as functions of time within a simulation.

3.4.3 Protocol for the measure of hysteresis on an inclined plane

Flow arrest and avalanche onset are studied by varying the inclination angle θ of the inclined plane with respect to gravity at a fixed inclination velocity $\delta\theta/\delta t = 10^{-4}\,°/\sqrt{d/g}$, $\delta\theta$ being the angle step and δt the duration between two angle variations. The slope evolution is quasi-static in the simulations performed, see Figure 3.7. The choice of quasi-static evolution of the inclination angle is motivated by the stochastic nature of the granular flow that is an issue near the transition as discussed in Section 2.3 and in the articles of *Ciamarra et al.* (2011); *Srivastava et al.* (2019). The stress imposition rate must be selected in order that the system has enough time at each stress step to explore various configuration and find a stable one. This will be detailed in a following Section 3.6. We choose to start the simulation in the dense flow regime in order to observe the arrest of the system and then the avalanche from the arrested configuration. Such choice is motivated by the fact that the jammed state in which the system is stable is common for both the jamming (arrest) and the unjamming (avalanche) transitions. Thus, the angle difference that is measured is a consistent signature of hysteresis.

Figure 3.7 shows the inertial number and the plane inclination angle as function of the time within a simulation, in order to present the protocol used for the simulations. The angle of the plane is first set at a high enough angle to set the granular layer in motion. This is associated with a finite value of inertial number, as can be seen on Figure 3.7. Then the plane inclination angle is continuously decreased at angular velocity $-\delta\theta/\delta t$, as shown by Figure 3.7, leading to a decrease of the inertial number, $\mathcal{I}$, until the medium stops flowing and the inertial number suddenly drops to zero. At that time, the granular medium has reached the static state, the stopping angle, θ_{stop} also called jamming angle, is measured. The plane angle is then increased with the same angular velocity $\delta\theta/\delta t$ until the medium flows again when the inertial number suddenly and significantly increases as observed in Figure 3.7. At that point the medium starts to flow and the avalanche angle, θ_{start} also called starting angle or unjamming angle, is measured. Hysteresis $\Delta\theta =$

$\theta_{start} - \theta_{stop}$ is calculated from these critical angles.

3.5 Time step analysis and validation

Figure 3.7 was obtained with the numerical resolution of the momentum equations of motion of each grains detailed in the second Section of this chapter. The resolution requires some parameters to be imposed, such as the coefficient of restitution or the time step. The latter is defined within the simulation process which rises issues about the behavior of the granular flow. As such a sensitivity analysis has been performed on this parameter in the configuration of the inclined plane. Similarly, the restitution coefficient and the normal stiffness

Then, the characterisation of the dense granular flow on an inclined plane is considered in order to define a flowing criterion.

3.5.1 Analysis of the maximum time step

This section presents the study of the maximum bound of the time step that needs to be set in the function 'GlobalStiffnessTimeStepper' within the code for the numerical resolution. The maximum time step is also restricted in order to observe a granular flow that is physically consistent. The main restriction of the maximum time step to impose lies on the contact time for a collision between two particles as depicted in the Section 3.3. It is possible to estimate the maximum time step restriction considering the

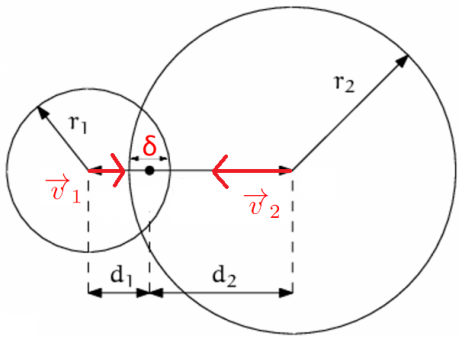

Figure 3.8 – Scheme of two particles that inter-penetrate each other by a length noted δ

collision between two particles of velocities v_1 and v_2 before impact. The particles will inter-penetrate by a maximum length δ (see Figure (3.8)). This distance is bounded in order to respect the rigid grain limit at $\delta \leq 10^{-3}d$. For such maximum inter-penetration length the grains behaves like rigid grains and, in presence of collisions within the granular medium, the dynamics is not influenced by this length. Moreover, we noticed that while flowing on a rough inclined plane, the maximum relative velocity between two grains is $v_{max} = |v_1 - v_2|_{max} \approx 5\sqrt{dg}$. In order to respect the restriction on δ, the time step must respect:

$$\Delta t \leq \frac{10^{-3}d}{5\sqrt{dg}} = 2.10^{-4}\sqrt{d/g}$$

The idea is to perform a sensitivity analysis at fixed time steps, i.e without using 'Global-StiffnessTimeStepper' function, and to increase the time step value for each simulation in

order to determine numerically the maximum time step for which the results converge. Simulations have been performed for
$\Delta t/\sqrt{d/g} \in [2.10^{-4}; 4.10^{-4}; 1.10^{-3}; 1.5.10^{-3}; 2.10^{-3}; 4.10^{-3}]$. It is then interesting to plot for each time step the maximum percentage of inter-particle interactions for which the inter-penetration length exceeds $10^{-3}d$. The result is presented in Figure (3.9). This

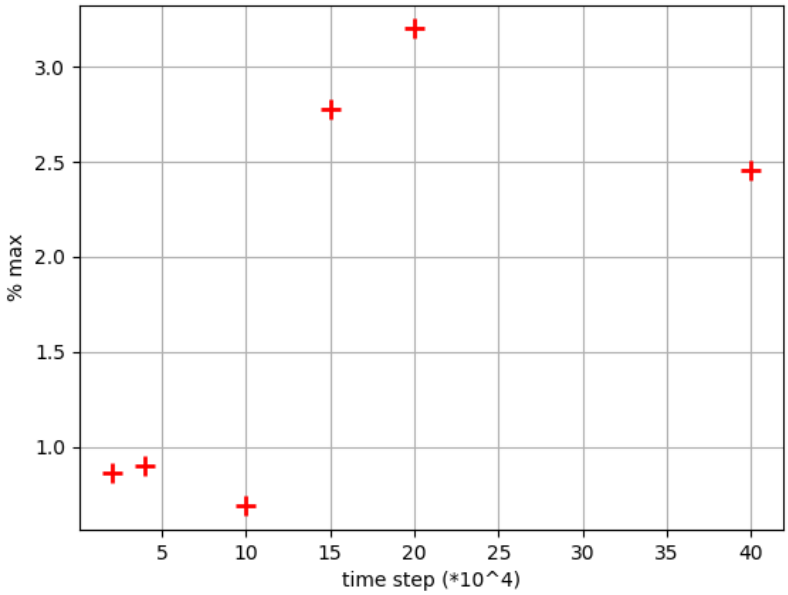

Figure 3.9 – Maximum percentage of interactions for which $\delta \geq 10^{-3}d$ as a function of the time step

percentage is very low whatever the time step. However there is a noticeable increase for $\Delta t \geq 1.5.10^{-3}\sqrt{d/g}$.

In order to compare how the medium behaves with varying time step, simple simulations with classical inter-particle friction coefficient and restitution coefficients ($\mu_p = 0.5$, $e_n = 0.9$) are performed on a rough inclined plane where the inclination angle of the plane is varied with the simulation time, see Section 3.4.3. The time step have been modified from one simulation to another. The average kinetic energy per particle is measured in order to compare the level of energy per particle in the system. For these classical particle properties (as well as plane roughness and layer thickness) the kinetic energy is supposed to decrease with the plane angle and be near zero when the inclination angle is near 21°, see *Silbert et al.* (2002a). Figures 3.10 and (3.11) shows the average kinetic energy over time of simulation for the different time steps. Figure (3.10) presents the result for each time step and Figure (3.11) is a zoom of Figure (3.10) where only the kinetic energy for the lower time step values are plotted. The zoom is made since the kinetic energy differences are large and they cannot be properly seen on Figure (3.10) for lower time steps. Figure (3.10) highlights that the kinetic energy diverges at $\Delta t = 1.5.10^{-3}\sqrt{d/g}$. Indeed, in spite of a general decrease of the kinetic energy, its values are significantly higher and fluctuate significantly more for the higher time steps. In addition, the kinetic energy does

not drops to zero at inclination angles lower that 21°. These results are the signature of an unstable flow.

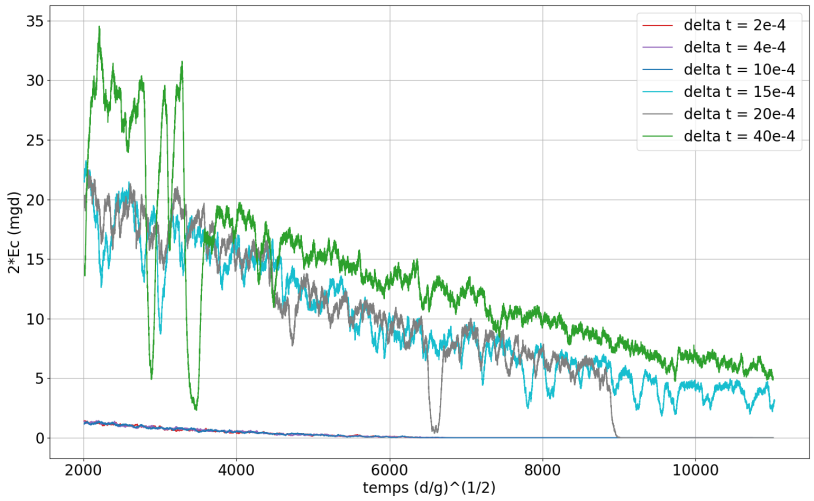

Figure 3.10 – Average kinetic energy of particles as a function of time for several time step (with $1, 5.10^{-3}\sqrt{d/g}$, $2.10^{-3}\sqrt{d/g}$ and $4.10^{-3}\sqrt{d/g}$)

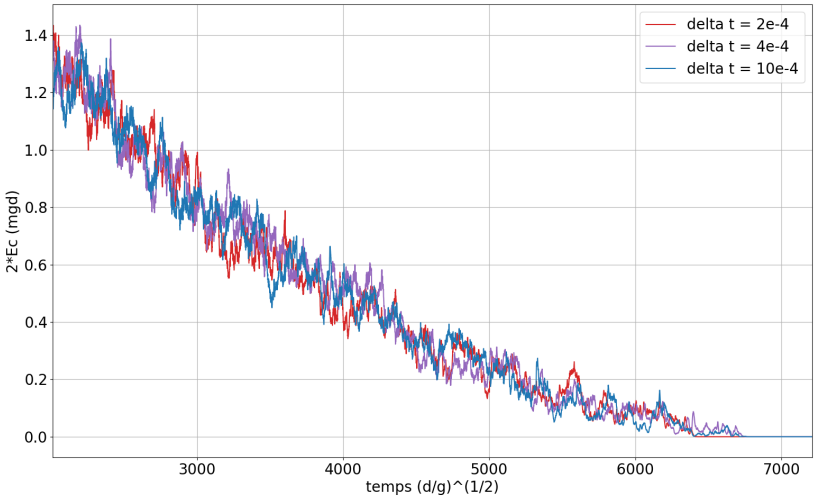

Figure 3.11 – Average kinetic energy of particles as a function of time for several time step (without $1, 5.10^{-3}\sqrt{d/g}$, $2.10^{-3}\sqrt{d/g}$ and $4.10^{-3}\sqrt{d/g}$)

Finally, the highest time step allowing to generate a grain flow with a consistent behavior in terms of kinetic energy is $\Delta t = 10^{-3}\sqrt{d/g}$. This time step is best trade-off between consistent physical behavior and computational time so that it will be selected as maximum time step in the time stepper function for the simulations performed in the present study.

3.5.2 Flow characterization

The criterion that allows us to previously say that the kinetic energy evolution with the inclination angle was consistent at low time step was that its dropped to zero at low angles. In fact, the kinetic energy value never drops to zero but dramatically decrease to several orders when the medium stops, equivalently to the inertial number on Figure 3.7. Then, it is important to define a criteria that allows us to consider that the granular media has stopped and reached the static regime. Indeed, in order to change the sign of the velocity of inclination angle after the medium stops (see Figure 3.7), a criterion is needed.

The variable we choose to do so is the kinetic energy per particles. We notice on the Figure 3.11 that at a certain angle, around 22°, the kinetic energy drops abruptly to very low values. From this angle the granular medium reaches the solid static regime and does not go back to the liquid regime as long as we do not increase the inclination angle. In order to determine this criterion of kinetic energy, we have performed tests/simulations on several criteria between $E_c = 1.10^{-10}mdg$ and $E_c = 1.10^{-5}mdg$. We observed that is all simulations the value $E_c = 1.10^{-8}mdg$ is a good criterion. We will then use this criterion in simulations to determine when to switch from decreasing to increasing θ and/or to determine the critical angles in post-processing.

3.5.3 Validation of dry granular flow on rough inclined plane configuration

In this section, we performed simulations with $h/d = 20$ and $\mu_p = 0.5$ and $e_n = 0.9$ in order to compare the average velocity and volume fraction profiles obtained at various angles with results from other numerical simulations, i.e. *Baran et al.* (2006). The results are presented on Figure 3.12. The first two Figures 3.12a and 3.12b show that the granular layer is slower, hence denser, in our simulations at various angles, especially at $\theta \geq 23°$, than in the results of *Baran et al.* (2006). This difference can be explained by a various plane roughness which is probably more rough in our case than in their study. In order to show that we performed two other simulations varying the roughness of the bottom plane. The roughness characteristics in simulations of *Baran et al.* (2006) are not given. As such, we decided to vary the roughness by varying the interval of the randomised vertical positions of particles that constituted the plane, i.e. the condition $z_{plane} \in [-d/2; d/2]$. In this latter condition, used in the simulations of Figures 3.12a and 3.12b, the maximum distance between the centers of two particles in the plane is $\Delta z_{max} = 1d$. We varied this value to $\Delta z_{max} = 0.75d$ giving results from Figures 3.12c and 3.12d and $\Delta z_{max} = 0.5d$ giving results from Figures 3.12e and 3.12f. We can see the lowering the roughness of the plane increases the velocity at all angles and slightly decreases the volume fraction. Figures 3.12c and 3.12d show closer values of velocity and volume fraction profiles but some departure is still observed at high angles. Decreasing the roughness at even lower value, i.e. $\Delta z_{max} = 0.5d$ see Figures 3.12e and 3.12f, shows a granular flow with velocity profiles that significantly exceeds the values of *Baran et al.* (2006), with velocities that are higher at lower angles demonstrating non-stable steady state flow. Hence, the proper roughness conditions in order to fit results from *Baran et al.* (2006) probably lies between $\Delta z_{max} = 0.5d$ and $\Delta z_{max} = 0.75d$. Nevertheless, the profiles of Figures 3.12c, 3.12d, 3.12e

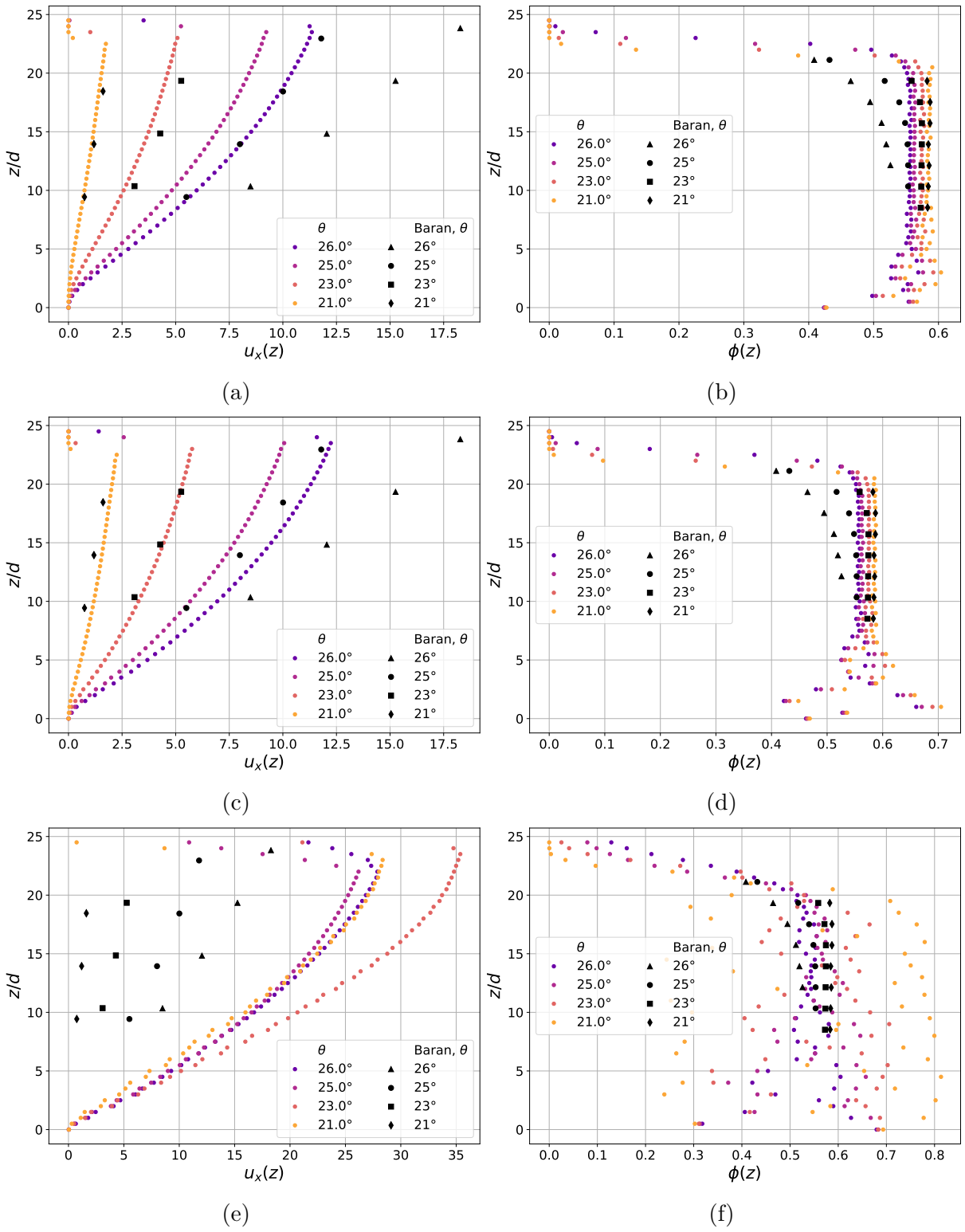

Figure 3.12 – Average velocity profiles at various angles compared to results of *Baran et al.* (2006) (a) with higher roughness condition $\Delta z_{max} = 1d$ (c) intermediate roughness condition $\Delta z_{max} = 0.75d$ and (e) lower roughness condition $\Delta z_{max} = 0.5d$. (b), (d) and (f) same for the volume fraction

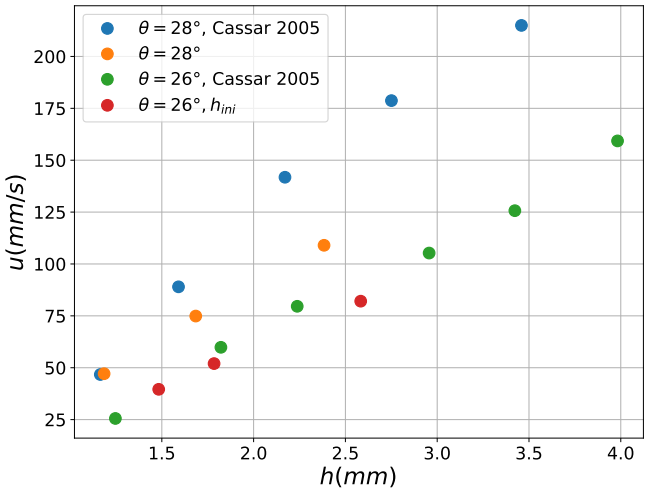

Figure 3.13 – Time averaged velocity per grains at various layer thicknesses for $\theta = 26°$ and $\theta = 28°$ compared to results from *Cassar et al.* (2005).

and 3.12f remains close enough to validate the DEM code used, especially at low angles so near the jamming transition which is of interest in our work.

3.5.4 Validation of immersed granular flow down inclined plane

In this section, we performed simulations in the immersed case in order to compare the results to experiments of *Cassar et al.* (2005) to validate the first-order fluid-grains interactions modeled in our code. To do so, we set the grains parameters of the large glass beads from *Cassar et al.* (2005), with $d = 0.208mm$, $\rho_p = 2470kg/m^3$ and we set inter-particle friction at $\mu_p = 0.5$. We also set the fluid parameters corresponding to the aerial case $\rho_f = 1.29kg/m^3$ and $\eta_f = 1.85 \times 10^{-5}$ since it gives intermediate Stokes number values, $15 \leq St \leq 37$, for which fluid-grains interactions starts to have an influence on hysteresis (*Courrech Du Pont et al.*, 2003). We fixed the inclination angle at two values investigated by *Cassar et al.* (2005), $\theta = 28°$ and $\theta = 26°$, and fixed the layer thicknesses at corresponding values from their work. Then, the average velocity per particle, u, is calculated and averaged in time in the steady state. The results are presented on Figure 3.13. Note that the layer thicknesses are slightly different in our simulations than in their experiments since, in our protocol, the layer thickness is imposed considering the system at rest. The thicknesses are then slightly larger when flowing. However, we can see on the figure, that the trends $u(h)$ from our simulations are close to the ones of *Cassar et al.* (2005) for both inclination angles. Some departure is observed on the slope of the trend at $\theta = 28°$ that decreases at $\theta = 26°$. This departure could potentially come from the inter-particle friction value that is estimated around 0.5 for glass beads but can slightly vary from a sample to another. Nevertheless, the results are of the same order which enable us to validate the first-order fluid-grain interaction modeled in our code.

3.6 Sensitivity analysis of the protocol parameters

The configuration and the protocol depends on the following numerical parameters: the velocity of angle imposition $\delta\theta/\delta t$ and the size of the domain $L \times W$. In order to ensure the rigor of the analysis, sensitivity analysis are performed on all the identified parameters. As presented in Section 3.4.3, the evolution of the time averaged inertial number with time is quasi-static since the plane angle variation velocity $\delta\theta/\delta t$ is low enough to simulate a continuous-like evolution of the inclination angle. This value was selected performing a sensitivity analysis of such velocity that includes variations of the angle step $\delta\theta$ and the time duration between two angle variations δt. Both can then influence the critical angles at which the medium stop and start flowing.
Another parameter that may influence the critical angles is the size of the domain in the streamwise and spanwise directions, i.e. L and W.

Both sensitivity analysis are presented in the following Sections with a classical inter-particle friction coefficient $\mu_p = 0.5$ and restitution coefficient $e_n = 0.9$. Each simulation is repeated at between three and ten times with different random plane roughness distribution for each simulation.

3.6.1 Duration δt and velocity of angle variation

The values of critical angles depends on the rate of the stress imposition (or packing density imposition in the case of volume-imposed simulations). Indeed,(*Ciamarra et al.*, 2011; *Srivastava et al.*, 2019) show that at constant imposition (respectively ϕ and μ), the time, t_c, to wait in order to observe the jamming of the system diverge near the critical order parameter values, respectively ϕ_c or μ_c. These characteristic times are also widely distributed around the mean value showing the complexity of predicting the jamming or unjamming conditions. In other words, these latter quantities are estimated as asymptotic values in the limit $t_c \to \infty$ and cannot be strictly measured in practice. This divergence is interpreted in *Srivastava et al.* (2019) as a decrease of the probability that the assembly of grains reach a stable configuration when exploring various unstable states. The critical stress ratio μ_{stop} for example at the jamming transition would then be the values at which the probability vanishes implying that any infinitesimal value of μ above μ_{stop} could not lead to the arrest of flow.
As a consequence, in our simulations, the angles being continuously varies, the critical angles depends on the rate of stress imposition, here $\delta\theta/\delta t$. Its value needs to be sufficiently low for the critical angles to converge. In this Section we vary the velocity of evolution of the slope by varying both the angle increment $\delta\theta$ and the duration between two angle variations δt. The size of the domain is fixed at $L \times W = 20d \times 20d$. First, $\delta\theta$ is fixed at $0.1°$ and the velocity is varied by varying δt in order to have a range of velocities between $4.10^{-4°}/\sqrt{d/g}$ and $5.10^{-5°}/\sqrt{d/g}$. The stopping angles, θ_{stop}, the avalanche angle, θ_{start}, and the associated hysteresis are plotted at various $\delta\theta/\delta t$ on Figure (3.14). The averaged of each quantities in the simulations with fixed $\delta\theta$ are marked with pink triangles on the Figures. The error-bars corresponds to the standard deviations of three repeated simulations with a different random plane configuration.
We also performed simulations with fixed duration δt at $1\sqrt{d/g}$ and an angle increment

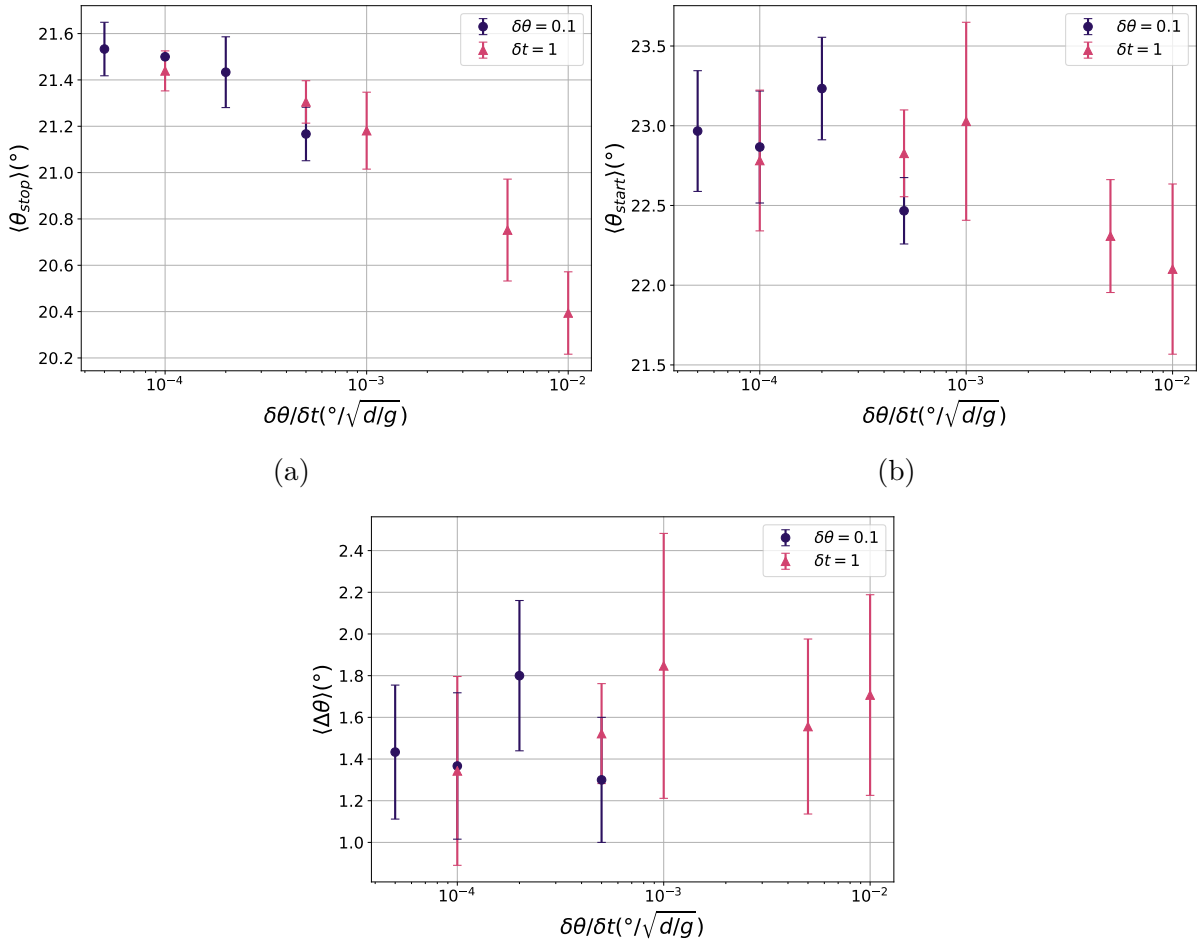

(a) (b)

(c)

Figure 3.14 – (a) Stopping angle versus the velocity of angle variation $\delta\theta/\delta t$. (b) Avalanche angle versus the velocity of angle variation $\delta\theta/\delta t$. (c) Hysteresis versus the velocity of angle variation $\delta\theta/\delta t$. For each of these plots the colors corresponds to the variations of the domain size which is equivalently varied in the spanwise W and streamwise L directions following the value of L. In addition the markers corresponds to a fixed value of angle step $\delta\theta = 0.1°$ and variations of the duration δt for the circles and a fixed value of duration $\delta t = 1\sqrt{d/g}$ and variations of angle step.

varied giving a range of velocities between $1.10^{-2°}/\sqrt{d/g}$ and $1.10^{-4°}/\sqrt{d/g}$. Here, the average values are marked with dark circles on the Figures and the calculated equivalently.

First, for each plot of Figure (3.14), we can see that at $\delta\theta/\delta t = 1.10^{-4°}/\sqrt{d/g}$ the triangle and circle markers are either really close or superimposed meaning that both ways of varying the velocity gives the same results of stopping, avalanche and hysteresis. Indeed, at a same ratio $\delta\theta/\delta t$ the critical angles are the same whatever the values of $\delta\theta$ and δt. This means that the velocity of angle variations is the appropriate parameter to study the influence of the external stress increment (stress rate) on the transition.

On Figure (3.14a), the stopping angle increases when the velocity decrease. As discussed above, The influence of the velocity of angle variations on the stopping angle is as expected, the longer the duration between two angle increment, the higher the probability to reach a stable configuration at a given angle. Hence the higher the critical angle at which stability occurs, θ_{stop}. Although no clear convergence is observed, at low values of $\delta\theta/\delta t$, especially at $\delta\theta/\delta t = 1.10^{-4\circ}/\sqrt{d/g}$ and $5.10^{-5\circ}/\sqrt{d/g}$, the stopping angle is relatively the same. The difference of the average values is lower than 0.1°.

The influence of $\delta\theta/\delta t$ on the avalanche angle is shown on Figure (3.14b). The avalanche angle also increases with decreasing velocity down to $10^{-3\circ}/\sqrt{d/g}$. Below this value, small variations are observed on the average values around a constant angle $\theta_{start} = 23^\circ$. Higher error-bars than for the stopping angle are also observed. In addition, the error-bars associated to the triangles markers (fixed $\delta\theta$) are slightly higher than the ones associated to the circles markers (fixed δt). Altogether, these variations of avalanche angle are probably related to two things: the absence of a sufficient number of simulations with only three repetition. As well as less precise angle values in one case at fixed $\delta\theta = 0.1^\circ$, than in the other case at fixed δt giving values of $\delta\theta$ below $10^{-3\circ}$ at those velocities. As a consequence, we consider that the avalanche angle converge for velocities lower than $10^{-3\circ}/\sqrt{d/g}$.

Finally, the influence of the velocity of angle variation on hysteresis is presented on Figure (3.14c). No clear trend is observed. Hysteresis not significantly influenced by this parameter. Nevertheless, except the hysteresis value at $2 \times 10^{-4\circ}/\sqrt{d/g}$ for which θ_{start} is the highest, the lower hysteresis are obtained for velocities below $10^{-3\circ}/\sqrt{d/g}$ since the avalanche angle is constant at these velocities and the stopping angle increases towards the avalanche angle.

Since both critical angles are constant at low velocities of angle variations it allows us to choose an optimal value for which the critical angles are insensitive to $\delta\theta/\delta t$ and at which the simulation time is smaller. We choose to restrict the velocity to a relatively low value: $\delta\theta/\delta t = 10^{-4\circ}(d/g)^{-1/2}$ since the measured hysteresis is quite low and may vary slightly with imposition speed. This velocity will be used in the following simulations presented in this work fixing $\delta\theta = 10^{-4\circ}$ and $\delta t = 1\sqrt{d/g}$. Such low angle increment enables to have continuous-like evolution of the angle, as shown by Figure (3.7) and to measure the critical angles with fine precision.

3.6.2 Domain size

The domain size also has an influence on the critical angles and hysteresis. The presence of a boundary wall (the inclined plane) imply finite-size effect on the curves $\theta_{stop}(h)$ and $\theta_{start}(h)$ as presented in the Introduction (see Sections 1.4.1 and 2.5). In the experiments that enabled to plot such curves, the inclined plane surface area is much larger than hundred times the grain diameter and no size effects in the spanwise and streamwise directions are observed on the bulk rheology. By contrast, numerical simulations do not allow us to model such a large area, as this would require too many grains to fill the

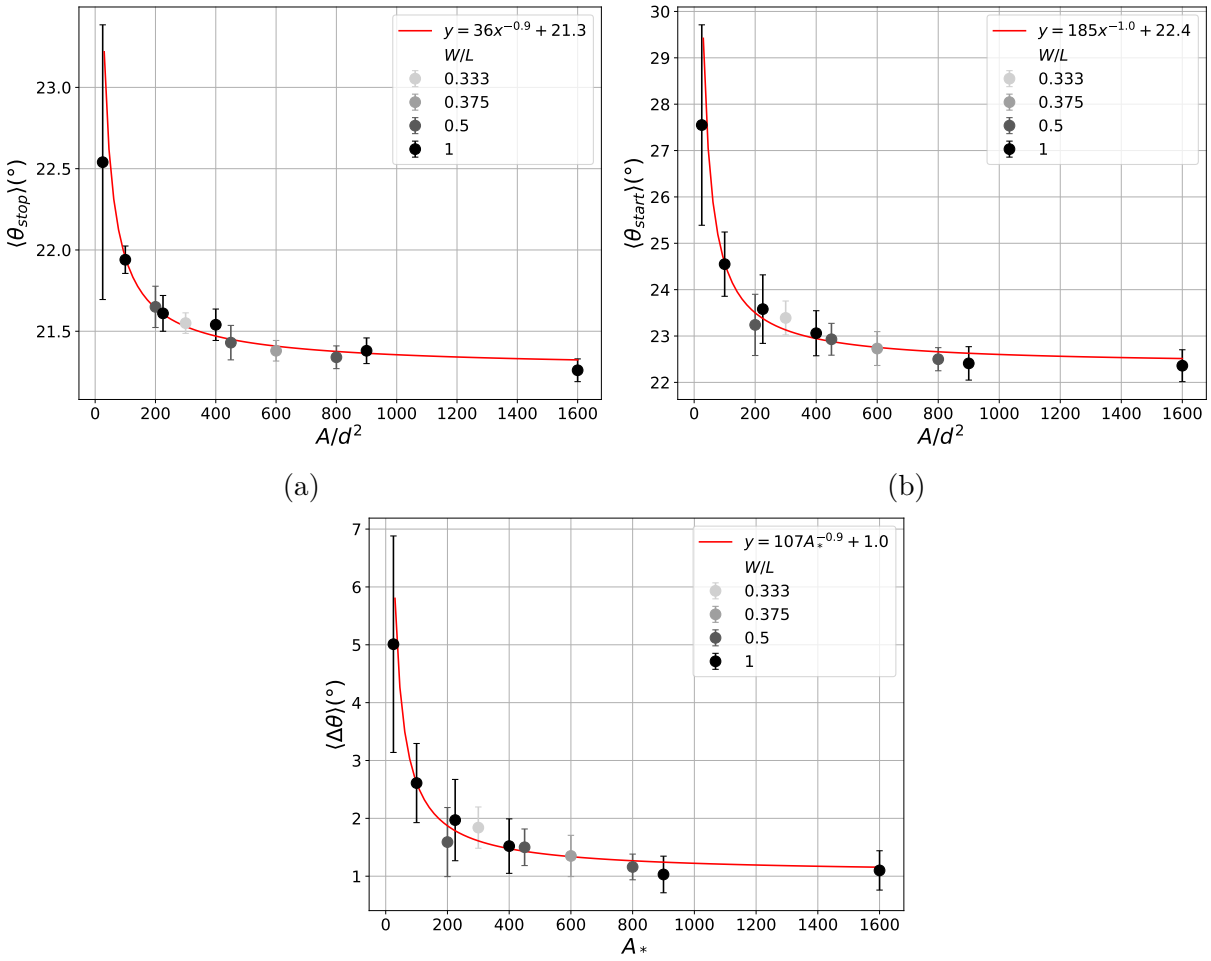

Figure 3.15 – (a) Stopping angle (b) Avalanche angle and (c) Hysteresis versus the normalised area of the plane $A_* = (L \times W)/d^2$. For each of these plots the colors correspond to the variations of the aspect ratio W/L between the width of the plane in the spanwise direction W and the length in the streamwise direction L. All simulations were performed ten times with different random distributions of the grains of the plane. The power law regression is also plotted to show the convergence of the variables with A_*.

domain. As a consequence, the domain size defined at values close to the size of a grain in both directions leading to finite-size effects.

In order to study the sensitivity of the critical angles and hysteresis to the domain size, $A = L \times W$, it varies between $25d^2$ and $1600d^2$. The aspect ratio W/L between the width of the domain in the span-wise direction and the length in the stream-wise direction is also varied. Conversely to the previous simulations, for each values of domain area, the simulations are repeated ten times rather than three with various plane roughness configurations. Critical angles and hysteresis are plotted versus $A_* = A/d^2$ on Figure 3.15. The error-bars still corresponds to the standard deviations between the different runs.

First, it is observed on each plots that the area of the domain is indeed the main

parameter at the expense of the length L since the angles and hysteresis values collapse with variations of the area at various aspect ratio W/L.
In addition, on all plots the measured variable is decreasing when the area increase. It means that both critical angles as well as hysteresis decrease when the domain size increase. These decrease follow a power law with A_* of the form $\theta_c \sim \alpha A_*^{-\beta} + c$ with α, β and c fitting constants that are determines for each variable with a logarithm regression. The regression and the related constants are plotted in red on each Figures. This power law shows that more than decreasing, the critical angles and hysteresis converge for large domain size. This allow us to select an optimal domain size for which the measured angles and hysteresis is close to the asymptotic value but low enough to have lower simulation time. This latter being proportional to the number of grains simulated, we choose a low value of domain area but with high enough value of length: $A_* = L/d \times W/d = 30 \times 15 = 450$. This value is optimal for lowering the simulation time. Nevertheless, at these values hysteresis is slightly higher than for bigger domain sizes, see Figure 3.15c. As such, one should take care of checking the domain size influence if small values of hysteresis are obtained.

Conclusion

The numerical model has been presented and the related stability analysis allowing us to optimize the simulation time while maintaining consistent results.
The inclined plane configuration studied in this thesis have been presented as well as the associated protocol. A sensitivity analysis was computed on the protocol parameters in order to study the transition between fluid-like and solid-like behavior of the granular system without effect of the domain size or the stress rate. As such the results obtain will be performed in quasi-static evolution of the imposed stresses and the size is such that the response of the system can be considered as a bulk response to imposed stresses.

Chapter 4

Granular regimes and phase transition on an inclined plane

The core subject of this manuscript is the study of hysteresis in granular media at the transition between fluid-like and solid-like regimes on an inclined plane. This phenomenon involves two different regimes of granular behavior under imposed stress: the dense flow regime (liquid-like) and the static regime (solid-like). These two states are therefore presented in Section 4.1 to identify what characterizes them. The inclined plane configuration inducing a source of anisotropy due to the geometry itself, i.e. the presence of gravity and a wall boundary, the states are studied by looking at the depth's evolution of the macroscopic and the micro-structure response to external stress.
The hysteresis phenomenon also involves two transitions: the cessation of flow, or jamming, and the initiation of flow, or unjamming, which are studied in Section 4.2. A phenomenology of these transitions is therefore proposed and discussed by visualising the velocities at the grain scale and the depth's evolution of the state variables of the system (macro and micro) near the transitions.
The evolution of the state variables, averaged along the layer depth, with the plane inclination angle will be discussed in Section 4.3. In particular, hysteretic cycles of these variables highlighting the granular states and the hysteretic behavior of the transition.
Finally, this approach enable us, in Section 4.4, to investigate the influence of the physical sources of energy dissipation at the contact scale on the transitions and hysteresis.

4.1 Granular regimes on an inclined plane

Overall, the transition between the static and flowing regimes of granular media is characterized by two distinct granular states, flow and rest, and two distinct transitions, the cessation and the initiation of motion. The idea of this section is to look qualitatively at the behavior of the flowing layer in the distinct regimes, following the simulation protocol defined in the above chapter. To do so, we first look at the vertical profiles of several classical state variables describing the granular medium behavior under imposed stress. The idea being to qualitatively describe the vertical evolution of the medium, two thicknesses are computed and compared in the flowing regime: $h/d = 10$ at the limit between thin and thick layers, and $h/d = 20$.

4.1.1 The flowing state for various layer thicknesses

The dense flow regime of granular materials on a rough inclined plane has been widely studied experimentally as well as numerically (e.g. *GDR MiDi*, 2004; *Silbert et al.*, 2001; *Forterre and Pouliquen*, 2008; *Baran et al.*, 2006). When the angle of the plane is in between the avalanche angle and the maximum angle of stable flow, the dynamic of the granular dense flow is steady and uniform in the whole grain layer. In that context, studying a steady uniform flowing layer on a rough plane allows one to have a direct access to the granular response to external stress. Such response is investigated on an inclined plane by measuring the evolution of several state variables with the inclination angle as depicted in Section 3.4.1, Equation (3.45).
First, the main flow property that arises from the presented results are state variables that describe the flow evolution at the macroscopic scale: the velocity profile $u_x(z)$ and the packing density profile $\phi(z)$.

Velocity profiles

The dynamic of the granular layer flowing on a rough plane is characterized by a velocity profile along the vertical axis, normal to the plane, at position noted z. Here, the velocities are calculated at each position z separated by an interval $dz = 0.5d$ forming sub-layers in which the velocities of the particles is averaged in space on the span-wise, y, and stream-wise, x, directions given instant velocity profiles as followed:

$$u_x(z,t) = \frac{1}{N_p(z,t)} \sum_{i=1}^{N_p(z,t)} u_x^i(z,x,y,t), \text{ for } z^i \in [z - dz/2; z + dz/2], \tag{4.1}$$

with $N_p(z,t)$ the number of particles in the sub-layer at position z and $u_x^i(z,x,y,t)$ their instant velocities. These instant velocity profiles are averaged in time at a given angle as followed:

$$u_x(z) = \frac{1}{t_w} \sum_{t=t_0}^{t_0+t_w} u_x(z,t), \tag{4.2}$$

t_0 is the initial time and $t_w = 100\sqrt{d/g}$ is the duration of time averaged. The latter time is selected in order to average at an inclination angle almost constant, i.e. that varies from $\delta\theta = 0.01°$, during the measurement. In addition, the angle plotted for each label on the following figures are selected as the angle value at the simulation time $t_0 + t_w/2$.
The profiles are plotted in the following on Figure 4.1a for thick layer, i.e. $h/d \approx 20$, and Figure 4.1c for thin layer, i.e. $h/d \approx 10$, at various angles. First, it can be observed for both layer sizes that the velocity profiles are lower in the whole layer when the plane angle is decreased. It shows that the lower the shear to normal stress ratio imposed on the layer the slower the medium. In addition, for thick layer, the shape of the velocity profiles at those angles is a Bagnold-like shape velocity profile, i.e. it follows the Equation (3.50) (*Bagnold*, 1966; *Silbert et al.*, 2001; *GDR MiDi*, 2004). The profile at $\theta = 24°$ is superimposed to a theoretical Bagnold scaling profile on Figure 4.2a. The profile follows the following equation:

$$u_x(z) = C\left[h^{3/2} - (h - z + z_0)^{3/2}\right], \tag{4.3}$$

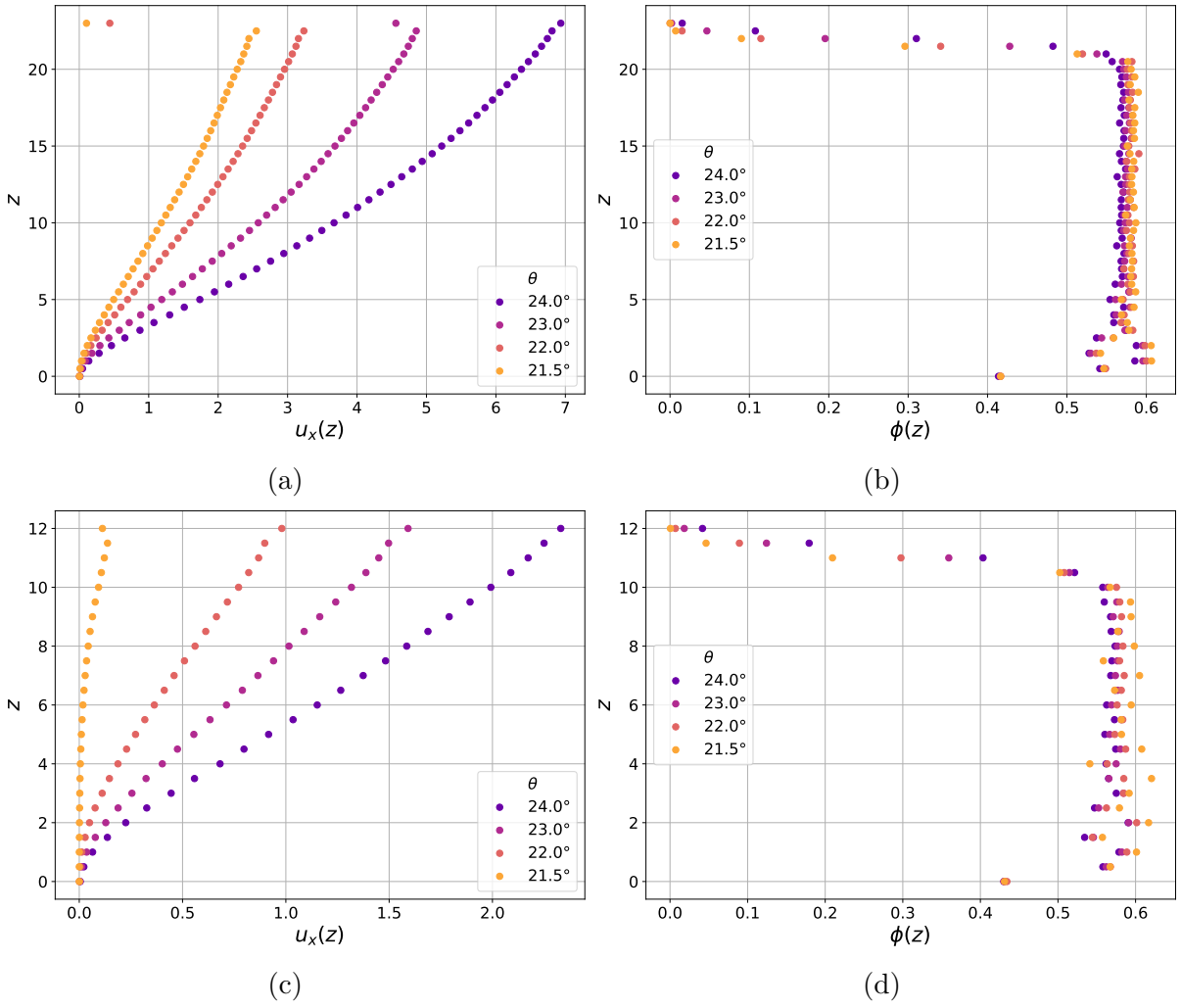

Figure 4.1 – Velocity profiles at $\mu_p = 0.5$ at various angles (a) for thick layer, $h/d = 20$ (c) for thin layer, $h/d = 10$. Volume fraction profiles at $\mu_p = 0.5$ at various angles (b) for thick layer, $h/d = 20$ (d) for thin layer, $h/d = 10$.

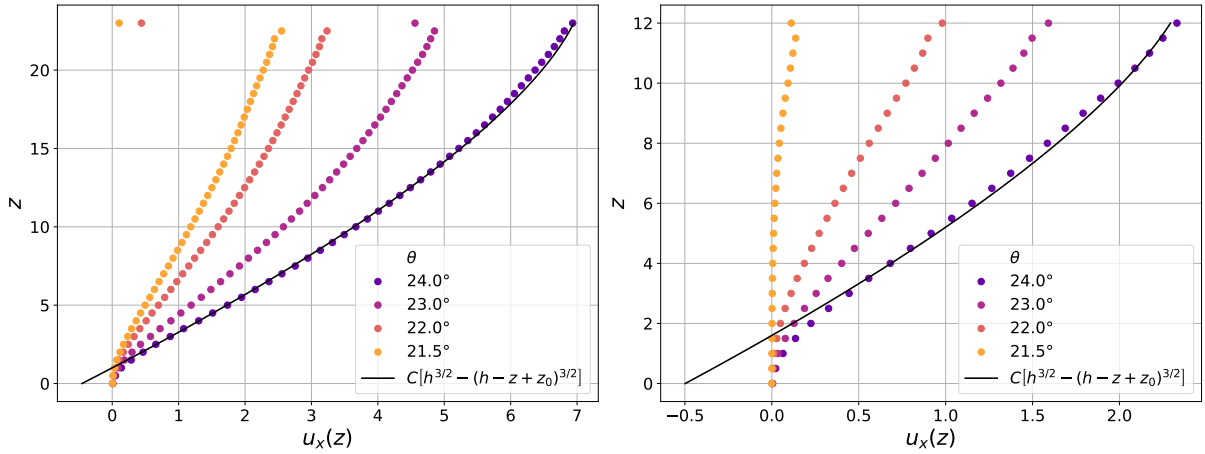

(a) (b)

Figure 4.2 – Velocity profiles superimposed with a theoretical Bagnold scaling profile at $\mu_p = 0.5$ for thick layer, $h/d = 20$ (a) and thin layer, $h/d = 10$ (b).

with C a prefactor calculated to fit the curve, h is the layer thickness and z_0 is an additional parameter that allows us to recover the velocity profile near the bottom roughness. It characterizes the altitude at which grains have no velocity due to the no-slip condition, which is finite due to the presence of the bottom roughness. At this angle, their values are typically $C = 0.062\sqrt{g}/d$, $h = 23.5d$ and $z_0 = 1d$. Although some slight discrepancies are observed near the free surface, we can see that the theoretical profile fit the profiles in the bulk region and near the bottom plane. This shape characterizes the averaged steady state velocity field of a granular layer uniform flow down a rough inclined plane.

For thin layer simulations ($h/d = 10$), the velocity profile far from the jamming transition can be approached by Equation 4.3, with $C = 0.058\sqrt{g}/d$, $h = 12d$ and $z_0 = 1.4d$ at $\theta = 24°$, as shown by Figure 4.2b. Nevertheless, some discrepancies are observed along the whole depth since the profile is closer to a linear profile (*Silbert et al.*, 2001; *GDR MiDi*, 2004). This shape variation at high angles between thick and thin layers shows that the finite size effect is not negligible on the dynamic of the layer. Nevertheless, these variations does not prevent the granular system to have similar critical angles between thin and thick layers (*Pouliquen and Forterre*, 2002). As such, the effect of thickness on critical angles and hysteresis becomes negligible for layers greater than $10d$ (see e.g. *GDR MiDi*, 2004; *Staron*, 2008). This enabled us to run simulations with thin layers in order to simulate fewer grains and have shorter simulation times.

Packing density profiles

Equivalently to velocity profiles, the instant packing density profiles are averaged over time following the same method. They are calculated at each time by:

$$\phi(z,t) = \frac{N_p(z,t)\pi d^3}{6LWdz}, \tag{4.4}$$

with $N_p(z,t)$ the number of particles at time t which center's position is in between $z - dz/2$ and $z + dz/2$ (inside the sub-layer).

Packing density profiles are plotted next to velocity profiles for thick piles on Figure 4.1b and for thin piles on Figure 4.1d at various angles. For both layer thicknesses, packing fraction profiles are constant in the bulk and sharply varies near the bottom and at the free-surface. A constant packing density profile at various angles for thin layers is different from the results in 2 dimensions from *Silbert et al.* (2001) and *GDR MiDi* (2004) showing that the assumption of constant packing density given by the equations (3.43) and (3.44) holds in three dimensions even for thin layers.
The volume fraction profiles also evolve with the plane angle, especially in the bulk region. The less dynamic the system is the denser the layer.

Shear rate, granular pressure and inertial number profiles

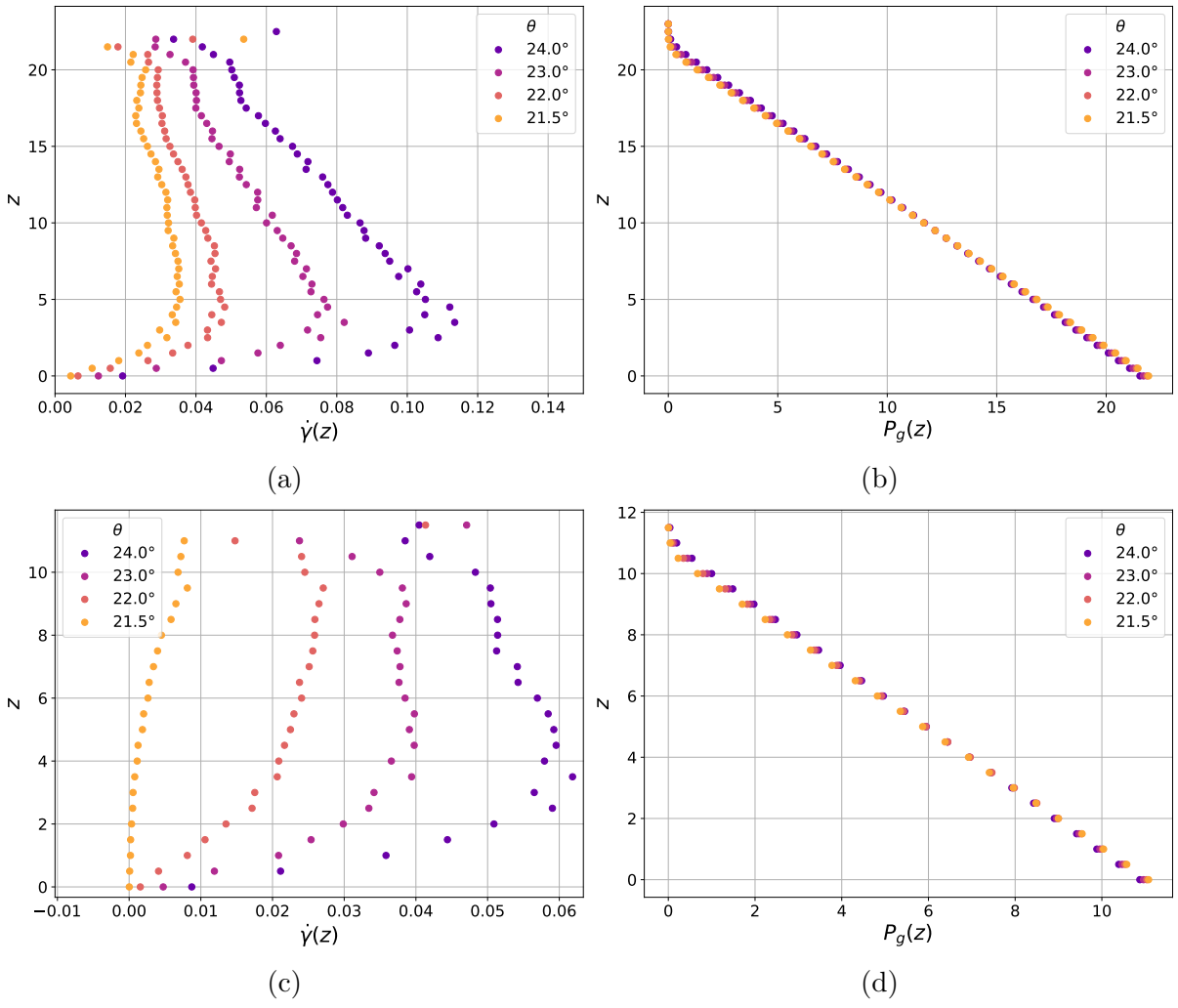

Figure 4.3 – Strain rate profiles at $\mu_p = 0.5$ at various angles (a) for thick layer, $h/d = 20$ (c) for thin layer, $h/d = 10$. Granular pressure profiles at $\mu_p = 0.5$ at various angles (b) for thick layer, $h/d = 20$ (d) for thin layer, $h/d = 10$.

Under the conditions of steady and uniform flow, which was shown in the previous section, the inclination angle is directly related to the dimensionless shear rate, $tan(\theta) =$

$\mu(\mathcal{I})$, see Section 3.4.1. Varying the slope allows one to explore the different granular flow regimes. The instant profile of inertial number is expressed as:

$$\mathcal{I}(z,t) = \frac{d\dot{\gamma}(z,t)}{\sqrt{P_g(z,t)/\rho_p}} \tag{4.5}$$

with the shear rate $\dot{\gamma}(z,t)$ which can be directly determined from the vertical velocity profile, see Equation (3.48). The vertical granular pressure profile is given as:

$$P_g(z,t) = \rho_p g cos(\theta(t)) \int_z^h \phi(z,t)\, dz, \tag{4.6}$$

that depends on the instant volume fraction profile $\phi(z,t)$ from the above section. The pressure and shear rate profiles are first plotted on Figure 4.3 for both layer thicknesses. Firstly, the granular pressure profile is for both thicknesses a classical linear hydro-static pressure profile. The pressure is zero at the free surface, since no granular pressure is applied, and the maximum pressure is at the bottom, since at that position grains are subjected to the pressure of the whole layer. The slope of the linear profile is proportional to the inclination angle, see Equation (4.6).
Secondly, the shear rates profiles for thick layer, presented by Figure 4.3a are coherent with the Bagnold-like shape velocity profiles. They appear to have square-root-like profiles with depth for $z \in [5-20]d$, i.e. in the bulk, and sharply evolves at the bottom and the free-surface. By contrast, for thin layer the bulk behavior is closer to linear, with almost constant shear rate profiles.

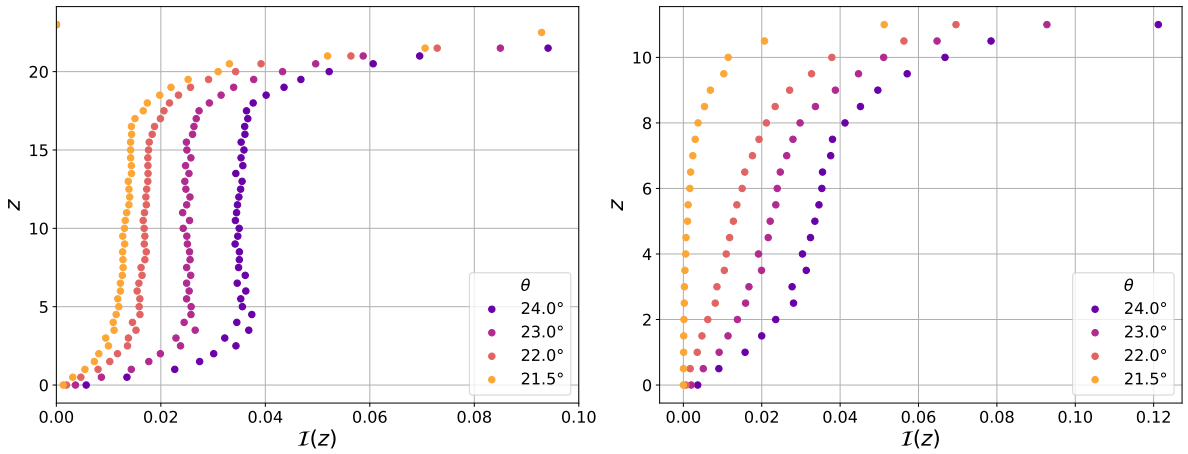

(a) (b)

Figure 4.4 – Inertial number profiles at $\mu_p = 0.5$ at various angles (a) for thick layer, $h/d = 20$ (b) for thin layer, $h/d = 10$.

The inertial number profiles are plotted at various inclination angles on Figure 4.4a for thick layer and Figure 4.4b for thin layer. It can be observed that the inertial number is in a typical S-shape with a constant value within the grain layer. Its value diverges close to the free surface since the pressure is dropping close to zero at the free-surface. It also sharply decreases near the bottom plane, for $z \to 0$, due to the decrease of shear rate near the bottom induces by the variations of velocity profile near the boundary. For thick

layers, the constant value of the inertial number in the bulk allows us to check that it is a relevant macroscopic dimensionless number to characterize the evolution of the flow dynamic. Indeed, it measures equivalently the dynamic of the whole grain layer in the bulk and enables to validate the local-rheology assumption of uniform dynamic process (*Pouliquen and Forterre*, 2002; *GDR MiDi*, 2004). Nevertheless, the Bagnold rheology was shown to display discrepancy with measured velocity profiles near the bottom plane for thick layers (*GDR MiDi*, 2004). With that, the non-constant value of inertial number and quasi-linear velocity profiles for thin layers show the heterogeneity of the flow due to the geometry. It is therefore necessary to introduce other state variables. In particular, variables describing the state of the micro-structure.

Coordination number profiles

One of the classical variable that enables to describe the evolution of the micro-structure, specifically the contact network, is the coordination number $\mathcal{Z}$. This quantity provides information on the average number of contacts within the medium, and therefore along the depth of the layer. The coordination number profile is calculated at time t and position z following the equation:

$$\mathcal{Z}(z,t) = \frac{2N_c^{dyn-dyn}(z,t) + N_c^{dyn-plane}(z,t)}{N_p^{dyn}(z,t)}. \tag{4.7}$$

$N_c^{dyn-dyn}(z,t)$ is the number of contact in the sub-layer at position z between pairs of dynamic particles (free to move). $N_c^{dyn-plane}(z,t)$ is the number of contact in the sub-layer at position z between dynamic particles (free to move) and static particles of the plane. Finally, $N_p^{dyn}(z,t)$ is the number of dynamic particles in the sub-layer at position z. This equation is adapted from the classical form, $\mathcal{Z} = 2N_c/N_p$ with simply the total number of contacts N_c and the total number of particles N_p, in order to not to count the grains in the plane as part of the granular layer being able to flow. This calculation only differ from the classical formulation near the bottom plane.
The coordination number profiles are plotted on Figure 4.5a for thick layer and Figure 4.5c for thin ones. The higher amount of contacts are near the bottom plane when the lower amount are close to the free-surface. These observations are consistent with the inertial number profiles. Indeed, the grains at the free surface are the ones that are the less constrains by the presence of other grains. They experience fewer contacts in their motion and therefore are the more inertial. By contrast, near the bottom plane the grains are constrained in their motion by the plane and the layer above them. As such, they experience the most contacts in the medium. For thick layer, see Figure 4.5a, the coordination number continuously increases with decreasing z with a quasi-constant value in the middle of the layer (in the bulk). This suggests that for higher layer thicknesses, the coordination number may be well established and constant in the bulk region of the flow. By contrast, for thin layers the amount of contacts is continuously increasing with decreasing z as quasi-linear profiles with no particular region with quasi-constant $\mathcal{Z}$. In addition, in both cases there is a significantly higher number of contacts close to the bottom than in the bulk even if the volume fraction is constant through the whole layer. This result shows a clear anisotropy in the contact network, not measured by the volume fraction. This result is unexpected since the number of contact is expected to be correlated

to the packing fraction. Thus, it suggests that the packing fraction, being a macroscopic variable, does not enable one to capture such heterogeneity in the flow that is measured by the coordination number.

Nevertheless, we observe more and more contacts when the angle is lowered, going together with the increase of packing density. For both layer thicknesses the average number of contacts decreases significantly less with the angle near the free surface than in the rest of the medium. This observation is similar to the inertial number profiles evolution. The values of $\mathcal{I}$ at the free surface remain large with decreasing angle, whereas they decrease sharply with the angle in the rest of the layer, see Figure 4.4. This suggests that the grains at the free surface are less affected by shear stress decay than the bulk and near-bottom regions of the layer.

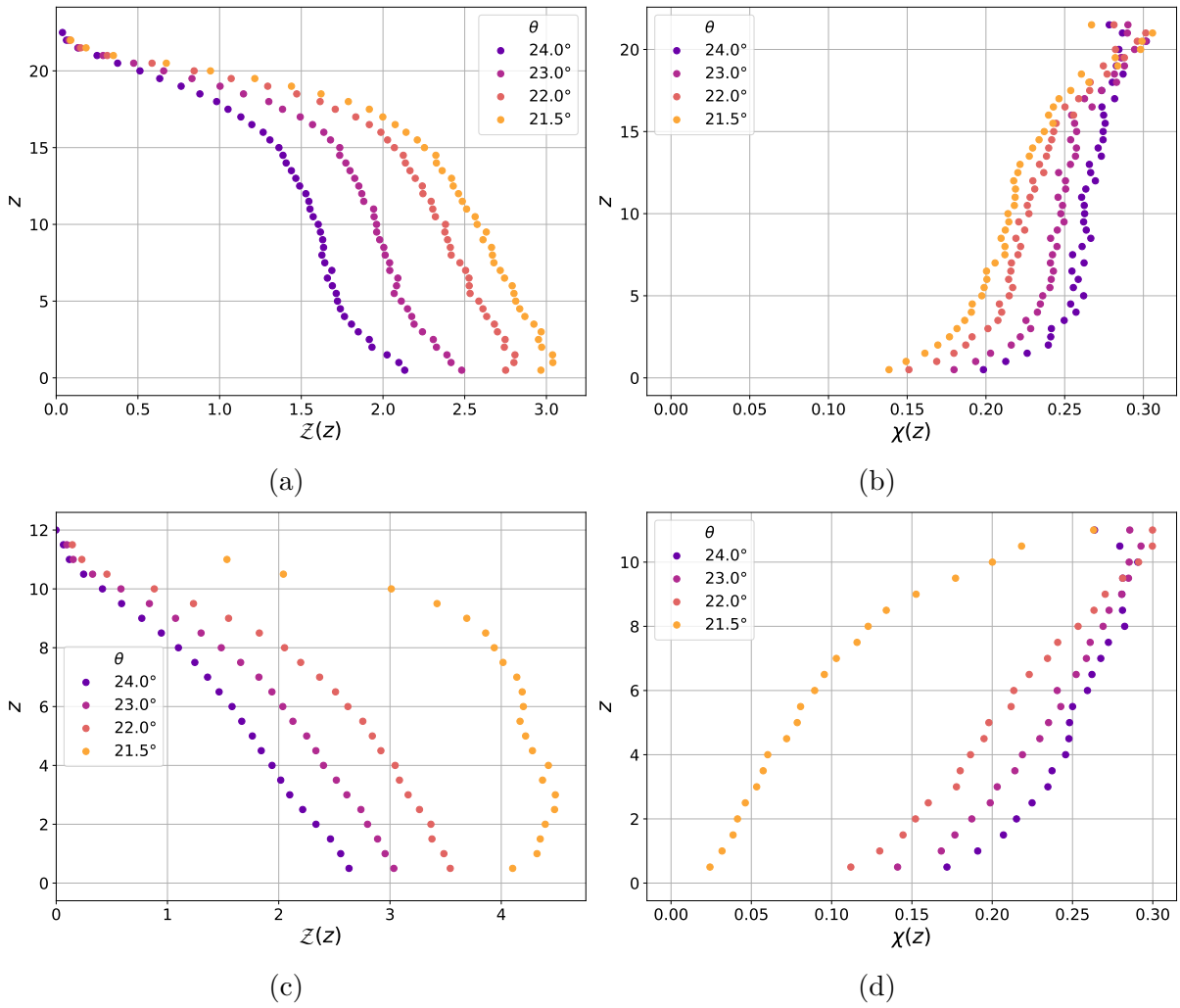

Figure 4.5 – Coordination number profiles at $\mu_p = 0.5$ at various angles (a) for thick layer, $h/d = 20$ (c) for thin layer, $h/d = 10$. Fraction of sliding contacts profiles at $\mu_p = 0.5$ at various angles (b) for thick layer, $h/d = 20$ (d) for thin layer, $h/d = 10$.

Sliding contacts profiles

The other classical variable that gives information on the micro-structure, specifically the tangential contact force network, is the sliding contact proportion χ. It provides information on the number of proportion of contacts that are not tangentially constrained. The instantaneous sliding contact proportion at position z is calculated as follow:

$$\chi(z,t) = \frac{N_c^{sliding}(z,t)}{N_c^{tot}(z,t)}. \tag{4.8}$$

$N_c^{sliding}(z,t)$ is the number of contacts that slides, i.e. surpassing the Coulomb criterion of tangential sliding, in the sub-layer. $N_c^{tot}(z,t)$ is the total number of contacts in the sub-layer.
Contrary to the coordination profiles, the sliding contact proportion profiles plotted for thick layer on Figure 4.5b and thin layer on Figure 4.5d, is higher at the free surface and lower near the bottom plane. Near the free surface the contacts are likely to slide hence not tangentially constrained the grains in their motion but the closer it gets from the bottom the more tangentially constrained the grains are in their contacts. This result also highlights the heterogeneity of the flow on a rough inclined plane and an anisotropy in the micro-structure.
For thick layer, Figure 4.5b shows that the ratio of sliding contacts is also quasi-constant in the bulk but still continuously decrease with z. This supports the fact that for larger layer thicknesses, the presence of the plane and the free-surface is expect to be negligible on the contact and tangential force network in the bulk region. For thin layer, the ratio is, equivalently to the coordination number, quasi-linear with z.
The sliding contact proportion also evolves with the angle, decreasing with the latter. Decreasing the shear stress and increasing the normal stress then decreases the ratio of sliding contacts. In addition, similarly to the coordination and inertial numbers, the shear stress decay induce more decay within the layer than near the free surface, particularly for thin layer. As a result, the bulk tends faster to the static state than the grains near the free surface when decreasing the shear rate.

Finally, we have seen that the flow of granular layers on a rough inclined plane presents some heterogeneous behaviors. In the case of thick layers, the bulk behavior is homogeneous at high angles with well established Bagnold-like profiles and constant inertial number, packing fraction as well as a quasi-constant coordination number profile and sliding contact ratio. The flow remains heterogeneous near the free surface and near the bottom plane. For thick layer, the flow is heterogeneous through the whole depth demonstrating a finite size effect. In addition, we have seen that for both thicknesses the coordination number and sliding contact ratio highlights an anisotropy of the contact network and the network of tangential forces within the depth of the layer, depending on the inclination angle and suggesting that it is due to the presence of both shear stress and the bottom rough plane. Finally, this anisotropy is more localised near the free surface when the shear stress is decreased.

4.1.2 The static state

By contrast with the flowing state, the static state is characterized by no velocity. A residual velocity exists in the static state due to the vibration of the contact network. Nevertheless the average velocity values are very low $u_x \approx 1.10^{-7}\sqrt{dg}$. Similarly, the inertial number is very low (below 1.10^{-8} in depth average) meaning that the system is no more flowing in that regime.

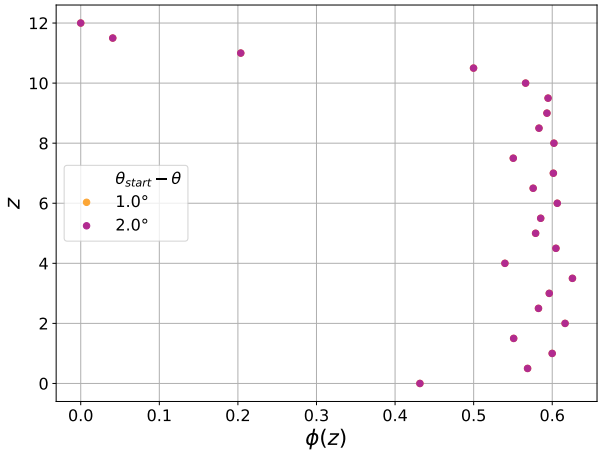

Figure 4.6 – Volume fraction profiles at $\mu_p = 0.5$ at various angles in the static regime for thin layer, $h/d = 10$.

Packing density profiles

In the static regime, the volume fraction is plotted on Figure 4.6. It is constant with variations of angles and equal in depth averaged to ϕ_c its critical value in the static state. This value characterizes the static state, in which variations of external stresses does not induce change in the packing density of the layer.

Coordination number profiles

The coordination number in the static regime is plotted on Figure 4.7a. Interestingly, it has a similar shape than the volume fraction with a critical constant value along depth, noted $\mathcal{Z}_c$. By contrast with the flowing state, shown by Figure 4.5c, the maximum amount of contacts in the static state is in the bulk region near the free-surface instead of near the bottom plane. In another word, when the medium is jammed, the layer gains a significant amount of contact near the free surface. In addition, the number of contacts does not significantly vary with the external stress in the static regime.

Sliding contacts profiles

The sliding contact proportion is plotted on Figure 4.7b in the static regime. Its averaged value along depth is very low, lower or about 0.1% of contacts are sliding. Nevertheless this value is slightly evolving with the external stress. Especially near the bottom plane, the fraction of contact that slides doubles when increasing the inclination angle of 1° in

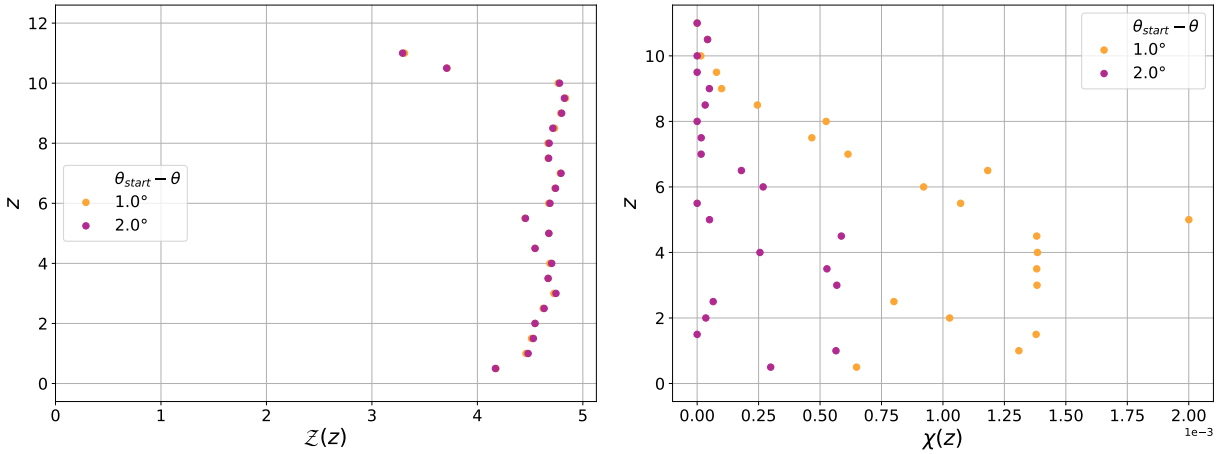

(a) (b)

Figure 4.7 – (a) Coordination number profiles at $\mu_p = 0.5$ at various angles in the static regime for thin layer, $h/d = 10$. (b) Fraction of sliding contacts profiles at $\mu_p = 0.5$ at various angles in the static regime for thin layer, $h/d = 10$.

the static state. This increase occurs in the bulk region near the bottom plane. It shows that despite no dynamic is microscopically observed, some contacts are sliding suggesting the presence of rearrangements in the system, i.e. local plastic displacements within the system, equivalently to what was observed by *Staron et al.* (2002). Interestingly, these rearrangements occurs near the bottom plane and not near the free surface. It may be interpreted as a consequence of the increasing granular pressure with depth pushing grains to tangentially slides.

4.2 The transitions processes

Now that the granular layer response to stress was qualitatively studied in both regimes, we focus on the two distinct transitions at play in the hysteretic phenomenon: the jamming and the unjamming. They are two complex mechanisms that appears to occurs with different phenomenology and that depends on the state of the system. Hence, the phenomenology of both these transitions is discussed in order to better characterize them in a reference case. To do so, we first look at the evolution of velocities at the granular scale for the flow cessation and initiation. Then, we look at the vertical profiles of several classical state variables in both regimes near the transitions.

4.2.1 The jamming process or cessation of flow

In this section, flow cessation and avalanche are observed and studied for a given simulation of dry granular material with a classical inter-particle friction coefficient, $\mu_p = 0.5$. The idea is to visualise how both processes of cessation and onset of flow works at the scale of the grain and the granular layer.

Flow cessation is first observed by visualising the whole assembly of grains, opacifying them and colourising them when their velocity is below a given limit. This limit is fixed at

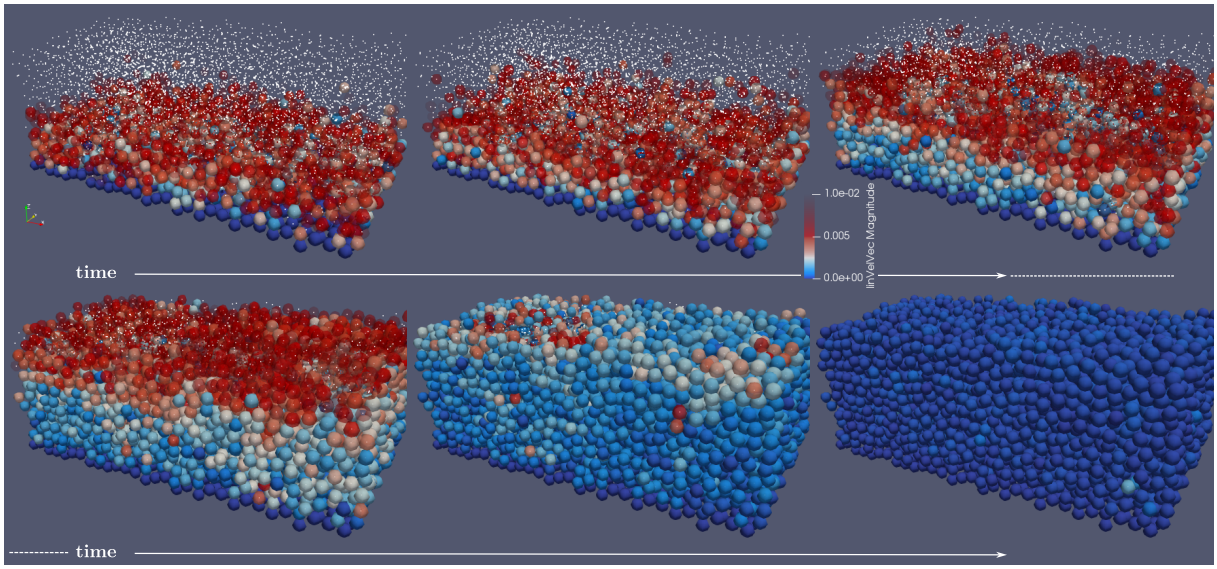

Figure 4.8 – Evolution of the velocity of grains in the system with time at jamming. The velocity scale is set such that grains with higher velocity than $\|u\| = 1.10^{-2}\sqrt{dg}$ are transparent. Under this limit they are colorized by their velocity from red for the highest to blue for the lowest velocities.

$\|u\| = 1.10^{-2}\sqrt{dg}$. Under this limit the grains are considered to be in the way to be static. Figure 4.8 shows the evolution of the velocity of each grains with the time of simulation near the jamming transition. It can be observed on the first snapshot, upper-left panel, that most of the grains within the flowing layer are not visible (we can only see their center in white) since they are flowing at a velocity higher than the defined limit. The blue grains at the bottom are the fixed grains constituting the rough bottom plane and are always static. In the last snapshot, on the lower-right panel, all grains are considered in the way to be static. Indeed, the closer the snapshot is from the jamming transition the slower the flow.
As such, the important mechanism to observe on these snapshots is that the stability of grains, induced by energy dissipation, is initially localised at the bottom. It is then progressively diffused into the whole grain layer when the medium is approaching the static state. The grains that are nearly static, i.e. below the velocity limit, are initially near the bottom plane. These grains are flowing slower than the rest of the layer because a zero velocity condition is imposed at the bottom by the static rough plane. We can observe that the nearly static layer in diffusing with time upon depth into the free surface. Inter-particle friction, grains collisions as well as the geometrical plane shape, i.e. plane roughness, are expected to induce energy dissipation at the contact scale and push the grains to reach the static stable state. This effect is added to the increasing normal stress and decreasing shear stress with the reduction of the inclination angle leading the medium to be almost completely jammed on the last snapshot.

4.2.2 Velocity profiles near jamming

For such thin layer, near the jamming transition, when the angle is decreased in the flowing state, the velocity profiles are plotted on Figure 4.9. On this figure and the

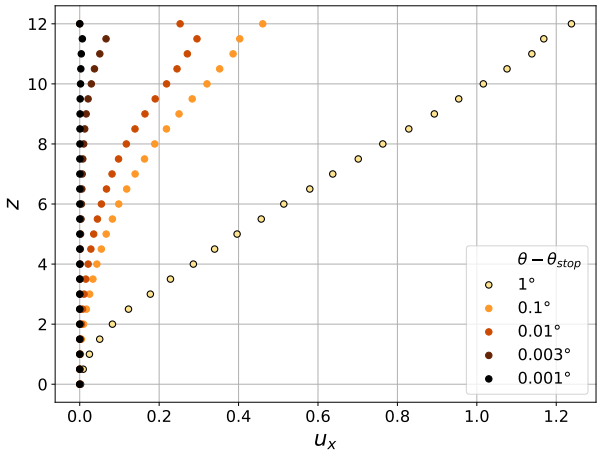

Figure 4.9 – Velocity profiles at $\mu_p = 0.5$ at various angles near jamming.

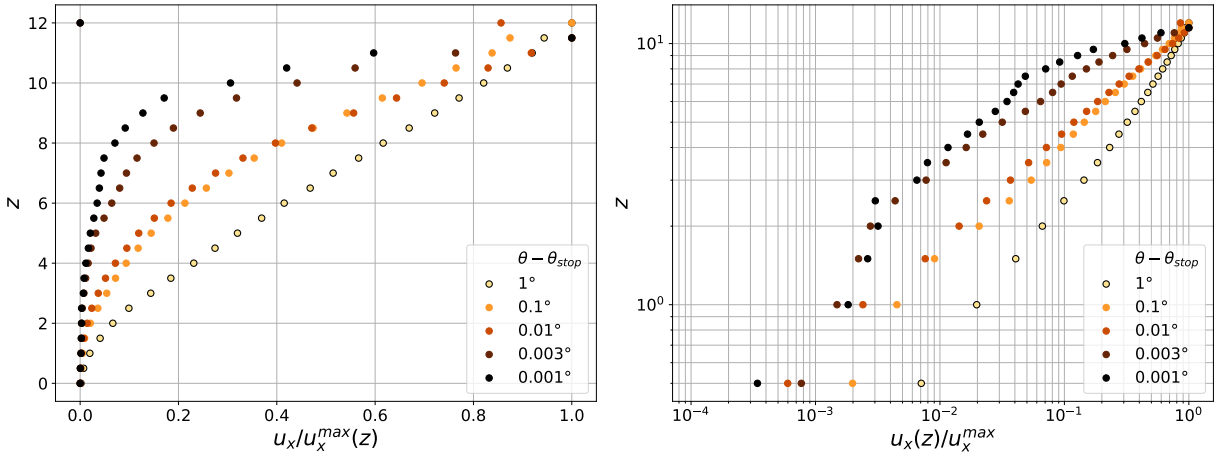

(a) (b)

Figure 4.10 – Velocity profiles at $\mu_p = 0.5$, normalised by the free-surface velocity V_{max}, at various angles close to θ_{stop} in linear scale (a) and log scale (b).

following ones, the velocity profiles are plotted at different angle differences, $\theta - \theta_{stop}$, from the stopping angle. As a result, the time average window t_w has been lowered to $t_w = 5\sqrt{d/g}$ in order to have quasi-instantaneous profiles slightly smoothed around $\theta - \theta_{stop}$, enabling us to see the evolution near jamming without time lag induced by the time average window. Figure 4.9 shows significant decrease of the velocity profiles while approaching the jamming transition. In addition, the shape of the velocity profiles is evolving. In order to compare this evolution, the velocity profiles are normalised by the velocity at the free-surface and plotted at various angles near the jamming angle θ_{stop}. The plots are presented on Figure 4.10a. The figure shows the velocity profiles normalised with a linear axis scale. The second Figure 4.10b shows them with a logarithm axis scale. The normalised velocity profiles initially scale with the vertical position at the power about 3/2 with concave profile. This power is evolving into a linear profile and then into convex profiles where a region of the layer is static and a region is flowing. Such velocity profiles were predicted near the onset of flow and arrest by the partially fluidized theory of *Aranson et al.* (2008) showing a fluidized region above a static layer. The evolution of the velocity profiles shape supports the idea that the dissipation mechanism is diffusing up from the bottom to the free-surface. Indeed, the grains sub-layers closer to the bottom plane are getting more and more stable near the jamming transition and push the upper sub-layers to reach stability. Destabilisation is then the winning process far from the jamming angle. Near the jamming angle stabilisation is the winning process changing the shape of velocity profiles.

Inertial number profiles near jamming

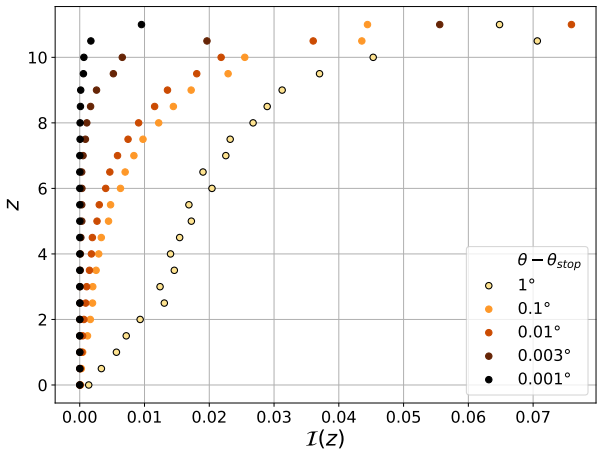

Figure 4.11 – Inertial number profiles at $\mu_p = 0.5$ at various angles near jamming.

Similarly, the inertial number profiles are plotted at one angle far from the jamming angle and various angles near the jamming angle. The shape of the inertial number profiles are evolving from the S-shape without constant bulk values into convex profiles where a majority of the bulk region, from the bottom plane to 2/3 of the thickness, are significantly slower than the flow at the free surface. This is a signature of the increase of heterogeneity within the flowing layer near the jamming transition. It supports the idea depicted above that the flow decay, due to shear stress decay, is larger in the bulk and

near the bottom than at the free surface where grains continue to flow.

Coordination number profiles near jamming

The coordination number profiles near jamming are plotted on Figure 4.12a. It first has the shape in the flowing regime for thin layers as shown by Figure 4.5c. Then, in the bulk region where the flow is getting slower and near the bottom plane, the coordination number is significantly increasing with decreasing angle towards the stopping angle θ_{stop}. Yet, at the closest value to the stopping angle, $\theta - \theta_{stop} = 0.001°$, the profile is constant and the excess of contacts near the free surface, observed in the static regime (see Figure 4.7a), is not present. It supports the idea of a flowing small layer above the static bulk just before jamming that ultimately comes to rest leading the system to jams.

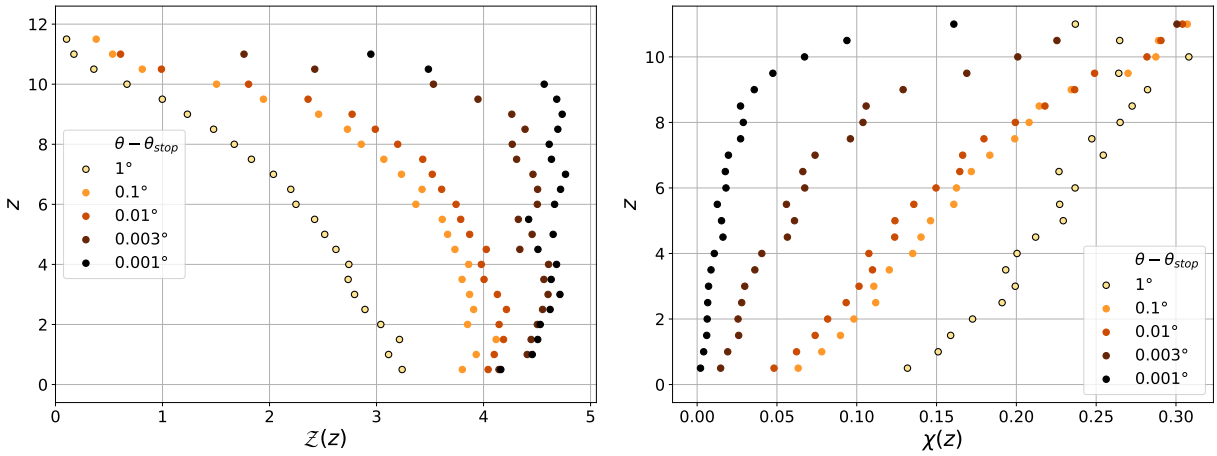

(a) (b)

Figure 4.12 – (a) Coordination number profiles at $\mu_p = 0.5$ at various angles near jamming for thin layer, $h/d = 10$. (b) Fraction of sliding contacts profiles at $\mu_p = 0.5$ at various angles near jamming for thin layer, $h/d = 10$.

Sliding contact proportion profiles near jamming

The sliding contacts proportion profiles are plotted on Figure 4.12b near jamming. One observe that the amount of sliding contacts is significantly decreasing in the bulk region near the bottom plane when the angle goes towards θ_{stop}. This behavior, coupled with the observations made on Figure 4.12a, show that close to the jamming transition there are more and more contacts that are more and more tangentially stables, especially in the bulk region near the bottom plane.

Finally, we have seen that when decreasing the angle between 1° to 0.001° from θ_{stop}, there is a continuous decrease of the flow in the bulk characterized by an increase of the number of contacts that are less and less sliding. This decrease is diffusing from the bottom plane up to the free surface where the grains are slow to follow the behavior of the bulk. As such, the anisotropy in the contact and tangentially sliding force network is more and more localised near the free surface approaching the static state.

4.2.3 Phenomenology of the initiation of flow

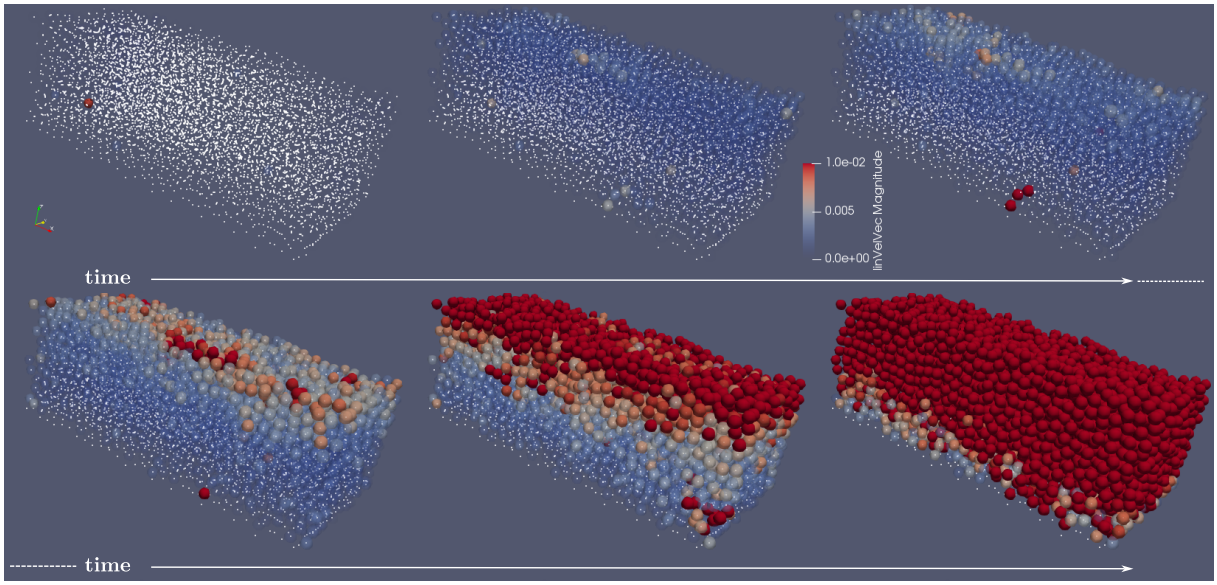

Figure 4.13 – Evolution of the velocity of grains in the system with time at unjamming. The velocity scale is set such that grains with low velocities, around $\|u\| = 0\sqrt{dg}$ are transparent. Above, they are colorized by their velocity from blue for the lowest to red for the highest velocities.

The evolution of the velocities in the whole granular medium at the initiation of flow, when the angle is increased in the static state, is presented on Figure 4.13. This figure shows different snapshots of the velocity of grains at different simulation times during the unjamming transition. By contrast with flow cessation, the grains are now visible when they have non-zero velocity and are colorized by their veolocity between zero (blue) into the defined limit value 1.10^{-2} (red). It can be observed on the three first snapshots, that a rearrangement occurs (first snapshot) that unjams an important quantity of grains near the free-surface (second snapshot). It forms a layer, for which the velocity is a bigger that the rest of the system. It can be seen on the third snapshot, that within this slowly displaced layer, a local rearrangement at a higher velocity occurs. Another rearrangement also occurs at the same time near the bottom plane. These rearrangements increases the velocity of the flowing layer. Then, on the last three snapshots, the flowing layer gains velocity until the whole layer flows. Conversely to the cessation of flow, that appears to be due to a progressive dissipation mechanism diffusing from the bottom plane up to the free-surface, the avalanche mechanism appears to be a succession of local events, i.e. local rearrangements, inducing an instability near the free-surface unjamming the medium that quickly starts to flow on the whole vertical. A similar phenomenology has been shown by *Silbert et al.* (2003), demonstrating the presence of instabilities near the free surface creating a flowing layer first in this region of the medium which then initiates the flow of the whole medium.

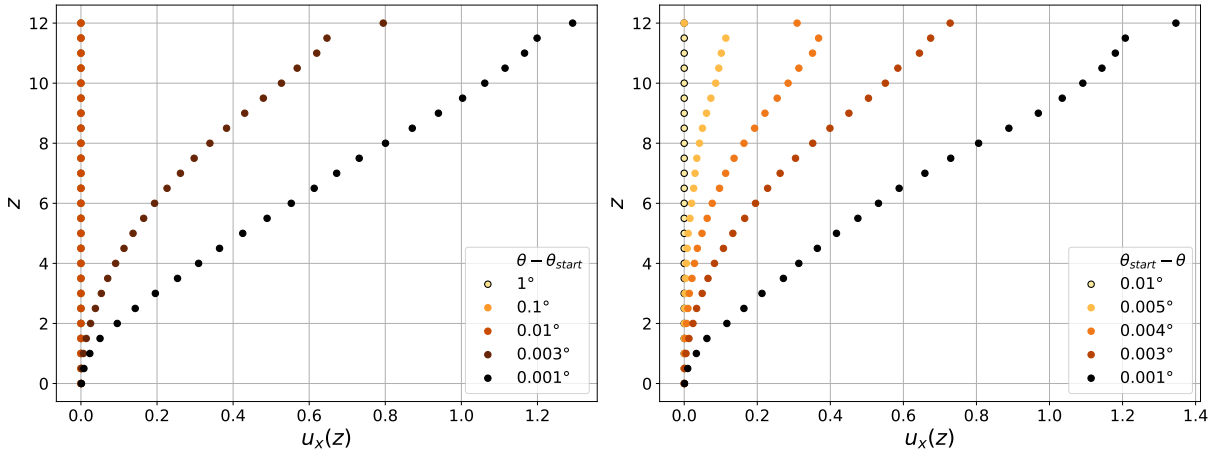

(a) (b)

Figure 4.14 – (a) Velocity profiles at $\mu_p = 0.5$ at various angles in the static regime at unjamming for thin layer, $h/d = 10$. (b) Instant velocity profiles at $\mu_p = 0.5$ with refined angles in the static regime at unjamming for thin layer, $h/d = 10$.

Velocity profiles at unjamming

The velocity profiles are plotted at various angles within the unjamming transition on Figure 4.14a. Similarly to jamming, the angles are expressed as $\theta - \theta_{start}$ with the angle differences related to the avalanche angle here. First, we choose to calculate θ_{start} in a way that at $\theta - \theta_{start} = 0.001°$, the velocity profile has similar values that the flowing state at the highest distance $\theta - \theta_{stop} = 1°$ on Figure 4.9. It enables us to compare the velocity profiles evolution at jamming and at unjamming with the same initial and final states, i.e. the same initial and final velocity values at the free surface.
The profiles demonstrate a significant difference between the static state, at $\theta - \theta_{start} = 1°$, and the initiation of flow at $\theta - \theta_{start} = 0.001°$. It also shows that the initiation of flow is a quicker process than the cessation of flow since no continuous variations are observe between the static state and the start of flow when increasing the angles between 1° and 0.003° from the avalanche angle. In order to observe the continuous evolution of the flowing layer, we need to refine the angle differences between 0.01° and 0.001°. The corresponding profiles are plotted on Figure 4.14b. This figure shows that despite a quicker transient process of destabilisation than stabilisation, the evolution is similar, yet symmetric, than for the jamming process with a flowing layer near the free surface that tends to destabilise the stable grains below. This type of velocity profile's shape was predicted by the theory of *Aranson et al.* (2008) near the onset of flow and were also observed by *Silbert et al.* (2001).

Packing fraction profiles at unjamming

Packing fraction profiles are plotted at unjamming on Figure 4.15a. The figure does not enable to observe significant evolution of ϕ. Nevertheless, slight variations are observed especially where the flow starts, i.e. close to the free surface. However, these variations does not capture a sharp evolution in the packing density of the medium when the flow starts.

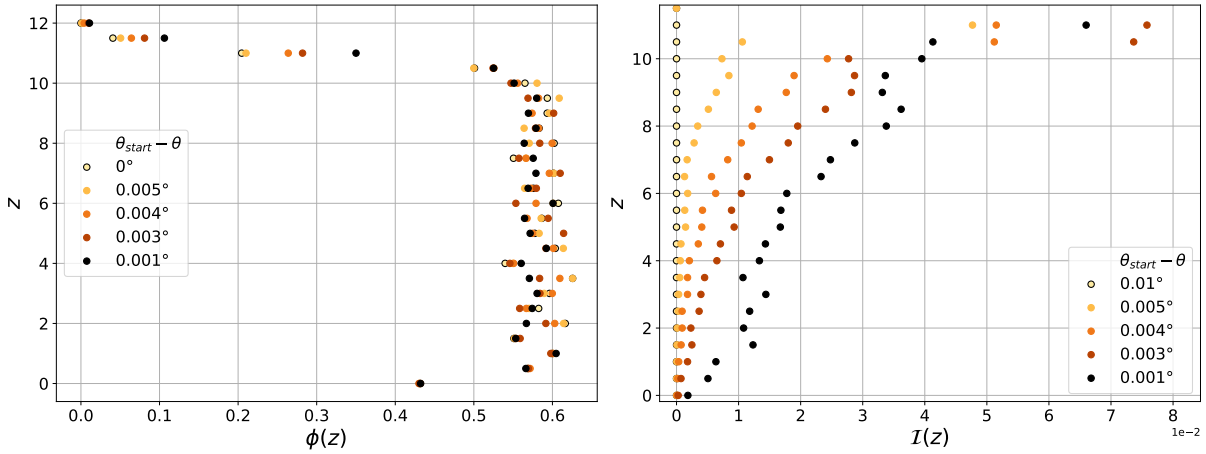

(a) (b)

Figure 4.15 – Instantaneous velocity profiles (a) and inertial number profiles (b) at $\mu_p = 0.5$ and various angles in the static regime at unjamming for thin layer, $h/d = 10$.

Inertial number profiles at unjamming

By contrast with packing fraction, the inertial number profiles at unjamming, plotted on Figure 4.15b increases at unjamming. It highlights that the flow quickly starts to become inertial with $\mathcal{I} \approx 2 \times 10^{-2}$ within $100\sqrt{d/g}$ when it dropped of the same amount within $10^4\sqrt{d/g}$ at jamming. This time difference is probably a direct consequence of hysteresis since θ_{start} is higher than θ_{stop}, the shear stress is relatively higher at unjamming than at jamming accelerating the transient process.

Coordination number profiles at unjamming

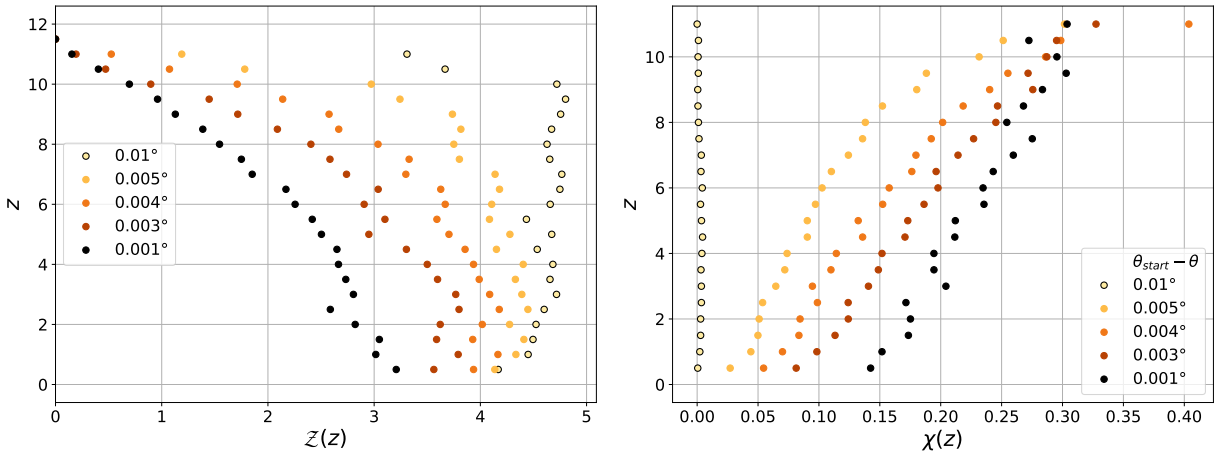

(a) (b)

Figure 4.16 – (a) Instant coordination number profiles and (b) instant fraction of sliding contacts profiles at $\mu_p = 0.5$ at various angles in the static regime at unjamming for thin layer, $h/d = 10$.

The evolution of the coordination number profile at unjamming is plotted on Figure 4.16a. The figure shows first, a larger loss of contact at the free surface than at the bulk for $\theta - \theta_{start} = 0.005°$, evolving into a quasi-linear profile when the flow is well initiated at $\theta - \theta_{start} = 0.001°$. Although quicker, the evolution of the number of contacts within the layer at unjamming also appears as the symmetric of its evolution at jamming.

Sliding contacts proportion profiles at unjamming

Figure 4.16b presents the evolution of the sliding contact proportion profiles at unjammig. In the static state, at $\theta - \theta_{start} = 0.01°$, it shows first a low but finite proportion of contacts that slides in the bulk as depicted in Section 4.1.2, in the static regime. Then, the sliding contact proportion profile abruptly drops to its quasi-linear shape at $\theta - \theta_{start} = 0.005°$ with a larger percentage of sliding contacts near the free surface than near the bottom plane. By contrast to the coordination number, the profiles of sliding contact proportion at unjamming, presented on Figure 4.16b, do not evolve as its symmetric at jamming. Indeed, here the contacts initially slides in the bulk and near the bottom plane conversely to the jamming where the last contacts that slides before it completely jams are located near the free surface. In addition, the sliding contact proportion increases more suddenly and quickly than the other quantities. It suggests that a non-negligible proportion of contacts are on the verge to slide, but are still stable in the static regime, thus the unjamming of the layer quickly destabilises them and leads to a destabilisation of the assembly supporting the phenomenology proposed above.

In conclusion, this Section brought information about the dynamic of the granular layer in the dense flow regime and at both jamming and unjamming transitions. In the flowing state far from jamming, the flow is steady and established within the layer and the sources of dissipation at the contact scale balanced the gravity drive imposition. Heterogeneities are nonetheless observed both at the free surface and the bottom plane. These heterogeneities have more effect on the bulk flow for thin layer than thicker ones since the distance between the boundary conditions is thinner. When the shear to normal stress, gravity driven imposition, does not balance the dissipation processes, the flow approach jamming, significantly decreases and displays a transient observed in the evolution and shapes of the various variables profiles. There is a growing region that tends to staticity near the bottom plane. In this region an increase of contacts that are tangentially stabilised is observed, suggesting that dissipation processes are becoming stronger than shear. Near the free surface, grains are less constrains in the motion and continues to flow when approaching the jamming transition. However, the static region diffuses through the layer upon the transition. When the layer is fully static and the stress loading increases, the medium does not dynamically response to stress variations. The tangential force network however displays local plasticity at the contact scale, especially near the bottom plane, leading to rearrangements that destabilise the grains near the free surface and start flowing. As a consequence, the contacts on the verge to slide quickly destabilises initiating the faster unjamming transient leading ultimately the whole layer to flow.

This section allowed us to qualitatively describe the evolution of the grain layer response to inclination angle variations in a reference case. The granular states and both the cessation and initiation of flow were described using macroscopic state variables as well

as descriptors of the micro-structure. It led us to propose a phenomenology for both the jamming and unjamming transitions coherently with results from the literature.

4.3 Hysteretic cycles of macroscopic and micro-structure state variable on an inclined plane

The objective here is to measure the evolution observed, in the above sections, for the several state variables in both regimes and at both transitions. Although the flow has be depicted to be heterogeneous, both macro and micro variables have demonstrated significant evolution with stress variations at transitions and in the dense state. As such, in this section, the variables studied within the grain layer in the previous Sections 4.1 and 4.2 are averaged in depth and plotted versus the inclination angle. In particular, hysteresis cycles are observed on the inertial number and the volume fraction on one hand. On the other hand hysteresis cycles of the coordination number, the fraction of sliding contacts and the contact anisotropy are discussed. Characteristic values are highlighted and will be used for a qualitative and quantitative study varying sources of dissipation at the contact scale in the following section.

4.3.1 Hysteretic cycles of the inertial number and the volume fraction: highlighting granular regimes, hysteresis and dilatancy

The simulation is the same that in the previous section, following the protocol defined in Section 3.4.3 and displayed by Figure 3.7 for classical inter-particle friction coefficient $\mu_p = 0.5$ in the dry case. Starting from a flowing state, the angle of the inclined plane is progressively and continuously decreased down to the cessation of the flow, before ramping up the inclination angle until the flow starts. Measuring the mean inertial number associated with the granular flow, it is possible to observe the hysteretic loop in the context of the $\mu(\mathcal{I})$ rheology, Figure 4.17a. In this framework, the granular rheology can be described in terms of the shear-to-normal stress ratio as a unique function of the inertial number, see Equation (1.7). The depth average instant inertial number I is derived from Equation (4.5):

$$\mathcal{I}(t) = \frac{1}{h}\int_0^h \mathcal{I}(z,t)\,dz, \tag{4.9}$$

For steady uniform flow on the an inclined plane, the shear-to-normal stress ratio is directly set by the inclination angle of the plane, see Equation (3.45). Figure 4.17a shows a typical hysteretic loop on $\mu(\mathcal{I})$ that demonstrates the asymmetry of the transition. Decreasing the inclination angle, the corresponding inertial number decreases. The variations of inertial number with the imposed stress is a characterisation of the flowing state that is defined as a state in which a dynamic is observe at the macroscopic scale, i.e. $\mathcal{I} > 0$ as seen in Section 4.1. Oscillations of the inertial number are also a signature of the flowing regime. In this regime, state variables are oscillating around steady state values. The decrease of inertial number with the angle of inclination shows that the lower is the plane angle (or the shear to normal stress ratio) the less inertial is the flowing layer. The inertial number then eventually drops to zero at stopping angle, $\mu = \mu_{stop} = tan(\theta_{stop})$.

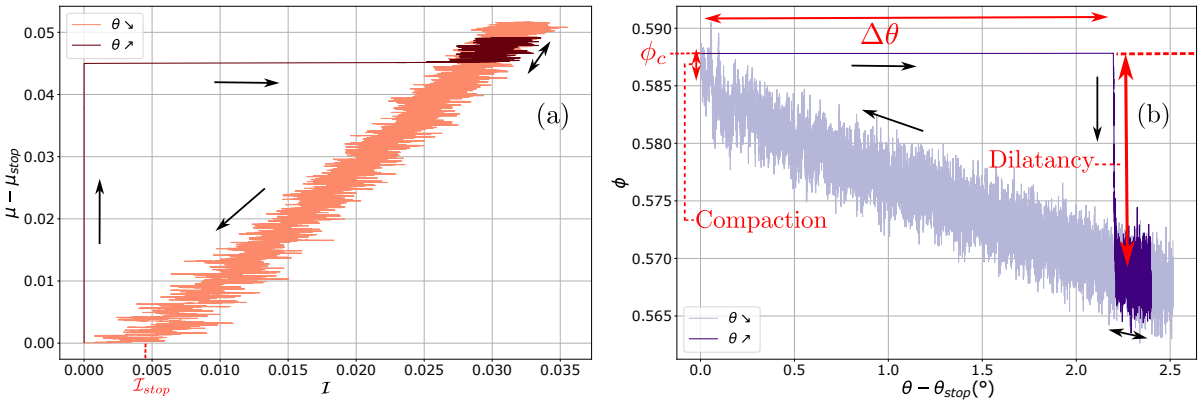

Figure 4.17 – (a) Hysteretic loop of the relative shear-to-normal stress ratio $\mu(I) - \mu_{stop}$ as function of the inertial number, $\mathcal{I}$, for inter-particle friction $\mu_p = 0.5$ leading to $\mu_{stop} = 0.39$. (b) Hysteretic loop of the solid fraction ϕ as function of the relative inclination angle $\theta - \theta_{stop}$ for inter-particle friction $\mu_p = 0.5$ leading to $\theta_{stop} = 21.47°$. The arrows as much as the color and legend indicates for each plots the stress path within hysteretic cycles.

The cessation of flow, or the static state, is then defined as a state where no dynamic is observe at the macroscopic scale, see Section 4.1. In this regime, the inertial number is constant and equal to zero, as shown by Figures 3.7 and 4.17a. The stress path is then reversed and the inclination angle is progressively increased. The granular medium remains static up to the avalanche angle, where the flow comes back to the initial $\mu(I)$ branch. The difference between the stress ratio at avalanche and stopping transitions characterizes the hysteresis, $\Delta\mu = \mu_{start} - \mu_{stop} = tan(\theta_{start}) - tan(\theta_{stop})$.
The critical inertial number at which the medium stops flowing is $\mathcal{I}_{stop} \approx 5.10^{-3}$. This value is consistent with results from other simulations and experiments on the inclined plane with similar parameters (*GDR MiDi*, 2004; *Cassar et al.*, 2005).

For the sake of simplicity and for a more intuitive view of the results, the data will be plotted in the following in terms of inclination angle θ. It is classical to consider the solid volume fraction variation close to the fluid-like to solid-like behavior transition (*Xu and O'Hern*, 2006; *Peyneau and Roux*, 2008). It is interesting to note that it is equivalent as considering the $\mu(\mathcal{I})$ rheology in terms of solid volume fraction $\mu(\phi)$, as done in the literature (*Da Cruz et al.*, 2005). Figure 4.17b shows the hysteretic loop observed for the volume fraction. As the inclination angle decreases, the granular flow becomes denser, up to the critical solid volume fraction at which the medium comes to rest. Reversing the loading, the solid volume fraction stays constant up to the onset of motion at larger inclination angle. Hysteresis is characterized here as the difference between the stress ratio at avalanche and stopping angles $\Delta\theta = \theta_{start} - \theta_{stop}$.
The solid volume fraction displays a discontinuity at the initiation of flow, $\Delta\phi_{start}$. This dicontinuity is a signature of Reynolds dilatancy. Indeed, a static granular system dilates when yielding under shear in order to flow (*Bagnold*, 1966; *Andreotti et al.*, 2013; *Behringer and Chakraborty*, 2019). This effect is observed here with a clear discontinuity at the avalanche angle showing that the medium dilates when the avalanche angle is reached.

Conversely to the initiation of flow, the granular packing density does not seem to exhibit a significant discontinuity in the transient when coming to rest. Nevertheless, there is a slight gap between the average evolution of packing density in the flowing regime near jamming and the constant critical value in the jammed regime, $\Delta\phi_{stop}$. This slight variation can be interpreted as compaction of the granular system when the flow stops.

4.3.2 Hysteretic cycles of descriptors of the micro-structure

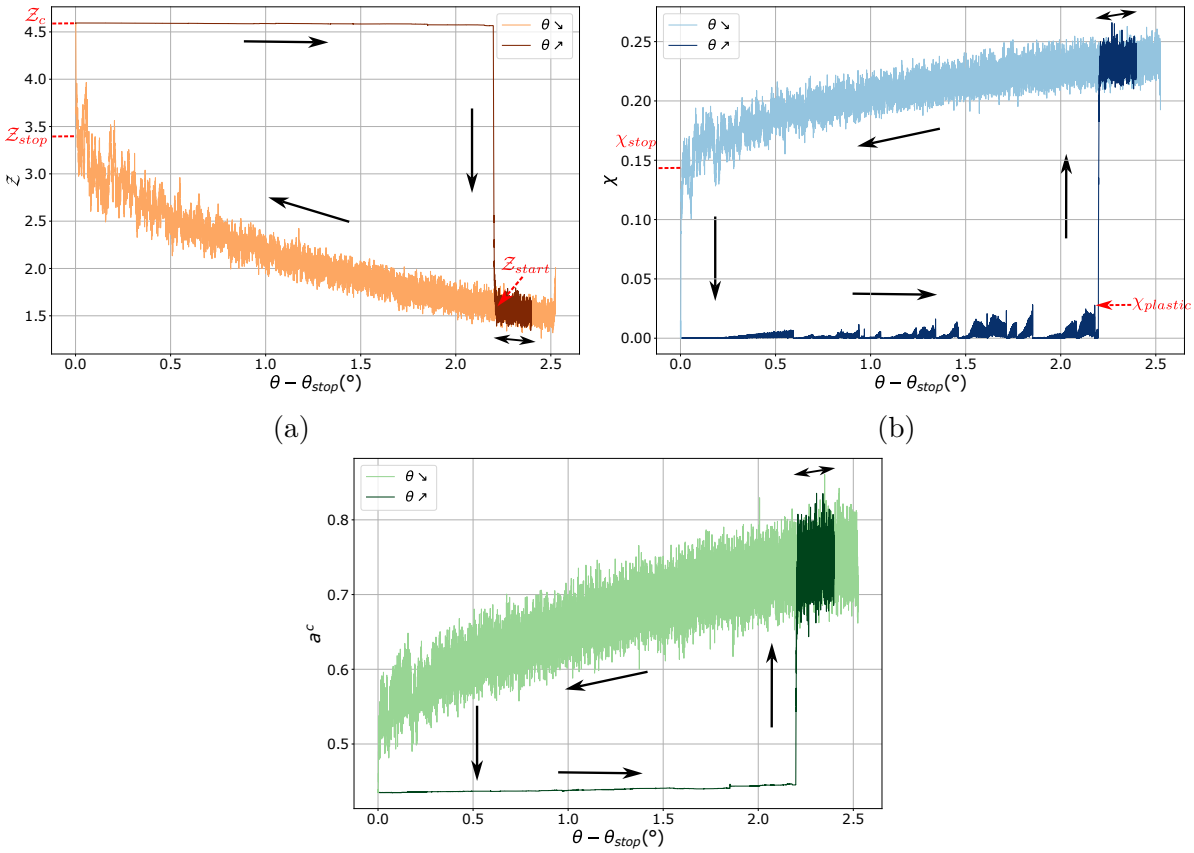

Figure 4.18 – (a) Hysteretic cycle of the average coordination number per particle $\mathcal{Z}$. (b) Hysteretic cycle of the fraction of sliding contact χ. (c) Hysteretic cycle of the amplitude of contact anisotropy a^c. All cycles are plotted for an inter-particle friction coefficient of $\mu_p = 0.5$ in the dry case.

In order to look further into the evolution of the granular medium response to external stress on an inclined plane, especially near jamming and unjamming transitions, several variables that characterize the behavior of the granular micro-structure at first order are measured within simulations. The first one is the coordination number, $\mathcal{Z}$, that calculates the average number of contacts per particle. The coordination number is not strictly a depth average of the profile of Equation (4.7), it is defined from the whole sample as:

$$\mathcal{Z} = \frac{2N_c^{dyn-dyn} + N_c^{dyn-plane}}{N_p^{dyn}}. \tag{4.10}$$

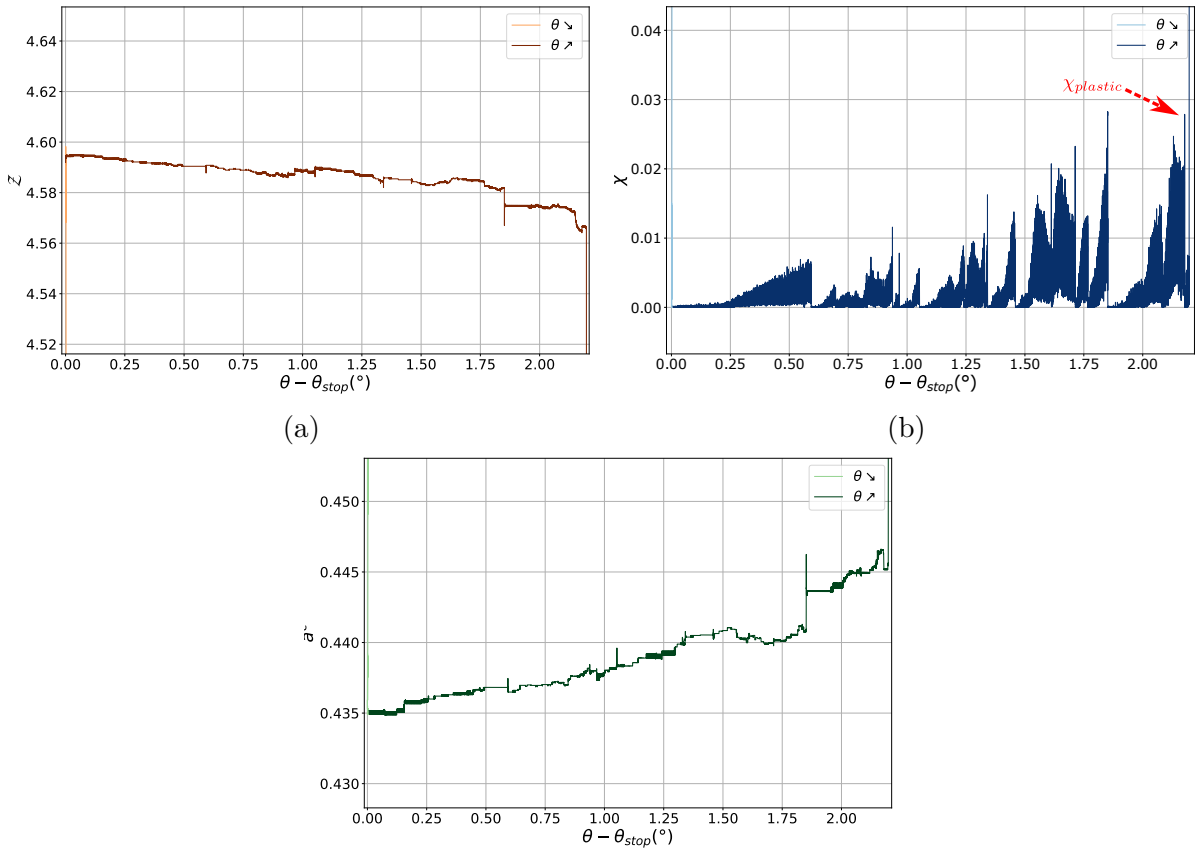

Figure 4.19 – (a) Zoom of Figure 4.18a in the static state. Some slights variations of $\mathcal{Z}$ demonstrate rearrangement within the system. (b) Zoom of Figure 4.18b in the static state. Variations of χ demonstrate plasticity at the contact scale within the system. (c) Zoom of Figure 4.18c in the static state. Variations of a^c demonstrate an evolution of anisotropy with the angle.

In the one hand, the calculation consider the contacts between two dynamic particles, i.e. particles that are allowed to be in motion in the system, $N_c^{dyn-dyn}$ which is counted twice to account for both particles. In the other hand a contact between a dynamic particle and a fixed particle, glued at the bottom, that constituted the plane, $N_c^{dyn-plane}$, is only considered once. This calculation of the coordination number allows us to consider the average number of contacts by particle that constitute the flowing layer.

The typical hysteretic cycle of coordination number, or in other words the evolution of

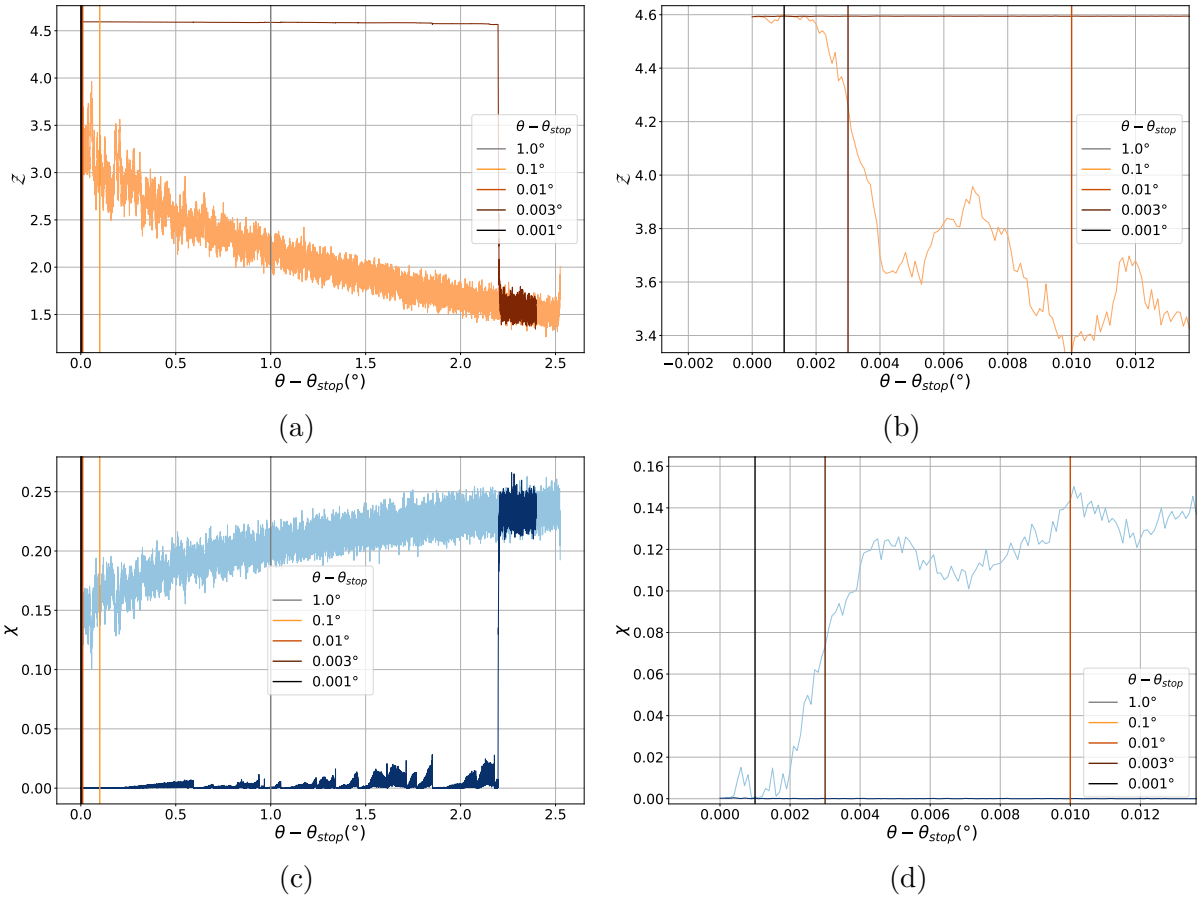

Figure 4.20 – (a) Hysteretic cycle of the average coordination number per particle $\mathcal{Z}$ with vertical lines corresponding to the angles at which the coordination number profiles are plotted on Figure 4.12a near jamming. (b) Zoom of the latter near jamming. (c) Hysteretic cycle of the fraction of sliding contact χ with vertical lines corresponding to the angles at which the coordination number profiles are plotted on Figure 4.12b near jamming. (d) Zoom of the latter near jamming.

coordination number with the plane angle within a simulation, is plotted on Figure 4.18a. Similarly to packing fraction, the coordination number is increasing when the plane angle is decreasing. This evolution of the coordination number is the micro-structure signature of the increasing packing density of the flowing layer when the plane angle is decreased. It goes hand in hand with a reduction in the layer dynamic, i.e. reduction of $\mathcal{I}$ with θ. Then the coordination number drops from $\mathcal{Z}_{stop}$ to a critical constant value $\mathcal{Z}_c$ when the media stops flowing at $\theta = \theta_{stop}$. The critical coordination number in the jammed state is constant but some little variations occurs when zooming on its evolution with the

angle in the jammed state, see Figure 4.19a. These little variations are signatures of local rearrangement that slightly influence the value of the average number of contacts in the system. In addition, the average number of contacts slightly decrease when increasing the angle in the static state. These variations are much lower than variations in the flowing state but still demonstrate a slight evolution of the structure due to increasing imposed shear stress.
When the medium starts flowing again at $\theta = \theta_{start}$, the average number of contacts suddenly drops at $\mathcal{Z}_{start}$ to the initial branch of coordination number where it varies with the angle. Similarly to the packing density, the discontinuity of coordination number $\Delta\mathcal{Z}_{start} = \mathcal{Z}_c - \mathcal{Z}_{start}$ that quantify the drop of coordination number when the media starts flowing at the avalanche angle, is very sharp. This is a signature of dilatancy effect at the scale of the contact network. Conversely to the volume fraction, the coordination number also displays a sharp discontinuity at the cessation of flow, $\Delta\mathcal{Z}_{stop} = \mathcal{Z}_c - \mathcal{Z}_{stop}$. This discontinuity is a signature of the compaction of the contact network when the medium jams. To compare the coordination number profiles, plotted near jamming on Figure 4.12a in the previous Section 4.2, with the first-order average value, we plot on the hysteretic cycle vertical lines at the angles where the profiles are plotted, see Figures 4.20a and 4.20b. Figure 4.20b show that the profile at $\theta - \theta_{stop} = 0.01°$ is plotted before the transient drop while the one at $\theta - \theta_{stop} = 0.003°$ is within the gap and the one at $\theta - \theta_{stop} = 0.001°$ is after the gap. As such, this discontinuity is also the signature of the significant increase of the amount of contacts in the bulk and especially near the free-surface observed between the profiles approaching jamming. Despite no clear discontinuity was observed on the volume fraction, the presence of a sharp drop of coordination number is consistent with the observation of a first-order phase transition at jamming for frictional grains on a rough inclined (*Liu and Nagel*, 2010; *Pan et al.*, 2023).

Another interesting variable that allows us to describe the evolution of the tangential contact network with imposed stress is the fraction of sliding contacts χ. This fraction is, similarly to the space-averaged coordination number, not strictly a depth average of the profile of Equation (4.1.1), it is defined as:

$$\chi = \frac{N_c^{sliding}}{N_c^{tot}}, \tag{4.11}$$

with $N_c^{sliding}$ the number of contact for which the tangential contact force has reached the Coulomb criterion and N_c^{tot} the total amount of contacts (note that $N_c^{tot} = N_c^{dyn-dyn} + N_c^{dyn-plane}$).
The classical hysteretic cycle of fraction of sliding contacts is presented on Figure 4.18b. The fraction of sliding contacts is slightly decreasing with the plane angle from $\chi = 0.23$ at $\theta_{stop} + 2.5°$ until it reaches about $\chi_{stop} = 0.15$ at the cessation of flow. At that moment, the fraction of sliding contacts drops to zero in the jammed state. When the medium is static no tangential contacts are sliding at first. Then when increasing the plane angle some contacts are sliding which slighlty increases the fraction χ up to about 3%. Figure 4.19b presents the evolution of χ in the jamming state. The figure shows some peaks of sliding contacts which amplitudes are increasingly growing with the angle until the medium flows again and χ reaches the initial branch. These increasing peaks of sliding contact percentage are a signature of rearrangements within the system and specifically of

local plasticity of the granular medium as presented by *Staron et al.* (2002) and observed in the profiles of χ. Indeed, when contacts slides the medium is locally plastic which enables small displacements and rearrangements in the assembly.

A new quantity introduced here is a measure of the anisotropy of the contact network. The amplitude of contact anisotropy, a^c is defined as proposed by *Srivastava et al.* (2019, 2022) as the second invariant the contact anisotropy tensor, A^c, related to the deviatoric part of the fabric tensor, see Section 1.4.3. This second-order tensor provides information on the anisotropy of the orientation of contacts with respect to the 3 directions of space, see Appendix A.3 for more details on the definition of this tensor. Its amplitude is given by:

$$a^c = \frac{1}{2}\sqrt{A^c : A^c}. \tag{4.12}$$

With $A^c : A^c$ the doubly-contracted product of the contact anisotropy tensor, it can also be expressed as $tr(A^c \cdot A^c)$. This quantity provides information on the anisotropy of the contact network with no precision on the preferential directions of anisotropy. Nevertheless, higher a^c means higher anisotropic orientation of contacts. In other words, higher anisotropy means higher amount of contacts orientations that are not aligned with the principal directions of space.
The contact anisotropy is plotted versus the plane inclination angle within a simulation on Figure 4.18c. We notice first, that the level of anisotropy is decreasing with the plane angle which is coherent with the idea that higher angle implies higher anisotropy due to shear stress leading to an increase of contact orientations in directions orthogonal to the three principal directions.
In addition, it is constant in the static state compared to the variations in the flowing state. Nevertheless, it slightly increases with the angle in the static state as shown by Figure 4.19c. Moreover, the level of anisotropy is lower in the static regime that in the flowing regime. This shows that the flowing regime is more anisotropic than the static regime at a given external stress.

In order to measure a degree of staticity, see Section 2.3 and Equation (2.10), in the

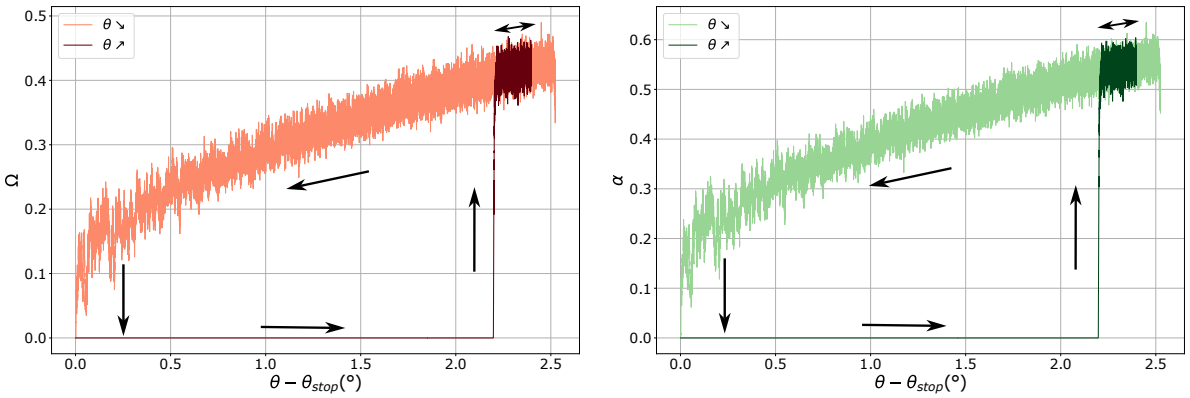

(a) (b)

Figure 4.21 – (a) Hysteretic cycle of the fraction of particles free in their rotation Ω. (b) Hysteretic cycle of the fraction of particles with one or less contacts α.

system at the approach from jamming and unjamming transitions, we also calculated the

fraction of particles free to rotate Ω in the system. This variable is calculated as:

$$\Omega = \frac{N_{free}}{N_{dyn}}, \tag{4.13}$$

with N_{free} the number of particles free in their rotation. This quantity is calculated considering the particles with no contacts and the particles for which all contacts are sliding. The hysteretic cycle of Ω is plotted on Figure 4.21a. The fraction of particles that are free to rotate decreases with the angle from about 40% in the flowing state near the avalanche angle down to about 10% near jamming. Although non-negligible fraction of contacts are sliding in the static state, no particles are fully free to rotate.

Finally, the last variable that will be needed to calculate a staticity criterion is the fraction of particles that have one or less contacts α. This variable is plotted on Figure 4.21b. This quantity decreases with the angle as Ω. Interestingly, although the system is in the dense flow regime, a non-negligible fraction of particles have one or less contacts from about 55% near the avalanche angle down to about 15% near jamming.

4.3.3 Staticity criterion

As depicted in Chapter 4, it is possible to calculate an isostatic coordination number value, $\mathcal{Z}_{iso}$, from the Maxwell criterion of staticity, see Equation (2.10). It corresponds to the number of constrained the system must gain by contacts in order to balance the number of degrees of freedom. Such idea was proposed in several works (*Silbert et al.*, 2002a; *Henkes et al.*, 2010; *Song et al.*, 2008) to characterize the mechanical degree of staticity of the system. Theoretically, if the average number of contacts, $\mathcal{Z}$, is equal to the isostatic value $\mathcal{Z}_{iso}$, the system is isostatic hence stable. The idea here is to plot the evolution of $\mathcal{Z}_{iso}$ within the simulation, and normalizing its value by the measured average number of contacts $\mathcal{Z}$. This ratio is plotted on Figures 4.22a and 4.22b. we observe on Figure 4.22a, that in the flowing regime, $\mathcal{Z}_{iso}/\mathcal{Z} > 1$ meaning that the system is hypostatic and the effective number of contacts is too low to match the isostatic value needed to reach the static state. The ratio linearly decreases with the angle down to about 1.2 in average and approaches 1 with fluctuations near jamming, see Figure 4.22b. It then drops, with a sharp discontinuity, below unity at about 0.87, meaning that the average number of contacts is above the isostatic value $\mathcal{Z}_{iso} = 4$ in the static state right after jamming ($\Omega = \chi = 0$). As such, the medium stops flowing in an hyperstatic state with respect to mechanical equilibrium. In the static state the system remains hyperstatic and the ratio increases sharply above unity only at unjamming. Hence, the ratio only reaches unity at transitions when it sharply evolves in the transient discontinuity but is always hypostatic in the flowing regime and hyperstatic in the static regime. As a consequence, it seems non-trivial to possibly predict the stress conditions of jamming and unjamming by calculating the isostatic coordination number in the various granular regimes. Indeed, the accession to the static state cannot be defined as a consequence of mechanical stability in the whole system when the number of constraints match the number of degrees of freedom at first order, i.e. when $\mathcal{Z}_{iso}/\mathcal{Z} = 1$ (*Silbert et al.*, 2002a). One of the possibilities to explain this departure lies in the calculation of $\mathcal{Z}_{iso}$ with Equation (2.10) that consider that each particle has a normal force that contributes to the number of normal force

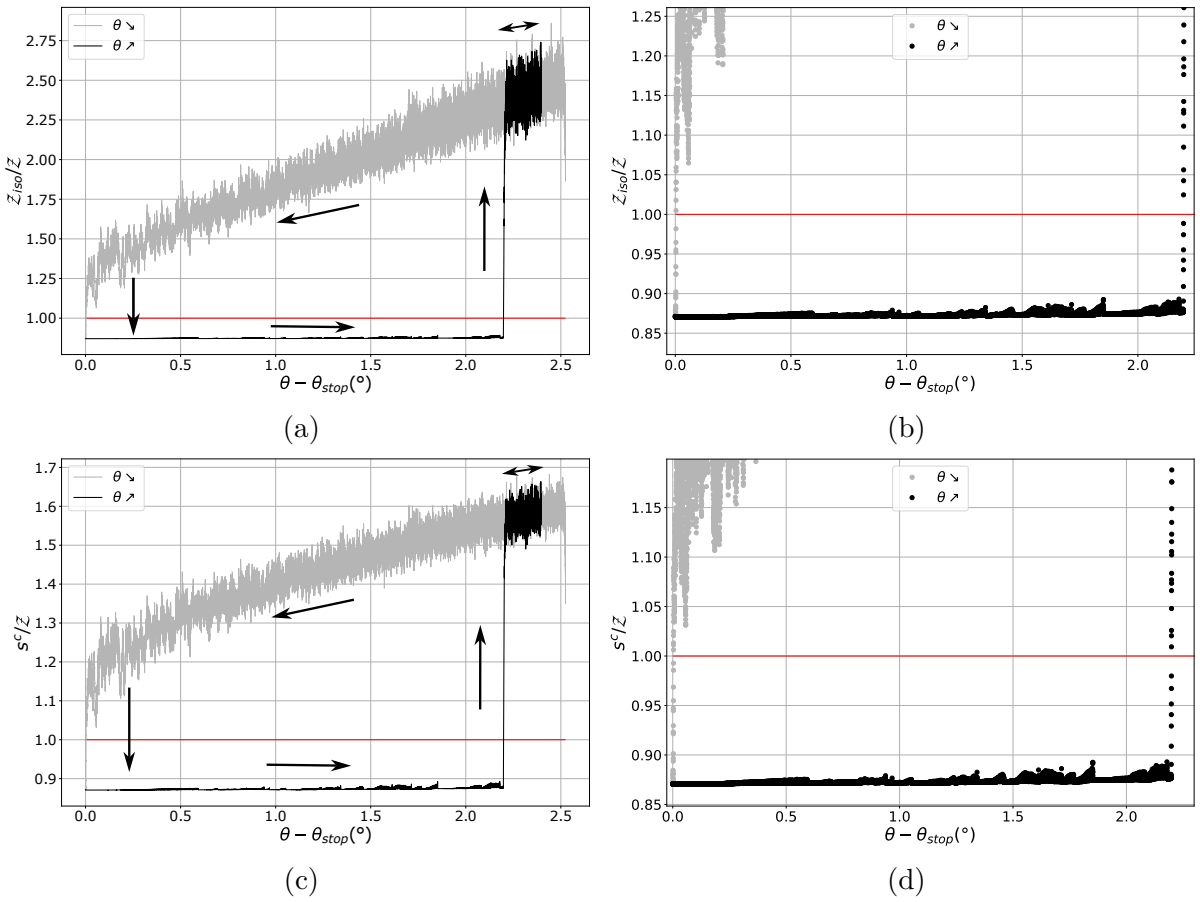

Figure 4.22 – (a) Hysteretic cycle of the ratio between the isostatic coordination number $\mathcal{Z}_{iso}$ from Equation (2.10) and the averaged number of contacts $\mathcal{Z}$. (b) Zoom of the latter near 1. (c) Hysteretic cycle of the ratio between the staticity index s^c from Equation (4.14) and the averaged number of contacts $\mathcal{Z}$. (d) Zoom of the latter near 1.

balanced equations and then mechanically constrained the system. A particle with no contacts does not contribute to mechanical equilibrium of the whole system since it has no normal force balanced equation. A particle with one contact does have a normal contact force that does not constrained the system since a particle needs at least two contacts to be stable. As such, if the ratio of particles that have one or less contacts is non-negligible, which is the case in the flowing regime, see Figure 4.21b, the number of normal force balanced equations became $E_f = 3N_{dyn}(1-\alpha)$ and the staticity criterion adapted from Equation (2.10) is written:

$$s^c = \frac{3(1-\alpha)+3(1-\Omega)}{1/2+(1-\chi)}. \tag{4.14}$$

Similarly to $\mathcal{Z}_{iso}$, what is interesting is to plot the ratio between s^c and the average number of contacts in the system $\mathcal{Z}$. The ratio evolution with the angle is presented on Figure 4.22c. This ratio is slightly lower in the flowing regime than $\mathcal{Z}_{iso}/\mathcal{Z}$ since s^c is lower than $\mathcal{Z}_{iso}$ due to the reduction of the normal force balanced equation through $1-\alpha$. As a consequence, the ratio $s^c/\mathcal{Z}$ is closer to unity near jamming but still cross unity only in the transient to static regime. In the static state, since $\alpha = 0$, the variations are the same between both ratios. The increase observed on the number of degrees of freedom, due to the increase of the ratio of sliding contacts, do not match the critical average number of contacts $\mathcal{Z}_c$ and unity is reached for both staticity ratios only in the transient.
Finally, although this generalisation of first-order staticity criterion, i.e. considering the mechanical system as a whole, brings information on how much the average number of contacts balanced the number of degrees of freedom in the system, it cannot predict the conditions of transitions, i.e. the critical angles at which the system become mechanically static from the flowing state and loses mechanical stability in the static state. This result suggests that mechanical staticity criterion is then distributed in the system, with regions where the system is isostatic or hyperstatic, and regions where the system is hypostatic, leading to a globally unstable hypostatic system in the flowing regime and hyperstatic stable system in the static regime. In order to demonstrate that, one may look at the spatial distribution of staticity criterion within the depth of the layer or at the scale of grains equivalently to what *Henkes et al.* (2016) developed using the pebbel game to track rigid clusters within the system at the approach to jamming.

4.4 Contact dissipation effects: friction and collisions

The phenomenology, proposed in Section 4.2, associated to the jamming and unjamming transitions involved in hysteresis shows the key role of contacts between grains. It suggests an influence of sources of energy dissipation at the contact scale.

Indeed, interactions at the contact scale plays a major role on the dynamics and static of grains assemblies as well as on the jamming and unjamming transitions and hysteresis, see Sections 2.3, 2.5 and 2.6 of Chapter 2. Especially, dissipation processes occurs during collisions, characterized by the restitution coefficient e_N, and by inter-particle friction when contacts last, characterized by the inter-particle friction coefficient μ_p. *DeGiuli et al.* (2016) have shown a complex non-trivial combination of both dissipation mechanisms on the flowing state even at the limit of quasi-static flow, i.e. near the jamming

transition. This suggests a possible complex effect of both μ_p and e_N on the critical angles and hysteresis.

In this section, we focus on the combined influence of inter-particle friction and restitution coefficient on the hysteretic cycles of the several variables. First, a qualitative analyse is done on the influence of the the inter-particle friction coefficient, μ_p, on the state variables within their loading cycles (defined in the previous Section). To do so, the inter-particle friction coefficient is first varied at a constant restitution coefficient $e_N = 0.9$, between $\mu_p = 0.5$ (reference case) and $\mu_p = 0.2$.
Then, the influence of the restitution coefficient is similarly qualitatively studied by varying e_N between $e_N \in [0.1, 0.5, 0.9]$, at both inter-particle friction coefficient 0.2 and 0.5. Quantitative results are finally presented for the restitution coefficient.

4.4.1 Qualitative evolution of the hysteretic cycles with inter-particle friction

The evolution of the hysteretic cycles of the macroscopic state variables, $\mathcal{I}$ and ϕ, and first order descriptors of the micro-structure, $\mathcal{Z}$, χ and a^c, are presented on Figure 4.23. On this figure, only two inter-particle friction coefficients are plotted, $\mu_p = 0.5$ and $\mu_p = 0.2$, in order to look qualitatively at the effect of friction. Conversely to the previous Section, the hysteretic cycles are not plotted versus $\theta - \theta_{stop}$ but versus θ. This allows us to see the evolution of the average variables at constant inclination angle θ between both inter-particle friction coefficient and to observe the evolution of the critical angles θ_{stop} and θ_{start}.
Two main results emerge from all of the plots of Figure 4.23: (i) We can see on each Figures that the stopping angle θ_{stop}, or stopping stress ratio μ_{stop}, and the avalanche angle θ_{start}, or starting stress ratio μ_{start}, both decrease when decreasing friction between grains.
(ii) Also, hysteresis is lower when decreasing friction between grains.
The first result, (i), shows that lowering friction between grains lowers significantly the angles at which the system is stable which means that the granular stability highly depends on friction. The second result show that the asymmetry in the transitions angles, or hysteresis, when defined as an absolute difference of angles $\Delta\theta = \theta_{start} - \theta_{stop}$ also depends on the friction between grains. Although this result needs a quantitative systematic study to be robust, which will be done in the following Chapter 5, it remains a first signature of the major role friction plays in this phenomenon.

In order to give a first qualitative analysis of the latter results, we go with more details into the analyse of each plots of Figure 4.23.
First, the macroscopic state variables $\mathcal{I}$ and ϕ, are plotted on Figures 4.23a and 4.23b. In the flowing regime at a given angle, for example at 22° or 23°, the inertial number is more than two times higher when decreasing the inter-particle friction coefficient. At the same time, the packing fraction, ϕ slightly decreases when reducing friction between grains. Hence, in the flowing state, reducing friction in the same stress conditions appears to increase the dynamic of the layer that is less compact. This behavior is observed at the micro-structure scale since the coordination number $\mathcal{Z}$ cycles for $\mu_p = 0.5$ and 0.2, plotted

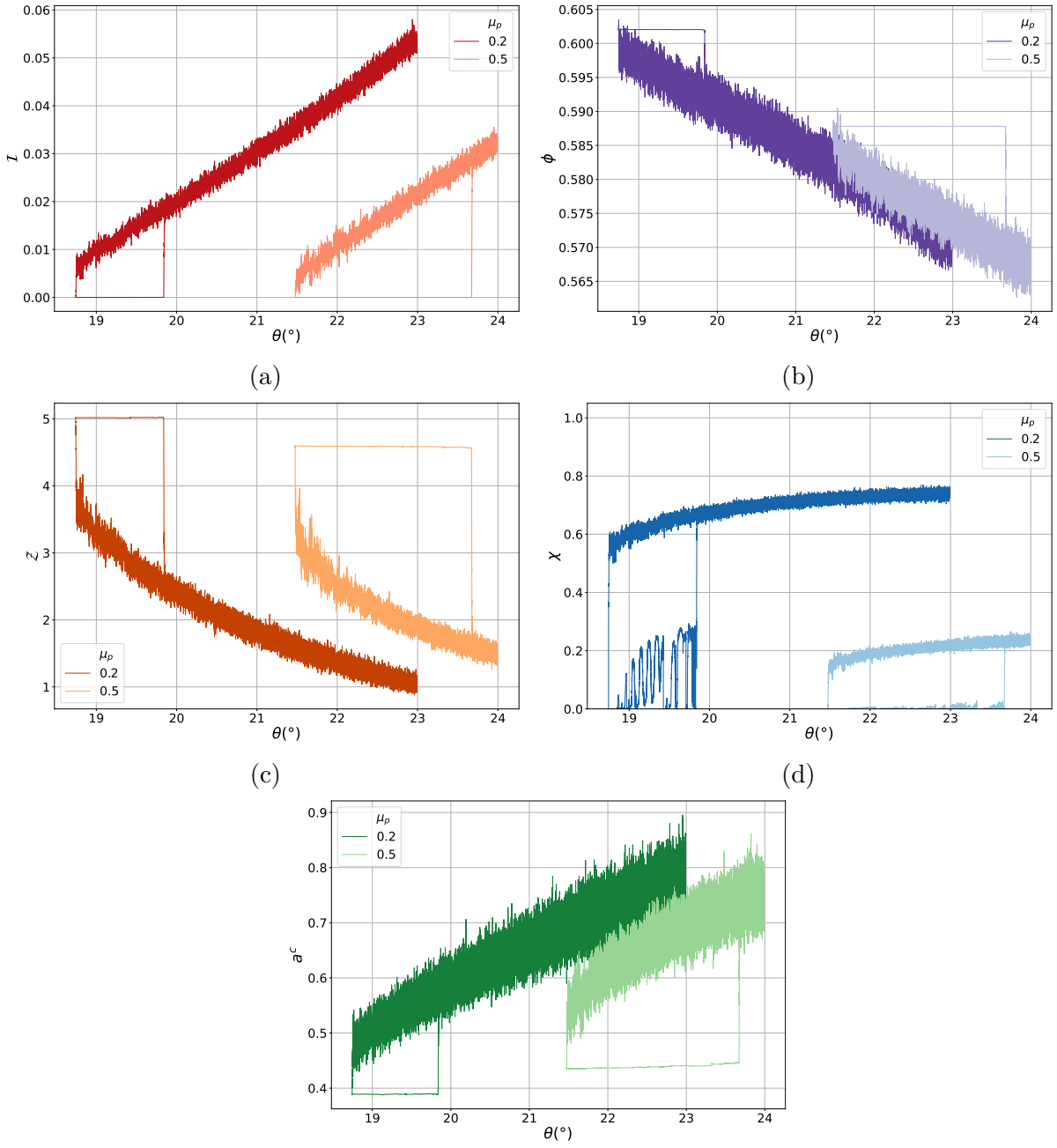

Figure 4.23 – (a) Hysteretic cycle of the inertial number as a function of the inclination angle for inter-particle friction $\mu_p = 0.5$ and $\mu_p = 0.2$. (b) Hysteretic cycle of the solid volume fraction ϕ as function of the inclination angle for inter-particle friction $\mu_p = 0.5$ and $\mu_p = 0.2$. (c) Hysteretic cycle of the average coordination number per particle $\mathcal{Z}$ for inter-particle friction $\mu_p = 0.5$ and $\mu_p = 0.2$. (d) Hysteretic cycle of the fraction of sliding contact χ for inter-particle friction $\mu_p = 0.5$ and $\mu_p = 0.2$. (e) Hysteretic cycle of the amplitude of contact anisotropy a^c for inter-particle friction $\mu_p = 0.5$ and $\mu_p = 0.2$. All cycles are plotted in the dry case.

on Figure 4.23c, shows that the average number of contacts decreases when decreasing μ_p. In addition, it can be observed on Figure 4.23d that the fraction of sliding contacts is higher when reducing inter-particle friction coefficient in the same stress conditions. This result is consistent with the fact that lower Coulomb friction coefficient implies higher probability for a given contact to respect the Coulomb criterion. Hence, reducing friction increases the fraction of contacts that are sliding. This picture is also consistent with the increase of inertial number when reducing μ_p. Indeed, a sliding contact enables tangential motion where a sticking contact does not enables tangential motion. Hence, reducing friction reduces the ability of grains to dissipate motion in the direction of flow leading to faster layers at a given angle. Finally, Figure 4.23e presents the evolution of contact network anisotropy for both friction coefficient. The figure shows that reducing friction increases the amplitude of contact anisotropy at a given angle. This is also consistent with the idea developed in the previous Section that the faster is the flowing layer the higher the amplitude of contact anisotropy due to the misalignment of contacts with the principal directions of the system.

These findings, together with the stopping and avalanche angles reduction when reducing inter-particle friction, leads to variations of the critical values of each variables near jamming and unjamming. These quantities are important to characterize the conditions of transitions and their asymmetry due to the hysteretic phenomenon. The critical inertial number, $\mathcal{I}_{stop}$ or $\mathcal{I}_*$ for example is a characteristic limit of the transition between flowing and static regimes in stress imposed configurations used in constitutive relations. The critical values are calculated by fitting the trend of each variable in the flowing state and extrapolating the results at $\theta = \theta^-_{stop}$ and $\theta = \theta^+_{start}$.
It can be observed on Figure 4.23a that the critical inertial number, $\mathcal{I}_{stop}$, appears to be equivalent or maybe slightly lower when increasing friction. This means that the medium jams at similar relative inertial dynamic at lower inter-particle friction coefficient than at higher one. By contrast, since hysteresis is lower for lower friction, the inertial number reached just after the unjamming transition, $\mathcal{I}_{start}$ is higher for higher friction coefficient. Figure 4.23b shows that for the packing fraction, both values ϕ_{stop} and ϕ_{start} are higher when reducing the friction coefficient. This means that when reducing friction between grains the granular flow can support higher packing density before it jams. This is consistent with the fact that the medium flows faster, motion dissipation requires denser layer in order to stabilise this higher inertial dynamic.
Similarly to volume fraction, Figure 4.23c shows that both coordination number values $\mathcal{Z}_{stop}$ and $\mathcal{Z}_{start}$ are higher when reducing grains friction. It shows that when reducing the friction between grains, the granular medium can support more contacts in the flowing regime before jamming. Another way to interpret that is that since the medium flow at higher inertial number (more inertial dynamic), the medium needs more contacts in order to stabilise leading to higher coordination number value near jamming at lower jamming angle.
The fraction of sliding contacts, Figure 4.23d, is significantly higher near jamming, χ_{stop}, and after unjamming, χ_{start}, when reducing friction between grains. This result can be a first interpretation of how the medium can support more contacts before it jams or why the medium needs more contact in order to stabilise. It can even give a first idea of how the granular flow near jamming can be more inertial even when it is denser right before

jamming when reducing friction between grains. Indeed, if a higher proportion of contacts are sliding near jamming when reducing friction, then the system will be less dissipated by those contacts and lead to a higher relative inertia (higher $\mathcal{I}_{stop}$).
Finally, Figure 4.23e shows that the amplitude of contact anisotropy is lower at both cessation, a^c_{stop}, and initiation, a^c_{start}, of flow when reducing the friction coefficient. This result appears as a contradiction with the idea that the contact anisotropy is higher when the inertial number is higher. Nevertheless, this interpretation can be qualified by the fact that the number of contacts in the system may play a role in the level of anisotropy. A higher amount of contact could lead indeed to a lower contact anisotropy since these additional contacts can be oriented in the principal directions of flow, especially near jamming where the system is more disorder in every directions.

In the static jammed regime the changes that occurs by varying inter-particle friction are the critical values of the different variables that are quasi-constant for most variables. Discontinuities observed at both transitions can then be quantified from the differences between values in the static regime and the critical values in the flowing regime. Figure 4.23a shows that the inertial number is equal to zero for all friction coefficients showing that the medium is fully static in the jammed state, $\mathcal{I}_c = 0$. As such, the discontiuities of inertial number are stricly equal to the critical value $\mathcal{I}_{stop}$ and $\mathcal{I}_{start}$.
By contrast, the packing fraction and coordination number displays non zero values in the static regime. The critical volume fraction and coordination number, ϕ_c and $\mathcal{Z}_c$, are higher when reducing friction. When jammed, the medium is denser then with more contacts per particles when reducing friction between grains resulting of the fact that jamming occurs at a lower angle for lower friction coefficient. On the one hand, the discontinuity of packing fraction at jamming, $\Delta\phi_{stop}$, is not significant for both friction coefficients because of the same order than the oscillations of volume fraction near jamming. On the other hand, the dilatancy measured at the initiation of flow, $\Delta\phi_{start}$ is significant for both friction coefficients and is decreasing with decreasing μ_p.
The coordination number, on Figure 4.23c, has conversely to the volume fraction two clear discontinuities that both decreases with friction. The discontinuities of coordination number and packing density are three main quantities that characterizes the asymmetry of the transition hence the hysteresis phenomenon. As depicted in Chapter 2, dilatancy is a feature of frictional unjamming and its presence suggest that the transition is asymmetric. Indeed, a transition without dilatancy, i.e. without inter-particle-friction, would be smooth in terms of packing fraction suggesting a second-order phase transition without hysteresis. An equivalent interpretation can be made in the case of vanishing coordination number discontinuity. This will be discussed with more details in the following Chapter.
The fraction of sliding contacts, Figure 4.23d, is always equal to zero in the static state near jamming. Nevertheless, the peaks of sliding contacts in the jammed state, demonstrating an increasing amount of plasticity at the contact scale with increased stress, increase in amplitude for lower friction between grains than higher one. In the following the notation $\chi_{plastic}$ will be used to denote the maximum value (for the last peak) of sliding contacts proportion in the stable state. This could be a first clue for the reduction of hysteresis when reducing the friction between grains. Indeed, if reducing friction increases the proportion of contacts that slides, then the destabilisation process (detailed in the previous Section) is easier and occurs at angles closer to the stopping angle.

Finally, Figure 4.23e shows that the critical value of contact anisotropy in the jammed state, a_c^c, is decreasing when decreasing the inter-particle friction coefficient. This value may be related to the angle at which the system jams since in the static stable state no contact anisotropy is induced by flow. The contact anisotropy in the static state is then due to the geometrical entanglement of grains on the plane which is directly related to the inclination angle of the plane. It also have two clear discontinuities that appear to decrease with friction.

In conclusion, on the one hand the inertial number and the fraction of sliding contacts measures the dynamical aspects of the variations of friction respectively at the macroscopic and at the micro-structure scale. When friction is decreased the granular layer flows more faster in the flowing regime and stops at equivalent inertial number values. This increase of the layer dynamic comes with an increase of sliding contacts showing the major role of friction in the dynamic of the system. The average number of contacts and the packing fraction are similarly increasing when friction is decreased showing that the system needs to be more compact then gain significantly more contacts to sustain the increase of sliding contacts in order to jams and reach the stable state.
On the other hand, the flow starts at a less inertial regime after the avalanche occurs despite a much higher sliding contacts proportion at lower μ_p. This effect results from lower critical angles as well as hysteresis when the friction is decreased, showing that the asymmetry in the critical inertial number values is lower for friction which is consistent with the decrease of hysteresis. Similarly, the decrease of discontinuity with friction at the avalanche for all state variables shows that the state of the granular system in the flowing regime near transitions are closer to the static regime when decreasing friction. This is a first clue to understand how hysteresis is also lower when decreasing μ_p. Indeed, if the system is allowed by a decrease of friction to flow closer to its critical static limit, then it will stops or start to flow with less effort.

4.4.2 Effect of the restitution coefficient

Qualitative analysis of the effect of e_N

The other dissipation mechanism at the contact scale that is interesting to investigate is the normal contact dissipation. Although contact dissipation has been shown to have little or no influence on the liquid-solid transition of granular media on rough inclined (*Silbert et al.*, 2001), it remains a dissipation mechanism that could play a role in a process as fine as hysteresis. Indeed, *DeGiuli et al.* (2016) shown the complex combination of collisions and friction dissipation in the flowing state and the quasi-static state suggesting a potential effect on the dynamic near jamming. The idea is to vary normal dissipation without varying contact rigidity and observe its influence on critical angles and hysteresis. To do so we have to vary the dissipation term of the contact law, Equation (3.32), which is γ_N. As γ_N depends on k_N and e_n and k_N is kept constant, the restitution coefficient e_n is varied. The values computed are: $e_n = 0.9$ $e_n = 0.5$ and $e_n = 0.1$. The inter-particle friction coefficient is taken at two different values $\mu_p = 0.5$ and $\mu_p = 0.2$.

Figures 4.24 and 4.25 present the hysteretic cycles of inertial number, volume fraction, coordination number and contact anisotropy for $\mu_p = 0.2$ and $\mu_p = 0.5$ at various restitu-

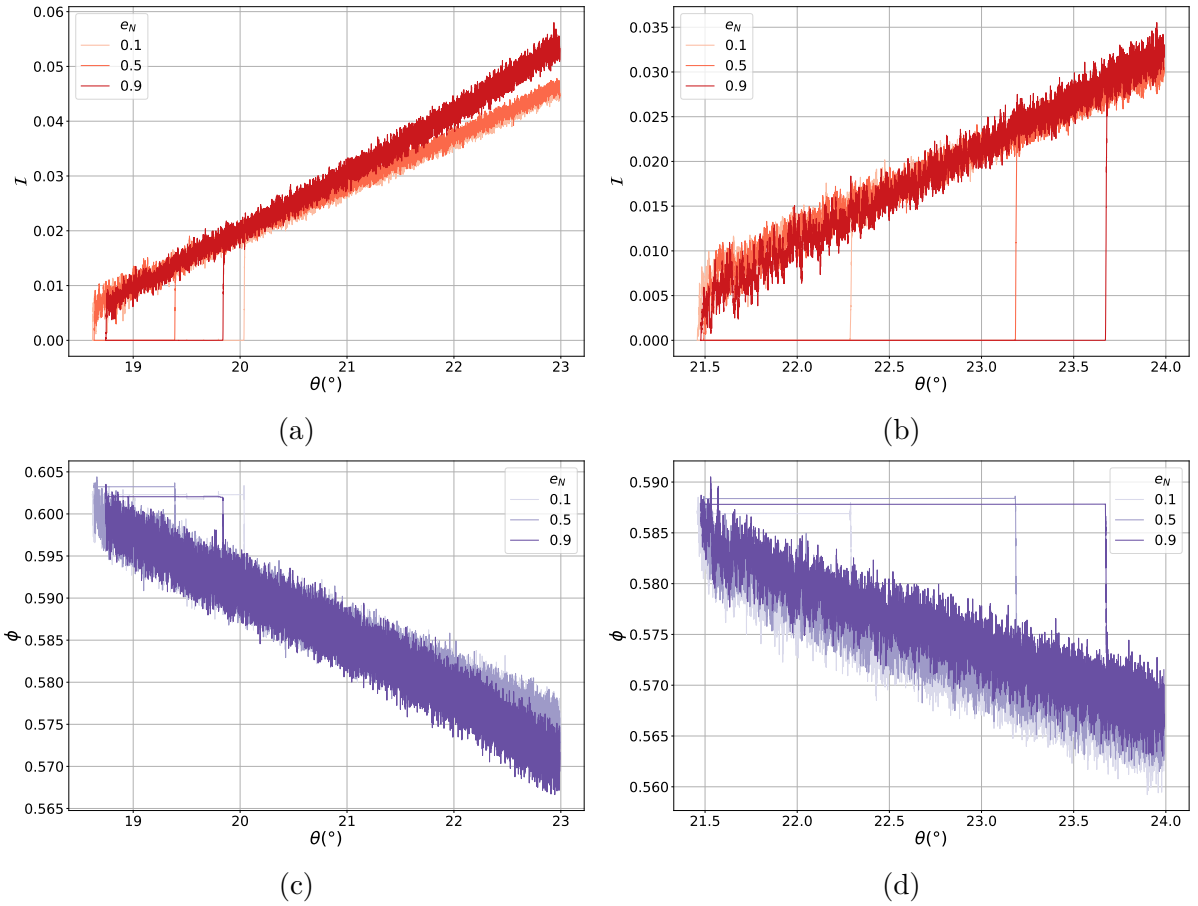

Figure 4.24 – Hysteretic cycle of the inertial number as a function of the inclination angle at various restitution coefficients for inter-particle friction (a) $\mu_p = 0.2$ (b) $\mu_p = 0.5$. Hysteretic cycle of the solid volume fraction ϕ as function of the inclination angle at various restitution coefficient for inter-particle friction (c) $\mu_p = 0.2$ (d) $\mu_p = 0.5$.

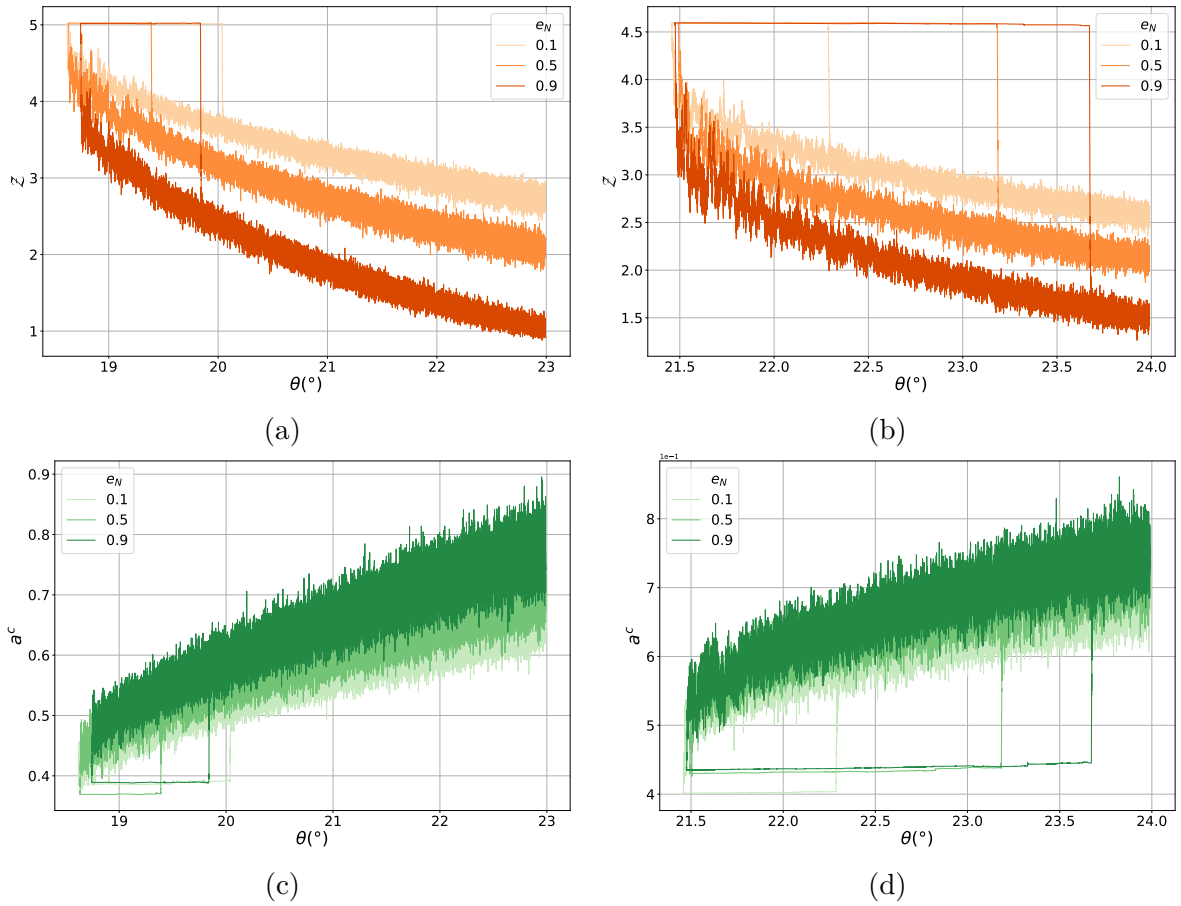

Figure 4.25 – Hysteretic cycle of the coordination number as a function of the inclination angle at various restitution coefficients for inter-particle friction (a) $\mu_p = 0.2$ (b) $\mu_p = 0.5$. Hysteretic cycle of the amplitude of contact anisotropy as function of the inclination angle at various restitution coefficient for inter-particle friction (c) $\mu_p = 0.2$ (d) $\mu_p = 0.5$.

tion coefficients. Figure 4.24 shows that the dynamic is slightly varied with e_N far from the transition but near the transition, the curves of $\mathcal{I}(\theta)$ and $\phi(\theta)$ are superimposed at all e_N. Slight variations at the transitions are also observed since the critical angles are slightly varied but the variations are not significant. Nevertheless, at $\mu_p = 0.5$ the avalanche angle significantly decrease with decreasing e_N which is not observed at $\mu_p = 0.2$. As such, additional simulations are needed to quantify if these variations depends on the friction coefficient value or results from the stochastic effect.

Figure 4.25 shows a more significant variation in the average number of contacts that increase when decreasing the normal contact dissipation in the flowing state. The critical values near jamming $\mathcal{Z}_{stop}$ also increase as a consequence but the critical values in the static state $\mathcal{Z}_c$ are the same which means that the jamming state of the medium does not depends on the normal contact dissipation. Finally, the contact network is slightly less anisotropic at lower e_N but no significant variations are observed. However this slight variations strengthen the idea that an increase of contacts lower the anisotropy of the network.

Quantitative influence of e_N on hysteresis and critical angles

The restitution coefficient appears to have no much effect on the system and hysteretic cycles of state variables. Only the coordination number displays significant change with varying e_N. Nevertheless, qualitative results suggest a potential influence of normal contact dissipation on hysteresis at $\mu_p = 0.5$. In order to quantify this effect, an extensive study is performed repeating simulations ten times with different random distribution of grains at the bottom plane with equivalent global roughness. Then, the critical angles and hysteresis are measured for each simulations.
Figures 4.26a and 4.26b presents the results of the critical angles, θ_{stop} and θ_{start}, when varying the restitution coefficient at inter-particle friction coefficient fixed respectively at $\mu_p = 0.5$ and $\mu_p = 0.2$. The influence of the restitution coefficient on both critical angles is remarkably not significant for $\mu_p = 0.2$ and 0.5.
Similarly, hysteresis $\Delta\theta$ is plotted on Figures 4.26c and 4.26d at both μ_p. Hysteresis displays no significant variations with e_N. The full picture showing the absence of influence of e_N on hysteresis for all inter-particle friction coefficients computed in our work is presented in Appendix C.1.
Slight variations observed on hysteretic cycles were then due to the stochastic nature of the transition.

By contrast, the values of both critical angles and hysteresis significantly varies from one inter-particle friction to the other. Especially, the decrease observed qualitatively is shown to be systematic.

4.5 Conclusion

In this chapter we presented an overview of the transition between the fluid-like and solid-like behavior of granular materials on an inclined plane. We have seen that phase transition diagrams have emerged from study of the influence of the size of the granular

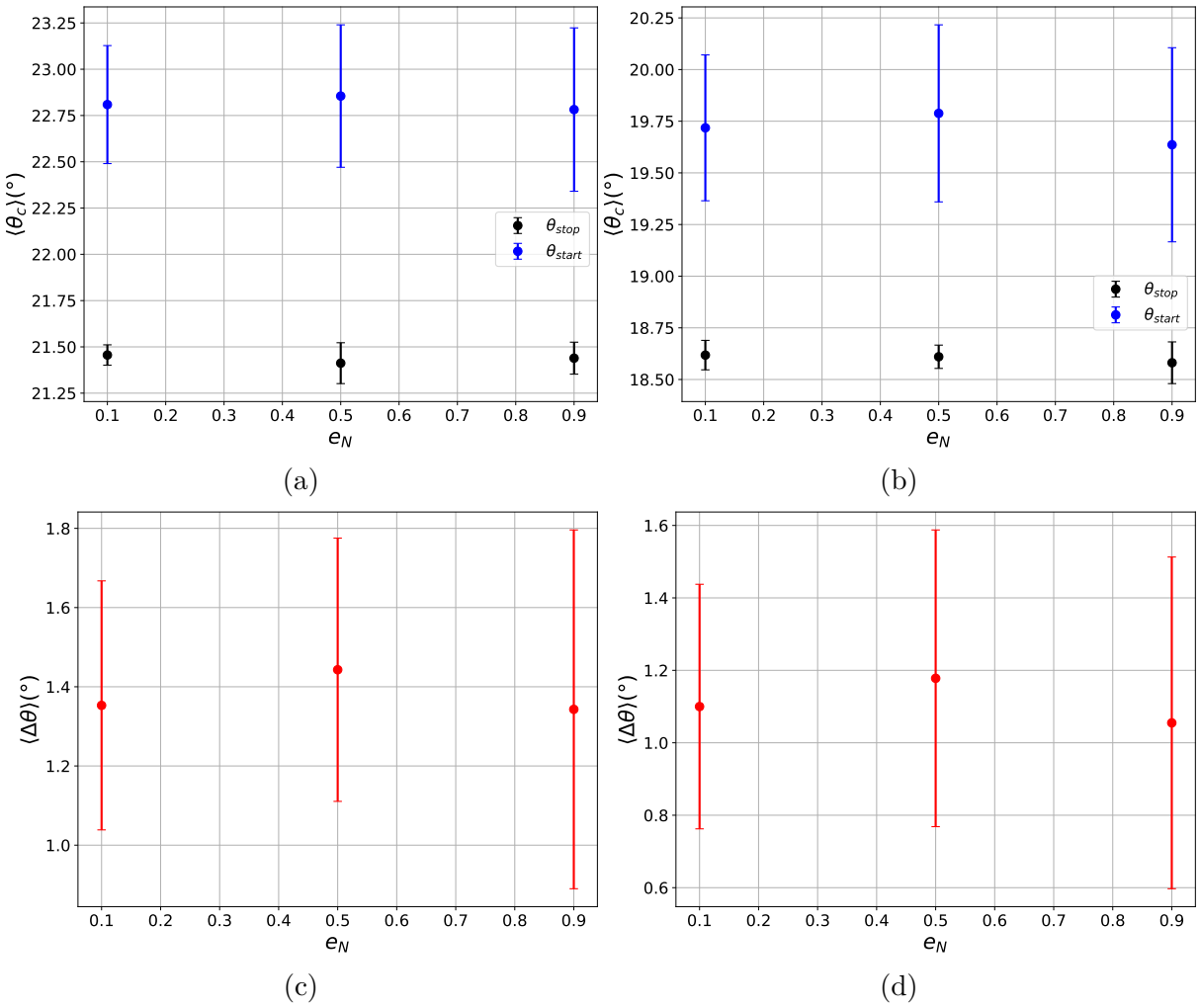

Figure 4.26 – Stopping (black points) and avalanche (blue points) angles versus the restitution coefficient (a) at $\mu_p = 0.5$ (b) at $\mu_p = 0.2$. Hysteresis versus the restitution coefficient (c) at $\mu_p = 0.5$ (d) at $\mu_p = 0.2$. All simulations were performed ten times with different random distributions of the grains of the plane. The error bars corresponds to the standard deviation over the ten runs and the markers to mean value.

system considered as well as contact properties such as inter-particle friction or grains stiffness. We saw that this transition is sub-critical since an hysteretic behavior is observed leading to different critical external stress values needed to initiate or stop a granular flow defining two separate transitions: jamming and unjamming. In addition near these transitions, the granular properties depend on the evolution of the micro-structure, especially the contact network, characterized by the average amount of contact per particles and the contact anisotropy.

In this context we have shown by analysing the evolution of the granular layer in the different granular phases and near the jamming and unjamming transitions that both cessation and initiation of flow are two distinct processes. The cessation of flow is a bottom up stability process that gradually leads the layer to stability. The initiation of flow is a succession of local rearrangements that generate instability of the layer near the

free-surface leading to the destabilisation of the whole layer.
In addition, we have studied the stress loading cycles of the various variables that characterize the granular response to external stress at the macroscopic and microscopic scale and highlighted the presence of hysteretic cycles, granular regimes and characteristic values.
We have shown that the effect of dissipation by collisions is slight on the amount of contacts made by grain in the flowing regime and that the dynamical quantities of the flowing layer are modified only at high angles (far from jamming). Nevertheless, no significant influence of normal contact dissipation is observed on critical angles and hysteresis. These results are consistent with observations of *Silbert et al.* (2001). By contrast, the granular system evolution under stress highly depends on inter-particles friction coefficient μ_p, which significantly influences the values of critical angles as well as hysteresis. As a consequence, the effect of friction will be studied with further details in the following Chapter.

Chapter 5

Study of the combined effect of friction and inertia

The effect of friction on the flow of a granular medium (*DeGiuli et al.*, 2016; *DeGiuli and Wyart*, 2017; *Srivastava et al.*, 2022), its stability (*Srivastava et al.*, 2022; *Silbert et al.*, 2002b; *DeGiuli and Wyart*, 2017) and the hysteresis at the transition between these states (*DeGiuli and Wyart*, 2017; *Perrin et al.*, 2019, 2021; *Peng et al.*, 2023) is well established. However, the role of inertia on this phase transition and its hysteresis is still debated (*Courrech Du Pont et al.*, 2003; *DeGiuli and Wyart*, 2017; *Perrin et al.*, 2019). Especially, the absence of hysteresis for frictionless particles has been experimentally shown only for immersed granular materials in the viscous regime (*Perrin et al.*, 2019, 2021), i.e. where the inertia of grains is negligible. It has been numerically found in simulations with velocity imposed plane shear-cell configuration, i.e. where the inertia of the system is imposed. The framework that emerges from theses works, proposed by *DeGiuli and Wyart* (2017) assigned the hysteresis behavior to the "self-fluidisation" of the granular medium in the flowing state. As detailed in Chapter 2 some aspects remain to be elucidated. In particular the vibrations induced by collisions are not cancelled for frictionless material, and one expect the self-fluidization process to be partly present, even for frictionless particles. Since the experiments of *Perrin et al.* (2019) are performed in the viscous Stokes limit, i.e. with negligible particle's inertia and zero effective restitution coefficient, the residual energy is expected to be damped. The link with the self-fluidization process described in *DeGiuli and Wyart* (2017) is therefore not obvious. In addition, the hysteresis obtained in *Perrin et al.* (2019) is suprisingly high (of the same order than for highly frictional dry materials (*Peng et al.*, 2023)) considering the presence of a fluid damping the self-fluidization process. This could be due to their experimental setup that leads to variations of the type of contact forces continuously from the classical Coulomb solid-solid contact model into an electrostatic repulsive force (*Clavaud et al.*, 2017) which is discussed in Appendix A.6.

The state of the art about the origin of hysteresis is then still in debate about the role of inertia in this asymmetric transition. In the present chapter, hysteresis is studied for an inclined configuration by the mean of three-dimensional (3D) Discrete Element Model (DEM) simulations of dry and model-immersed granular media as detailed in Chapter 3. This allows us to vary both inter-particle friction and particle inertia independently.

We show that frictionless granular media exhibit a finite hysteresis, contrary to what is expected. Going further, we show that the hysteresis depends on a combined effect of particle friction and inertia.
We qualitatively analyse the influence of grains' inertia on the state variables of the system, critical angles and hysteresis on Section 5.1. Then, the influence of both the microscopic friction coefficient and grains inertia on critical angles and hysteresis is quantitatively studied on Section 5.2. Then, we show that a study of higher-order micro-structural description of the medium is needed to characterize well both critical angles in Section 5.3 as much as the asymmetry of the transition and unify the studies of both microscopic friction and inertia effect on hysteresis in Section 5.4.

5.1 Qualitative analysis of the evolution of the state variables with the inertia of grains

In order to qualitatively study the evolution of the granular medium transition between fluid-like and solid-like behaviors with grains inertia, the inter-particle friction coefficient is fixed at $\mu_p = 0.5$. Then the Stokes number is varied between the dry case ($St = \infty$) and a viscous regime where $St = 1$. The results are presented on Figure 5.1. It is observed on all plots that conversely to friction, when reducing the Stokes number, the stopping angle significantly increase and the avalabche angle slightly decrease here but does not show large variations as θ_{stop}. Also, hysteresis reduces with grains inertia.

Going into more details for each plots, Figure 5.1a presents the evolution of the inertial number with Stokes number. It is clear that reducing the Stokes number from the dry case (aerial free-fall regime) to the viscous regime $St = 1$ decreases drastically the inertial number. Also, the inertial number does not significantly evolves with variations of angle in the flowing regime at low Stokes compared to the dry case. Finally, the critical values, $\mathcal{I}_{stop}$ and $\mathcal{I}_{start}$, significantly decrease when decreasing grains inertia. The results are a signature at the scale of the whole medium of the decrease of grains inertia when reducing the stokes number.
Figure 5.1b shows on the one hand that the granular layer is denser and that no more clear discontinuity of dilatancy is observed between the static and the flowing states in the viscous regime.
Figure 5.1c shows that the coordination number also drastically increases in the flowing state when decreasing the Stokes number. By contrast with the volume fraction, clear discontinuities of coordination number are observed at the initiation and cessation of flow in the viscous regime. They are nonetheless lower than in the dry case. In addition, Figure 5.1e shows that the contact network is significantly less anisotropic at $St = 1$ than in the dry case. As such, the system has significantly more contacts and these contacts are significantly less anisotropic meaning that the orientations of contacts are more uniformely distributed. In order to investigate how the frictional network is influenced by inertia, the fraction of sliding contacts is presented on Figure 5.1d. It shows that χ decreases in the flowing regime when decreasing the Stokes number. Interestingly, the evolution of χ in the flowing regime is similar between the dry case and the viscous regime except that the amplitude of χ decreases with St. The effect of viscous damping on the tangential

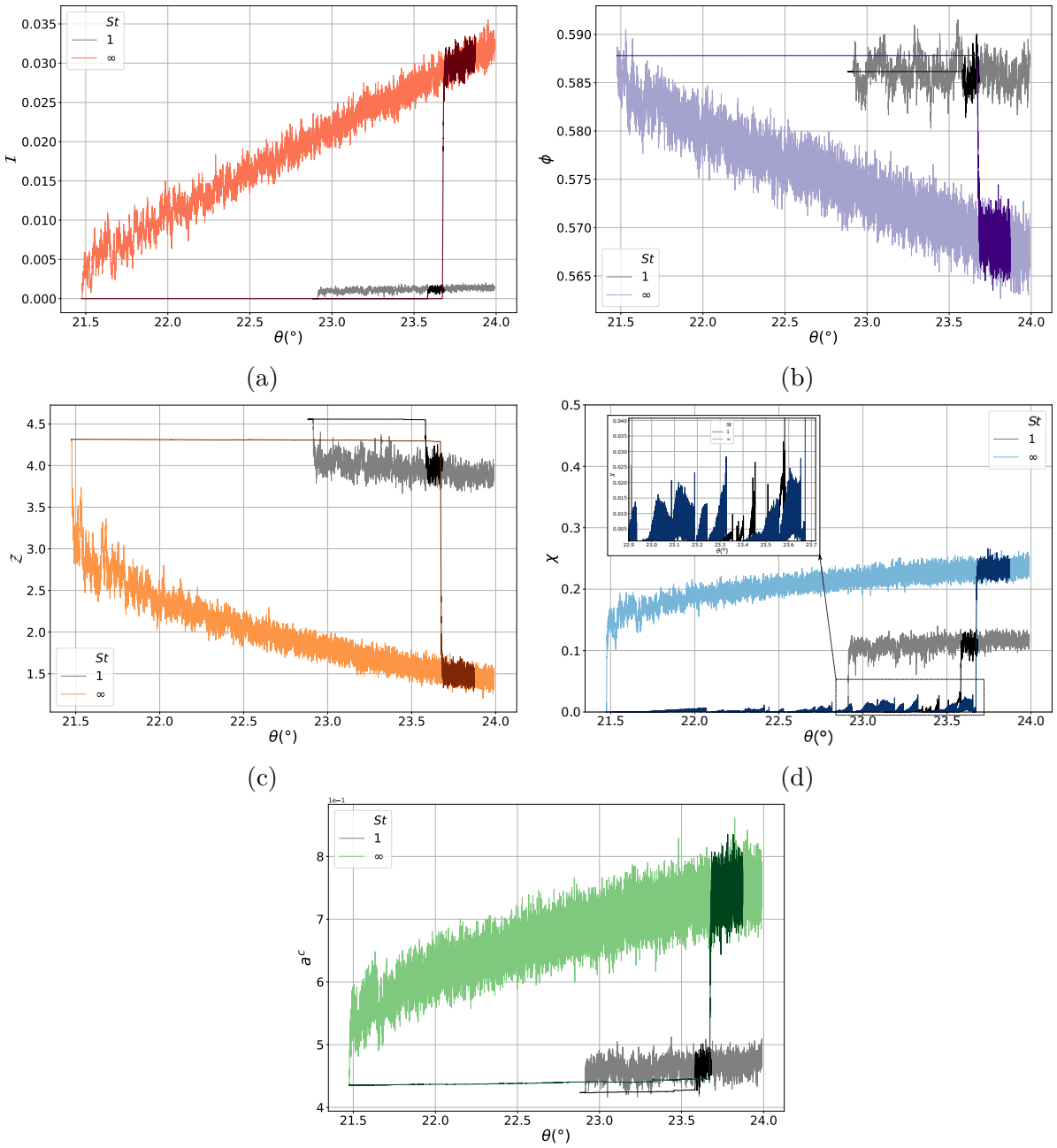

Figure 5.1 – Hysteretic cycle of the inertial number $\mathcal{I}$ (a), the solid fraction ϕ (b), the average coordination number per particle $\mathcal{Z}$ (c), the fraction of sliding contact χ (the inset is a zoom in the static state) (d) and the amplitude of contact anisotropy a^c (e) versus the inclination angle for Stokes number $St = 1$ and in the dry case, $St = \infty$ at inter-particle friction $\mu_p = 0.5$.

network has a similar effect on χ than slightly increasing the inter-particle friction coefficient, see previous chapter.

The above results show that in the viscous regime the medium is flowing significantly slower than in the dry case. As a consequence, it flows at higher densities and average number of contacts hence closer to their critical values in the static stable state. In addition, the contact network is more geometrically disordered and tangentially more constrained with a lower proportion of contacts that are able to slides. Reducing grains inertia then enables the system to flow with a higher constrained system in terms of number of contacts and tangential sliding leading to a more geometrically isotropic network that can easily leads to stability and therefore a higher stopping angle at similar microscopic frictional conditions.

The critical values of volume fraction and coordination number in the static state, see Figures 5.1b and 5.1c, do not significantly vary when decreasing grains inertia. Nevertheless, the former interestingly slightly decreases while the latter slightly increase. Similarly, since no dynamic process is involved in the static regime, the variations of χ are similar when increasing the angle between the viscous and dry regimes, see inset of Figure 5.1d. At $St = 1$, the peaks observed on χ in the static state reach quickly the maximum value reached in the dry case which interestingly does not lead the system to flow. Finally, Figure 5.1e shows that the static geometrical contact network anisotropy in the viscous regime is slightly below the one in the dry case. This slight evolution can be interpreted as an influence of the evolution of the stopping angle since geometrical contact anisotropy in the static state is linearly related to the stress ratio (*Srivastava et al.*, 2022).

Nevertheless, we have seen in the previous chapter that jamming is a bottom-up process and unjamming results from rearrangements, i.e. break of stability near the bottom creating an instability on the above grain layers that are less constrained. In addition, the discontinuity of coordination number occurs mainly near the free surface at jamming which means that the stabilisation process of the grain layers near the bottom plane occurs in the flowing regime near jamming. As a consequence, these result allow us to qualify the evolution of avalanche angle with Stokes number. If the contact network is slightly more disordered for the same number of contacts then the contact network is probably harder to break, meaning that the same proportion of sliding contacts does not necessarily leads to flow, because less organise in a coherent direction than in the dry case. This behavior is a clue to understand the increase of the avalanche angle in the viscous regime compared to its value in the dry case.

The transition being stochastic and plane roughness dependent, one may repeat the simulations in order to investigate if the above results are systematic. The following Section presents the systematic study performed while varying both the inter-particle friction and grains inertia.

5.2 Combined influence of friction and inertia on the critical angles and hysteresis

We performed a systematic study on the effect of friction and inertia on the granular layer in order to generalized the qualitative analysis observed in the previous section. Hence, first, in order to better characterize and understand physical mechanisms behind the observed hysteresis, it is interesting to discuss the results observed in terms of jamming and avalanche angles. Then, hysteresis will be quantify and studied through friction and inertia effect. Each simulation corresponding to a set of parameters (μ_p, St) is repeated 10 times with newly generated bottom roughness, in order to assess the geometrical variability due to the boundary from one case to another. The data are plotted in terms of averaged parameters, $\langle\cdot\rangle$, and the error bars are characteristic of the geometrical variability.

5.2.1 Influence of the inter-particle friction on the critical angles

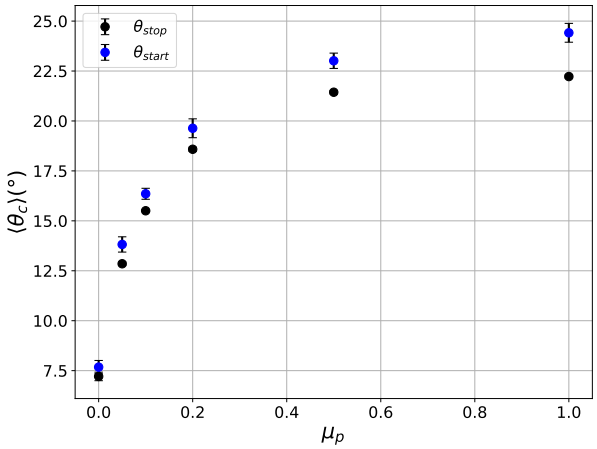

Figure 5.2 – Evolution of the stop and avalanche angles, θ_{stop} and θ_{start} with the microscopic friction coefficient in the dry case.

As presented by Figure 5.2, the avalanche and stopping angles defining the stability angles of the granular media and the hysteresis on the inclined plane are varying importantly with inter-particle friction. The variations of angles are not sharp at high friction coefficients, i.e. $\mu_p \geq 0.5$, at lower friction the angles sharply decreases showing that the medium loses stability quickly when going towards the frictionless regime. The variations of critical stress ratio or angles with friction are similar on Figure 5.2 than to trends in previous simulations (*DeGiuli and Wyart*, 2017; *Srivastava et al.*, 2022; *Perrin et al.*, 2019). All these results show that inter-particle friction plays a major role in the stability of the granular system. Interestingly, in the frictionless regime the stability angles are quite higher than the values for experiments in rotating drums of *Perrin et al.* (2019) and on an inclined plane (*Perrin et al.*, 2021).

5.2.2 Influence of inertia on the critical angles

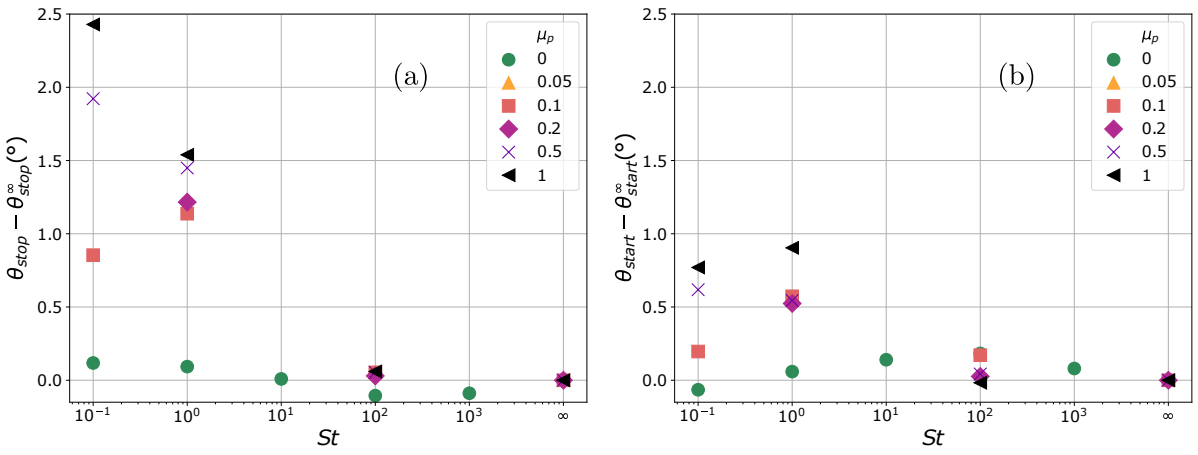

Figure 5.3 – (a) Evolution of the stop angle pound on hysteresis $\theta_{stop} - \theta_{stop}(St = \infty)$ with the Stokes number at various friction coefficient. (b) Evolution of the start angle pound on hysteresis $\theta_{start} - \theta_{start}(St = \infty)$ with the Stokes number at various friction coefficient

The important variations of critical angles with inter-particle friction does not allows one to observe well the impact of a given parameter on hysteresis. Indeed, fine variations of the avalanche or stopping angle with respect to its absolute value leads to important impact on hysteresis. Therefore, in order to characterize the influence of the Stokes number on the avalanche and stopping angles and their impact on hysteresis, we consider the difference between the avalanche (and stop) angle at a given Stokes number and the avalanche (and stop) angle in the dry case (see Figures 5.3a and 5.3b). The evolution observed for both angles are not monotonous and present the most important relative variations for Stokes number one and 0.1. The variations are approximately twice higher on the stopping angle than on the avalanche angle. In this case, the fluid viscous dissipation has the effect of increasing the stopping angle towards the avalanche angle leading to lower hysteresis when Stokes tends to zero, as presented in the previous Section 5.1.

5.2.3 Combined influence of friction and inertia on hysteresis

Figure 5.4a presents the global picture of the variation of hysteresis with inter-particle friction and Stokes number. It shows that the hysteresis varies globally with both parameters defining different regions in the parameter space: the hysteresis is minimum at low Stokes and low inter-particle friction, while it is maximum for dry highly frictional particles. Overall, it tends to decrease with decreasing Stokes number at given inter-particle friction coefficient, and to decrease with inter-particle friction coefficient at given Stokes number.

Going into more details, hysteresis is presented as a function of inter-particle friction on Figure 5.4c for Stokes number one, $St = 1$, and in the dry case, $St = \infty$. First, in the dry case it can be observed that the average hysteresis, $\langle \Delta\theta \rangle$, is an increasing function

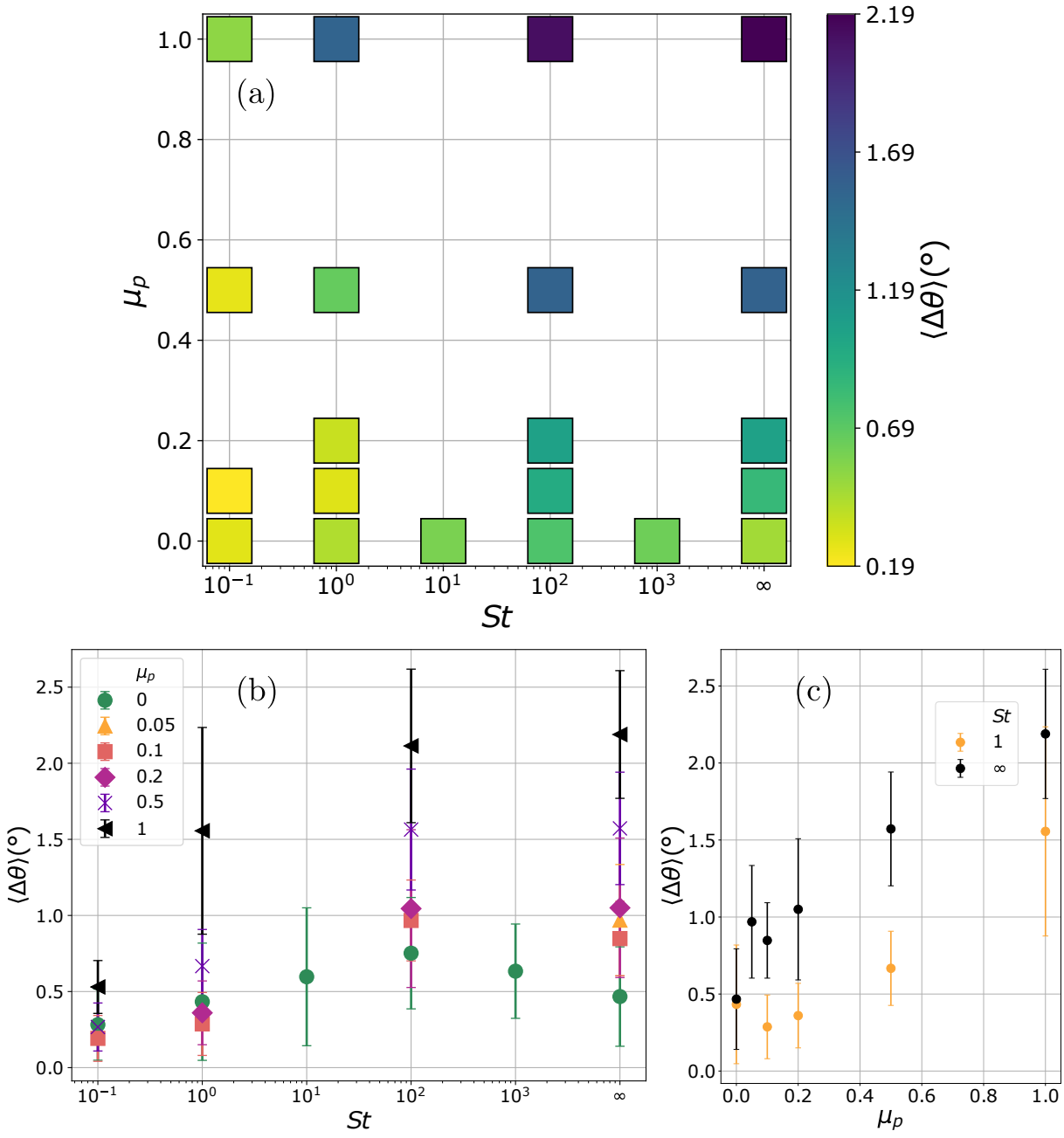

Figure 5.4 – (a)Hysteresis as a function of the Stokes number and the microscopic friction coefficient. (b) Evolution of the hysteresis $\Delta\theta$ with Stokes number at various inter-particle friction coefficient. (c) Evolution of the hysteresis versus inter-particle friction coefficient μ_p at low Stokes, $St = 1$, and in the dry case, $St = \infty$.

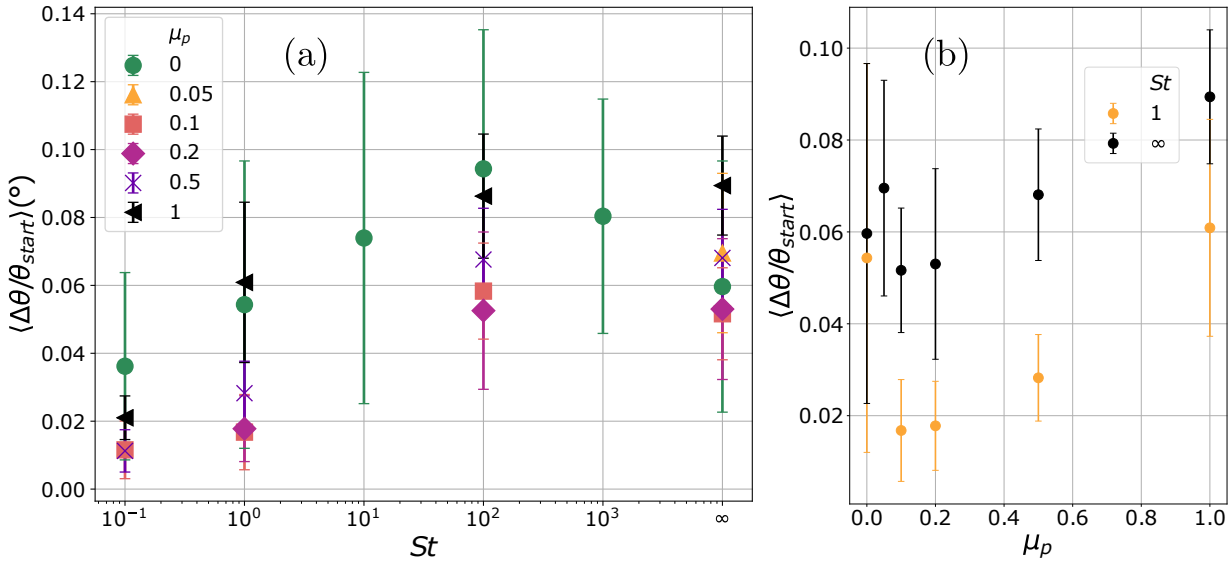

Figure 5.5 – (a) Hysteresis relative to the avalanche angle $\Delta\theta/\theta_{start}$ as a function of the Stokes number for various microscopic friction coefficient. (b) Hysteresis relative to the avalanche angle $\Delta\theta/\theta_{start}$ versus microscopic friction coefficient μ_p at low Stokes, $St = 1$, and in the dry case, $St = \infty$.

of the inter-particle friction μ_p. It is approximately divided by four between $\mu_p = 1$ and for frictionless particles. This result shows the systematic strong effect inter-particle friction plays in hysteretic behavior validating the qualitative observations from hysteretic cycles in the previous Chapter. This strong friction effect is consistent with the literature (*Peng et al.*, 2023; *DeGiuli and Wyart*, 2017; *Perrin et al.*, 2019). In addition, one of the main result from our simulations is the finite hysteresis observed for frictionless particles ($\mu_p = 0$) in the dry configuration ($St = \infty$). Earlier work from *DeGiuli and Wyart* (2017) in plane shear velocity imposed configuration had shown vanishing hysteresis at $\mu_p = 0$. Similarly, *Perrin et al.* (2019, 2021) have obtained no hysteresis for inertia-less frictionless particles. These results then shown a strong effect of friction on hysteresis and suggested that inter-particle friction was only needed to observe hysteresis at the transition. As such, the results of *DeGiuli and Wyart* (2017) had lead them to build a theoretical framework to model hysteresis within the stress ratio flow function $\mu(\mathcal{I})$ by adding a non-monotonous function of the sliding contact proportion χ as order parameter controlling hysteresis, see Section 2.6.2. Since $\chi = 1$ in the frictionless case, this model predicts monotonous flow curve hence no hysteresis for frictionless particles. Our results then contradicts this idea of inter-particle friction as unique parameter necessary to observe hysteresis. The other parameter we studied is the Stokes number, decreased into the viscous regime at $St = 1$ on Figure 5.4c. In that regime, hysteresis also decrease with friction with a similar trend that in the dry case but shifted at lower values except at $\mu_p = 0$ where both values are the same.

In order to look further into the effect of inertia, the results are presented in terms of hysteresis as a function of the Stokes number for various microscopic friction on Figure 5.4b. The figure shows that hysteresis decreases with the Stokes number for low $St < 100$

and remains nearly constant for $St \geq 100$ at all μ_p. In addition, for frictionless particles, the hysteresis tends to zero with decreasing Stokes number. For the lower Stokes number value, i.e. 0.1, hysteresis is significantly low for all μ_p. As such, the values do not significantly vary with μ_p at that Stokes showing a dominant effect of viscous dissipation.

These results show that microscopic friction effect on hysteresis is dominant compared to inertia effect for $St \geq 1$. Meanwhile, the influence of the Stokes number on the results shows that there is a non-negligible effect of the fluid viscous dissipation on hysteresis. This effect is dominant for highly viscous fluid, i.e. $St = 0.1$, in front of friction, showing that hysteresis is also influenced by grains inertia, in agreement with *Courrech Du Pont et al.* (2003). The trend observed for frictionless particles with decreasing Stokes number suggests that the absence of hysteresis observed in *Perrin et al.* (2019) is linked to the fluid regime considered in their experiment where the Stokes number is below $St = 10^{-1}$ and the absence of inter-particle friction.

Varying the Stokes number and, more importantly, the inter-particle friction coefficient modifies strongly the angles of stability of the granular medium (see Figure 5.2). As such, it has an influence on both the stability angles and the hysteresis. With this perspective, it is interesting to consider the relative modification of the hysteresis with respect to the avalanche angle, as a function of the Stokes number and the inter-particle friction. Figure 5.5a shows that the relative variation of the hysteresis is of the same order of magnitude for all the simulations with different inter-particle friction. This shows that the relative importance of the hysteresis is not at all negligible for frictionless particles ($\sim 5-10\%$ at various Stokes number). Also, one can observe more clearly the non-trivial combined effect of inter-particle friction and Stokes number, with a decreasing trend of the relative hysteresis with decreasing Stokes number that is more important for intermediate inter-particle friction than for frictionless and highly frictional particles. This is well highlighted when plotting the relative hysteresis as a function of the friction coefficient for low Stokes number, specially $St = 1$ and in the dry case, $St = \infty$, shown by Figure 5.5b. This non-trivial combined influence of microscopic friction and grains' inertia might be related to changes in the main local particle behavior, which can shift from rolling to sliding as a function of the parameters. *DeGiuli et al.* (2016) have shown that the effect of microscopic friction on granular flow curve is non-trivial due to a competition between frictional and collisional dissipation. They defined three regimes of friction, the rolling regime for high inter-particle friction coefficients $\mu_p \geq 0.5$ where the Coulomb criterion is mainly respected for each contacts, the frictionless regime at $\mu_p = 0$ where all tangential contacts are sliding, for these two regimes dissipation by collisions is dominant. The last regime is for intermediate μ_p, it is called frictional sliding, in this regime dissipation by friction is dominant. The increase of relative hysteresis in the frictionless case on Figure 5.5b demonstrates that the asymmetry of the transition is lower relatively to the critical stress that defined stability when there is no more friction between grains compared to intermediate μ_p values. This result then highlights the behavior of the system in the various frictional regimes and underlines the fact that completely removing friction between grains also removes a dissipative mechanism that has an influence on hysteresis. Nonetheless, as had been shown in the previous chapter, at the transition between dense flow and stable state the dynamic as well as critical angles and hysteresis are not significantly

influenced by normal contact dissipation. Collisions are rare leading to a dominant effect of the microscopic friction coefficient at the expense of the dissipation by collisions which explains the slight variations of relative hysteresis when switching frictional regime.

The results are compared to the measured hysteresis from literature on Figures 5.6 and 5.7. The latter is a zoomed version of the former that excludes error bars and the highest results from *Perrin et al.* (2019) in order to visually compare the trends from our results and results from *Courrech Du Pont et al.* (2003). The figures shows first that at high Stokes number, hysteresis is always higher in a rotating drum than on an inclined plane. It suggests an influence of the configuration geometry through the roughness of the wall boundary as well as the boundary geometry itself. This is an interesting outlook for future work on the subject and will be discussed in Chapter 6.
Besides, the figures show that the trend of hysteresis variations with Stokes at a given inter-particle friction coefficient from our work, follows the trend from the results of *Courrech Du Pont et al.* (2003). In addition, both trends then appears to tend to the vanishing hysteresis points from *Perrin et al.* (2019) at lower Stokes numbers and no inter-particle friction. The large hysteresis observed from *Perrin et al.* (2019) in the viscous regime for frictional particles is greatly above our results at $St = 0.1$ and $\mu_p = 1$. These large hysteresis values are also higher than hysteresis for glass beads in rotating drum in dry cases from *Courrech Du Pont et al.* (2003) and *Peng et al.* (2023). As a consequence, it suggests an additional influence of the electrostatic contact force on grains stiffness in their setup although at these ionic concentration no effect is expected (*Clavaud et al.*, 2017).

To conclude, the present results show that hysteresis is linked to both particle friction and inertia, rationalizing the different results from the literature highlighting hysteresis dependency on either friction (*Perrin et al.*, 2019; *Peng et al.*, 2023) or inertia (*Courrech Du Pont et al.*, 2003), and suggesting the need for further improvement of established framework.

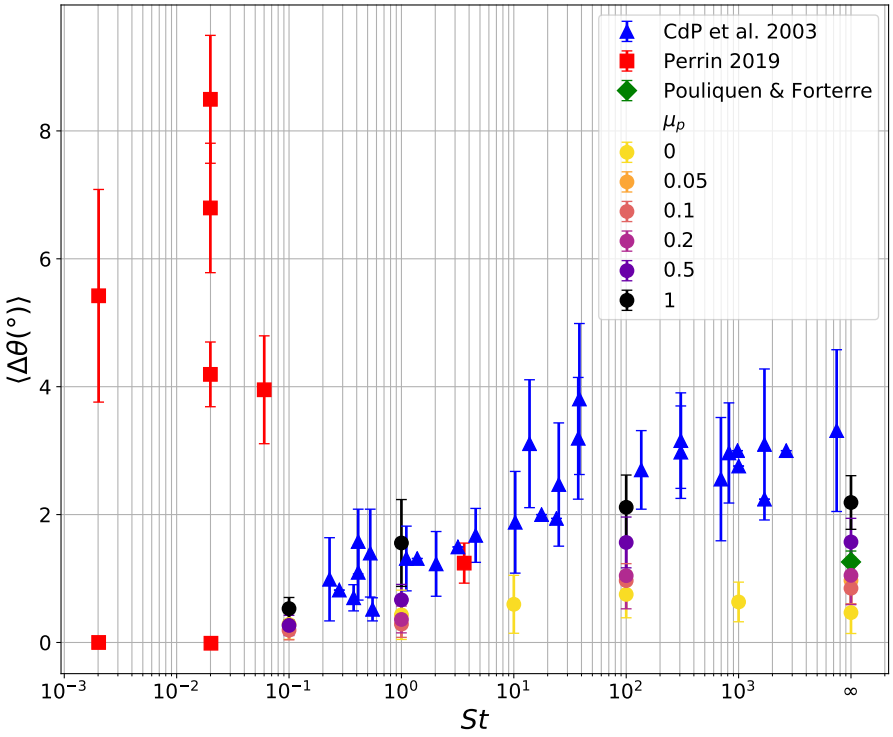

Figure 5.6 – Hysteresis $\Delta\theta$ versus Stokes number from our work compared to results from the literature in a rotating drum (*Courrech Du Pont et al.*, 2003; *Perrin et al.*, 2019) and on an inclined plane (*Forterre and Pouliquen*, 2008).

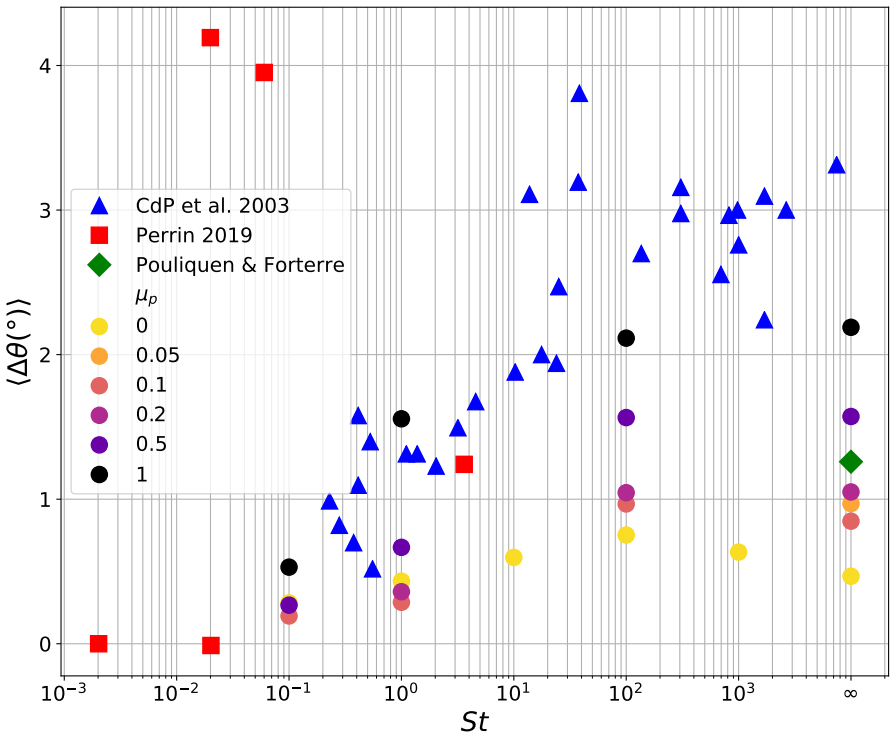

Figure 5.7 – Zoomed version of Figure 5.6, without error bars and excluding the highest results from (*Perrin et al.*, 2019).

5.2.4 Robustness of hysteresis results in frictionless case

The latter section presented hysteresis results when varying friction shown that finite non-negligible hysteresis was measured for dry frictionless material. Since this result contradict earlier results from *DeGiuli and Wyart* (2017); *Perrin et al.* (2019, 2021), we performed sensitivity analysis on several parameters that could influence hysteresis value in the frictionless case. The sensitivity analysis in Chapter 3 were performed at $\mu_p = 0.5$, hysteresis result at $\mu_p = 0$ may be sensitive to the domain size, the velocity of angle variation, the granular layer thickness as well as the restitution coefficient and the normal stiffness.

Velocity of angle variation

Hysteresis has been measured in the frictionless case for slower velocity of stress imposition $\delta\theta/\delta t = 5 \times 10^{-5\circ}\sqrt{g/d}$ than in the reference case, presented in Chapter 3 and used in previous simulations, $\delta\theta/\delta t = 10^{-4\circ}\sqrt{g/d}$. The result is presented on Figure 5.8a. The figure shows no variation of hysteresis when reducing the angle rate. Hysteresis is then not influenced by a lower velocity at which the inclination angle is varied in the frictionless case. The stochastic nature of the transition is not responsible for the finite hysteresis measured at $\mu_p = 0$.

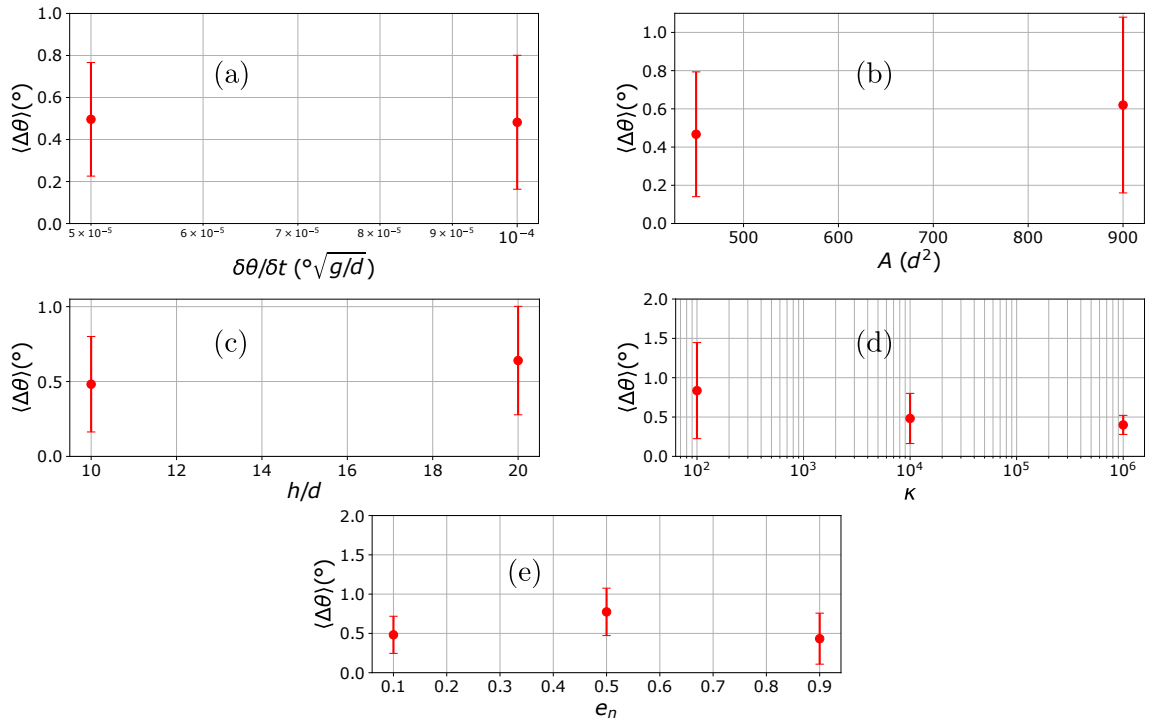

Figure 5.8 – Evolution of hysteresis $\Delta\theta$ with the velocity of angle imposition (a), the size of the domain $A = L \times W$ (b), the thickness of the grain layer h (c), the dimensionless stiffness κ (d) and the restitution coefficient e_N (e) in the frictionless case for dry granular media.

Domain size

Similarly, simulations has been computed in the frictionless case for bigger domain size $A = L \times W = 30d \times 30d$ than the one in the reference case $L \times W = 30d \times 15d$. The result is presented on Figure 5.8b. Hysteresis is slightly higher for the bigger domain. Such increase of hysteresis with A was not observed in the sensitivity analysis of Chapter 3, the trend shown a convergence with decreasing hysteresis. Nevertheless, this result allows us to qualify that the domain size is not responsible for hysteresis in the frictionless case.

Layer thickness

A bigger layer thickness $h/d = 20$ has also been tested on Figure 5.8c. This result show that hysteresis is slightly higher at the bigger layer thickness than $h/d = 10$. Nevetheless, the amount of hysteresis measured does not significantly vary with the layer thickness. This corresponds to the results of *Pouliquen and Forterre* (2002); *Staron* (2008); *Perrin et al.* (2019) showing no more effect of the layer thickness on the critical angles and hysteresis for layer thicknesses above ten times the grains diameter.

Restitution coefficient

The normal dissipation of dynamic contacts is modeled through the restitution coefficient e_n which could also eventually play a role in the value of critical angles hence hysteresis. Simulations have been conducted in the frictionless case for lower restitution coefficient than the reference one in the simulations $e_n = 0.9$. The results are shown in Figure 5.8e. This figure shows that for the lower value of restitution coefficient, $e_n = 0.1$, hysteresis is unchanged. Nevertheless a higher value is measured for the intermediate value of restitution coefficient, $e_n = 0.5$. Despite the slight variations for the intermediate value, the results are suggesting that contact dissipation is not a crucial parameter to characterize the transition between solid-like and liquid-like behavior of granular materials as depicted on the previous Chapter.

Normal stiffness

In the contact law presented in Chapter 3, the normal stiffness k_N model the stiffness of grains and plays a role in both the dynamic and static of contacts. This parameter is adimensionalised by the maximum pressure a grain holds in the system under the weight of a grain column of size equal to the layer thickness. It gives the dimensionless relative stiffness κ which sets the regime of rigidity of grains. Above $\kappa \approx 10^4$, the grains are considered rigid (*Roux and Combe*, 2002). In the rigid grain limit, the granular system deformations are purely plastic, the dominant energy mechanism is geometrical rearrangement that scale with the granular pressure and the jamming theory is relevant (*Favier De Coulomb et al.*, 2017). In that regime, critical angle and hysteresis results are in agreement with real grains experiments of *Pouliquen and Forterre* (2002) for example. For low relative stiffness values, low $\kappa \approx 10^2$, some elasto-plastic deformation-like behavior can appear as studied by *Favier De Coulomb et al.* (2017) which influences the critical stress

ratio and the critical coordination number. In order to study this effect which could play a role in the value of hysteresis measured, especially in the frictionless case, we computed simulations for different values of the relative stiffness κ. The results are presented on Figure 5.8d. The reference value of relative stiffness in the previous simulations is the rigid grain limit defined by *Roux and Combe* (2002) $\kappa = 10^4$. Two other values are computed, $\kappa = 10^2$ and $\kappa = 10^6$. The results show that hysteresis does not vary for relative stiffness higher than 10^4 validating this value as rigid grain limit. It also show that this parameter is not responsible for the amount of hysteresis measured in the frictionless case.

Finally, the above results demonstrate that varying the various parameters defining the limit of quasi-static evolution and infinite size system, i.e. $\delta\theta/\delta t$, A/d^2 and h/d as well as parameters driving normal contacts dissipation and stiffness, i.e. e_N and κ, does not lead to a reduction of hysteresis in the frictionless dry case. As a consequence, it shows the robustness of the finite hysteresis measured for frictionless particles.

5.3 Characterization of the effect of friction and inertia on the granular layer states

Now that critical angles and hysteresis variations with friction and inertia has been quantified, we focus on the quantification of the evolution of the granular states in order to characterize the evolution of critical angles with friction and inertia.
Firstly, the static state is characterized through the evolution of the packing fraction, the number of contacts, the fraction of sliding contacts and the anisotropy of the contact network. Hence, the critical angles are characterized by some of these variables evolution with μ_p and St in the static state.
Secondly, the evolution of the flowing state near jamming is studied, giving an insight on the granular structure and dynamic upon jamming transition.

5.3.1 Evolution and characterization of the jammed state

As presented in a previous Chapter and Section 5.1, the coordination number as well as the volume fraction evolves in the static state with friction and slightly with inertia. The main issue of this section is to characterise how the granular layer evolves in the static state at the macroscopic scale and at the scale of the contact network with friction and inertia and how both are linked.

Figure 5.9a shows the evolution of the critical coordination number on the stable state as a function of the microscopic friction coefficient for various Stokes number. It is observed that $\langle \mathcal{Z}_c \rangle$ is in between the lower bound for infinite friction coefficient $\mathcal{Z}_c(\mu_p \rightarrow \infty) = 4$ and the higher bound in the frictionless case $\mathcal{Z}_c(\mu_p = 0) = 6$ and varies with microscopic friction coefficient. Theses bounds and variation of the coordination number in the stable state was studied in several works (*Silbert et al.*, 2002b; *Song et al.*, 2008; *Wyart*, 2009). They demonstrated that the bounds could be calculated by counting the number of constraints and degrees of freedom in the system and calculating the limit values for frictionless particles and infinitely frictional ones with the Maxwell criteria of

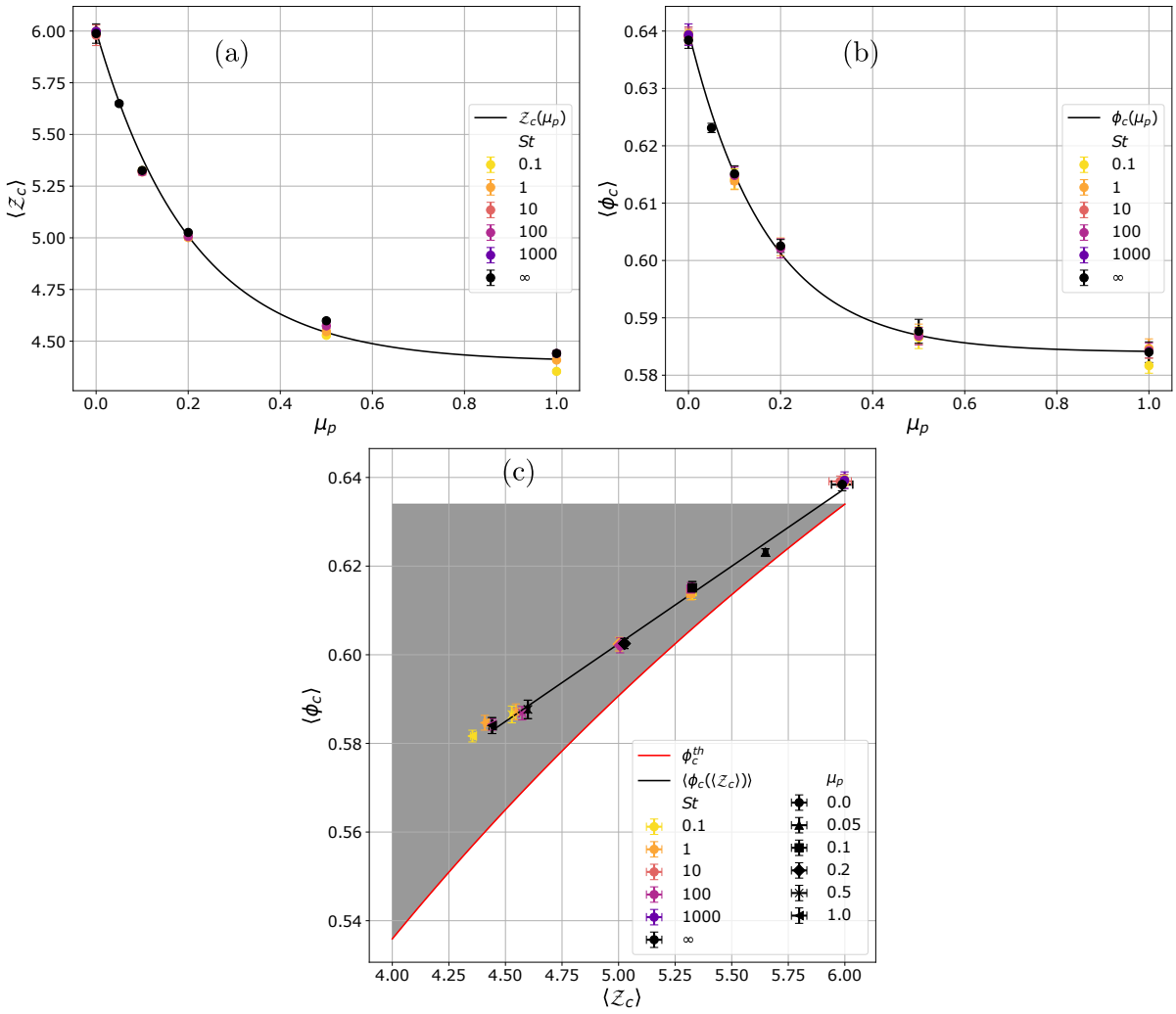

Figure 5.9 – (a) Evolution of the critical coordination number in the stable state $\mathcal{Z}_c$ with the inter-particle friction coefficient at various Stokes number. (b) Evolution of the critical volume fraction in the stable state ϕ_c with the micro friction coefficient at various Stokes number. (c) Critical volume fraction versus coordination number at various micro friction coefficient and Stokes number. It is compared to the phase diagram of jammed matter developed theoretically by *Song et al.* (2008).

stability of a mechanical system, see Sections 2.2 and 2.3. This figure show the dominant effect of the microscopic friction coefficient on the state of the contact network in the stable state. That had been highlighted by *Silbert et al.* (2002b) where they shown the effect of the restitution coefficient and the grain stiffness on the contact network density $\mathcal{Z}_c$ and the macroscopic density ϕ_c in the stable state. This latter effect on the coordination number have also been highlighted by *Favier De Coulomb et al.* (2017).
Interestingly, the variations of the macroscopic density, i.e the volume fraction ϕ, with both friction and Stokes number is presented on Figure 5.9b and appears to be similar to the one of the coordination number. The variations are also dominated by the Coulomb criteria μ_p which drives the density of the system in the jammed state. The volume fraction is also bounded, between the Random Close Packing, $\phi_{RCP} = 0.64$ in the frictionless case and the Random Loose Packing, $\phi_{RLP} = 0.55$ in the high frictional case *Song et al.* (2008). This similar evolution of both the coordination and the volume fraction in the jammed state had been highlighted by *Silbert et al.* (2002b). It appears that the density of the contact network and the density measured at the macro-scale are linked in the stable state. This idea was developed in the work of *Song et al.* (2008) where they defined a phase diagram of jammed granular materials. In this phase diagram plotted here on Figure 5.9c the evolution of the volume fraction is linear with the coordination number when varying inter-particle friction and inertia in our simulations. This lead us to express the linear relation between $\mathcal{Z}_c$ and ϕ_c. Considering that in the frictionless case $\mathcal{Z}_c = 6$ and $\phi_c = \phi_{RCP}$ and in the limit of infinite friction $\mathcal{Z}_c = 4$ and $\phi_c = \phi_{RLP,min}$ it gives the following equation between the coordination number and the volume fraction in the stable state for the inclined plane configuration:

$$\phi_c = \frac{1}{2}(\phi_{RCP} - \phi_{RLP,min})\mathcal{Z}_c + (3\phi_{RLP,min} - 2\phi_{RCP}), \tag{5.1}$$

with $\phi_{RLP,min} = 0.57$ a fitting parameter in our results which is pretty close to observed values (*Silbert*, 2010). Note that the linear behaviour of $\phi_c(\mathcal{Z}_c)$ with μ_p and St in the configuration of the inclined plane shows that ϕ_i, the initial volume fraction that leads to the static state, constantly evolves with θ within our simulations (*Song et al.*, 2008). This shows that when not constrained by packing a granular medium on an inclined plane will adapt the amount of contact and the density in order to stabilise following the linear Equation (5.1) when friction or inertia are varied.
Equation (5.1) shows the link between the macroscopic packing density of the granular layer and the density of the contact network, characterised by the amount of contact per particle.

As discussed in the previous section, the amplitude of contact anisotropy in the stable state also evolves with the inter-particle-friction and slightly with inertia. Figure 5.10 presents these evolution. It can be observed that as shown by the qualitative analysis, the average contact anisotropy is decreasing with the friction coefficient from $a_c^c \approx 0.42$ at high $\mu_p = 0.5$ and $\mu_p = 1$ down to $a_c^c \approx 0.17$ at $\mu_p = 0$. These values and evolution are consistent with results from *Srivastava et al.* (2022). In contrast with friction, contact anisotropy slightly increases when the Stokes number decreases. These variations are very similar to the variations of the critical angles and suggest that the the level of contact anisotropy of a granular system in the stable state is related to the angle at which the system reaches or leave stability. Nonetheless, the contact anisotropy saturates at high

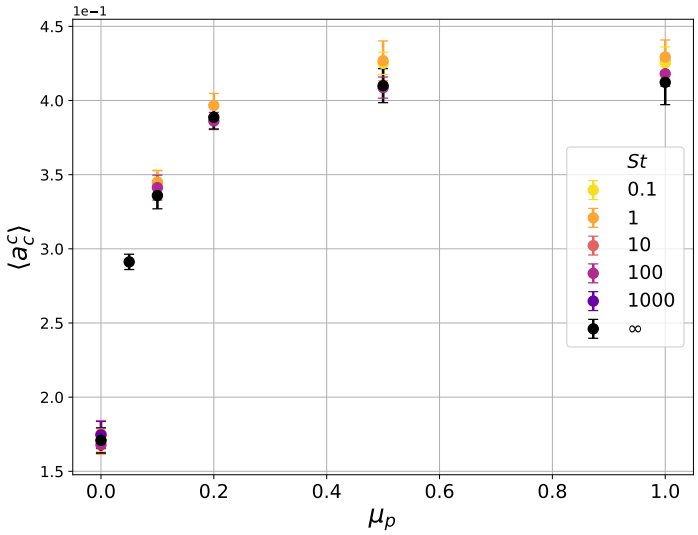

Figure 5.10 – Evolution of the critical contact anisotropy in the jammed state with the inter-particle friction coefficient at various Stokes number.

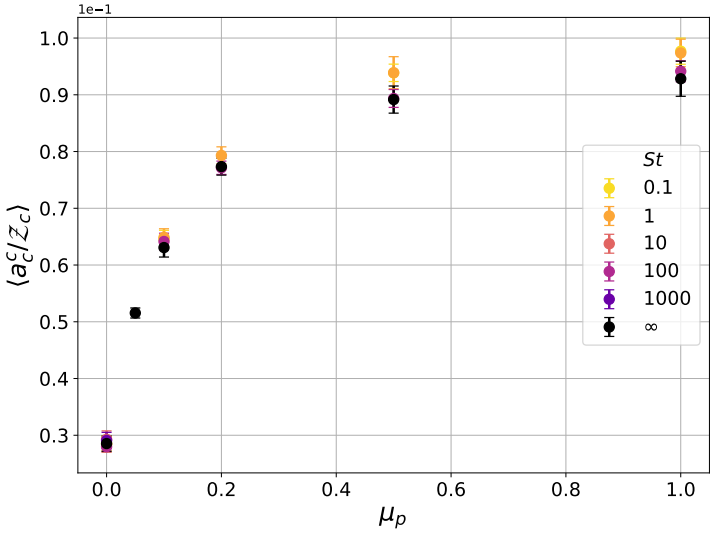

Figure 5.11 – Evolution of the critical contact anisotropy relative to the average number of contacts in the jammed state with the inter-particle friction coefficient at various Stokes number.

friction, the values between $\mu_p = 0.5$ and $\mu_p = 1$ are stricly the same although the critical angles evolves between these friction values.

An interesting variable defined by *Srivastava et al.* (2022) that characterises the jammed state is the ratio between contact anisotropy a^c and the average number of contact $\mathcal{Z}$. This variable quantify how anisotrop is the contact network with respect to the average number of contacts in the system. This variable is plotted in the jammed state versus inter-particle friction at various Stokes on Figure 5.11. The Figure shows that in contrast to Figure 5.10, the contact anisotropy does not saturate at high friction and follow the evolution of critical angles.

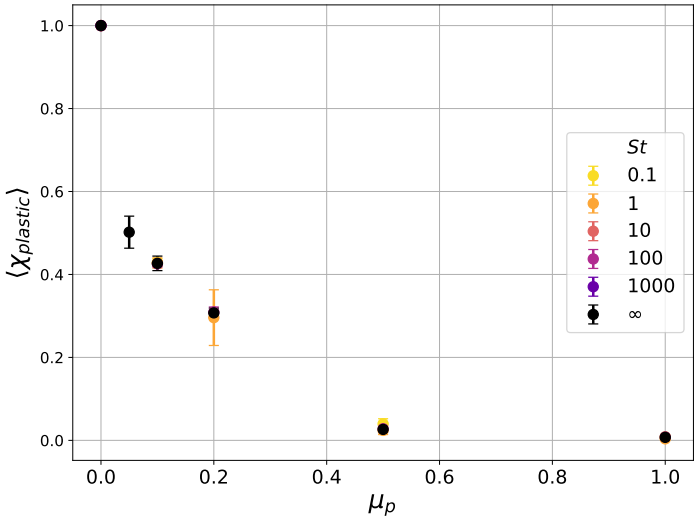

Figure 5.12 – Evolution of the highest pick of fraction of sliding contacts in the jammed state with the inter-particle friction coefficient at various Stokes numbers.

Similarly, the evolution of the highest pick of the fraction of sliding contacts in the jammed state, $\chi_{plastic}$, that occurs near the avalanche is plotted as a function of the inter-particle friction coefficient at various Stokes number on Figure 5.12. It decreases when increasing the friction between grains and is independent to the Stokes number. The independence with the Stokes number is related to the fact that in the static state the rearrangement observed in the system are signatures of local displacement of grains. The velocities of these rearrangements are then extremely small as observed on the Section 4.2.3. Since the drag force is proportional to the velocities of grains at low Stokes, no significant dissipation is observed on these rearrangements. In contrast, the effect of friction is non-negligible. Interestingly, three different behaviors are observed on the contact sliding fraction: in the frictionless case $\chi(\mu_p = 0) = 1$ since all contacts are sliding; at high friction coefficient, i.e $\mu_p \geq 0.5$, almost no contacts are sliding; for intermediate inter-particle friction coefficients, i.e $0 < \mu_p < 0.5$ the fraction of sliding contacts is progressively decreasing with when increasing friction. Those behaviors are consistent with the observations of *DeGiuli et al.* (2016) in 2D numerical simulations where they defined the phase diagram of friction behaviors between respectively "frictionless", "frictional sliding" and "rolling" regimes of friction between grains.

5.3.2 Characterisation of the critical angles with the micro-structure in the jammed state

On this section we look back at the critical angles in order to see if their variations with friction and inertia can be characterised by the values of the micro-structure state variables in the jammed state.

On the one hand, the avalanche angle resulting from destabilisation from the static state, some state variables within that state might be good candidates to characterise its evolution. As presented in the Section 5.2, the avalanche angle is significantly dependant on the friction between grains and slightly with grains inertia. Figure 5.13a presents the evolution of the avalanche angle with the static coordination number at various friction and inertia values. The figure shows that the avalanche angle is directly related to the coordination number in the static state. The avalanche angle depending only on the static coordination number, it is the result of the granular medium arrangement at rest. Meanwhile, the loading process from the static state, has been observed to be a dynamic process in the literature (*Staron et al.*, 2002; *Aranson and Tsimring*, 2006; *Zaitsev et al.*, 2008) as well as in the present study, with re-arrangement occurring continuously with increasing angle before reaching failure. The present result therefore suggests that the onset of motion linked to progressive re-arrangement is weakly influenced by the presence of an interstitial fluid, which is also captured by the weak variations of the static coordination number, even down to avalanche Stokes number of order one. This idea is related to the independence of the fraction of sliding contacts in the stable state near the avalanche onset of the previous Section. Despite the variations of the fraction of sliding contacts with the inter-particle friction, the existence of a single function that relates the static coordination number to the avalanche angle suggest that the fraction of sliding contacts is not a necessary proxy to characterize the variations of the avalanche angle with friction between grains.

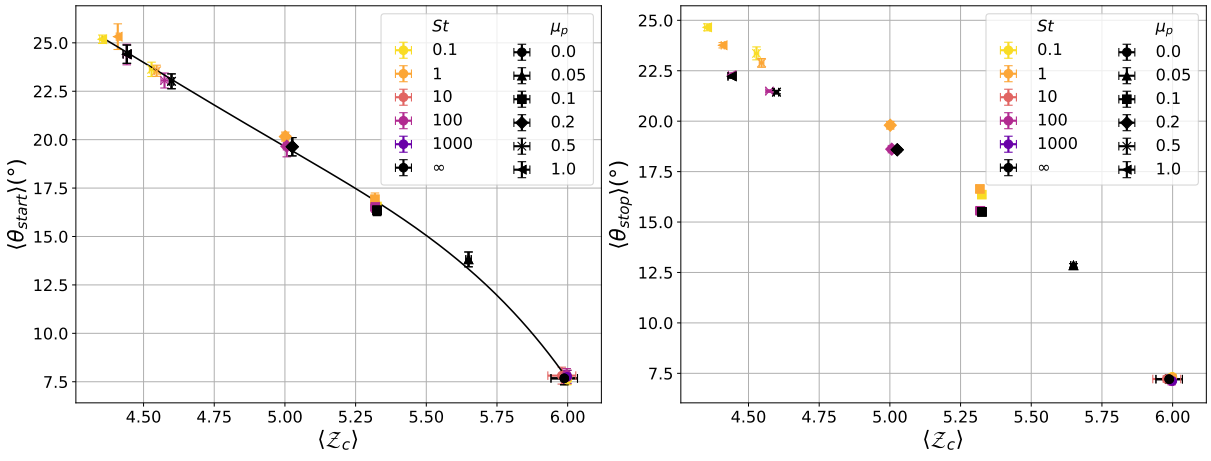

(a) (b)

Figure 5.13 – Evolution of (a) the avalanche angle θ_{start} and (b) the jamming angle θ_{stop} with the coordination number in the stable state at various microscopic friction coefficient and Stokes number.

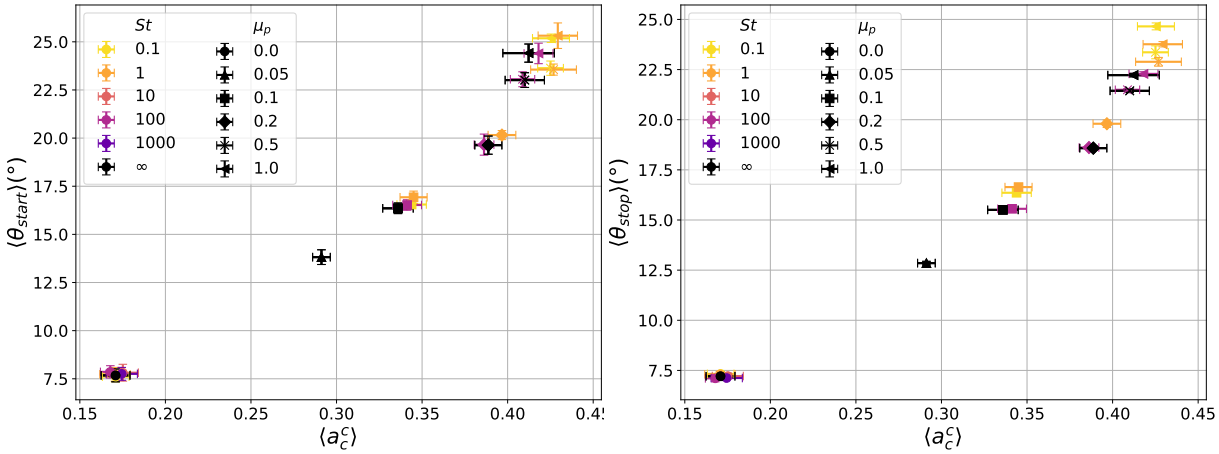

(a) (b)

Figure 5.14 – Evolution of (a) the avalanche angle θ_{start} and (b) the jamming angle θ_{stop} with the contact anisotropy in the stable state at various microscopic friction coefficient and Stokes number.

The fact that the avalanche angle is related to the amount of contacts per particles in the system is supported by the link between the similar evolution of the critical angles and the contact network anisotropy with μ_p and St. In order to see that, the avalanche angle is plotted as a function of the contact network anisotropy in the jammed state at various friction and inertia values. This plot is shown by Figure 5.14a. The Figure shows that equivalently to the static coordination number, the avalanche angle is following a single function of the static contact anisotropy with Stokes and μ_p for the frictionless and the intermediate friction regimes. At high friction coefficients (≥ 0.5) the avalanche angle variations are no more similarly captured by variations of the static contact anisotropy conversely to the static coordination number. This result show the saturation of the geometrical anisotropy at high inter-particle friction, i.e the signature of the early convergence of the static contact anistropy observe on the Figure 5.10 compared to the convergence of the avalanche angle of Figure 5.2. Dividing the geometrical contact anisotropy by the average number of contact allows us to characterise the avalanche angle with a variable that evolves similarly at all frictional regimes. Figure 5.15a present this result. It shows that the avalanche angle evolves linearly with $a_c^c/\mathcal{Z}_c$ with variations of μ_p. However, at high friction, some departures are observed with variations of Stokes.

On another hand, the variations of the jamming angle, θ_{stop}, with both the static coordination number, the static contact anisotropy and their ratio are presented respectively on Figures 5.13b, 5.14b and 5.15b. They all show that the variations of stopping angle with the inter-particle friction coefficient in the dry case and at low Stokes number ($St = 1$ and $St = 0.1$) does not follow the same functions of $\mathcal{Z}_c$, a_c^c and their ratio $a_c^c/\mathcal{Z}_c$. Indeed, the non-negligible effect of inertia on the stopping angle is not characterised by the variations of the micro-structure state variables in the stable state. Nevertheless, the variations of θ_{stop} and a_c^c with Stokes in the rolling regime are more similar than for the avalanche angle. This suggests that the static contact anisotropy is similarly influenced by variations of the stopping angle when it comes from friction effect and inertia effect.

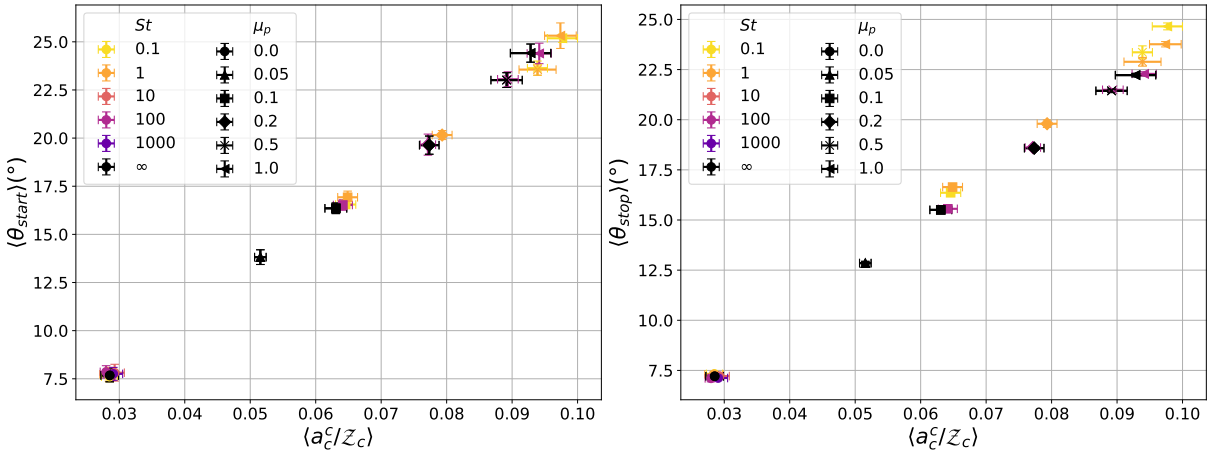

(a) (b)

Figure 5.15 – Evolution of (a) the avalanche angle θ_{start} and (b) the jamming angle θ_{stop} with the contact anisotropy relative to the average number of contacts in the stable state at various microscopic friction coefficient and Stokes number.

In all cases, the absence of a single function between the stopping angle and the static coordination number with variations of friction and Stokes number is a signature that the stopping angle values are dependent on the evolution of the micro-structure in the flowing state rather than in the static regime.

5.3.3 Evolution of the flowing state near jamming with friction and inertia

Macroscopic state variables

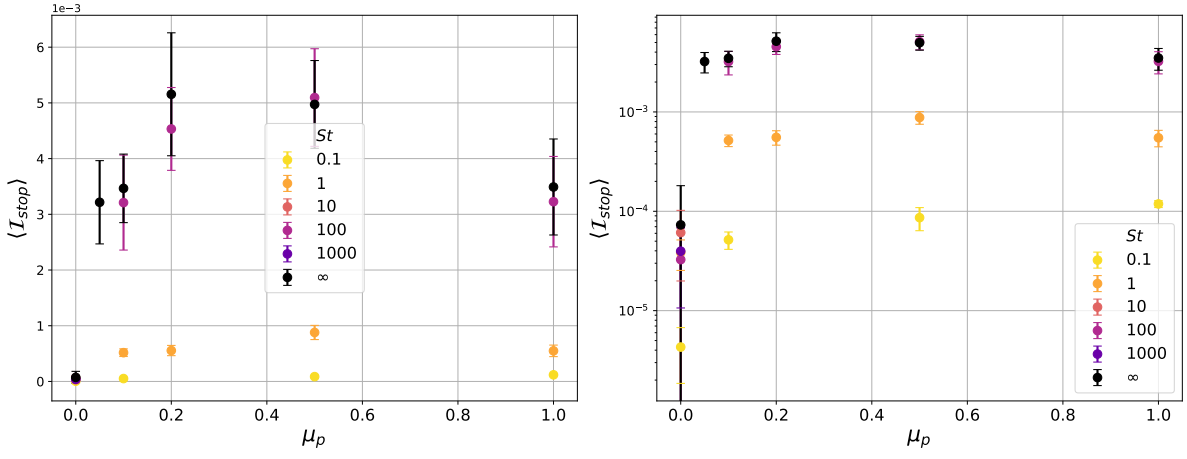

(a) (b)

Figure 5.16 – Inertial number in the flowing state just before jamming, i.e $\mathcal{I}_{stop}$, as a function of the inter-particle friction coefficient at various Stokes numbers (a) in linear scale (b) in logarithm scale.

This section focuses on the evolution of the macroscopic state variables in the flowing state near jamming with the inter-particle friction and the Stokes number in order to quantitatively characterize the state of the granular system in the flowing regime and therefore the stopping angle.

First, the critical inertial number in the flowing state at the transition from flow to rest, i.e $\mathcal{I}_{stop}$, is plotted versus the friction coefficient between grains at various Stokes number on the Figure 5.16a. The first observation is that $\mathcal{I}_{stop}$ is increasing when decreasing μ_p between the rolling regime at high μ_p into the frictional sliding regime at $\mu_p = 0.2$. Below this regime the inertial number is decreasing with decreasing μ_p into a strongly low value for frictionless particles. Figure 5.16b presents the same results in logarithm scale showing the low but finite inertial number values in the frictionless case. The inertial number is also very influenced by the Stokes number since its values are fifth time lower at $St = 1$ than in the dry case. This shows that lowering grains inertia has the influence of lowering the pressure-relative inertia of the assembly of grains. This plot also provides an insight into the sharp drop in hysteresis observed at intermediate friction coefficients ($\mu_p \in [0.1, 0.2]$) when decreasing the Stokes number on Figures 5.4 and 5.5. Indeed, the drop of inertial number is also very sharp at these friction coefficients between the dry case and the viscous case where the differences in inertial numbers are not that sharp in the frictionless case. As a consequence, although the inertial number is not sufficient to predict neither the stopping angle evolution nor the hysteresis evolution with friction and inertia, it enables to characterises the various frictional and inertial/viscous flowing regimes near jamming.

The volume fraction is also plotted in the flowing regime near jamming on Figure 5.17.

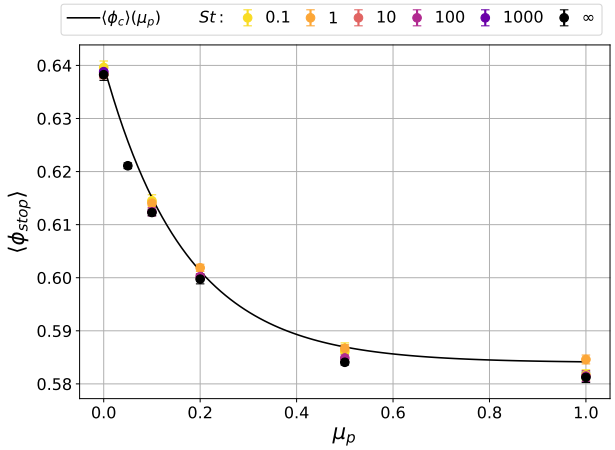

Figure 5.17 – Volume fraction in the flowing state just before jamming as a function of the inter-particle friction coefficient at various Stokes numbers.

The figure shows that the volume fraction evolves similarly with friction and inertia than the static volume fraction that is represented with the black curve. This similar evolution shows that packing density values in the flowing state near jamming is coherently evolving and mainly driven by friction between grains as its values in the static state. In addition, the plot allows us to see that it gets closer and closer to the critical static volume fraction when reducing the friction between grains or the inertia of grains. This result shows that

the slight amount of compaction observed at high friction coefficient on the hysteretic cycle of the volume fraction in Section 4.3 is vanishing at lower friction (especially in the frictionless case) or at lower Stokes numbers, as discussed in the previous Section and Chapter. It shows that the approach to the static state is continuous in terms of packing density when killing sources of hysteresis, i.e friction and inertia. This continuity suggest a reversible transition. Nevertheless hysteresis is still observed for these values of friction and inertia of grains.

Micro-structure's state variables

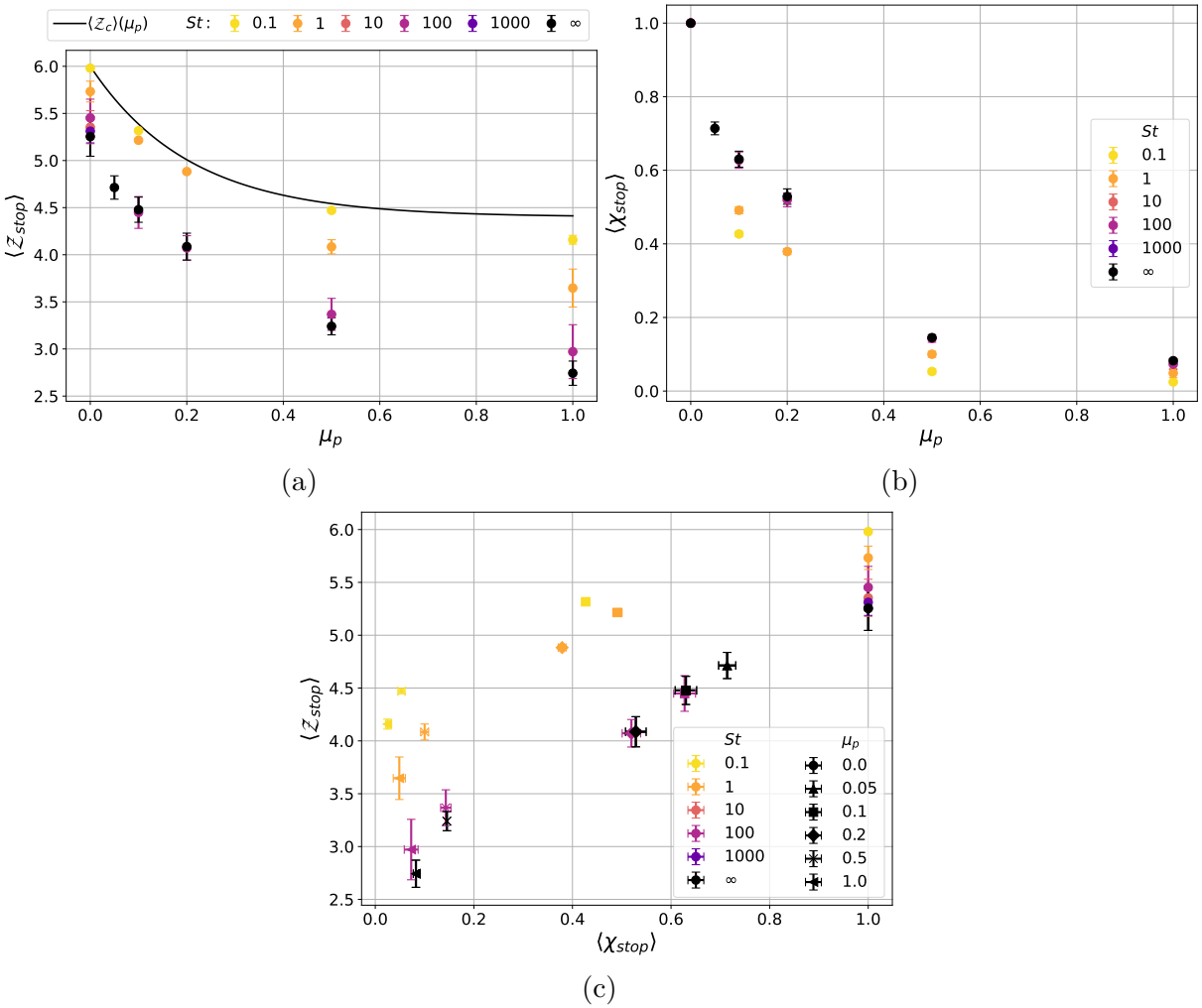

Figure 5.18 – (a) Coordination number in the flowing state at jamming versus the inter-particle friction coefficient at various Stokes numbers. (b) Fraction of sliding contacts in the flowing state at jamming versus the inter-particle friction coefficient at various Stokes numbers. (c) Coordination number in the flowing state versus the fraction of sliding contacts in the flowing state at jamming for various inter-particle friction coefficient and Stokes numbers.

The focus of this part is to study how the micro-structure evolves in the flowing state near the jamming transition, in order to characterize the processus of accession to stability.

First, the coordination number is plotted near jamming as a function of the coefficient of friction between grains for various Stokes number on Figure 5.18a. The coordination number near before the jamming transition, $\mathcal{Z}_{stop}$, is evolving in a similar way than the critical value in the stable state when varying the friction coefficient at a given Stokes number. In order to compare them the curve $\mathcal{Z}_c(\mu_p)$ is also plotted on the Figure. In contrast to the critical static evolution, it also displays a non-negligible variation with the Stokes number leading to closer value near jamming to the critical value at jamming. This latter results means that the discontinuity of coordination number at the jamming transition $\Delta\mathcal{Z}_{stop} = \mathcal{Z}_c - \mathcal{Z}_{stop}$ quantifying the sharp gain of contacts when the medium change of state and becomes rigid is lower when reducing inertia. Decreasing the friction between grains also brings $\mathcal{Z}_{stop}$ towards $\mathcal{Z}_c$ hence reduce the discontinuity. It shows that decreasing friction or inertia plays a similar role in allowing the medium to flow at higher coordination numbers, i.e higher amount of contacts in the system.

The fraction of sliding contacts is also plotted in the flowing regime near the jamming transition versus inter-particle friction at various Stokes numbers. This is presented on Figure 5.18b. The Figure shows an increase of the fraction of sliding contacts when the friction is decreasing which is a signature of the evolution of the Coulomb criteria on the whole tangential contact network. One can observe that similarly to the variations of sliding contacts in the static state, the three friction regimes are observed on the plot of Figure 5.18b. In the frictionless case all contacts are sliding, in the frictional sliding regime most of the contacts are sliding near jamming and it strongly decreases when increasing μ_p. Finally in the frictional rolling regime the fraction of sliding contacts are low (about 10%) and variations of inertia does not vary much the amount of sliding contacts. This evolution also shows how constrained the tangential contact network become at high friction and how easily tangential contacts are mobilised when decreasing friction. Figure 5.18c presents the coordination number plotted versus the fraction of sliding contacts both in the flowing state near jamming at various μ_p and St. The Figure shows that increasing the fraction of sliding contacts by decreasing friction leads to an increase of the amount of contacts per particle in the flowing state just before jamming. Sliding contacts allows particles to flow in the tangential direction of the contact, tangential stability is then harder to reach for particles at low inter-particle friction. In that case, since particles have a lower criterion of tangential stability at each contacts, they need more contacts in order to reach stability which occurs at lower inclination angles.

The decrease of inertia at a given friction coefficient implies a lower value of sliding contacts on Figure 5.18b. This can be interpreted as an additional motion dissipation mechanism that helps contacts to reach tangential stability hence to stop sliding. This dissipation of motion is also responsible for the increase of amount of contacts in the system observed on Figure 5.18c and Figure 5.18a as discussed above.

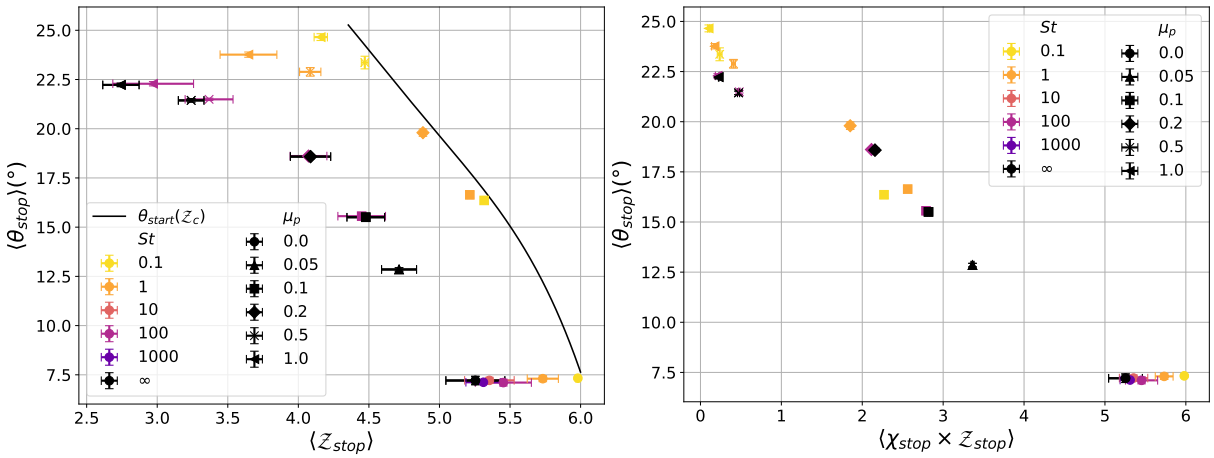

(a) (b)

Figure 5.19 – (a) Evolution of the jamming angle θ_{stop} with the coordination number in the flowing state near jamming at various microscopic friction coefficient and Stokes number. (b) Evolution of the jamming angle θ_{stop} with the coordination number in the flowing state near jamming times the fraction of sliding contacts near jamming at various microscopic friction coefficient and Stokes number.

5.3.4 Characterisation of the jamming angle with the micro-structure in the flowing state

Jamming occurs with complex dissipation processes in the flowing state since it results from the self-sustainability of perturbations. Characterizing the stopping angle with micro-structure state variables is then more complex than with the avalanche angle and no micro-structure variable captures equivalently viscous and friction dissipation influence on the stopping angle. Meanwhile, it is possible to understand the mechanisms at play by considering the evolution of the coordination number in the flowing state before jamming, $\mathcal{Z}_{stop}$. Figure 5.19a presents the evolution of the stopping angle as a function of this variable. The black curve is the fit of the starting angle dependence on the coordination number in the static state $\theta_{start}(\mathcal{Z}_c)$. For a given Stokes number, the stopping angle is observed to be a decreasing function of the coordination number in the flowing state before jamming, similarly to the trend observed for avalanche angle with the critical coordination number. When lowering the Stokes number at given friction coefficient, $\mathcal{Z}_{stop}$ tends toward the static coordination number, so that the discontinuous jump at jamming tends toward zero. This suggests that the stopping goes toward the avalanche angle, and hysteresis decreases. This result motivates the choice of characterising hysteresis with the discontinuities observed at transitions in the following Section 5.4.

Nevertheless, in order to try to characterize the variations of stopping angle with friction and inertia, we look back at the results of Figure 5.18c given in the previous Section 5.3.3. It can be observed on Figure 5.18c that the plots does not collapse for low and high Stokes numbers. This can be seen as a signature of the non collapsing evolution of the stop angle with the friction coefficient at various Stokes number. In order to show that and model the stopping angle, it is important to take into account both evolution

of contacts and the sliding ratio. To do so, the stop angle is plotted as a function of the fraction of contacts per particle that is sliding in the flowing regime: $\mathcal{Z}_{stop}\chi_{stop}$ on Figure 5.19b. This variable measures the density of sliding contacts in the system and appears to make St and μ_p effects collapse on the same curve $\theta_{stop}(\mathcal{Z}_{stop}\chi_{stop})$ at least for the intermediate frictional sliding regime. Indeed, in the frictionless case since all contacts are sliding, $\chi = 1$, the curve display only the evolution of the stop angle with the coordination number near jamming (similar to Figure 5.19a). At high friction, $\mu_p \geq 0.5$, the friction effect saturates and the ratio of sliding contacts became very low. Then, in that regime the variable $\mathcal{Z}_{stop}\chi_{stop}$ does not measure the effect of inertia on the stopping angle. Finally, for intermediate friction coefficient the variable captures the combined effects of friction and inertia and the stopping angle appears to be linear with $\mathcal{Z}_{stop}\chi_{stop}$ for various friction and inertia. In another words, in the intermediate frictional sliding regime the density of sliding contacts, which can be varied with variations of the Coulomb criteria or the viscous dissipation, defines the stop angle. It suggests a non trivial evolution of the rheology near the jamming transition with the friction coefficient.

Further analysis are required in order to model the stopping angle in the three separate regimes of friction, especially in the frictionless regime and the frictional rolling regime.

5.4 Transition's asymmetry

In this section discontinuities of several variables that highlighted the asymmetry of the transitions between the static and the flowing regime of the granular medium are discussed. These discontinuities are also used in order to characterize the measure of the asymmetry of the transition, i.e. the absolute hysteresis $\Delta\theta$. This latter measure of asymmetry is plotted versus the inter-particle friction coefficient at various Stokes number on Figure 5.20 in order to visually compare the other measures of asymmetry to this curve in the whole section.

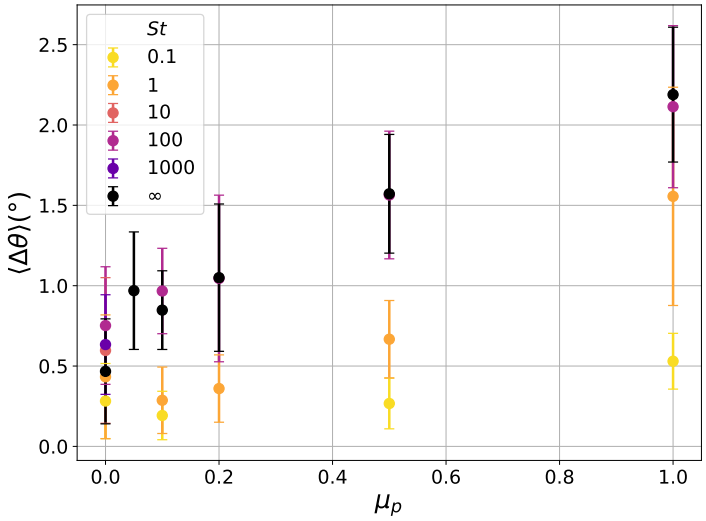

Figure 5.20 – Evolution of the absolute hysteresis versus the inter-particle friction coefficient at various Stokes numbers.

5.4.1 Discontinuities of volume fraction

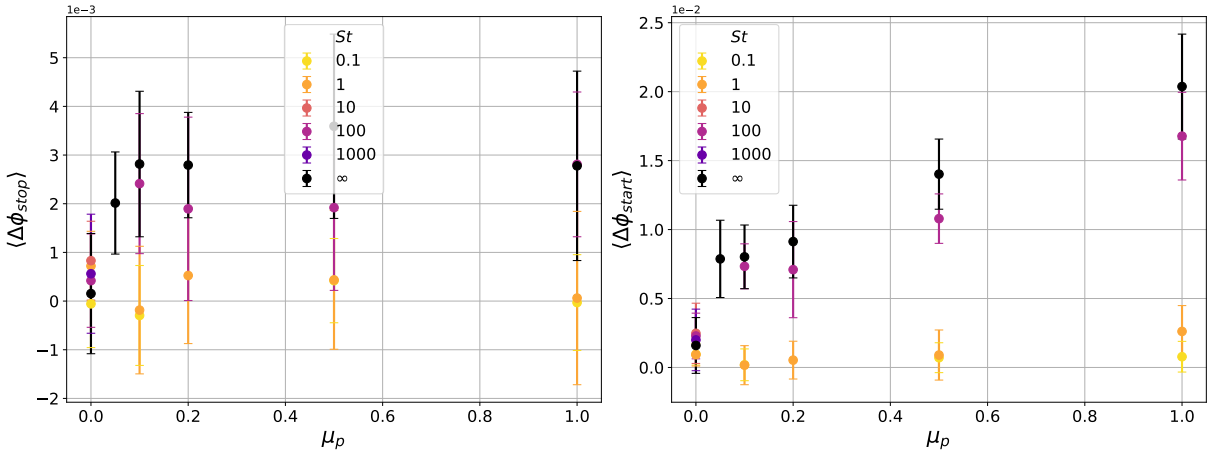

(a) (b)

Figure 5.21 – (a) Evolution of the discontinuity of volume fraction, or compaction, at jamming versus microscopic friction coefficient at various Stokes number. (b) Evolution of the discontinuity of volume fraction, or dilatancy, at unjamming versus microscopic friction coefficient at various Stokes number.

The discontinuities of volume fraction that were observed slightly at the jamming transition (compaction at the stability accession) and clearly at the unjamming transition (dilatancy at the initiation of flow) are respectively plotted versus the inter-particle friction coefficient at various Stokes numbers on Figures 5.21a and 5.21b. First, Figure 5.21a shows that as discussed in the previous chapter, Section 4.3, no clear compaction is observed on the volume fraction except for highly frictional dry grains. This shows that the accession to stability is continuous with regards to the average density of the layer at the macroscopic scale.

By contrast, the discontinuity at the avalanche transition, or yield dilatancy, evolves pretty similarly than hysteresis. Indeed, it decreases with friction following an equivalent function of μ_p and also decreases when decreasing the inertia of grains. These results are coherent with the analysis developed in the qualitative analysis Section 4.3 that the less asymmetrical is the transition the lower is the yield dilatancy. Hence, hysteresis may be linked to the discontinuity of packing density at the avalanche transition, i.e. the measurement of a yield dilatancy of the system. This link will to be highlighted in the following Section.

5.4.2 Link between hysteresis and dilatancy

In order to compare the evolution of $\Delta\phi$ and $\Delta\theta$ the latter is plotted versus the first one on Figure 5.22. This figure shows that Hysteresis is globally related with the yield dilatancy at the avalanche by a linear relation. This relation shows that for finite friction coefficients and high Stokes number the dilatancy at the avalanche transition is a good measure of the hysteretic asymmetry of the transitions. Nevertheless, the presence of

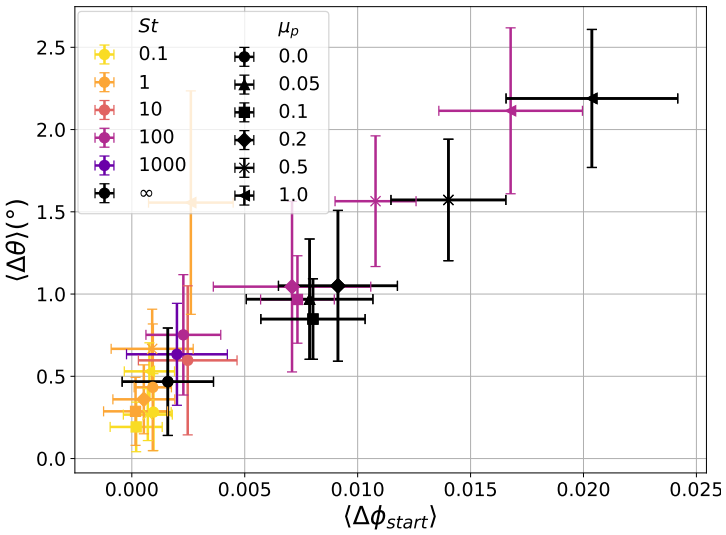

Figure 5.22 – Hysteresis versus the discontinuity of packing density, i.e dilatancy effect, at the initiation of flow for various inter-particle friction and Stokes numbers.

hysteresis for frictionless particles in our results seems in apparent contradiction with the vanishing dilatancy observed in such case (*Peyneau and Roux*, 2008). The latter suggested a smooth unjamming transition, and accordingly the absence of hysteresis for frictionless particles *Perrin et al.* (2019); *Bagnold* (1966). Here, similar vanishing dilatancy is observed, it drops to zero for low values of inter-particle friction and Stokes number while hysteresis is finite. As such, it does not capture the hysteresis nature of the transition when the sources of hysteresis are almost negligible. Hence, the dilatancy is not the good proxy to characterize hysteresis on a rough inclined plane. In addition, it shows that the volume fraction can displays continuous evolution at both transitions suggesting second-order phase transitions hence no hysteresis. This result then shows that volume fraction is not fine enough to capture the slight variations of the system at transitions when inter-particle friction and/or Stokes number are low.

5.4.3 Discontinuities of Coordination number

Similarly to volume fraction, the discontinuities of coordination number are plotted at the cessation of flow on Figure 5.23a and at the initiation of flow on Figure 5.23b.

The figures show decreasing discontinuities respectively at the jamming and unjamming transitions when decreasing friction as well as grains inertia. In addition, conversely to volume fraction, as discussed in the qualitative Section, the coordination number always displays a discontinuity, even very low (at $\mu_p = 0$ and $St = 0.1$) at the cessation and initiation of flow. The evolution of these discontinuities are similar to the variations of hysteresis with μ_p and St which will be discussed in the following Section.

The second Figure 5.23b shows that the unjamming discontinuity of coordination number is higher than the one at jamming. This is coherent with the fact that the flowing

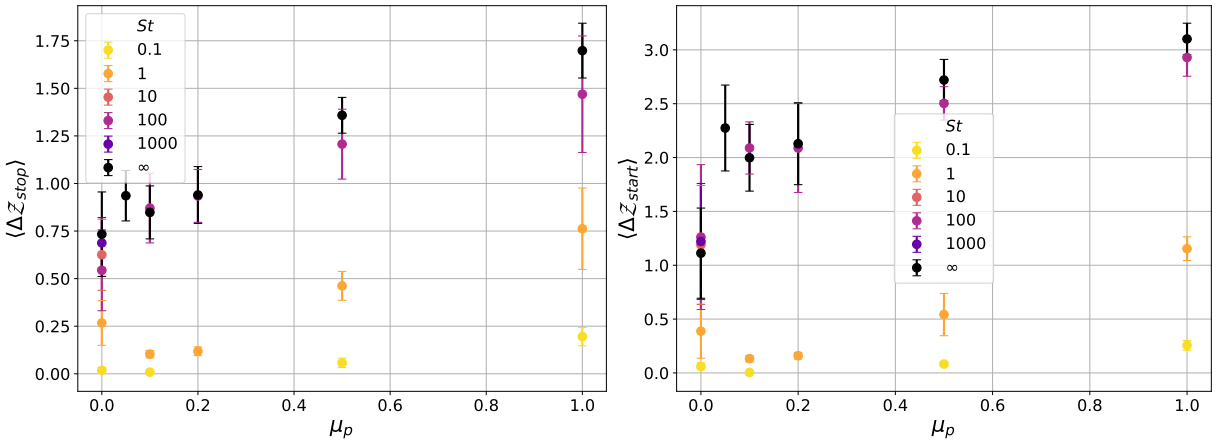

(a) (b)

Figure 5.23 – (a) Evolution of the discontinuity of coordination number, or compaction of the contact network, at jamming versus microscopic friction coefficient at various Stokes number. (b) Evolution of the discontinuity of coordination number, or decompaction of the contact network, at unjamming versus microscopic friction coefficient at various Stokes number.

regime at $\theta = \theta_{start}$ is faster and looser and grains have less contacts than in the flowing regime at a lower angle ($\theta = \theta_{stop}$). Nevertheless, these differences tend to disappear for low inertia. Indeed, when the flow is dissipated by a viscous fluid, the medium flows with a significant amount of contact as shown in Section 5.1 and the variations of contact number in the flowing regime between the avalanche and the stopping angles are negligible. In other words the amount of contacts in the flowing regime near the transitions does not significantly varied with the inclination angle.

5.4.4 Link between hysteresis and discontinuities of contact number

Accordingly, Figure 5.24a presents hysteresis as a function of the discontinuity of coordination number at the jamming transition. It can be observed that hysteresis scales correctly with this discontinuity, making microscopic friction and viscous dissipation collapse on the same curve $\Delta\theta(\Delta\mathcal{Z}_{stop})$. The discontinuity measures how much the self-sustainability process leads to higher hysteresis by lowering the number of contacts in the flowing state $\mathcal{Z}_{stop}$ compared to the value required to be stable $\mathcal{Z}_c$. In other words, when decreasing independently the microscopic friction coefficient or the Stokes number, hysteresis as much as the discontinuity of coordination number at jamming, are equivalently decreasing. This shows that the asymmetry of the transition between the liquid-like and solid-like behaviors of granular media down inclined plane can be characterized by the discontinuity of coordination number at jamming. In particular, the absence of coordination number discontinuity at jamming should be characteristic of an absence of hysteresis. In this case the transition is expected to be reversible and without hysteresis. Here, it can be observed that the hysteresis is not dropping to zero while the discontinuity of coordination number is almost vanishing in Figure 5.24a. The artificially low contact

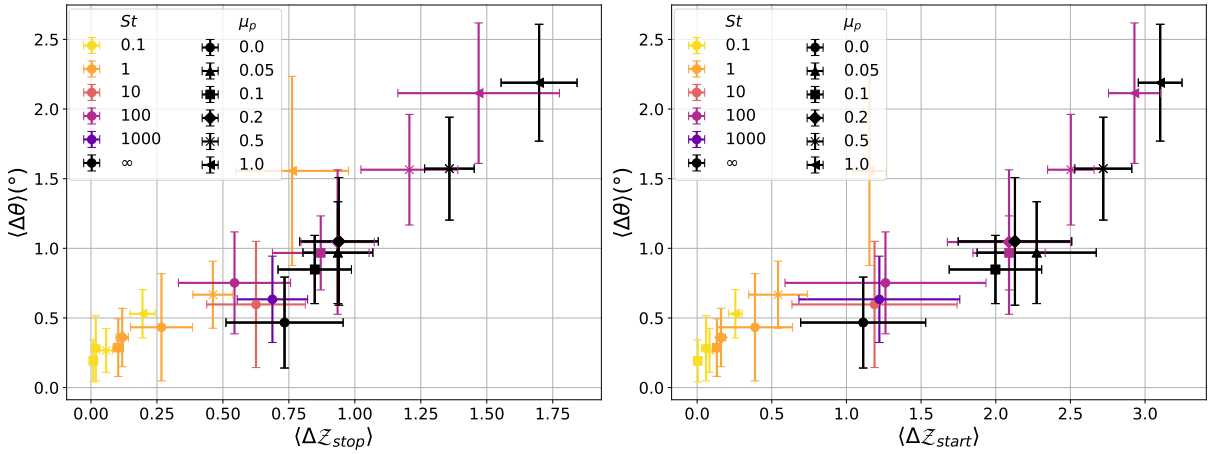

(a) (b)

Figure 5.24 – Hysteresis versus the discontinuity of coordination number at the cessation of flow (a) and at the initiation of flow (b) for various inter-particle friction and Stokes numbers.

stiffness used in the simulations for computational reasons leads to an underestimation of the discontinuity of coordination number for a given hysteresis as shown by Figure 5.25a. This underestimation should shift the points of Figure 5.24a to the right, and we expect to recover the right trend accordingly.

Similarly, hysteresis scale with the discontinuity of coordination number at the avalanche as it can be observed on Figure 5.24b. The scale appears to saturate at high friction coefficients and Stokes numbers. However this scale can be interpreted as a characterisation of the hysteresis with the distance between the amount of contact the medium is supposed to have while flowing at $\theta = \theta_{start}$ in order to continuously reach the static state (which is $\mathcal{Z}_c$) and the actual amount of contacts the medium made at $\theta = \theta_{start}$ which is $\mathcal{Z}_{start}$. Although close to zero this discontinuity is slightly higher than the discontinuity at jamming, it remains underestimated by stiffness effect as shown by Figure 5.25b.

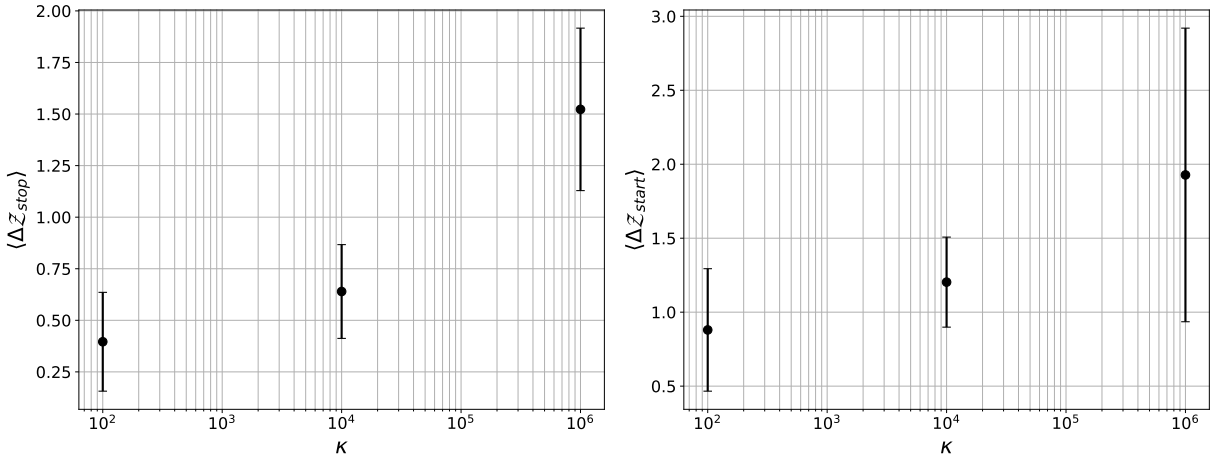

(a) (b)

Figure 5.25 – Coordination number discontinuity (a) at jamming and (b) at unjamming versus relative stiffness in the dry frictionless case ($\mu_p = 0$, $St = \infty$).

Conclusion

The results have shown that hysteresis depends on the combined effect of both particle friction and inertia. The hysteresis is observed to decrease with decreasing friction, and to decrease with decreasing inertia. The present results and analysis allows us to rationalize the different existing results on hysteresis dependency through either friction or inertia. This contrasts with the framework proposed by *DeGiuli and Wyart* (2017), linking hysteresis model to inter-particle friction through the sliding contact proportion which cannot predict the finite amount of hysteresis measured for frictionless particles in our simulations, and suggests the need for further development to account for inertia effects.

The present work has shown that solid volume fraction is not sufficiently sensitive to display an apparent compaction or dilatancy at the cessation and the initiation of flow in the frictionless case and at low friction and Stokes number values. Yet, the discotinuity of coordination number characterizes the transition asymmetry, and hysteresis has been shown to scale with the coordination number discontinuity at jamming and unjamming. These results highlight the strong link between the jamming-unjamming transition and the evolution of the granular micro-structure through friction and inertia.

Especially, the results higlighted the three regimes of inter-particle friction defined by *DeGiuli et al.* (2016), which render the evolution of the stopping angle with both friction and inertia non-trivial to model. Further analysis are needed to develop a theoretical framework that allows one to model the stopping angle through stability criterion of the whole grain layer.

Besides, the static amount of contact in the stable state and the anisotropy of the contact network have shown to characterize the angle of destabilisation, i.e. the avalanche angle θ_{start}. This shows that despite non-local plasticity processes that leads to the destabilisation of the grain layer, the variations of the contact network anisotropic orientation relatively to the average amount of contact in the static state can predict the variations of avalanche angle with friction and inertia.

Overall, further work are required in order to model hysteresis as a function of microstructure descriptors, and implement such description in a continuous rheological model accounting for the hysteresis at the static-flowing transition, such as *Edwards et al.* (2019).

Chapter 6

Conclusion and outlook

6.1 Conclusion

The present work has enabled us to investigate the hysteresis phenomenon which is a complex combination of jamming and unjamming. They appear as two distinct phase transitions with different processes that we investigated. Our study led us to find and highlight the various findings in the literature on the subject. We have thus seen, on the one hand, that the stopping process is a mechanism of stabilisation that results from the decrease of the shear stress relatively to the normal pressure. The velocity of the system as well as the inertial dynamic decreases with the plane inclination through the whole grain layer, together with an increase of the volume fraction, as predicted by $\mu(\mathcal{I})$ rheology. This process stabilises grains near the rough bottom plane where a no-slip condition is imposed due to the roughness of the bottom. Interestingly, our results added to this vision the evolution of the average number of contacts in the layer, showing that the maximum amount of contacts is observed in that region of the layer. In the mean time, the number of contacts also increases with decreasing stress. The stable layer starts diffusing up to the free surface when the system dramatically approaches the jamming transition, together with an increase of contact number in the bulk. This dramatic change is observed on the depth average values of inertial number as well as on the average number of contact in the system that displays discontinuities at the jamming transition between their flowing values and their values in the static state. These results reveal the feature of a first-order phase transition at jamming for frictionless and frictional particles.
On the other hand, the static state is characterized by no dynamic and constant volume fraction and coordination number values with variations of inclination angle. However in that regime the sliding contact proportion displays small increases in the layer close to the bottom plane leading to a succession of local rearrangements that eventually lead to an instability near the free surface implying a quick initiation of flow in that region of the system, that develops into the whole layer. This sudden change is also observed in the depth averaged inertial number value, volume fraction and average number of contacts that drops from their static values to the initial flowing branch at the avalanche angle, highlighting a feature of first-order phase transition resulting from the unjamming of the assembly of grains. This range of angles between the stopping angle and the avalanche angle highlights the hysteretic phenomenon on an inclined plane.

Then, we showed that collisional dissipation was not a mechanical process involved in the hysteretic behavior since no significant influence is observed on hysteresis or critical angles when varying the restitution coefficient. This suggests that there are few momentum transfer by collisions in the flowing state when approaching jamming. By contrast, we have seen that inter-particle friction plays a major role in both the critical angle values and hysteresis. This shows that the dynamics of grains is dominated by momentum transfer by friction. However, we showed that inertia plays a significant role in the value of the stopping angle, since it greatly influences grains dynamic. As a result, adding viscous dissipation also significantly lower hysteresis. Then, the inertial effect which plays a role in hysteresis phenomenon does not lie in the momentum transfer by collisions but in the grains dynamics itself. Finally, our results show that hysteresis has a combined origin between inertial effect due to the dynamic of grains and frictional dissipation that greatly influence the dynamic and static of the system. This contribution enabled us to establish both frictional and inertial mechanisms significant influence on hysteresis and allow us to rationalize the results of the literature.

One of the major contribution of our work is the presence of hysteresis in the frictionless dry case, i.e. when grains inertia is not damped. In that case, the system do not displays any remarkable dilatancy at the initiation of flow suggesting a continuous second-order phase transition with no hysteresis. Dilatancy is therefore not strictly related to the presence of hysteresis and show that the volume fraction is not a good proxy to characterize hysteresis phenomenon. On this basis, our work has focused on studying the evolution of the micro-structure through various quantities describing the contact network and tangential force network. For this, the idea was to adapt the jamming literature approach to look in detail at the micro-structure in order to identify some key variables to characterize hysteresis on a canonical configuration as the inclined plane. Thus, conversely to the volume fraction, the coordination number displays discontinuities at both jamming and unjamming in the frictionless case and for frictional particles in the viscous regime. It shows a feature of first-order discontinuous phase transition highlighting the presence of hysteresis. Although characterizing both distinct transitions with the same descriptors is complex, this approach sheds light on the results discussed above on the combined influence of friction and inertia on the flow, the static and the hysteresis of granular systems. This thesis contributed to show that the decrease of frictional dissipation, when the inter-particle friction decreases, enables grains to flow faster by increasing the fraction of contacts that can slides. This mechanism increases the number of contacts needed to reach the stable state leading to lower values of stopping angle and higher the coordination number in the stable state. Hence, this influence the geometrical and tangential conditions of the assembly of grains in the static state. These variations are measured by the the variations of sliding contact proportion that increases with decreasing μ_p in the static state and by the contact network anisotropy and its average number of contacts. All this, leads to lower avalanche angle. Overall, lowering frictional dissipation enables the system to be stable at lower angles when flowing and enables the destabilisation to occurs in easier stress conditions which lower the absolute hysteresis.
Our work also contributed to show that the decrease of inertia due viscous dissipation increases the ability of grains to make contacts in order to reach the stable state and decreases the fraction of these contacts that slides leading to easier stabilization condi-

tions at a given angle and therefore higher stopping angle. Also, the coordination number in the static increases as well as the contact network anisotropy with decreasing inertia. These variations of the geometrical state of the contact network enabled us to rationalize the effect of both friction and inertia on the geometrical contact network state that is correlated to the avalanche angle. The avalanche angle then slightly evolves as a result of these geometrical variations. These findings finally lead us to found a scaling of hysteresis with the discontinuities of coordination number at jamming and unjamming.

Overall, this thesis has contributed to better define and understand the origin of hysteresis in granular media and to highlight the central role of micro-structure in this phenomenon. This study is in line with the current approach that consist in using micro-structure descriptions to characterize the evolution of the system at the phase transition between the dense and static flow regimes of granular media. The aim of this approach is to gain a better understanding of the evolution of the complex state of the granular micro-structure and to identify key state variables that can be used to better describe the transition between regimes and the underlying physical mechanisms involved. These variables can then be used as internal order parameters in the development of continuous description models, with the aim of unifying the description of granular media.

6.2 Outlook

The present work enabled to depict a clear picture of hysteresis origin and identify some outlook in the continuity of the thesis that remains to be investigated. Here, current research avenues are presented to clarify some of the work related to the thesis that emerges as the next issues of the subject as well as various tools that may help provide characterization of the several physical mechanisms involved in hysteretic behavior of granular assemblies in order to develop complete constitutive models using finer internal variables. Finally, other more distant perspectives are proposed.

6.2.1 Generalization of hysteresis nature and geometrical effect of configuration

As discussed in the state of art, Chapter 2, differences in hysteresis amplitude are observed between the different configurations reported in the literature. The thesis have shown the inertial and frictional nature of hysteresis for a granular material on an inclined plane and interpreted these results with the scope of the description of micro-structure. Since the geometry of various configuration and boundary conditions influences the micro-structure of the assembly of grains, an effect on hysteresis is expected. In addition, although the dense flow regime is well described by $\mu(\mathcal{I})$ rheology far from the liquid/solid transition, some heterogeneous behaviors, such as finite size effects, shear banding and creeping, are observed near the transition and depends on the geometry as detailed in the Introduction. These observations lead to a central issue of the influence of the configuration for the generalization of hysteresis nature. Since the central point of hysteresis nature on an inclined plane is the finite hysteresis observed in the dry frictionless case, can this result be generalized to other configurations? Two configurations seem appropriate for studying this question: the rotating drum and the plane shear cell. The former is the most

studied configuration due to its simplicity to set up long time experiments, yet no study for frictionless particles with no fluid damping the grains dynamics was conducted. In addition, hysteresis is only observed for intermittent flow where the free surface alternate between static state and quick avalanches. The latter are then transient and the the flow does not have time to reach a steady state within avalanches by contrast to the inclined plane configuration.
The other configuration, also studied to analyse hysteresis is the plane shear cell without gravity. This configuration is particularly interesting since it enables one to perform both stress imposed and shear rate imposed simulations in the same geometry. As such, it possible to compare the hysteresis resulting from both protocols and to identify the fundamental differences between the influence of imposing either velocity or stress at the boundary walls on hysteresis. In the former, the velocity field is not imposed so grains inertia is not controlled but adapts to the imposed stress. In the former protocol, grains inertia is controlled by the boundary condition and stress adapts within the system in response. In addition, finite-size effects can be compared to the inclined plane configuration by applying or not gravity which enables one to compare the influence of an additional wall or, without gravity, the differences between stress imposed by a boundary or by gravity.

As such, simulations are therefore underway with these two other configurations. First results are giving for the rotating drum configuration on Figure 6.1. Figures 6.1a and 6.1b presents the evolution of the inclination angle of the free surface with simulation time for two distinct inter-particle friction coefficients $\mu_p = 0.5$ and $\mu_p = 0$. Figures 6.1c and 6.1d presents the corresponding evolution of the average coordination number with simulation time. The rotating speed is represented by the slope of the red curves. In the frictional case, we observe an alternate regime between static states and avalanches. In the static state, the inclination angle evolves at the same rate as the rotating speed, indicating no flow at the free surface. This state is also characterized by constant values of the coordination number as depicted by the plateaus on Figure 6.1c. When θ_{start} is reached, represented by a local maximum of inclination angle (red points), quick avalanches occur where the inclination angle drops down until the medium stops again at the stopping angle θ_{stop}. In this regime, the coordination number evolves, it decreases at lower values and increases back to the constant static value when the avalanche stops. Hysteresis is clearly defined here and is measured as the difference between the avalanche angle for one avalanche, and the stopping angle preceding this avalanche. Further analysis on these results are given in Appendix D.1.
By contrast, in the frictionless case, Figure 6.1b shows local maximums and minimums in the inclination angle. However, when the inclination angle increases, it does not linearly evolves with time as for $\mu_p = 0.5$. In addition, the evolution of the coordination number, Figure 6.1d, does not displays any plateau characteristic of the static regime. As such, $\theta(t)$ and $\mathcal{Z}(t)$ does not show clear arrested state but oscillations indicating flow at the free surface. As a consequence, if no clear arrested state is observed, the system does not displays any hysteresis. Additional analysis are needed to conclude on the result, especially at lower rotating speed for the frictionless case, nevertheless it shows that in a rotating drum, hysteresis can vanish for frictionless particles conversely to the inclined plane configuration. This result then suggest that the conditions leading to vanishing hys-

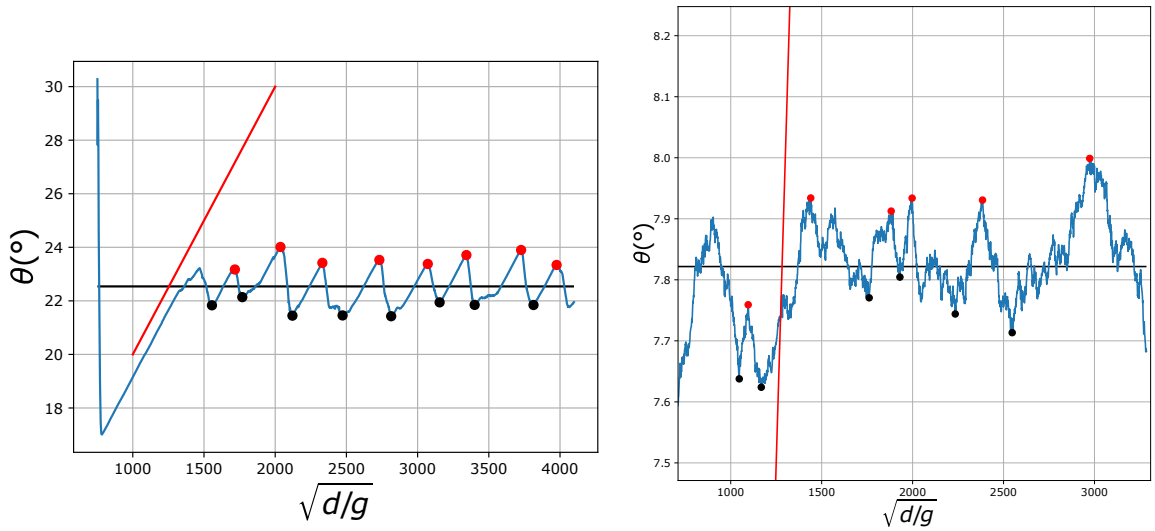

(a)

(b)

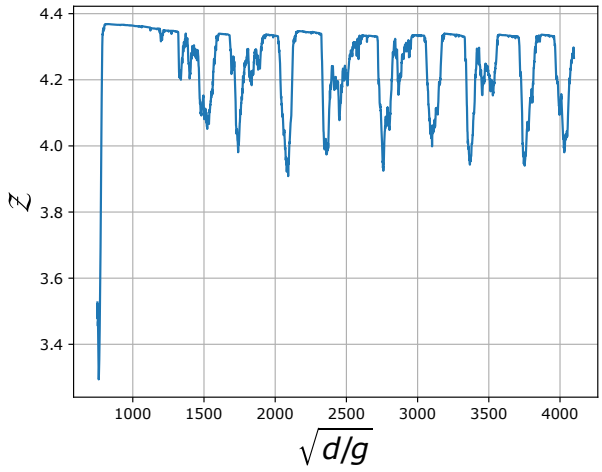

(c)

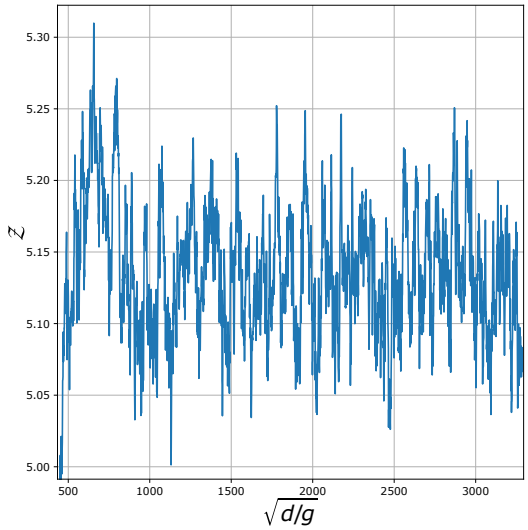

(d)

Figure 6.1 – Temporal evolution of the inclination angle of the free surface of the granular medium in rotating drum at inter-particle friction $\mu_p = 0.5$ (a) and $\mu_p = 0$ (b). Temporal evolution of the average coordination number in the granular medium in rotating drum at inter-particle friction $\mu_p = 0.5$ (c) and $\mu_p = 0$ (d).

teresis are configuration dependent and that the combined influence of both inter-particle friction and grains inertia is not trivially generalizable.

Simulations at $\mu_p = 0$ are underway to compare if hysteresis can be observed for frictionless assembly in stress imposed and velocity imposed planar shear cell. Some first results for frictional particles are presented in Appendix D.1.

6.2.2 Influence of wall conditions: plane roughness effect

The results of hysteresis presented above displays significant variability between one run to another when varying the plane configuration with constant roughness parameter. As these variability do not decrease with friction and inertia, we can postulate a bottom roughness effect potentially coupled to a finite size effect. The bottom plays an important role in the geometry of the system, which is central in the stochastic and geometric nature of the transition. Plane roughness sets the geometric energy landscape of the system. Indeed, as detailed in Chapter 2, the conditions of jamming and unjamming of frictional materials depends on the preparation of the system under isotropic conditions. Under anisotropic conditions, when the flow is established, i.e. steady, the role of the boundary condition is central in the grains dynamic, their velocity, their packing density and coordination number. The geometry of the boundary and its roughness parameters plays a key role in the geometrical and mechanical ansiotropy. This effect is emphasized near the transition where the boundary condition drives the phase diagram and is intrinsically related to finite-size effects as depicted by *Goujon et al.* (2003) on an inlined plane. It is therefore fundamental to investigate its effect on the amplitude of hysteresis. Initial simulations are underway on an inclined plane, varying the background roughness for two inter-particle friction coefficient $\mu_p = 0$ and $\mu_p = 1$ in the dry case. Coupling this effect with a study of the effect of layer size on hysteresis is an interesting outlook for further work.

6.2.3 The search of internal variables and descriptor of stability

The main idea of the study of the phase transition and the characterization of hysteresis is to identify key variables that are good candidates to be the order parameter or in a combination of order parameters driving the behavior of the system. As such, we have seen in the work developed in this thesis that the coordination number was an interesting parameter as well as the contact network anisotropy to characterize the avalanche angle. The former is also a good proxy to characterize hysteresis. However it does not characterize well the evolution of the stopping angle which depends not only on the contact network but on the dynamic of the system. Hence, its is interesting to presents possible variables and approaches that we did not investigated in this work and could be good candidates to characterize the behavior of the system at the transition.

Although the generalization of a first order staticity criterion in the flowing regime did not allowed us to conclude on a potential criterion predicting the jamming and unjamming of the system, this description may be interesting for further research. Indeed, measuring a staticity criterion at the grain scale could by extension of the work of *Henkes*

et al. (2016) allow one to define a rigid cluster mapping depending on the geometry and configuration studied. Then, it could predict the jamming and unjamming transitions of the system under various frictional and inertial conditions.

Going further into the energetic description with a quantification of sources of energy dissipation as well as a study of granular temperature could help characterize the inertial effects on hysteresis.

Finally, a finer description of the contact distribution, the normal and tangential forces distribution as well as their anisotropy coupled with a study of the stress tensor anisotropy may be interesting. By using a similar approach than *Srivastava et al.* (2020, 2021) it could be interesting to extend their work and analyze the hysteresis phenomenon with the mechanical anisotropy. This may help providing information about the geometrical and mechanical evolution of contact and force networks and potentially helps finding finer descriptors of hysteresis.

6.2.4 Hysteresis in more realistic granular samples

Finally, with a more general picture, the influence of some well-known features of actual granular samples on hysteresis would be interesting to investigate with the aim of generalizing hysteresis nature to more realistic granular systems. The shape of grains was shown to have an effect on the packing density, the coordination number as well as the critical stress ratio (*Pouliquen and Renaut*, 1996; *Salerno et al.*, 2018). In the same way, the influence of cohesion on hysteresis was already introduced by *Mandal et al.* (2021b). Extending their work would be of great interest for future research. Then, studying these effects as well as polydispersity would be interesting outlook to study hysteresis phenomenon and its application on systems closer to actual granular media.

Appendices

Appendix A

Introduction and state of art appendices

A.1 Basics of continuum mechanics

In this section we develop the basic tensorial variables describing a continuous medium that will be used in this manuscript. We consider thus a continuous medium for which each points of the medium has a position x at time t. Here, x is considered as a vector with three coordinates in each directions. We can consider $X(x,t)$ the vector that defines the displacement relatively to the initial state at each positions x and time t. We assume small deformations.

A.1.1 Strain and strain-rate tensors

The strain tensor, ϵ, then is defined as:

$$\epsilon_{ij} = \frac{1}{2}\left(\frac{\partial X_i}{\partial x_j} + \frac{\partial X_j}{\partial x_i}\right). \tag{A.1}$$

This tensor characterizes the deformations of the system in all directions. Consider V the volume of the system. The changes in volume of the system is given by the trace of the strain tensor which gives with Newton sum notation:

$$tr(\epsilon) = \epsilon_{ii} = \frac{\delta V}{V}. \tag{A.2}$$

This tensor is no more relevant when the deformations of the system are high, the deformations highly depends on time, as such, the relevant tensor that is used is the strain rate, $\dot{\epsilon}$, which is the time derivative of the strain tensor:

$$\dot{\epsilon}_{ij} = \frac{1}{2}\left(\frac{\partial u_i}{\partial x_j} + \frac{\partial u_j}{\partial x_i}\right). \tag{A.3}$$

With $u(x,t)$ the time derivative of the displacement X corresponding to the velocity of the material at point x at time t. This latter tensor is usually decomposed between isotropic part and deviatoric part as follow:

$$\dot{\epsilon} = \frac{1}{3} tr(\dot{\epsilon}) I + \tilde{\dot{\epsilon}}. \tag{A.4}$$

Here, I is the identity tensor implying that the isotropic part $1/3tr(\dot{\epsilon})I$ characterizes the rate volume changes with time and the deviatoric part (or anisotropic part) $\tilde{\dot{\epsilon}}$ characterizes the rate deformation by shear. As such, the shear rate $\dot{\gamma}$ is usually defines as:

$$\dot{\gamma} = 2\tilde{\dot{\epsilon}}. \tag{A.5}$$

A.1.2 Stress

The stress tensor, σ, is equivalent to a pressure field in the sense that it represents a force per unit area on the whole system. As such, if one consider an infinitesimal surface dS within the continuum medium, the corresponding components of the force applied on this surface dF will be expressed as function of this surface and the stress σ projected on the vector n normal to the surface :

$$dF_i = \sigma_{ij} n_j dS. \tag{A.6}$$

Equivalently to the strain rate, the stress tensor can be decompose in isotropic tensor, equivalent to pressure P and a deviatoric tensor or shear stress tensor τ as follow:

$$\sigma = PI + \tau, \tag{A.7}$$

with $P = \frac{1}{3} tr(\sigma)$ and I the identity tensor.

A.1.3 Conservation laws

Here, we consider the density $\rho(x,t)$ of the continuum system at position x and time t. The mass conservation equation is given for the density as follow (with Newton notation):

$$\frac{\partial \rho}{\partial t} + \frac{\partial \rho u_i}{\partial x_i} = 0. \tag{A.8}$$

The equations of conservation of momentum in the translation and in presence of gravity acceleration is given as follow:

$$\rho \left(\frac{\partial u_i}{\partial t} + u_j \frac{\partial u_i}{\partial x_j} \right) = \frac{\partial \sigma_{ij}}{\partial x_j} + \rho g_i. \tag{A.9}$$

A.1.4 Constitutive relations

In the latter Equation (A.9), the stress tensor is unkown and has to be given through a constitutive relation (or constitutive law). In other words, one may study the strain or strain rate response of the continuum system to stress in order to give a constitutive relation between both quantities and close the momentum equations. Here, we present the simpler constitutive relation given for continuum solids and developed by Hooke. The Hooke's law gives a relation between stress and strain:

$$\sigma = Ktr(\epsilon) I + 2G(\epsilon - \frac{1}{3} tr(\epsilon) I). \tag{A.10}$$

Note that $\epsilon - 1/3tr(\epsilon)I$ is the deviatoric part of the strain tensor with the identity tensor I. This relation lies on the assumption of constant isotropic bulk modulus K and shear modulus G with strain evolution. These constants can be expressed as functions of two characteristics of the material, the Young's modulus E and the Poisson's ratio ν that can be measured with a simple test when pulling a cylinder with free edges. The Young's modulus represents the ratio $E = \frac{\sigma_{zz}}{\epsilon_{zz}}$ between the stress applied in the axial direction and the corresponding axial strain. The Poisson's ratio represents the ratio between the radial and axial strain. Hence, the relations between these quantities are the following (*Andreotti et al.*, 2013):

$$G = \frac{E}{2(1+\nu)}, \tag{A.11}$$

and

$$K = \frac{E}{3(1-2\nu)}. \tag{A.12}$$

A.2 Rheology of dense non-Browninan suspensions

In the case of non-Brownian suspensions, that are assembly of grains fully immersed in a fluid, two separates cases needs to be defined depending on the imposition process. In one case, the volume is imposed and the order parameter that defines when the medium will flow or rest is the volume fraction ϕ. In the other case, the pressure is imposed and gravity become the driving mechanism.

First, for volume imposed density-matched suspensions with non-Brownian motion, the flow rule can be simply express in terms of equivalent viscosity of the suspension η_s. When subjected to shear, the flow rule is given as follow (*Guazzelli and Pouliquen*, 2018):

$$\tau = \eta_s \eta_f \dot{\gamma}, \tag{A.13}$$

with η_f the viscosity of the fluid. The equivalent viscosity does not depends on the shear rate here which makes these kind of suspensions a Newtonian fluid. The viscosity depends solely on the volume fraction $\eta_s(\phi)$ and diverges when the volume fraction approach the critical volume fraction at which the system jams, ϕ_c. At low volume fraction, *Einstein* (1911) proposed a linear form of the viscosity with volume fraction:

$$\eta_s = 1 + \frac{5}{2}\phi. \tag{A.14}$$

This forms is nevertheless not true for high volume fraction where η_s diverge near ϕ_c. Several models of the $\eta_s(\phi)$ function has been proposed (e.g. *Guazzelli and Pouliquen*, 2018) and the one that fits the most in all regimes, i.e. linear relation of Einstein at low volume fraction and power law that diverge at high volume fraction, is the following correlation (*Guazzelli and Pouliquen*, 2018):

$$\eta_s = \left(1 + \frac{5\phi}{4(1-\phi/\phi_c)}\right)^2. \tag{A.15}$$

More complex models were developped in order to model the effective viscosity, see *Boyer et al.* (2011); *Guazzelli and Pouliquen* (2018).

For pressure imposed density-matched suspensions, the suspensions do not behaves as a Newtonian fluid and the viscosity depends on the shear rate (*Bonn et al.*, 2017; *Guazzelli and Pouliquen*, 2018). In such materials, a friction law equivalent to the dry case can be developed introducing a new dimensionless number, in the absence of gravity and at low Stokes number where viscous dissipation is dominant, the viscous inertial number J:

$$J = \frac{\eta_f \dot{\gamma}}{P}. \tag{A.16}$$

Hence, similarly to dry granular material constitutive laws are needed for the shear stress:

$$\tau = \mu(J)P. \tag{A.17}$$

And the volume fraction:

$$\phi = \phi(J). \tag{A.18}$$

Boyer et al. (2011) developed a correlation for the flow and density curves. The flow function is written as the sum of a contact friction coefficient μ_c equivalent to the one of dry materials see Equation (1.11) and an hydrodynamic friction coefficient μ_h that is written to recover Einstein's linear model at low viscous inertial number:

$$\mu(J) = \mu_c + \mu_h = \left[\mu_1 + \frac{\mu_2 - \mu_1}{J_0/J + 1}\right] + [J + \frac{5}{2}\phi_c J^{1/2}]. \tag{A.19}$$

The packing density evolution with J is given by:

$$\phi(J) = \frac{\phi_c}{1 + J^{1/2}}.$$

These relations were used to find the correlation of $\eta_s(\phi)$ in volume imposed cases unifying both descriptions (*Boyer et al.*, 2011).

Such models allows to predict the flow characteristic, stress, strain-rate or velocity profiles of dense suspensions in various configurations such as dense suspensions flow on rough inclined plane or for bedload transport (*Guazzelli and Pouliquen*, 2018).

A.2.1 Discontinuous shear thickening

Discontinuous shear-thickening (DST) is a phenomenon that occurs in volume imposed sheared suspensions and sheared dry granular media and is characterized by a discontinuous jump in the shear stress upon continuous strain rate imposition (*Seto et al.*, 2013; *Vågberg et al.*, 2017; *Grob et al.*, 2014). This phenomenon happens for high enough volume fraction between a characteristic value and the jamming volume fraction. Below this critical volume fraction, sheared suspensions displays continuous shear thickening (CST) as presented in the rheology of dense suspensions, see Section 1.3. Dry granular materials displays continuous transition between inertial flow and plastic flow under the critical volume fraction (*Grob et al.*, 2014).

DST have been shown to be dependent on friction between grains since the critical volume fraction that define the range of packing density in which DST occurs depends on the inter-particle friction coefficient (*Seto et al.*, 2013; *Grob et al.*, 2014). As such, it has been shown that no discontinuous jump is observed in the flow curve for dry granular materials of frctionless particles (*Ciamarra et al.*, 2011). However, friction is not necessary to observe DST in dense non-brownian suspensions (*Vågberg et al.*, 2017). The viscous dissipation of the interstitial fluid also appears to be a key mechanism for the presence of DST.

A.2.2 Hysteresis in DST

Discontinuous shear thickening is strongly related to hysteresis. Indeed, in the presence of friction between grains or/and viscous dissipation, the flow curve of DST are different with ramping-up shear rate than ramping down shear rate (*Grob et al.*, 2014; *Vågberg et al.*, 2017). This is a signature of hysteresis where the flow curve depends on the history of the strain rate imposition.

A.3 Micro-structure descriptors

Micro-structure descriptors are of several forms. The simpler one is scalar quantities that gives access to information averaged on the whole assembly of grains:

— The coordination number, $\mathcal{Z}$ with its classical form $\mathcal{Z} = 2N_c/N_p$, with N_c the amount of contact in the system and N_p the amount of particles calculates the average number of contacts in the system.

— The sliding contact proportion, $\chi = N_c^{sliding}/N_c$, calculates the amount of contact that slides, i.e. that exceeds the Coulomb criterion, relatively to the total amount of contacts.

— The granular temperature that characterizes the fluctuations of velocity in the system that have been shown to be non-affine (*Radjai and Roux*, 2002). This quantity is usually expressed as $T_g =< u_p' > /3$ with u_p' the fluctuation of velocity with respect to the average velocity in the system.

— The contact anisotropy, a_c calculates the amplitude of contact network anisotropy.

— The normal force anisotropy a_N calculates the amplitude of the normal forces network anisotropy.

— The tangential force anisotropy a_T calculates the amplitude of the tangential forces network anisotropy.

The three latters derived from tensorial calculations of the anisotropic contact Fabric tensor A^c and the anisotropic forces fabric tensors A^n and A^t that derived from the contact fabric tensor R and the forces fabric tensors N and T. Considering an assembly of contacts characterizes by their normal unit vector $\mathbf{n}$, tangential unit vectors $\mathbf{t}$, contact force f^c and branch vectors l^c, see Figure A.1 for a scheme of a contact between two spheres. The contact fabric tensor R, that quantifies the geometrical anisotropy of contacts, is calculated in a granular system as (*Oda*, 1982; *Satake*, 1982; *Bathurst and*

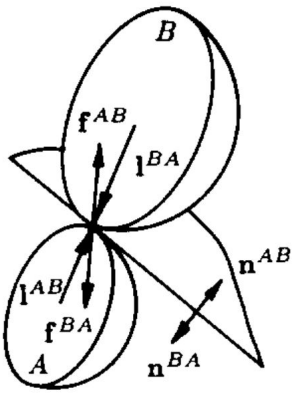

Figure A.1 – Scheme of contacts between two particles A and B. The forces f_{AB} and f_{BA} are in opposite direction as well as the unit vectors n_{AB} and n_{BA} that are normal to the contact plane. The tangential unit vector $\mathbf{t}$ is not represented here, it corresponds to the direction of projection of the contact force on the contact plane and is the orthogonal to the normal unit vector. The branch vector $l^c_{AB} = l^{AB} - l^{BA}$ connects the center of grains. Source: (*Bathurst and Rothenburg*, 1990)

Rothenburg, 1990):

$$R_{ij} = \frac{1}{N_c} \sum_{N_c} n_i n_j, \tag{A.20}$$

with n_i the i-th component of the unit vector $\mathbf{n}$ along the normal direction of the contact plane. Considering the orientation of this vectors $\mathbf{n}$ between $[0, 2\pi]$, the fabric contact tensor can be written as a continuous integral over the volume V of the system, if the number of grains is sufficient enough (*Bathurst and Rothenburg*, 1990), as:

$$R_{ij} = \frac{N_c}{V} \int_V E(\mathbf{n}) n_i n_j d\mathbf{n}, \tag{A.21}$$

with $E(\mathbf{n})$ the distribution probability function of vectors unit $\mathbf{n}$ that are oriented along $d\mathbf{n}$ such that the fraction of all assembly of contacts oriented within the orientation interval $d\mathbf{n}$ is $E(\mathbf{n})d\mathbf{n}$. It can either be expressed as an integral over the orientations Θ of the unit vector (*Oda*, 1982; *Satake*, 1982; *Guo and Zhao*, 2013) as:

$$R_{ij} = \int_\Theta E(\Theta) n_i n_j d\Theta. \tag{A.22}$$

These distribution functions (on the unit vector or its orientation) are usually expressed as a second-order Fourier expansion (*Bathurst and Rothenburg*, 1990; *Guo and Zhao*, 2013; *Srivastava et al.*, 2020) which in 3D reads:

$$E(\mathbf{n}) = \frac{1}{4\pi}[1 + A^c_{ij} n_i n_j], \tag{A.23}$$

with $1/4\pi$ the distribution of contacts in the isotropic directions and A^c_{ij} the symmetric and deviatoric contact anisotropy tensor that characterize the fabric anisotropy (geometrical anisotropy). Integrating Equation (A.22) enables to link this latter tensor to the

deviatoric part of the fabric tensor R^d as (*Guo and Zhao*, 2013; *Srivastava et al.*, 2020):

$$A^c_{ij} = \frac{15}{2} R^d_{ij}. \tag{A.24}$$

Guo and Zhao (2013) proposed similarly to the fabric tensor a form for the normal, N, and tangential, T, forces tensor as:

$$N_{ij} = \frac{1}{4\pi} \int_\Theta \overline{f}^n(\Theta) n_i n_j d\Theta = \frac{1}{N_c} \sum_{N_c} \frac{f^n n_i n_j}{1 + A^c_{kl} n_k n_l}, \tag{A.25}$$

with $\overline{f}^n(\Theta)$ the average normal forces oriented in the direction Θ, f^n the normal force at each contact. The idea being to characterize the mechanical anisotropy induced by normal force, it is normalized in the sum by the geometrical anisotropy $1 + A^c_{kl} n_k n_l$. The average normal forces can equivalently to E be written as second-order Fourier expansion of the unit vector $\mathbf{n}$ (*Srivastava et al.*, 2020) or its orientation Θ (*Guo and Zhao*, 2013):

$$\overline{f}^n(\mathbf{n}) = \overline{f}^0 [1 + A^n_{ij} n_i n_j], \tag{A.26}$$

with A^n_{ij} the deviatoric mechanical anisotropy induced by normal forces in the system which is related to the deviatoric part of the force tensor N^d by integrating Equation (A.25) with the relation A.26, it gives (*Guo and Zhao*, 2013):

$$A^n_{ij} = \frac{15 N^d_{ij}}{2\overline{f}^0}. \tag{A.27}$$

Similarly, *Guo and Zhao* (2013) proposed a formulation of the tensors distribution functions of tangential forces as:

$$T_{ij} = \frac{1}{4\pi} \int_\Theta \overline{f}^t(\Theta) t_i n_j d\Theta = \frac{1}{N_c} \sum_{N_c} \frac{f^t t_i n_j}{1 + A^c_{kl} n_k n_l}, \tag{A.28}$$

which gives, considering for that tensor the i-th component of the tangential unit vector, $\mathbf{t}$, orthogonal to $\mathbf{n}$ and co-linear to the tangential displacement, a following distribution function for i-th component of the of average tangential force is (*Guo and Zhao*, 2013; *Srivastava et al.*, 2020):

$$\overline{f}^t_i(\mathbf{n}) = \overline{f}^0 (A^t_{ik} n_k - (A^t_{kl} n_k n_l) n_i), \tag{A.29}$$

with A^t_{ij} the mechanical anisotropic tensor induce by tangential force and related to the deviatoric part of the tensor T as (*Guo and Zhao*, 2013):

$$A^t_{ij} = \frac{15 T^d_{ij}}{3\overline{f}^0}. \tag{A.30}$$

$\overline{f}^0$ is the average normal force, integrated for all unit vector orientation with the same weight (*Bathurst and Rothenburg*, 1990) meaning that $\overline{f}^0 = T_{ii}$ *Guo and Zhao* (2013) which differs from the average normal force over each contacts when the assembly of

grains is anisotropic and is equal to the latter when the assembly of grains is isotropic.

Finally, the coefficient a_c, a_N and a_T are the second invariants of the anisotropic tensors respectively A^c_{ij}, A^n_{ij} and A^t_{ij}. The three latter being deviatoric, it gives (*Srivastava et al.*, 2020):

$$a_* = \frac{1}{2}\sqrt{tr(A^* \cdot A^*)}, \tag{A.31}$$

with $* = c$, n or t. These coefficients then quantify respectively the amplitude of geometrical contact anisotropy, mechanical anisotropy induced by normal forces and mechanical anisotropy induced by frictional forces in the system.

The internal stress tensor is expressed with such framework for monodisperse sphere packings as (*Bathurst and Rothenburg*, 1990; *Srivastava et al.*, 2020):

$$\sigma_{ij} = \frac{N_c l_0}{V} \int_V \overline{f}_i(\mathbf{n}) n_j E(\mathbf{n}) d\mathbf{n}, \tag{A.32}$$

with l_0 the mean center-to-center distance in the packing that can be approximated as the diameter of grains for monodisperse spheres. The internal stress tensor is usually calculated in numerical simulations as the surface sum of contact forces over all contacts, which reads (*Guo and Zhao*, 2013):

$$\sigma_{ij} = \frac{1}{V} \sum_{N_c} f^c_i l^c_j, \tag{A.33}$$

with $f^c = f^n + f^t$, and l^c the branch vector linking the centers of particles.

A.4 Normal stress differences and shear induced anisotropy

One of the limit of the $\mu(\mathcal{I})$ rheology is the existence of first and normal stress differences. The generalized rheological model from *Jop et al.* (2006) indeed make the assumption of a Cauchy stress tensor with isotropic pressure and a colinearity between the stress and the strain rate tensors leading to Equation (1.9). Hence it supposed that $\sigma_{xx} = \sigma_{yy} = \sigma_{zz}$ with x, y and z being respectively the flow, vorticity and gradient directions. This assumption is known to be not true since differences between the normal stress components are observed in sheared granular systems. As such, there is no more one degree of freedom but three degrees of freedom (two added by the differences in normal stress components). The first one is still related to the flow curve by Equation (1.11) for dry granular materials and Equation (A.19) for dense suspensions. The two last degrees of freedom then also needs to get constitutive relations in order to close the equation and to solve for the transmission of stress in a granular system (*Silbert et al.*, 2001; *Seto and Giusteri*, 2018; *Srivastava et al.*, 2021).

These differences are defined as follow:

$$N_1 = \sigma_{zz} - \sigma_{xx}. \tag{A.34}$$

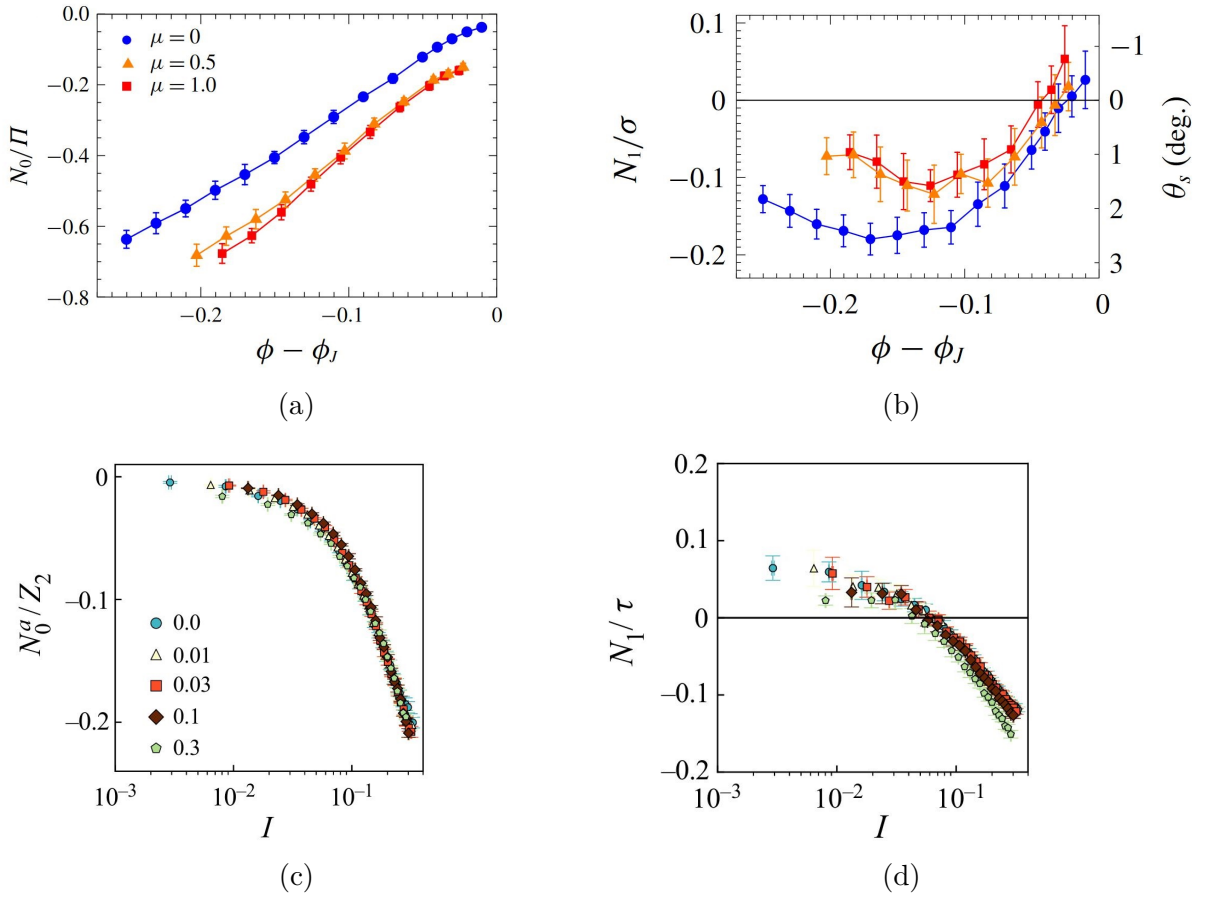

Figure A.2 – Results from *Seto et al.* (2013) for the (a) Second normal-stress difference normalized by the third of the trace of the stress tensor $\boldsymbol{\sigma}$, $\Pi = -(1/3)tr(\boldsymbol{\sigma})$ (b) First normal-stress difference normalized by the shear stress, noted $\sigma = \sigma_{xz}$. Results *Srivastava et al.* (2021) for the (c) Second normal-stress difference calculated on the contact fabric anisotropy tensor normalized by the average number of contact of non-rattler particles (d) First normal-stress difference normalized by the shear stress τ.

With N_1 the first normal stress difference. The second normal stress difference is calculated as:

$$N_2 = \sigma_{zz} - \sigma_{yy}. \tag{A.35}$$

The presence of such differences of order 5% for the first normal stress difference and 20% for the second one were observed in several studies in the dense flow regime far from the jamming transition. It was observed in numerical simulations on inclined planes (*Silbert et al.*, 2001; *Weinhart et al.*, 2013), in circular and plane split-bottom shear geometries (the shear boundary is split in two parts that shear in opposite directions) (*Depken et al.*, 2007) and in boundary-less sheared simulations (*Srivastava et al.*, 2021). It has also been experimentally investigated for dense suspensions in a bunch of articles with the help of several different rheometers as well as numerically. The rheometers and results are gathered in *Guazzelli and Pouliquen* (2018) for stress differences in the dense flow regime far from the jamming transition. In *Seto and Giusteri* (2018), normal stress differences have been investigated with numerical simulations of dense suspensions. In all cases, both

normal stress differences have non-trivial evolution in the dense flow regime. Nevertheless, they were shown to decrease at the approach of the jamming transition leading to an interpretation of their origin.

The origin of the first normal stress difference appears to be a consensus as a consequence of the misalignment (non-coaxiality or in other words an anisotropy) between the stress tensor and the symmetric strain rate tensor D (*Seto and Giusteri*, 2018; *Srivastava et al.*, 2021). Misalignment can be understood mathematically as the presence of a rotation angle between the eigenvectors of both tensors (*Seto and Giusteri*, 2018; *Srivastava et al.*, 2021). It can also be understood physically as a misalignment between the orientation of the force (or contact) network and the orientation of the flow in the flow plane (x, z). Such misalignment can have various origins depending on the dominant interactions of grains. In dense suspensions, the dominant interactions are hydrodynamic interactions at low packing densities and contact interactions at higher packing densities (close to the jamming transition) leading to the non-monotonic evolution of N_1 with the packing density (*Seto and Giusteri*, 2018), see Figure A.2b. In dry granular materials the only source of interactions are of contact type and the misalignment between the projected contact vectors and the principal flow direction in the flow plane are due to friction between grains since N_1 is lower near the quasi-static state for frictionless particles. Near the jamming transition the first normal stress difference is always increasing with packing fraction or decreasing strain rate (for dense suspensions or dry granular systems) showing less misalignment but still no completely vanishing values of N_1, see Figures A.2b and A.2d. This non-zero values are attributed to the geometrical entanglement of the system and is then a finite-size effect that is expected to vanish in infinite size systems (*Seto and Giusteri*, 2018; *Srivastava et al.*, 2021).

According to *Seto and Giusteri* (2018), the first normal stress difference allows to close one degree of freedom which is not the case of the second normal stress difference N_2 since it combine two effects: the misalignment of stress and strain rate tensors (captured by N_1) and the stress anisotropy between the stress in the flow plane and in the vorticity direction. In order to only capture the second effect, one needs to measure the stress difference between the average stress in the flow plane and the stress in the vorticity direction. It gives:

$$N_0 = (2\sigma_{yy} - \sigma_{zz} - \sigma_{xx})/2. \tag{A.36}$$

This form of second normal stress difference is highly decreasing near the jamming transition and vanishes for frictionless particles in the quasi-static limit, see Figure A.2a. Then, its origin rely in the excess of contacts in the flow plane compared to the vorticity direction that creates anisotropy of the stress tensor due to shear. This effect is increased by friction. Indeed, this anisotropy tends to zero in the quasi-static limit but remains non zero for frictional grains (*Seto and Giusteri*, 2018; *Srivastava et al.*, 2021) leading to non collapsing curves of $N_0(\phi)$ or $N_0(\dot{\gamma})$ at various inter-particle friction coefficients μ_p, see Figure A.2a. Interestingly, *Srivastava et al.* (2021) introduced an anisotropy measurement of the contact fabric tensor, defined in Equation (A.24). This anisotropy is equivalent to the second normal stress difference but for the geometrical anisotropic contact tensor, it gives:

$$N_0^a = (2A_{yy}^c - A_{zz}^c - A_{xx}^c)/2. \tag{A.37}$$

This anisotropy measured the excess of contacts in the flow plane compared to the vorticity direction and then highlights the origin of the stress anisotropy. *Srivastava et al.* (2021) shown that a possible collapse exist for N_0^a at various μ_p by normalizing the former with the average number of contacts, $\mathcal{Z}_2 = 2N_c/(N_p - N_r)$, of $N_p - N_r$ non rattler particles (N_c being the total amount of contacts, N_r the amount of rattler particles and N_p the total number of grains). Rattler particles are particles with less than two contacts that are then not constrained by contacts within the system. Such normalization then gives similar evolution at various μ_p of the excess contact anisotropy between the flow plane and the vorticity direction relatively to the average amount of contact in the system when varying the inertial number (relative shear rate), see Figure A.2c. This shows the importance of such relative variable $N_0^a/\mathcal{Z}_2$ in order to characterize the effect of friction on the anisotropy of normal stress and indicate that fabric tensor as well as coordination number are appropriate internal state variables to develop rheological models accounting for the evolution of the micro-structure (*Srivastava et al.*, 2021).

A.5 Contact and force distribution in granular packings

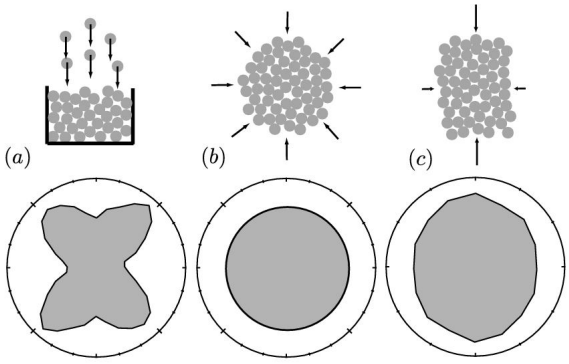

Figure A.3 – Contact distribution $E(\theta)$ plotted in the orientational space for 2D numerical simulations of (a) Deposition under gravity (b) Isotropic compression (c) Biaxial compression. Source: (*Andreotti et al.*, 2013)

In order to illustrate the quantities developed above, the distribution of contact are plotted for 2D numerical simulations in the orientational space in the granular packing for different configurations on Figure A.3. In 2D there is only one angle θ, and the quantities are simplified, see (e.g. *Bathurst and Rothenburg*, 1990). Similar distributions were observed by *Bathurst and Rothenburg* (1990) for biaxial compression. These distributions demonstrates preferential orientation of contacts in the direction of the principal boundary stress. It shows non equiprobable distribution of contacts within the system which contradicts the assumption made in the development of constitutive relations of static and quasi-static packings, see Section 1.2.

In addition, the probability density function of contact forces normalized by the average contact force over all contacts is plotted for granular packing under biaxial conditions on Figure A.4. The figure shows an exponential tail of the distribution of forces

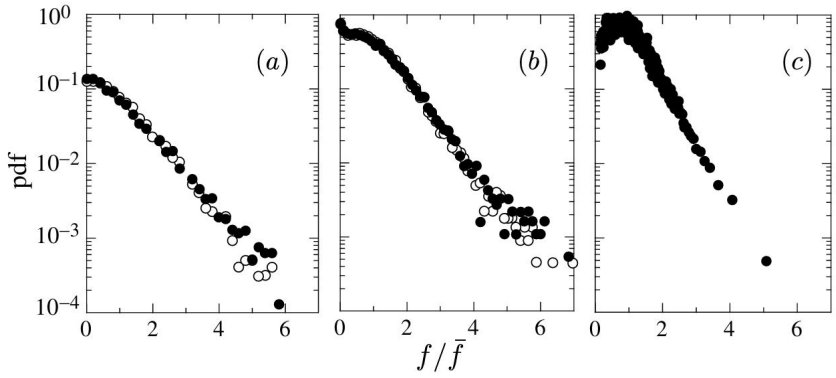

Figure A.4 – Probability density function (pdf) of contact forces amplitudes in the system normalized by the average contact force for (a) 2D numerical simulations from *Radjai et al.* (1999) with two inter-particle friction coefficients (b) Experimental measurement of contact forces on the wall boundary using force sensor (*Løvoll et al.*, 1999) (b) Experimental measurement of forces on the wall boundary using carbon-paper technique (*Mueth et al.*, 1998). Source: (*Andreotti et al.*, 2013; *Radjai et al.*, 1998)

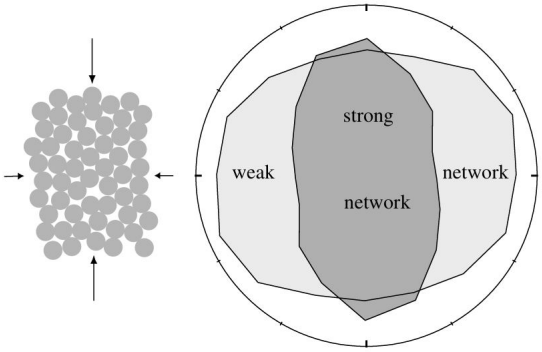

Figure A.5 – Contact distribution $E(\theta)$ plotted in the orientational space for 2D numerical simulations of biaxial compression. The contact network is partitioned in a strong network for which forces are greater that the average contact force in the system and a weak network for which forces are lower than the average contact force. Source: (*Andreotti et al.*, 2013; *Radjai et al.*, 1998)

with a number of contacts supporting forces above the average value that exponentially decrease with increasing measured contact force. As such, *Radjai et al.* (1998) defined a strong contact force network as forces above the average value and a weak contact force network as forces below the average value. They plotted the distribution of contacts in both networks, see Figure A.5, and show that the strong contact network is oriented in the direction of the principal stress compression whereas the weak contact network is oriented in the direction of the weaker stress compression. In addition, they show that the corresponding forces of the latter contact network contributes to the isotropic part of the internal stress tensor resisting to the isotropic biaxial compression while the forces corresponding to the former contact network (strong) contributes to the deviatoric part of the internal stress tensor allowing the system to resist to the shear induced by the anisotropy of external imposed stress, i.e. the difference of normal external stress in both

directions.

Andreotti et al. (2013) proposed a qualitative analysis of such result, they explained that

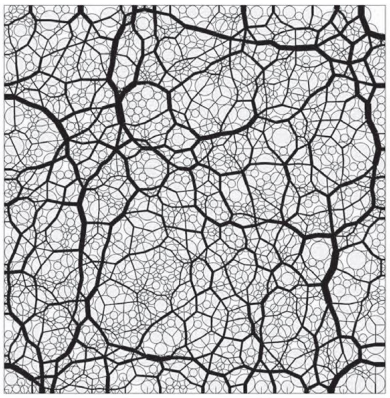

Figure A.6 – Contact forces network for 2D numerical simulations. The contact forces strength are represented with thickness of links representing the force between two particles. Source: (*Andreotti et al.*, 2013; *Radjai et al.*, 1999)

presenting the contact chains in a granular packing, obtained by *Radjai et al.* (1999) with numerical simulations and presented on Figure A.6. It shows that the medium displays strong and weak contacts (highlighted by the thickness of the links on the figure). The strong chain forces then develops and orientates to support anisotropy induced by the difference between the vertical and the horizontal loading creating a 'solid skeleton' of the packing that gives resistance to the assembly. This skeleton is in an 'isotropic phase' composed by the weak contacts network chains that stabilizes the skeleton.

A.6 Electrostatic repulsive force

In the work of *Clavaud et al.* (2017); *Perrin et al.* (2019, 2021), the classical solid-solid Hertz normal contact force defined in Section 3.1, is replaced by an electrostatic force of the form:

$$F_{rep} = F_0 e^{-z/\lambda_d}, \tag{A.38}$$

with $F_0/d = 1mN/m$ for silica beads and λ_d the Debye length that represents the range of the electrostatic force. This length depends on the concentration of ions as $\lambda_d = 0.304/\sqrt{[NaCl]}nm$. Which gives for a concentration of $[NaCl] = 10^{-4}mol.L^{-1}$ (which gives frictionless contacts in their results) a length $\lambda_d = 30.4nm$. l_r is the typical length of the roughness on the silica surface which is $l_r = 3.7nm$. We can consider that the maximum relative displacement of grains repulsed with that force is equal to $\delta_{rep} =_d -l_r$. The grains diameter is $d = 24\mu m$ which gives $F_0 = 2.5 \times 10^8 N$. Hence the corresponding effective stiffness of the contact can be estimated for such displacement as:

$$k_{rep} = \frac{F_{rep}}{\delta_{rep}} = \frac{F_0 e^{-l_r/\lambda_d}}{(_d - l_r)}. \tag{A.39}$$

This quantity then might be compared to the maximum pressure a grain is subjected to in the system corresponding to the maximum granulostatic pressure at the bottom of the

drum. Considering the drum half filled, with a radius of $R_d = 6mm$ in their experiment, it makes a maximum of $R_d/d = 250$ grains above one grain. The resulting relative stiffness, with a packing fraction of $\phi = 0.6$, is:

$$\kappa_{rep} = \frac{k_{rep}}{R_d * g * (\rho_p - \rho_f)d\phi} = 1.1 \times 10^3. \tag{A.40}$$

In order to compare with classical Hertz contact stiffness, we take the force given by Equation (3.4) with a Young's modulus for glass of $E = 70GPa$, a Poisson's ratio of $\nu_p = 0.2$ and a diameter in their study of $d_{glass} = 500\mu m$, considering the same displacement $\delta =_d -l_r$, it gives:

$$k_N = \frac{\pi\sqrt{d}E}{3(1-2\nu_p)}\delta^{1/2}, \tag{A.41}$$

And with a drum radius of $R_d = 27mm$ and $\phi = 0.6$, it gives:

$$\kappa = \frac{k_N}{R_d * g * (\rho_p - \rho_f)d\phi} = 1.9 \times 10^3. \tag{A.42}$$

There is a minimum ratio or 2 between the normal stiffness in both models with lower stiffness for electrostatic repulsive forces.

A.7 Lengthscales at the approach from unjamming in the frictionless case

In order to build lengthscales related to the apparition of rearrangements when approaching unjamming, we can consider a chunk of size l of grains that is artificially cut from the material. In three-dimensions, the chunk loses l^2 boundary contacts, and the chunk is not stable if the number of contacts in the chunk is lower than the isostatic value. The excess number of contacts within the chunk scales as $(\mathcal{Z} - \mathcal{Z}_{iso})l^3$, considering l^3 as the volume of the chunk. Hence, the number of soft-modes, N_{soft}, in the chunk is related to the difference between the contact loss at the boundary and the excess of contacts created within the chunk. Indeed, if the excess number of contacts within the chunk does not balance the loss of contacts at the boundary, the chunk is not stable (below isostaticity) and there is a finite amount of soft-modes. By contrast, if the excess number of contacts in the chunk is greater than the loss of contacts at the boundary, the number of soft-modes vanishes and the system is stable. It gives the following theoretical scaling (*Liu and Nagel*, 2010):

$$N_{soft} \sim l^2 - (\mathcal{Z} - \mathcal{Z}_{iso})l^3. \tag{A.43}$$

At a given compression, i.e. fixed $(\mathcal{Z} - \mathcal{Z}_{iso})$, if the size of the chunk is too small, it gives $l^2 > (\mathcal{Z} - \mathcal{Z}_{iso})l^3$ and the system is unstable. At large chunk sizes, l^3 compensate the low value of $(\mathcal{Z} - \mathcal{Z}_{iso})$ and the excess number of contacts in the chunk becomes greater than the loss of contacts at the boundary so that the chunk is stable. Then, the lenghtscale l^* represents the smallest chunk size that sustain rigidity. Below l^* the chunk will always be unstable and rearrange; above, it will be rigid (*Andreotti et al.*, 2013). l^* corresponds to the size at which N_{soft} vanishes (*Liu and Nagel*, 2010). This latter quantity depends on the excess number of contacts in the system as:

$$l^* \sim (\mathcal{Z} - \mathcal{Z}_{iso})^{-1} \sim (\phi - \phi_c)^{-1/2}. \tag{A.44}$$

This lengthscale has been observed by constructing the DOS upon compression in numerical simulations (*Silbert et al.*, 2005). Nevertheless, *Silbert et al.* (2005) observed another lengthscale in the case of shear modes built from ω^* that scale as:

$$l^*_{shear} \sim (\mathcal{Z} - \mathcal{Z}_{iso})^{-1/2} \sim (\phi - \phi_c)^{-1/4}. \tag{A.45}$$

Although the link between these lengthscales is not established yet, they diverge when approaching unjamming, i.e. when $\mathcal{Z}$ approaches $\mathcal{Z}_{iso}$. These theoretical development of diverging lengthscales show that the behavior of frictionless granular materials in the jammed state enables one to built lengthscales diverging at unjamming characteristic of second-order phase transition.

Appendix B

Method and model's appendices

B.1 Fluid-grains interactions

Buoyant weight

The buoyant weight is the sum of the weight of the grain with the Archimedes force. The latter correspond to the weight of a fluid particle of the same volume as the grain would have in the absence of the particle. This force is in the opposite direction of the grain weight. It gives for a sphere:

$$F_b = \frac{\pi d^3}{6}(\rho_p - \rho_f)g. \tag{B.1}$$

with g the gravity acceleration.

Stationary drag force

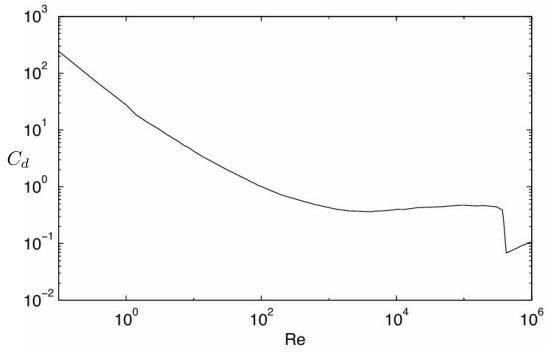

(a)

Coefficient de traînée	Domaine de validité	*Commentaires*
$C_D = \frac{24}{Re}$	$Re < 0,1$	Loi de Stokes (1851) Solution analytique
$C_D = \frac{24}{Re}\left(1 + \frac{3}{8}Re\right)$	$Re < 1$	Correction d'Oseen (1910) Solution analytique
$C_D = \frac{24}{Re}\left(1 + 0,15Re^{0,687}\right)$	$Re < 800$	Schiller et Nauman (1933) Corrélation empirique
$C_D \sim 0,45$	$Re < 3,5\,10^5$	Régime de Newton
$C_D \sim 0,07$	$Re = 3,5\,10^5$	Crise de résistance
$C_D \sim 0,19$	$Re > 3,5\,10^5$	

(b)

Figure B.1 – (a) Drag coefficient of a sphere versus the Reynolds number. (b) Correlations of the drag coefficient in the various regimes.

For stationary motion of the particle in a uniform and stationary flow, the drag force due to the resistance of the fluid is expressed as:

$$F_d = C_d \frac{\pi d^2 \rho_f}{8} \|v|_{x_p} - u_p\|(v|_{x_p} - u_p). \tag{B.2}$$

In the case of spherical particle, the drag coefficient C_d only depends on the particle Reynolds number, Re_p:

$$Re_p = \frac{\rho_f d \|v|_{x_p} - u_p\|}{\eta_f}. \tag{B.3}$$

The dependence of C_d with Re_p is plotted on Figure B.1a, the corresponding correlations in the various regimes are given in the Table presented on Figure B.1b.

History force

The history force, F_h, results from the delay of the drag force when the motion of the particle in the fluid is unstationary. As such it is a correction of the drag force that consider the unstationnary process as:

$$F_h = \int_0^t K(\tau) \frac{dF_d}{dt}(t_\tau) d\tau, \tag{B.4}$$

with the convolution kernel $K(\tau)$. Its expression depends on the flowing regime, i.e. $Re_p \leq 1$ or $1 < Re_p < 100$ (*Mei and Adrian*, 1992). This force is usually neglected for its mathematical and numerical complexity and the short-range regime where its expression is well known. In addition, being a correction of the drag force, the main drag effect is computed in the stationary drag force expressed above.

The added mass force and Tchen force

In the case of unstationary motion of particles and fluid flow, two unstationary forces are added to the unstationary drag effect. It reflects acceleration transfers between the particle and the fluid and is decomposed between the added mass force F_{am} that results from the acceleration transmitted to the fluid as:

$$F_{am} = C_M m_f \left(\frac{Dv}{Dt}|_{x_p} - \frac{d_u p}{dt} \right), \tag{B.5}$$

with C_M the added mass coefficient ususally set to $C_M = 0.5$ and $m_f = \rho_f \pi d^3/6$ the mass of fluid occupied by the particle of volume $\pi d^3/6$ (sphere). The notation $\frac{Dv}{Dt}$ is the acceleration of the fluid calculated at the center of the particle:

$$\frac{Dv}{Dt} = \frac{\partial v}{\partial t} + v.\nabla v. \tag{B.6}$$

In the expression B.5, the last term could be switch to the left part of Equation of motion 3.9, the result is equivalent as adding a mass $C_M m_f$ to the particle mass m_p resulting from an inertial acceleration due to the transfer of acceleration to the fluid. The remaining term of the expression B.5 refers to the variations of the fluid motion due to the transfer of momentum. Nevertheless this expression is not sufficient to fully consider the transfer of momentum to the fluid phase. As a consequence, another force, called the Tchen force, that represents the acceleration (or decelaration) that the same volume of fluid would undergo in the absence of the particle:

$$F_t = m_f \frac{Dv}{Dt}. \tag{B.7}$$

In a majority of applications, the flow is considered stationary and the first term of expression B.5 as well as the Tchen force vanishes, the added mass term only remains. In addition, the density of grains being usually greater than the density of the fluid, $m_p \gg m_f$, then the added mass term is also negligible.

Shear induced lift force

In the presence of velocity gradient, a lift force emerges due to the vorticity of flow. This force is expressed as:

$$F_l = C_l m_f (v|_{x_p} - u_p) \times \Omega, \tag{B.8}$$

with $\Omega = \nabla \times v|_{x_p}$ the vorticity, $v|_{x_p}$ is the fluid velocity at the center of the particle and C_l is the lift coefficient that depends on the flowing regime (*Saffman*, 1965; *McLaughlin*, 1991).

Magnus Force

The Magnus force results from the rotation of the particle, this force is expressed as:

$$F_m = C_{mag} m_f (v|_{x_p} - u_p) \times \Omega_p, \tag{B.9}$$

with Ω_p the rotating velocity of the particle and C_{mag} the constant Magnus coefficient that also depends on the flowing regime (*Barkla and Auchterlonie*, 1971).

Fluid moment on a sphere

The only moment a fluid force exerted on a sphere results from the viscosity of fluid that resist to the rotation of the particle. The corresponding moment depends on the rotational Reynlds number:

$$Re_p^\Omega = \frac{\rho_f d^2 |\Omega_p|}{4\eta_f}. \tag{B.10}$$

In the case of low rotational Reynolds, i.e. viscous rotational regime $Re_p^\Omega < 1$, the moment is written as (*Rubinow and Keller*, 1961):

$$M = -\pi \eta_f d^3 \Omega_p. \tag{B.11}$$

In the case of moderate and high Reynolds number, i.e. inertial regime $Re_p^\Omega > 1$, the moment is written as (*Dennis et al.*, 1980):

$$M = -2\eta_f d^3 (1 + 0.2\sqrt{Re_p^\Omega})\Omega_p. \tag{B.12}$$

Appendix C

Granular regimes and phase transition on an inclined plane appendices

C.1 Influence of the restitution coefficient on hysteresis at various inter-particle friction

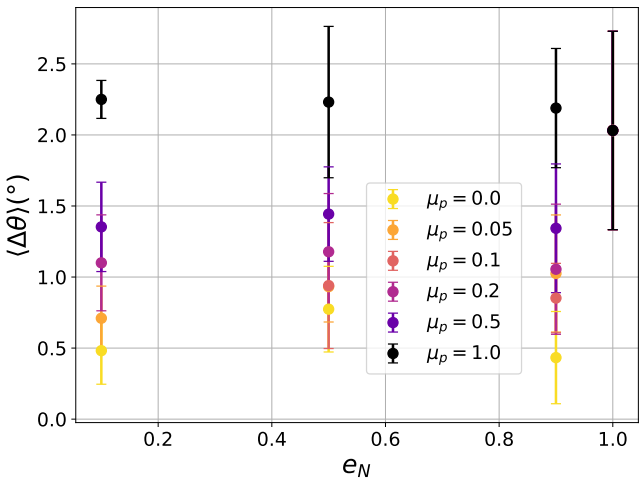

Figure C.1 – Hysteresis versus restitution coefficient at various inter-particle friction coefficient.

In order to study the influence of the restitution coefficient on hysteresis, we performed simulations at various restitution coefficient and inter-particles friction coefficients. As such, results at $e_N = 0.1$, $e_N = 0.5$ and $e_N = 1$ at $\mu_p = 1$, 0.1, 0.05 and 0 are added to the results presented in Chapter 4 for $\mu_p = 0.2$ and $\mu_p = 0.5$. Hysteresis is presented versus e_N at various μ_p in Figure C.1. The figure shows no significant variations of $\Delta\theta$ with e_N but a dominant inter-particle friction effect as shown in Chapter 4. The result then holds for all inter-particle friction coefficients simulated in our work. It is interesting to note that

for purely elastic collisions, i.e. in the limit case $e_N = 1$, for finite inter-particle friction coefficient, hysteresis is at the same order than for inelastic contacts. We also performed simulations with no contact dissipation both by collisions and friction, i.e. at $_N = 1$ and $\mu_p = 0$. Since no dissipation mechanism holds, the simulation starts at $\theta = 0$ in the static state. The the inclination angle is slightly increase until the medium starts flowing. Interestingly, the measured average avalanche angle in these case is $\theta_{start} = 0.06°$. In fact, the first rearrangement observed is not damped and dramatically leads the system to flow. Then, we it suggests that for larger domain sizes and layer thickness, the avalanche angle would tends to 0°. As a consequence, contact dissipation is then not required to observe hysteresis if a finite inter-particle is set such that there is a source of dissipation in the system. Similarly, inter-particle friction is not necessary to observed hysteresis if some finite grains collisions dissipation is set such that there is a source of dissipation at the contact scale. Finally, for dry granular media on inclined plane, the existence of a yield criterion as well as hysteresis require at least one source of dissipation at the contact scale between friction and collisions.

Appendix D

Outlook appendices

D.1 Generalization of hysteresis in the frictionless case for various configurations

D.1.1 Hysteresis in a rotating drum

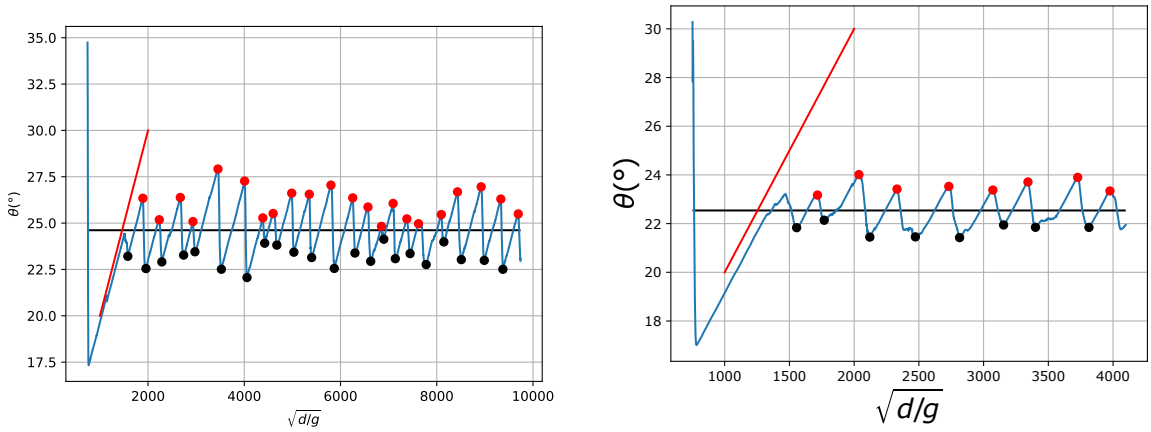

(a) (b)

Figure D.1 – Temporal evolution of the inclination angle of the free surface of the granular medium in rotating drum of width $W = 10d$ and diameter (a) $D = 50d$ (b) $D = 100d$ at $\mu_p = 0.5$.

We performed simulations in a rotating drum with $\mu_p = 0.5$ two various drum diameter $D = 100d$ and $D = 50d$ on Figure D.1. The values of hysteresis are calculated as average values over the number of avalanches observed on the figure. For $D = 50d$, hysteresis is $\langle \Delta\theta \rangle = 2.9 \pm 0.9°$. For $D = 100d$, hysteresis is $\langle \Delta\theta \rangle = 1.8 \pm 0.3°$. As expected, the value depends on the diameter of the drum (*Peng et al.*, 2023), similarly it is expected to depends on the width of the drum which is fixed here at $W = 10d$ for both diameter sizes. Nevertheless, the value measured for $D = 100d$ is close to the value measured at $\mu_p = 0.5$ on an inclined plane. It is also close to the values of *Perrin et al.* (2019) for glass beads at $St = 4$ but lower than the results from *Peng et al.* (2023) that measure an

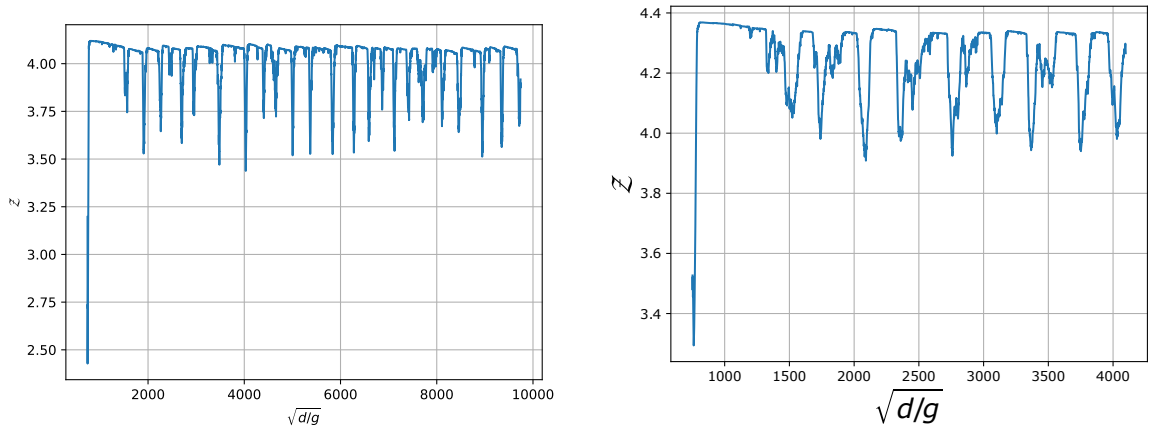

(a) (b)

Figure D.2 – Temporal evolution of the coordination number in a rotating drum of width $W = 10d$ and diameter (a) $D = 50d$ (b) $D = 100d$ at $\mu_p = 0.5$.

hysteresis above 2° for all glass beads experiments. Further study on the influence of D, W and the rotating speed needs to be set in order to ensure that the result is rigorous and to compare our results to literature properly. Nevertheless these results show us that the hysteresis observed yet in that configuration is globally not as high as in the results from the literature. One of the main reason may lie in the roughness condition of the drum that similarly to the inclined plane configuration needs to be studied although less impact on hysteresis is expected in a rotating drum than on an inclined plane.
Figure D.2 presents the average coordination number evolution with simulation time for both drum diameters. In both cases alternate cyclic behavior is also observed with constant values in the static state demonstrating no flow and downward peaks at the avalanches.

Figure D.3 presents results in the frictionless case with $D = 50d$ as detailed at Chapter 6. Further simulations, especially with various drum sizes and rotating speed are required. Also, further analysis near the drum boundary are required. Indeed, in such configuration, the slip tangential condition is expected to lead easily to slip at the boundary since this geometry imply variations of stress ratio along the drum. The effect of the drum roughness is then different from the inclined plane configuration but is non trivial.

D.1.2 Hysteresis in a plane shear cell

Simulations in plane shear cell have been conducted in order to study hysteresis in that configuration.

First, we computed simulations in stress imposed, imposing the same amount of normal and shear stress in opposite directions at both upper and lower boundary walls. The inertial number is measured and enables us to observe both flowing and static states as well as hysteresis. Figure D.5 presents hysteretic cycles of the flow curve $\mu_w(\mathcal{I})$ with μ_w the stress ratio imposed at boundaries and $\mathcal{I}_{global}$ the resulting inertial number. Two inter-particle friction were computed: $\mu_p = 0.5$ and $\mu_p = 0.2$. For both plots the markers are colorized from dark to bright indicating the stress path with time. The stress ratio

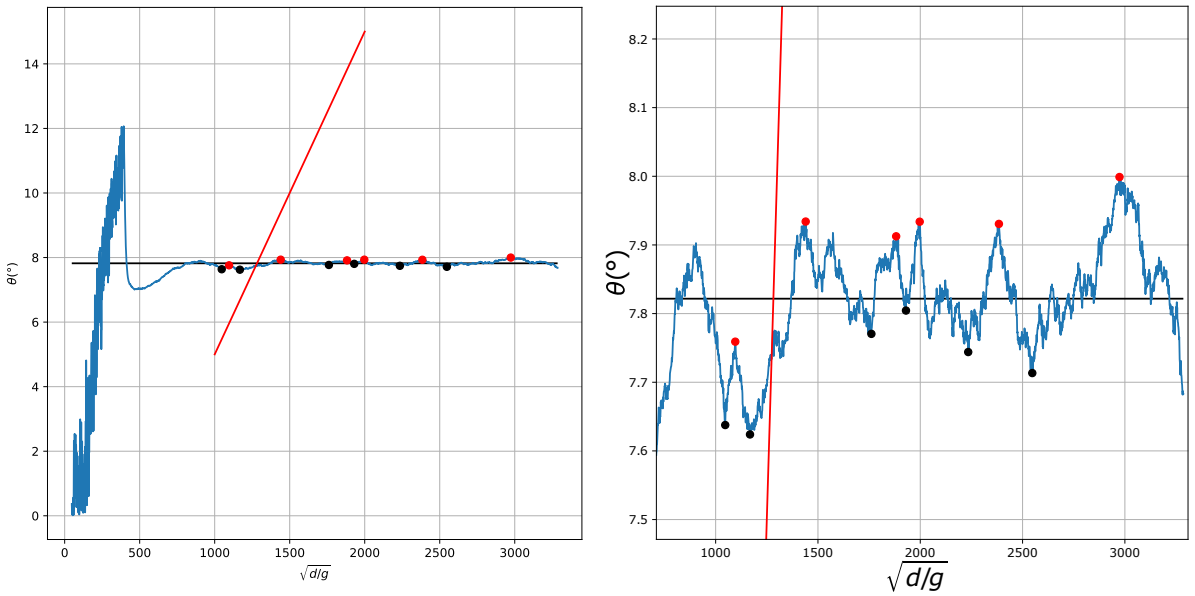

(a) (b)

Figure D.3 – (a) Temporal evolution of the inclination angle of the free surface of the granular medium in rotating drum of width $W = 20d$ and diameter $D = 100d$ in the frictionless case. In the first part the rotating speed is high $\omega = 1°/\sqrt{d/g}$ and the medium is continuously flowing. On the second part the rotating speed is set at $\omega = 10^{-2}°/\sqrt{d/g}$ to observe intermittent flow and arrest. (b) Zoom on the second part.

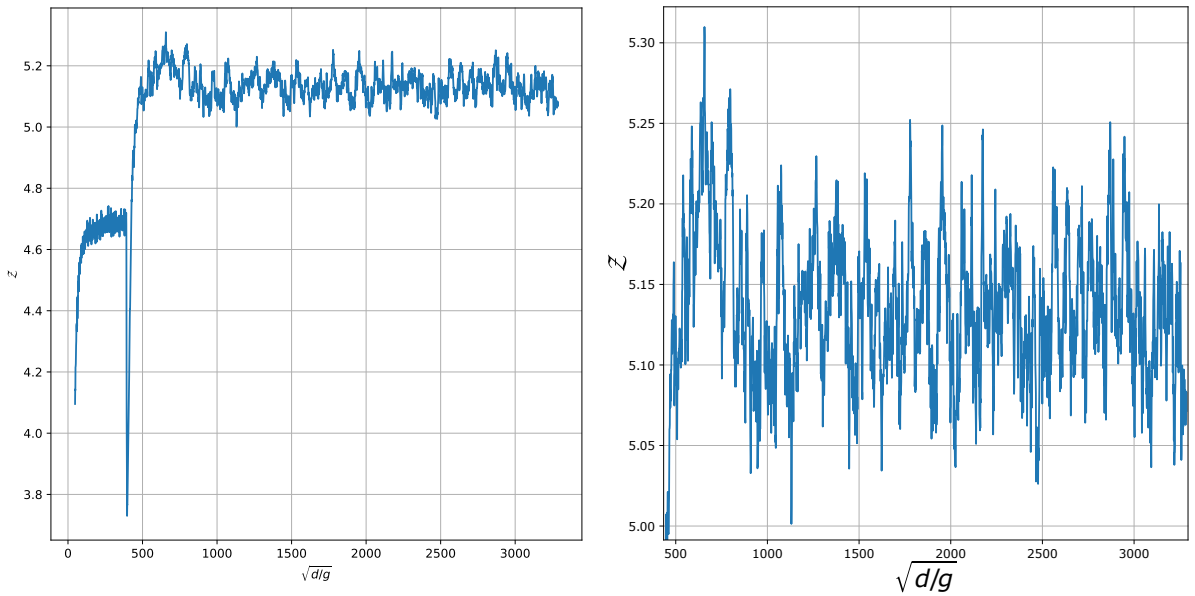

(a) (b)

Figure D.4 – (a) Temporal evolution of the coordination number in a rotating drum of width $W = 20d$ and diameter $D = 100d$ in the frictionless case. In the first part the rotating speed is high $\omega = 1°/\sqrt{d/g}$ and the medium is continuously flowing. On the second part the rotating speed is set at $\omega = 10^{-2}°/\sqrt{d/g}$ to observe intermittent flow and arrest. (b) Zoom on the second part.

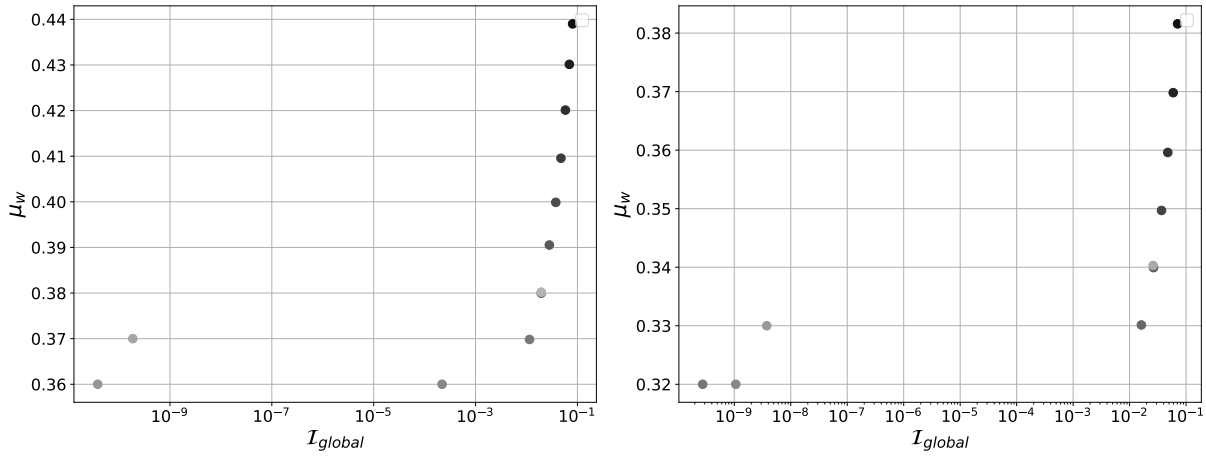

(a) (b)

Figure D.5 – Hysteretic cycle of $\mu_w(\mathcal{I})$ curve in a stress imposed planar shear cell configuration with inter-particle friction coefficient of (a) $\mu_p = 0.5$ and (b) $\mu_p = 0.2$.

is first decreasing until the medium stops, then it is increased until the medium starts flowing again. At $\mu_p = 0.5$ the critical stress ratios are $\mu_{w,stop} = 36$ and $\mu_{w,start} = 0.38$. The corresponding hysteresis is $\Delta\mu_w = 0.02$ corresponding to an hysteresis of 1° in terms of angle. At $\mu_p = 0.2$ the critical stress ratios are $\mu_{w,stop} = 32$ and $\mu_{w,start} = 0.34$. The hysteresis is then the same. Interestingly the measured hysteresis appears to be independent on the inter-particle friction coefficient, in addition, the critical stress ratio are really close between both inter-particle friction coefficients. Similarly, the coordination

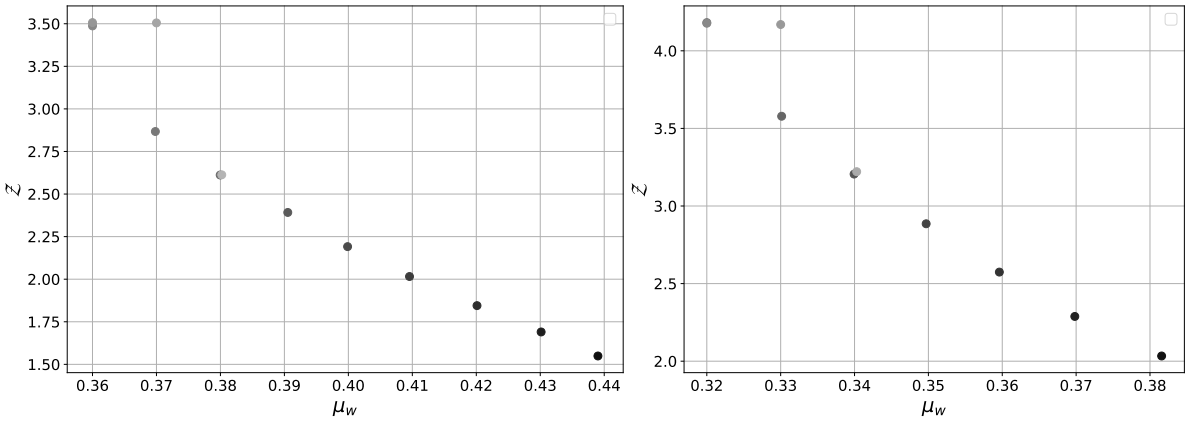

(a) (b)

Figure D.6 – Hysteretic cycle of the coordination number $\mathcal{Z}(\mu_w)$ in a stress imposed planar shear cell configuration with inter-particle friction coefficient of (a) $\mu_p = 0.5$ and (b) $\mu_p = 0.2$.

number hysteretic cycles at both μ_p are plotted on Figure D.6 showing an increase of the coordination when the stress ratio imposed decrease. The medium then starts showing a constant coordination number value when μ_w increases. The values in the static state are smaller than on an inclined plane and in a rotating drum. Further investigation, especially refining the stress ratio values near the hysteretic cycle are needed. Simulations at $\mu_p = 0$ are underway to compare if hysteresis can be observed for frictionless assembly in stress imposed planar shear cell. Velocity imposed simulations are also underway in order to compare the results with stress imposed values of hysteresis. Finally, similarly to the inclined plane configuration, the influence of the plane walls roughness is non negligible and require extensive studies.

Bibliography

Amon, A., R. Bertoni, and J. Crassous (2013), Experimental investigation of plastic deformations before a granular avalanche, *Physical Review E*, *87*(1), 012,204, doi:10.1103/PhysRevE.87.012204. 57

Andreotti, B., Y. Forterre, and O. Pouliquen (2013), *Granular media: between fluid and solid*, Cambridge Univ. Press, Cambridge. 15, 17, 18, 23, 24, 28, 29, 30, 31, 32, 33, 34, 47, 63, 72, 73, 79, 119, 185, 193, 194, 195, 196

Aranson, I. S., and L. S. Tsimring (2006), Patterns and Collective Behavior in Granular Media: Theoretical Concepts, *Reviews of Modern Physics*, *78*(2), 641–692, doi:10.1103/RevModPhys.78.641, arXiv:cond-mat/0507419. 38, 57, 158

Aranson, I. S., L. S. Tsimring, F. Malloggi, and E. Clément (2008), Nonlocal rheological properties of granular flows near a jamming limit, *Physical Review E*, *78*(3), 031,303, doi:10.1103/PhysRevE.78.031303. 38, 68, 112, 115

Artoni, R., A. Santomaso, and P. Canu (2011), Hysteresis in a hydrodynamic model of dense granular flows, *Physical Review E*, *83*(5), 051,304, doi:10.1103/PhysRevE.83.051304. 69

Bagnold, R. A. (1954), Experiments on a gravity-free dispersion of large solid spheres in a Newtonian fluid under shear, *Proceedings of the Royal Society of London. Series A. Mathematical and Physical Sciences*, *225*(1160), 49–63, doi:10.1098/rspa.1954.0186. 32, 34, 85

Bagnold, R. A. (1966), The shearing and dilatation of dry sand and the 'singing' mechanism, *Proceedings of the Royal Society of London. Series A. Mathematical and Physical Sciences*, *295*(1442), 219–232, doi:10.1098/rspa.1966.0236. 32, 57, 67, 85, 100, 119, 167

Balmforth, N. J., and J. N. McElwaine (2018), From episodic avalanching to continuous flow in a granular drum, *Granular Matter*, *20*(3), 52, doi:10.1007/s10035-018-0822-1. 64

Baran, O., D. Ertaıfmmode \mboxş\else ş\fi, T. C. Halsey, G. S. Grest, and J. B. Lechman (2006), Velocity correlations in dense gravity-driven granular chute flow, *Phys. Rev. E*, *74*(5), 051,302, publisher: American Physical Society. 18, 33, 34, 81, 91, 92, 100

Barenblatt, G. I. (2003), *Scaling*, 1 ed., Cambridge University Press, doi:10.1017/CBO9780511814921. 29

Barkla, H. M., and L. J. Auchterlonie (1971), The Magnus or Robins effect on rotating spheres, *Journal of Fluid Mechanics*, *47*(3), 437–447, doi:10.1017/S0022112071001150. 201

Bathurst, R. J., and L. Rothenburg (1990), Observations on stress-force-fabric relationships in idealized granular materials, *Mechanics of Materials*, *9*(1), 65–80, doi:10.1016/0167-6636(90)90030-J. 23, 187, 188, 189, 190, 193

Behringer, R. P., and B. Chakraborty (2019), The physics of jamming for granular materials: a review, *Reports on Progress in Physics*, *82*(1), 012,601, doi:10.1088/1361-6633/aadc3c. 48, 52, 53, 54, 119

Bi, D., J. Zhang, B. Chakraborty, and R. P. Behringer (2011), Jamming by shear, *Nature*, *480*(7377), 355–358, doi:10.1038/nature10667, publisher: Nature Publishing Group. 15, 16, 42, 51, 52

Biroli, G. (2007), A new kind of phase transition?, *Nature Physics*, *3*(4), 222–223, doi:10.1038/nphys580, publisher: Nature Publishing Group. 43

Bocquet, L., J. Errami, and T. C. Lubensky (2002), Hydrodynamic Model for a Dynamical Jammed-to-Flowing Transition in Gravity Driven Granular Media, *Physical Review Letters*, *89*(18), 184,301, doi:10.1103/PhysRevLett.89.184301, publisher: American Physical Society. 69

Bonn, D., M. M. Denn, L. Berthier, T. Divoux, and S. Manneville (2017), Yield stress materials in soft condensed matter, *Reviews of Modern Physics*, *89*(3), 035,005, doi:10.1103/RevModPhys.89.035005. 38, 43, 50, 52, 54, 186

Bouzid, M., M. Trulsson, P. Claudin, E. Clément, and B. Andreotti (2013), Nonlocal Rheology of Granular Flows across Yield Conditions, *Phys. Rev. Lett.*, *111*(23), 238,301, publisher: American Physical Society. 38

Boyer, F., Guazzelli, and O. Pouliquen (2011), Unifying Suspension and Granular Rheology, *Physical Review Letters*, *107*(18), 188,301, doi:10.1103/PhysRevLett.107.188301, publisher: American Physical Society. 34, 186

Cassar, C., M. Nicolas, and O. Pouliquen (2005), Submarine granular flows down inclined planes, *Physics of Fluids (1994-present)*, *17*(10), 103,301. 18, 77, 93, 119

Ciamarra, M. P., R. Pastore, M. Nicodemi, and A. Coniglio (2011), Jamming phase diagram for frictional particles, *Physical Review E*, *84*(4), 041,308, doi:10.1103/PhysRevE.84.041308, publisher: American Physical Society. 16, 54, 55, 87, 94, 187

Clavaud, C., A. Bérut, B. Metzger, and Y. Forterre (2017), Revealing the frictional transition in shear-thickening suspensions, *Proceedings of the National Academy of Sciences*, *114*(20), 5147–5152, doi:10.1073/pnas.1703926114. 64, 139, 148, 195

Courrech Du Pont, S., P. Gondret, B. Perrin, and M. Rabaud (2003), Granular Avalanches in Fluids, *Physical Review Letters*, *90*(4), 044,301, doi:10.1103/PhysRevLett.90.044301. 17, 18, 21, 39, 40, 60, 62, 63, 64, 65, 75, 77, 78, 85, 86, 93, 139, 147, 148, 149

Crassous, J., J.-F. Metayer, P. Richard, and C. Laroche (2008), Experimental study of a creeping granular flow at very low velocity, *Journal of Statistical Mechanics: Theory and Experiment*, *2008*(03), P03,009, doi:10.1088/1742-5468/2008/03/P03009. 35

Cundall, P. A., and O. D. L. Strack (1979), A discrete numerical model for granular assemblies, *Géotechnique*, *29*(1), 47–65, doi:10.1680/geot.1979.29.1.47. 38, 80

Da Cruz, F., F. Chevoir, D. Bonn, and P. Coussot (2002), Viscosity bifurcation in granular materials, foams, and emulsions, *Phys. Rev. E*, *66*, 051,305. 17, 39, 41, 62, 63, 66

Da Cruz, F., S. Emam, M. Prochnow, J.-N. Roux, and F. Chevoir (2005), Rheophysics of dense granular materials: Discrete simulation of plane shear flows, *Phys. Rev. E*, *72*(2), 021,309, publisher: American Physical Society. 15, 33, 34, 41, 119

DallaValle, J. M. (1948), *Micrometrics : The technology of fine particles*, vol. 2nd edition, Pitman Pub. Corp. 82

De Gennes, P. G. (1999), Granular matter: a tentative view, *Reviews of Modern Physics*, *71*(2), S374–S382, doi:10.1103/RevModPhys.71.S374. 27

DeGiuli, E., and M. Wyart (2017), Friction law and hysteresis in granular materials, *Proceedings of the National Academy of Sciences*, *114*(35), 9284–9289, doi:10.1073/pnas.1706105114. 16, 17, 18, 33, 34, 40, 41, 53, 56, 60, 62, 64, 66, 67, 68, 81, 84, 139, 143, 146, 150, 170

DeGiuli, E., J. N. McElwaine, and M. Wyart (2016), Phase diagram for inertial granular flows, *Physical Review E*, *94*(1), 012,904, doi:10.1103/PhysRevE.94.012904. 16, 56, 68, 81, 127, 132, 139, 147, 157, 170

Delannay, R., A. Valance, A. Mangeney, O. Roche, and P. Richard (2017), Granular and particle-laden flows: from laboratory experiments to field observations, *Journal of Physics D: Applied Physics*, *50*(5), 053,001, doi:10.1088/1361-6463/50/5/053001. 27

Dennis, S. C. R., S. N. Singh, and D. B. Ingham (1980), The steady flow due to a rotating sphere at low and moderate Reynolds numbers, *Journal of Fluid Mechanics*, *101*(2), 257–279, doi:10.1017/S0022112080001656. 201

Depken, M., J. B. Lechman, M. V. Hecke, W. V. Saarloos, and G. S. Grest (2007), Stresses in smooth flows of dense granular media, *Europhysics Letters (EPL)*, *78*(5), 58,001, doi:10.1209/0295-5075/78/58001. 191

Edwards, A. N., A. S. Russell, C. G. Johnson, and J. M. N. T. Gray (2019), Frictional hysteresis and particle deposition in granular free-surface flows, *Journal of Fluid Mechanics*, *875*, 1058–1095, doi:10.1017/jfm.2019.517. 69, 171

Edwards, S., and R. Oakeshott (1989), Theory of powders, *Physica A: Statistical Mechanics and its Applications*, *157*(3), 1080–1090, doi:10.1016/0378-4371(89)90034-4. 51

Einstein, A. (1911), Berichtigung zu meiner Arbeit: „Eine neue Bestimmung der Moleküldimensionen", *Annalen der Physik*, *339*(3), 591–592, doi:10.1002/andp.19113390313. 185

Favier De Coulomb, A., M. Bouzid, P. Claudin, E. Clément, and B. Andreotti (2017), Rheology of granular flows across the transition from soft to rigid particles, *Physical Review Fluids*, *2*(10), 102,301, doi:10.1103/PhysRevFluids.2.102301. 60, 82, 152, 155

Fenistein, D., and M. van Hecke (2003), Wide shear zones in granular bulk flow, *Nature*, *425*(6955), 256–256, doi:10.1038/425256a, publisher: Nature Publishing Group. 35, 38

Forterre, Y., and O. Pouliquen (2008), Flows of Dense Granular Media, *Annual Review of Fluid Mechanics*, *40*(1), 1–24. 15, 17, 21, 27, 32, 33, 34, 37, 59, 66, 84, 100, 149

GDR MiDi (2004), On dense granular flows, *The European Physical Journal E*, *14*(4), 341–365, doi:10.1140/epje/i2003-10153-0. 27, 32, 33, 34, 35, 37, 60, 69, 81, 100, 102, 103, 105, 119

Gondret, P., M. Lance, and L. Petit (2002), Bouncing motion of spherical particles in fluids, *Physics of Fluids*, *14*(2), 643–652. 18, 79

Goujon, C., N. Thomas, and B. Dalloz-Dubrujeaud (2003), Monodisperse dry granular flows oninclined planes: Role of roughness, *The European Physical Journal E*, *11*(2), 147–157, doi:10.1140/epje/i2003-10012-0. 15, 17, 36, 59, 60, 178

Greeley, R. (2013), *Introduction to Planetary Geomorphology*, Cambridge University Press, Cambridge, doi:10.1017/CBO9781139020961. 27

Grob, M., C. Heussinger, and A. Zippelius (2014), Jamming of frictional particles: A nonequilibrium first-order phase transition, *Physical Review E*, *89*(5), 050,201, doi:10.1103/PhysRevE.89.050201. 54, 64, 69, 186, 187

Guazzelli, , and O. Pouliquen (2018), Rheology of dense granular suspensions, *Journal of Fluid Mechanics*, *852*, P1, doi:10.1017/jfm.2018.548. 34, 37, 185, 186, 191

Guo, N., and J. Zhao (2013), The signature of shear-induced anisotropy in granular media, *Computers and Geotechnics*, *47*, 1–15, doi:10.1016/j.compgeo.2012.07.002. 188, 189, 190

Henkes, S., M. v. Hecke, and W. v. Saarloos (2010), Critical jamming of frictional grains in the generalized isostaticity picture, *Europhysics Letters*, *90*(1), 14,003, doi:10.1209/0295-5075/90/14003. 49, 125

Henkes, S., D. A. Quint, Y. Fily, and J. Schwarz (2016), Rigid Cluster Decomposition Reveals Criticality in Frictional Jamming, *Physical Review Letters*, *116*(2), 028,301, doi:10.1103/PhysRevLett.116.028301, publisher: American Physical Society. 38, 44, 53, 69, 127, 178

Hohenberg, P., and A. Krekhov (2015), An introduction to the Ginzburg–Landau theory of phase transitions and nonequilibrium patterns, *Physics Reports*, *572*, 1–42, doi:10.1016/j.physrep.2015.01.001. 62

Hong, X., M. Kohne, M. Morrell, H. Wang, and E. R. Weeks (2017), Clogging of soft particles in two-dimensional hoppers, *Physical Review E*, *96*(6), 062,605, doi:10.1103/PhysRevE.96.062605. 15, 36

Jean, M. (1999), The non-smooth contact dynamics method, *Computer Methods in Applied Mechanics and Engineering*, *177*(3), 235–257, doi:10.1016/S0045-7825(98)00383-1. 80

Jerolmack, D. J., and K. E. Daniels (2019), Viewing Earth's surface as a soft-matter landscape, *Nature Reviews Physics*, *1*(12), 716–730, doi:10.1038/s42254-019-0111-x. 27

Jop, P., Y. Forterre, and O. Pouliquen (2006), A constitutive law for dense granular flows, *Nature*, *441*(7094), 727–730. 33, 37, 84, 190

Kamrin, K., and G. Koval (2012), Nonlocal Constitutive Relation for Steady Granular Flow, *Phys. Rev. Lett.*, *108*(17), 178,301, publisher: American Physical Society. 38

Kamrin, K., K. M. Hill, D. I. Goldman, and J. E. Andrade (2024), Advances in Modeling Dense Granular Media, *Annual Review of Fluid Mechanics*, *56*(1), 215–240, doi:10.1146/annurev-fluid-121021-022045. 27, 33, 35, 36, 37

Komatsu, T. S., S. Inagaki, N. Nakagawa, and S. Nasuno (2001), Creep Motion in a Granular Pile Exhibiting Steady Surface Flow, *Physical Review Letters*, *86*(9), 1757–1760, doi:10.1103/PhysRevLett.86.1757, publisher: American Physical Society. 15, 35

Koval, G., J.-N. Roux, A. Corfdir, and F. Chevoir (2009), Annular shear of cohesionless granular materials: From the inertial to quasistatic regime, *Physical Review E*, *79*(2), 021,306, doi:10.1103/PhysRevE.79.021306. 37

Lecoq, N., R. Anthore, B. Cichocki, P. Szymczak, and F. Feuillebois (2004), Drag force on a sphere moving towards a corrugated wall, *Journal of Fluid Mechanics*, *513*, 247–264, doi:10.1017/S0022112004009942. 79

Liu, A. J., and S. R. Nagel (1998), Jamming is not just cool any more, *Nature*, *396*(6706), 21–22, doi:10.1038/23819, publisher: Nature Publishing Group. 15, 16, 41, 42, 43, 51, 52, 54, 55

Liu, A. J., and S. R. Nagel (2010), The Jamming Transition and the Marginally Jammed Solid, *Annual Review of Condensed Matter Physics*, *1*(1), 347–369, doi:10.1146/annurev-conmatphys-070909-104045. 43, 44, 45, 46, 48, 49, 123, 196

Løvoll, G., K. J. Måløy, and E. G. Flekkøy (1999), Force measurements on static granular materials, *Physical Review E*, *60*(5), 5872–5878, doi:10.1103/PhysRevE.60.5872. 23, 194

Mandal, S., A. Gans, M. Nicolas, and O. Pouliquen (2021a), Flows of cohesive granular media, *EPJ Web of Conferences*, *249*, 01,001, doi:10.1051/epjconf/202124901001. 35

Mandal, S., M. Nicolas, and O. Pouliquen (2021b), Rheology of Cohesive Granular Media: Shear Banding, Hysteresis, and Nonlocal Effects, *Physical Review X*, *11*(2), 021,017, doi:10.1103/PhysRevX.11.021017. 38, 179

Maurin, R. (2015), Investigation of granular behavior in bedload transport using an Eulerian-Lagrangian model, PhD Thesis, Université Grenoble Alpes. 27, 75, 82

Maurin, R., J. Chauchat, and P. Frey (2016), Dense granular flow rheology in turbulent bedload transport, *Journal of Fluid Mechanics*, *804*, 490–512, place: Cambridge, UK Publisher: Cambridge University Press. 32

McLaughlin, J. B. (1991), Inertial migration of a small sphere in linear shear flows, *Journal of Fluid Mechanics*, *224*, 261–274, doi:10.1017/S0022112091001751. 201

Mei, R., and R. J. Adrian (1992), Flow past a sphere with an oscillation in the free-stream velocity and unsteady drag at finite Reynolds number, *Journal of Fluid Mechanics*, *237*, 323–341, doi:10.1017/S0022112092003434. 200

Mills, P., P. G. Rognon, and F. Chevoir (2008), Rheology and structure of granular materials near the jamming transition, *EPL (Europhysics Letters)*, *81*(6), 64,005, doi:10.1209/0295-5075/81/64005. 54

Mollon, G. (2015), Mécanique des matériaux granulaires. 27

Moreau, J. J. (1983), Liaisons unilatérales sans frottement et chocs inélastiques, *Comptes rendus hebdomadaires des séances de l'Académie des sciences*, *296*, 1473–1476, publisher: Gauthier-Villars. 80

Mowlavi, S., and K. Kamrin (2021), Interplay between hysteresis and nonlocality during onset and arrest of flow in granular materials, *Soft Matter*, *17*(31), 7359–7375, doi:10.1039/D1SM00659B. 17, 39, 62, 63, 69

Mueth, D. M., H. M. Jaeger, and S. R. Nagel (1998), Force distribution in a granular medium, *Physical Review E*, *57*(3), 3164–3169, doi:10.1103/PhysRevE.57.3164, publisher: American Physical Society. 23, 194

Oda, M. (1982), Fabric Tensor for Discontinuous Geological Materials, *Soils and Foundations*, *22*(4), 96–108, doi:10.3208/sandf1972.22.4_96. 187, 188

O'Hern, C. S., S. A. Langer, A. J. Liu, and S. R. Nagel (2001), Force Distributions near Jamming and Glass Transitions, *Physical Review Letters*, *86*(1), 111–114, doi:10.1103/PhysRevLett.86.111. 41

O'Hern, C. S., L. E. Silbert, A. J. Liu, and S. R. Nagel (2003), Jamming at zero temperature and zero applied stress: The epitome of disorder, *Physical Review E*, *68*(1), 011,306, doi:10.1103/PhysRevE.68.011306. 16, 41, 43, 45, 46, 47

Pan, D., Y. Wang, H. Yoshino, J. Zhang, and Y. Jin (2023), A review on shear jamming, *Physics Reports*, *1038*, 1–18, doi:10.1016/j.physrep.2023.10.002. 16, 49, 50, 52, 53, 57, 123

Peng, A., Y. Yuan, and Y. Wang (2023), Granular avalanche statistics in rotating drum with varied particle roughness, *National Science Open*, *2*(3), 20220,069, doi:10.1360/nso/20220069. 39, 40, 56, 60, 62, 64, 65, 66, 68, 85, 139, 146, 148, 205

Perrin, H., C. Clavaud, M. Wyart, B. Metzger, and Y. Forterre (2019), Interparticle Friction Leads to Nonmonotonic Flow Curves and Hysteresis in Viscous Suspensions, *Physical Review X*, *9*(3), 031,027, doi:10.1103/PhysRevX.9.031027. 17, 21, 39, 40, 56,

60, 62, 64, 65, 66, 67, 68, 75, 77, 85, 86, 139, 143, 146, 147, 148, 149, 150, 152, 167, 195, 205

Perrin, H., M. Wyart, B. Metzger, and Y. Forterre (2021), Nonlocal Effects Reflect the Jamming Criticality in Frictionless Granular Flows Down Inclines, *Physical Review Letters*, *126*(22), 228,002, doi:10.1103/PhysRevLett.126.228002. 40, 60, 85, 139, 143, 146, 150, 195

Peyneau, P.-E., and J.-N. Roux (2008), Frictionless bead packs have macroscopic friction, but no dilatancy, *Physical Review E*, *78*(1), 011,307, doi:10.1103/PhysRevE.78.011307. 57, 67, 119, 167

Popova, E., and V. L. Popov (2015), The research works of Coulomb and Amontons and generalized laws of friction, *Friction*, *3*(2), 183–190, doi:10.1007/s40544-015-0074-6. 27

Pouliquen, O. (1999), Scaling laws in granular flows down rough inclined planes, *Physics of Fluids*, *11*(3), 542–548, doi:10.1063/1.869928. 61

Pouliquen, O., and Y. Forterre (2002), Friction law for dense granular flows: application to the motion of a mass down a rough inclined plane, *Journal of Fluid Mechanics*, *453*, 133–151, doi:10.1017/S0022112001006796. 15, 17, 39, 58, 59, 61, 62, 85, 102, 105, 152

Pouliquen, O., and N. Renaut (1996), Onset of Granular Flows on an Inclined Rough Surface: Dilatancy Effects, *Journal de Physique II*, *6*(6), 923–935, doi:10.1051/jp2:1996220. 57, 62, 179

Quartier, L., B. Andreotti, S. Douady, and A. Daerr (2000), Dynamics of a grain on a sandpile model, *Phys. Rev. E*, *62*(6), 8299–8307, publisher: American Physical Society. 58

Radjai, F., and S. Roux (2002), Turbulentlike Fluctuations in Quasistatic Flow of Granular Media, *Physical Review Letters*, *89*(6), 064,302, doi:10.1103/PhysRevLett.89.064302, publisher: American Physical Society. 43, 187

Radjai, F., D. E. Wolf, M. Jean, and J. J. Moreau (1998), Bimodal Character of Stress Transmission in Granular Packings, *Physical Review Letters*, *80*, 61–64, doi:10.1103/PhysRevLett.80.61, publisher: American Physical Society. 23, 24, 38, 194

Radjai, F., S. Roux, and J. J. Moreau (1999), Contact forces in a granular packing, *Chaos: An Interdisciplinary Journal of Nonlinear Science*, *9*(3), 544–550, doi:10.1063/1.166428. 23, 24, 38, 194, 195

Reynolds, O. (1885), LVII. *On the dilatancy of media composed of rigid particles in contact. With experimental illustrations*, *The London, Edinburgh, and Dublin Philosophical Magazine and Journal of Science*, *20*(127), 469–481, doi:10.1080/14786448508627791. 57

Rhodes, M. J. (1990), Principles of powder technology. 27

Rothenburg, L., and N. Kruyt (2004), Critical state and evolution of coordination number in simulated granular materials, *International Journal of Solids and Structures*, *41*(21), 5763–5774, doi:10.1016/j.ijsolstr.2004.06.001. 41

Roux, J.-N., and G. Combe (2002), Quasistatic rheology and the origins of strain, *Comptes Rendus Physique*, *3*(2), 131–140, doi:10.1016/S1631-0705(02)01306-3. 80, 82, 152, 153

Rubinow, S. I., and J. B. Keller (1961), The transverse force on a spinning sphere moving in a viscous fluid, *Journal of Fluid Mechanics*, *11*(3), 447–459, doi:10.1017/S0022112061000640. 201

Saffman, P. G. (1965), The lift on a small sphere in a slow shear flow, *Journal of Fluid Mechanics*, *22*(2), 385–400, doi:10.1017/S0022112065000824. 201

Salerno, K. M., D. S. Bolintineanu, G. S. Grest, J. B. Lechman, S. J. Plimpton, I. Srivastava, and L. E. Silbert (2018), Effect of shape and friction on the packing and flow of granular materials, *Physical Review E*, *98*(5), 050,901, doi:10.1103/PhysRevE.98.050901. 179

Satake, M. (1982), Fabric tensor in granular materials. 187, 188

Savage, S. B. (1998), Analyses of slow high-concentration flows of granular materials, *Journal of Fluid Mechanics*, *377*, 1–26, doi:10.1017/S0022112098002936. 41

Schwager, T., and T. Pöschel (2007), Coefficient of restitution and linear–dashpot model revisited, *Granular Matter*, *9*(6), 465–469, doi:10.1007/s10035-007-0065-z. 74, 81, 82

Seto, R., and G. G. Giusteri (2018), Normal stress differences in dense suspensions, *Journal of Fluid Mechanics*, *857*, 200–215, doi:10.1017/jfm.2018.743. 37, 190, 191, 192

Seto, R., R. Mari, J. F. Morris, and M. M. Denn (2013), Discontinuous Shear Thickening of Frictional Hard-Sphere Suspensions, *Physical Review Letters*, *111*(21), 218,301, doi:10.1103/PhysRevLett.111.218301. 23, 186, 187, 191

Silbert, L. E. (2010), Jamming of frictional spheres and random loose packing, *Soft Matter*, *6*. 155

Silbert, L. E., D. Ertaş, G. S. Grest, T. C. Halsey, D. Levine, and S. J. Plimpton (2001), Granular flow down an inclined plane: Bagnold scaling and rheology, *Physical Review E*, *64*(5), 051,302, doi:10.1103/PhysRevE.64.051302. 17, 32, 33, 34, 38, 56, 58, 59, 62, 68, 81, 84, 85, 100, 102, 103, 115, 132, 137, 190, 191

Silbert, L. E., D. Ertaş, G. S. Grest, T. C. Halsey, and D. Levine (2002a), Analogies between granular jamming and the liquid-glass transition, *Physical Review E*, *65*(5), 051,307, doi:10.1103/PhysRevE.65.051307. 41, 44, 49, 53, 81, 89, 125

Silbert, L. E., D. Ertaş, G. S. Grest, T. C. Halsey, and D. Levine (2002b), Geometry of frictionless and frictional sphere packings, *Physical Review E*, *65*(3), 031,304, doi:10.1103/PhysRevE.65.031304. 41, 45, 48, 50, 81, 139, 153, 155

Silbert, L. E., G. S. Grest, S. J. Plimpton, and D. Levine (2002c), Boundary effects and self-organization in dense granular flows, *Physics of Fluids*, *14*(8), 2637–2646, doi:10.1063/1.1487379. 81

Silbert, L. E., J. W. Landry, and G. S. Grest (2003), Granular flow down a rough inclined plane: Transition between thin and thick piles, *Physics of Fluids*, *15*(1), 1–10, doi:10.1063/1.1521719. 68, 114

Silbert, L. E., A. J. Liu, and S. R. Nagel (2005), Vibrations and Diverging Length Scales Near the Unjamming Transition, *Physical Review Letters*, *95*(9), 098,301, doi:10.1103/PhysRevLett.95.098301. 41, 46, 48, 197

Smilauer, V., and B. Chareyre (2015), DEM Formulation, Zenodo, doi:10.5281/ZENODO.34044. 81

Song, C., P. Wang, and H. A. Makse (2008), A phase diagram for jammed matter, *Nature*, *453*(7195), 629–632, doi:10.1038/nature06981. 16, 22, 25, 41, 45, 48, 49, 50, 51, 125, 153, 154, 155

Srivastava, I., L. E. Silbert, G. S. Grest, and J. B. Lechman (2019), Flow-Arrest Transitions in Frictional Granular Matter, *Physical Review Letters*, *122*(4), 048,003, doi:10.1103/PhysRevLett.122.048003. 38, 54, 55, 87, 94, 124

Srivastava, I., J. B. Lechman, G. S. Grest, and L. E. Silbert (2020), Evolution of internal granular structure at the flow-arrest transition, *Granular Matter*, *22*(2), 41, doi:10.1007/s10035-020-1003-6. 179, 188, 189, 190

Srivastava, I., L. E. Silbert, G. S. Grest, and J. B. Lechman (2021), Viscometric flow of dense granular materials under controlled pressure and shear stress, *Journal of Fluid Mechanics*, *907*, A18, doi:10.1017/jfm.2020.811. 23, 37, 54, 84, 179, 190, 191, 192, 193

Srivastava, I., L. E. Silbert, J. B. Lechman, and G. S. Grest (2022), Flow and arrest in stressed granular materials, *Soft Matter*, *18*(4), 735–743, doi:10.1039/D1SM01344K. 33, 41, 53, 54, 56, 62, 81, 84, 124, 139, 142, 143, 155, 157

Staron, L. (2008), Correlated motion in the bulk of dense granular flows, *Physical Review E*, *77*(5), 051,304, doi:10.1103/PhysRevE.77.051304. 17, 41, 54, 59, 102, 152

Staron, L., and F. Radjai (2005), Friction versus texture at the approach of a granular avalanche, *Physical Review E*, *72*(4), 041,308, doi:10.1103/PhysRevE.72.041308. 41, 57, 80

Staron, L., J.-P. Vilotte, and F. Radjai (2002), Preavalanche Instabilities in a Granular Pile, *Physical Review Letters*, *89*(20), 204,302, doi:10.1103/PhysRevLett.89.204302. 41, 57, 62, 80, 109, 124, 158

Staron, L., P.-Y. Lagrée, and S. Popinet (2012), The granular silo as a continuum plastic flow: The hour-glass vs the clepsydra, *Physics of Fluids*, *24*(10), 103,301, doi:10.1063/1.4757390. 37

Vågberg, D., P. Olsson, and S. Teitel (2017), Shear banding, discontinuous shear thickening, and rheological phase transitions in athermally sheared frictionless disks, *Physical Review E*, *95*(5), 052,903, doi:10.1103/PhysRevE.95.052903, publisher: American Physical Society. 35, 37, 186, 187

Weinhart, T., R. Hartkamp, A. R. Thornton, and S. Luding (2013), Coarse-grained local and objective continuum description of three-dimensional granular flows down an inclined surface, *Physics of Fluids*, *25*(7), 070,605, doi:10.1063/1.4812809. 191

Wyart, M. (2009), On the dependence of the avalanche angle on the granular layer thickness, *EPL (Europhysics Letters)*, *85*(2), 24,003, doi:10.1209/0295-5075/85/24003. 44, 153

Wyart, M., S. R. Nagel, and T. A. Witten (2005), Geometric origin of excess low-frequency vibrational modes in weakly connected amorphous solids, *Europhysics Letters*, *72*(3), 486, doi:10.1209/epl/i2005-10245-5, publisher: IOP Publishing. 16, 41, 46, 47, 48

Xu, N., and C. S. O'Hern (2006), Measurements of the yield stress in frictionless granular systems, *Physical Review E*, *73*(6), 061,303, doi:10.1103/PhysRevE.73.061303. 119

Zaitsev, V. Y., P. Richard, R. Delannay, V. Tournat, and V. E. Gusev (2008), Pre-avalanche structural rearrangements in the bulk of granular medium: Experimental evidence, *EPL (Europhysics Letters)*, *83*(6), 64,003, doi:10.1209/0295-5075/83/64003. 57, 158

RÉPUBLIQUE FRANÇAISE
Liberté
Égalité
Fraternité

Université de Toulouse

Titre : Analyse numérique de l'hystérésis en milieux granulaires sur plan incliné

Mots clés : Milieux granulaires, Hystérésis, Micro-structure, Avalanche, Inertie, Frottement

Résumé : La transition entre le régime d'écoulement dense et le régime statique des milieux granulaires est un enjeu scientifique dans la description de ces milieux pour des applications autant industrielles comme le stockage et transport de minerais que pour des applications géophysique dans la modélisation et prédiction d'avalanches granulaires par exemple. Développer des modèles théoriques permettant de modéliser cette transition de phase est donc majeur pour la physique des milieux granulaires. Cette transition de phase a la particularité de présenter un comportement hystérétique : les conditions de changement d'état dépendent de l'histoire, c'est-à-dire du chemin de contraintes empreinté. Ce phénomène n'est pas pris en compte dans les modèles classique et empêche une description unifié des milieux granulaires dans les régimes solides et liquides. Son origine physique, entre effets d'inertie et frottement des grains, fait aujourd'hui encore débat dans la littérature.
Le présent travail de thèse s'attache à étudier l'hystérésis d'un milieu granulaire idéal dans une configuration de plan incliné rugueux, à partir d'une modélisation par éléments discrets. Le travail s'attache dans un premier temps à étudier qualitativement le long de la couche de grain la réponse du milieu à la contrainte, c'est-à-dire à l'angle d'inclinaison du plan, mettant en évidence les états en jeu dans cette transition de phase à laquelle est associée l'hystérésis. La dynamique et la statique du milieu sont ensuite caractérisés de manière macroscopique à l'aide des variables d'états classique décrivant la densité et l'écoulement du système. Une description de la micro-structure du système est aussi développée afin de caractériser ces régimes, elle met en évidence l'importance du réseau de contact et plus particulièrement de l'évolution du nombre moyen de contacts entre grains avec l'angle d'inclinaison. L'effet de la dissipation collisionnelle est étudié et aucun effect notable n'est observé sur les angles critiques définissant les conditions de stabilité du système ainsi que sur leur difference qui quantifie l'hystérésis. Le frottement a, en revanche, un effet majeur sur ces quantités. Son effet est alors quantifié et montre que ce mécanisme de dissipation est, comme attendu, centrale dans la transition de phase et l'hystérésis.
Dans un second temps, le système de grains est immergé dans un fluide au repos afin de quantifier l'effet du fluide sur le milieu granulaire au premier ordre. Les résults permettent de montre un effet non négligeable de variation d'inertie des grains mettant en évidence un effet combiné de l'inertie et du frottement sur l'hystérésis et permettant de rationaliser les différents résultats de la littérature. Ensuite, les angles critiques ainsi que l'hystérésis sont charactérisés à l'aide de l'évolution de la micro-structure au niveau des transitions de phase lorsque sont variés le frottement et l'inertie des grains.
Finallement, l'absence d'effet de dissipation par collisions couplé avec l'effet combiné entre inertie et frottement permet d'établir une vision plus claire de l'origine de l'hystérésis dans l'optique de développer des modèles continus décrivant ce phénomène.

Title: Numerical analysis of hysteresis in granular media down inclined plane

Key words: Granular media, Hysteresis, Micro-structure, Jamming, Inertia, Friction

Abstract: The transition between dense flow and static granular regimes is a major scientific challenge in the description of granular media, both for industrial applications such as mineral storage and transport, and for geophysical applications such as the modeling and prediction of granular avalanches. Developing theoretical models for this phase transition is therefore of major importance for the physics of granular media. A particular feature of this phase transition is its hysteretic behavior: the conditions of transition between both regimes depend on the history, i.e. the stress path. This phenomenon is not taken into account in conventional models, and prevents a unified description of granular media in both solid and liquid regimes. Its physical origin, between inertia effects and grain friction, is still debated in the literature.
The aim of this work is to study the hysteresis of an ideal granular medium in a rough inclined plane configuration, using discrete element modeling. The work begins with a qualitative study of the response of the medium along the grain layer to stress, i.e. to the angle of inclination of the plane, highlighting the states involved in this phase transition at which hysteresis is associated. The dynamics and statics of the medium are then characterized macroscopically using classical state variables describing the density and flow of the system. A description of the micro-structure of the system is also developed to characterize these regimes, highlighting the importance of the contact network and, more specifically, the evolution of the average number of contacts between grains with the angle of inclination. On the one hand, the effect of collisional dissipation was studied and no significant effect was observed on the critical angles defining the system's stability conditions, or on their difference, which quantifies hysteresis. Friction, on the other hand, has a major effect on these quantities. Its effect is then quantified and shows that this dissipation mechanism is, as expected, central to the phase transition and hysteresis.
In a second step, the grain system is immersed in a fluid at rest to quantify the effect of the fluid on the granular medium at first order. The results show a non-negligible effect of inertia variation highlighting a combined effect of inertia and friction on hysteresis and rationalizing the various results reported in the literature. Then, critical angles and hysteresis are characterized by the evolution of the micro-structure at phase transitions when friction and grains inertia are varied.
Finally, the absence of collisional dissipation coupled with the combined effect of inertia and friction provides a clearer picture of the origin of hysteresis, with a view to developing continuous models to describe this phenomenon.